



Quantification of cardiac motion and deformation from three-dimensional tagged MRI on data acquired on Philips scanners

Yitian Zhou

► To cite this version:

Yitian Zhou. Quantification of cardiac motion and deformation from three-dimensional tagged MRI on data acquired on Philips scanners. Medical Imaging. INSA Lyon, 2017. English. NNT: . tel-01936983v1

HAL Id: tel-01936983

<https://theses.hal.science/tel-01936983v1>

Submitted on 27 Nov 2018 (v1), last revised 10 Oct 2023 (v2)

HAL is a multi-disciplinary open access archive for the deposit and dissemination of scientific research documents, whether they are published or not. The documents may come from teaching and research institutions in France or abroad, or from public or private research centers.

L'archive ouverte pluridisciplinaire **HAL**, est destinée au dépôt et à la diffusion de documents scientifiques de niveau recherche, publiés ou non, émanant des établissements d'enseignement et de recherche français ou étrangers, des laboratoires publics ou privés.



INSA

N°d'ordre NNT :

THESE de DOCTORAT DE L'UNIVERSITE DE LYON
opérée au sein de
L'Institut National des Sciences Appliquées de Lyon

Ecole Doctorale N° EDA160
ELECTRONIQUE, ELECTROTECHNIQUE, AUTOMATIQUE (EEA)

Spécialité de doctorat : Traitement du Signal et de l'Image

Soutenue publiquement le 03/07/2017, par :
(Yitian ZHOU)

Quantification du mouvement et de la déformation cardiaques à partir d'IRM marquée tridimensionnelle sur des données acquises par des imageurs Philips

Devant le jury composé de :

BLOCH Isabelle, Professeur des Universités, TELECOM ParisTech
BIJNENS Bart, Professeur des Universités, Pompeu Fabra University
THIRAN Jean-Philippe, Professeur des Universités, EPFL
DE CRAENE Mathieu, Ingénieur de recherche, Philips

Rapporteur
Rapporteur
Examinateur
Examinateur

BERNARD Olivier, Maître de Conférences, INSA-LYON
FRIBOULET Denis, Professeur des Universités, INSA-LYON

Co-directeur de thèse
Directeur de thèse

Département FEDORA – INSA Lyon - Ecoles Doctorales – Quinquennal 2016-2020

SIGLE	ECOLE DOCTORALE	NOM ET COORDONNEES DU RESPONSABLE
CHIMIE	CHIMIE DE LYON http://www.edchimie-lyon.fr Sec : Renée EL MELHEM Bat Blaise Pascal 3 ^e etage secretariat@edchimie-lyon.fr Insa : R. GOURDON	M. Stéphane DANIELE Institut de Recherches sur la Catalyse et l'Environnement de Lyon IRCELYON-UMR 5256 Équipe CDFA 2 avenue Albert Einstein 69626 Villeurbanne cedex directeur@edchimie-lyon.fr
E.E.A.	ELECTRONIQUE, ELECTROTECHNIQUE, AUTOMATIQUE http://edeea.ec-lyon.fr Sec : M.C. HAVGOUDOUKIAN Ecole-Doctorale.eea@ec-lyon.fr	M. Gérard SCORLETTI Ecole Centrale de Lyon 36 avenue Guy de Collongue 69134 ECULLY Tél : 04.72.18 60.97 Fax : 04 78 43 37 17 Gerard.scorletti@ec-lyon.fr
E2M2	EVOLUTION, ECOSYSTEME, MICROBIOLOGIE, MODELISATION http://e2m2.universite-lyon.fr Sec : Sylvie ROBERJOT Bât Atrium - UCB Lyon 1 04.72.44.83.62 Insa : H. CHARLES secretariat.e2m2@univ-lyon1.fr	M. Fabrice CORDEY CNRS UMR 5276 Lab. de géologie de Lyon Université Claude Bernard Lyon 1 Bât Géode 2 rue Raphaël Dubois 69622 VILLEURBANNE Cédex Tél : 06.07.53.89.13 cordey@univ-lyon1.fr
EDISS	INTERDISCIPLINAIRE SCIENCES-SANTE http://www.ediss-lyon.fr Sec : Sylvie ROBERJOT Bât Atrium - UCB Lyon 1 04.72.44.83.62 Insa : M. LAGARDE secretariat.ediss@univ-lyon1.fr	Mme Emmanuelle CANET-SOULAS INSERM U1060, CarMeN lab, Univ. Lyon 1 Bâtiment IMBL 11 avenue Jean Capelle INSA de Lyon 696621 Villeurbanne Tél : 04.72.68.49.09 Fax : 04 72 68 49 16 Emmanuelle.canet@univ-lyon1.fr
INFOMATHS	INFORMATIQUE ET MATHEMATIQUES http://infomaths.univ-lyon1.fr Sec : Renée EL MELHEM Bat Blaise Pascal, 3 ^e étage Tél : 04.72. 43. 80. 46 Fax : 04.72.43.16.87 infomaths@univ-lyon1.fr	M. Luca ZAMBONI Bâtiment Braconnier 43 Boulevard du 11 novembre 1918 69622 VILLEURBANNE Cedex Tél : 04 26 23 45 52 zamboni@maths.univ-lyon1.fr
Matériaux	MATERIAUX DE LYON http://ed34.universite-lyon.fr Sec : Marion COMBE Tél: 04-72-43-71-70 -Fax : 87.12 Bat. Direction ed.materiaux@insa-lyon.fr	M. Jean-Yves BUFFIERE INSA de Lyon MATEIS Bâtiment Saint Exupéry 7 avenue Jean Capelle 69621 VILLEURBANNE Cedex Tél : 04.72.43 71.70 Fax 04 72 43 85 28 Ed.materiaux@insa-lyon.fr
MEGA	MECANIQUE, ENERGETIQUE, GENIE CIVIL, ACOUSTIQUE http://mega.universite-lyon.fr Sec : Marion COMBE Tél: 04-72-43-71-70 -Fax : 87.12 Bat. Direction mega@insa-lyon.fr	M. Philippe BOISSE INSA de Lyon Laboratoire LAMCOS Bâtiment Jacquard 25 bis avenue Jean Capelle 69621 VILLEURBANNE Cedex Tél : 04.72.43.71.70 Fax : 04 72 43 72 37 Philippe.boisse@insa-lyon.fr
ScSo	ScSo* http://recherche.univ-lyon2.fr/scso/ Sec : Viviane POLSINELLI Brigitte DUBOIS Insa : J.Y. TOUSSAINT Tél : 04 78 69 72 76 viviane.polsinelli@univ-lyon2.fr	M. Christian MONTES Université Lyon 2 86 rue Pasteur 69365 LYON Cedex 07 Christian.montes@univ-lyon2.fr

*ScSo : Histoire, Géographie, Aménagement, Urbanisme, Archéologie, Science politique, Sociologie, Anthropologie

Abstract

Cardiovascular disease is one of the major causes of death worldwide. A number of heart diseases, such as hypertrophy, dilated cardiomyopathy and myocardial infarction, can be diagnosed through the analysis of cardiac images after quantifying shape and function. Recently, there is a surge in the development of fast 3D cardiac imaging techniques in both ultrasound (US) and magnetic resonance (MR) imaging, making it possible to quantify myocardial motion and strain fully in 3D. However, the application of these deformation quantification algorithms in clinical routine is somewhat held back by the lack of a solid validation. These quantification algorithms need to be thoroughly validated before being used in clinics. In this thesis, we mainly introduce a fast 3D tagged MR quantification algorithm, as well as a novel pipeline for generating synthetic cardiac US and MR image sequences for validation purposes. The main contributions are described below.

First, we proposed a novel 3D extension of the well-known harmonic phase tracking method. The point-wise phase-based optical flow tracking was combined with an anatomical regularization model in order to estimate anatomically coherent myocardial motions. In particular, special efforts were made to ensure a reasonable radial strain estimation by enforcing myocardial incompressibility through the divergence theorem. We tuned the parameters on a synthetic tagged MR dataset. The proposed HarpAR algorithm was further evaluated on both healthy volunteers and patients having different levels of ischemia. On volunteer data, the tracking accuracy was found to be as accurate as the best candidates of a recent benchmark. On patient data, strain dispersion was shown to correlate with the extent of transmural fibrosis. Besides, the ischemic segments were distinguished from healthy ones from the strain curves.

Second, we proposed a simulation pipeline for generating realistic synthetic cardiac US, cine and tagged MR sequences from the same virtual subject. Template sequences, a state-of-the-art electro-mechanical (E/M) model and physical simulators were combined in a unified framework. The E/M model was exploited for simulating groundtruth cardiac motion fields. The template sequences were registered to the simulations by a novel warping technique aimed at ensuring a synthetic motion consistent with the E/M model and a smooth transition between the myocardium and the background. Finally, backscattering amplitudes and effective proton densities were derived from the warped templates respectively for US and MR simulations to exploit the corresponding physical simulators for generating image data. In total, we simulated 18 virtual patients (3 healthy, 3 dyssynchrony and 12 ischemia), each with synthetic sequences of 3D cine MR, US and tagged MR. The synthetic images were assessed both qualitatively and quantitatively. They showed realistic image textures similar to real acquisitions. Besides, both the ejection fraction and regional strain values are in agreement with reference values published in the literature.

Finally, we showed a preliminary benchmarking study using the synthetic database. The HarpAR algorithm initially developed for processing tagged MR was extended to a generic motion tracking algorithm named as gHarpAR. We performed a comparison between gHarpAR and another tracking algorithm SparseDemons using the virtual patients simulated in this thesis. The results showed that SparseDemons outperformed gHarpAR in processing cine MR and US images. Regarding tagged MR, both methods obtained similar accuracies on motion and two strain components (circumferential and longitudinal). However, gHarpAR quantified radial strains more accurately, thanks to the myocardial incompressibility constraint. We conclude that motion quantification solutions can be improved by designing them according to the image characteristics of the modality and that a solid evaluation framework can be a key asset in comparing different algorithmic options.

Résumé

Les maladies cardiovasculaires sont parmi les principales causes de mortalité à l'échelle mondiale. Un certain nombre de maladies cardiaques (hypertrophie, cardiomyopathie dilatée, infarctus du myocarde, *etc*) peuvent être identifiées et localisées par l'analyse du mouvement et de la déformation cardiaques à partir de l'imagerie médicale. Dernièrement, le développement des techniques rapides d'imagerie cardiaque en échographie (US) et imagerie par résonance magnétique (IRM) permet de quantifier le mouvement et la déformation entièrement en 3D. Cependant, le transfert de ces techniques dans les centres cliniques est freiné par le manque d'outils de quantification efficaces et fiables. Les algorithmes de suivi de mouvements doivent être soigneusement validés avant d'être utilisés en routine clinique. Dans cette thèse, nous introduisons un algorithme de quantification appliquée aux images IRM marquées. Nous présentons ensuite un pipeline de simulation qui génère des séquences cardiaques synthétiques (US et IRM) pour la validation de l'algorithme de suivi de mouvements. Les principales contributions sont décrites ci-dessous.

Tout d'abord, nous avons proposé une nouvelle extension 3D de la méthode de suivi de la phase harmonique. Le suivi de flux optique en utilisant la phase a été combiné avec un modèle de régularisation anatomique afin d'estimer les mouvements cardiaques à partir des images IRM marquées. En particulier, des efforts ont été faits pour assurer une estimation précise de la déformation radiale en imposant l'incompressibilité du myocarde. Nous avons réglé les paramètres de modèle sur les données synthétiques. L'algorithme que nous avons proposé (dénommé HarpAR) a ensuite été évalué sur des volontaires sains et des patients ayant différents niveaux d'ischémie. HarpAR a obtenu la précision de suivi comparable à quatre autres algorithmes de l'état de l'art. Sur les données cliniques, la dispersion des déformations est corrélée avec le degré de fibroses. De plus, les segments ischémiques sont distingués des segments sains en analysant les courbes de déformation.

Deuxièmement, nous avons proposé un nouveau pipeline de simulation pour générer des séquences synthétiques US et IRM pour le même patient virtuel. Les séquences réelles, un modèle électromécanique (E/M) et les simulateurs physiques sont combinés dans un cadre unifié. Le modèle E/M est utilisé pour simuler les champs de mouvement de la vérité terrain. Les séquences réelles ont été recalées aux simulations E/M par une nouvelle technique de recalage visant à assurer un mouvement cohérent avec le modèle E/M et une transition lisse entre le myocarde et les structures environnantes. Enfin, les amplitudes de rétrodiffusion et les densités de protons sont dérivées des séquences déformées respectivement pour les simulations US et IRM afin d'exploiter les simulateurs physiques pour générer des images. Au total, nous avons simulé 18 patients virtuels (3 sains, 3 dyssynchronies et 12 ischémies), chacun avec des séquences synthétiques IRM cine, IRM marquée et US 3D. Les images synthétiques ont été évaluées qualitativement et quantitativement. Elles ont des textures d'images réalistes qui sont similaires aux acquisitions réelles. De plus, nous avons également évalué les propriétés mécaniques des simulations. Les valeurs de la fraction d'éjection et de la déformation locale sont cohérentes avec les valeurs de référence publiées dans la littérature.

Enfin, nous avons montré une étude préliminaire de benchmarking en utilisant les images synthétiques. L'algorithme HarpAR a été généralisé, donnant lieu à un algorithme de suivi de mouvement générique dénommé gHarpAR. Il a été comparé avec un autre algorithme générique SparseDemons en termes de précision sur le mouvement et la déformation. Les résultats montrent que SparseDemons surclasse gHarpAR en IRM cine et US. En IRM marquée, les deux méthodes ont obtenu des précisions similaires sur le mouvement et deux composants de déformations (circonférentielle et longitudinale). Toutefois,

gHarpAR estime la déformation radiale de manière plus précise, grâce à la contrainte d'incompressibilité du myocarde. Nous arrivons donc à la conclusion que les solutions de suivi de mouvements doivent être développées en prenant compte de la caractéristique d'image de la modalité donnée.

Acknowledgment

I would like to thank everyone who gave me their help and support during the past five years of my Master and Ph.D. study in France.

First and foremost, I would like to thank my supervisors Dr. Mathieu De Craene, Dr. Olivier Bernard and Prof. Denis Friboulet. Thanks for giving me this excellent opportunity to work on this exciting project. Your insightful and inspiring guidance, continuous support and encouragement are indispensable to the accomplishment of this thesis, which I cannot express in words. I feel really lucky to have you as my supervisors. Mathieu is maybe the kindest person I have ever met. Your kindness, generosity, as well as scientific attitude and critical thinking, have greatly influenced me over the past years. Olivier's scientific rigorousness, enthusiasm to research, openness to discussion, hard-working spirit and attention to details are unmatched. Thank you very much for all the support and help that you have done for me. Prof. Denis Friboulet is maybe the most enthusiastic person I have ever met. Your big smile and laughter taught us to be always positive and optimistic towards life and work.

I specially express my thanks to Prof. Isabelle Bloch and Prof. Bart Bijnens for reviewing this manuscript and Prof. Jean-Philippe Thiran for accepting to join the jury of my PhD thesis.

I want to acknowledge Dr. Pascal Allain, our project leader and Mr. Nicolas Villain, the head of Philips Research Paris (Medisys), for supporting my master and PhD theses financially. Besides, thank you very much for providing me opportunities to attend several international conferences which significantly stimulated my interest for research. Also, I want to thank Mr Olivier Beuf, the director of the Creatis lab, for providing us an amazing working environment, surrounded by knowledge and fantastic colleagues. Indeed, I am very happy and proud to be part of your team.

I would like to thank all my colleagues in Philips and Creatis for their help during my stay in France. Especially, I want to thank Mrs. Nathalie Bailly, for her help on all the administrative matters during the past four years. I also want to thank Mr. Jean Michel Rouet, for every advice he gave me on the IT services. Besides, it was a great pleasure sharing the office space, the air, the lunches, the coffee breaks, *etc* with a lot of friendly colleagues including Caroline Raynaud, Mariana Nogueira, Eric Lluch, Hadrien Bertrand, Alexandre This, Hernan Morales, Mathieu De Craene, Romain Lacroix and Bo Zhang. Thank you for teaching me the French culture, especially the French language. Besides, thank Bo Zhang for introducing me some traditional Chinese medical theories which are really helpful for reducing the stress. In addition, I would like to thank Dr. Miaomiao Zhang and Dr. Ge Xin. Indeed, it was a great pleasure to encounter you at Lyon.

Last but not least, my sincere thanks go to my family for their love since December 1989. Thanks my parents for bringing me up and encouraging me to pursue my postgraduate studies overseas. Thanks for your support and care in the past years. I also would like to express my deepest gratitude to my wife Fan. Thank you for all the love, support and encouragements you gave me. Thanks for all the happiness you have brought me.

Contents

Abstract	iii
Résumé	iv
Acknowledgment	vi
Contents	ix
I Introduction	1
1 Introduction	3
1.1 Motivation	3
1.2 Objectives	4
1.3 Thesis organization	5
II Background	7
2 Cardiac motion tracking	9
2.1 Introduction	9
2.2 Echocardiography	12
2.2.1 Image characteristics	13
2.2.2 Speckle tracking	13
2.3 Cardiac cine MR	15
2.3.1 Image characteristics	15
2.3.2 Motion tracking from cine MR	16
2.4 Cardiac tagged MR	17
2.4.1 Image characteristics	18
2.4.2 Motion tracking from tagged MR	20
2.5 Summary	22
3 The validation of cardiac motion tracking	25
3.1 Introduction	25
3.2 Using dedicated imaging techniques as reference	26
3.3 Imaging physical phantoms	27
3.4 Generating synthetic images	27
3.4.1 Simulation of cine MR images	28
3.4.2 Simulation of tagged MR images	28
3.4.3 Simulation of echocardiographic images	30

3.5	Summary	31
III	Contributions	33
4	3D harmonic phase tracking with anatomical regularization	35
4.1	Introduction	35
4.1.1	The open question and our contributions	36
4.2	Data Acquisition & Preprocessing	37
4.2.1	3D Tagged MR acquisition	37
4.2.2	Segmentation of LV	37
4.2.3	Mesh model	38
4.3	Tracking methodology	40
4.3.1	HARP tracking	41
4.3.2	Motion model	44
4.3.3	Regularization by window-weighted regression	44
4.3.4	Computing apex motion <i>a posteriori</i>	48
4.3.5	Multi-resolution framework	48
4.4	Generation of synthetic images	49
4.4.1	Registering LV meshes to real tagged MR images	49
4.4.2	Warping real tagged MR images by forces computed from meshes	50
4.5	Results	51
4.5.1	Synthetic images	51
4.5.2	Volunteer data sets	53
4.5.3	Patient data sets	54
4.6	Discussion	58
4.7	Summary	61
5	Multi-modal simulation of virtual patients	63
5.1	Introduction	63
5.2	Methodology	65
5.2.1	Template image sequences	66
5.2.2	MR modeling	67
5.2.3	Cardiac motion	70
5.2.4	Template warping	71
5.2.5	US simulation	76
5.3	Result	77
5.3.1	Image properties: qualitative assessment	77
5.3.2	Image properties: quantitative assessment	77
5.3.3	Mechanical properties	84
5.4	Discussion	85
5.5	Summary	89
6	A generic HarpAR algorithm and a preliminary benchmarking study	91
6.1	Introduction	91
6.2	Phase-based registration of tagged MR images	92
6.2.1	Introduction	92
6.2.2	Preprocessing	93
6.2.3	Methodology	94
6.2.4	Results	97

6.2.5	Conclusion and discussion	98
6.3	A generalized version of HarpAR: the gHarpAR	99
6.3.1	The generic anatomical registration algorithm gHarpAR	99
6.3.2	Results on the simulated virtual patients	100
6.3.3	Conclusion and discussion	105
6.4	Summary	107
IV	Conclusions and Perspectives	109
7	Conclusions and Perspectives	111
7.1	Conclusions	111
7.2	Perspectives	112
Résumé en français		117
8 Résumé en français		117
Appendix		173
A Appendix 1		173
A.1	Computation of the spatial derivatives and the temporal differences of the true phase	173
B Appendix 2		175
B.1	Compute RF flip angles	175
B.2	Refine the tracking of RV	175
B.3	Colormap used for displaying strain curves	176
Publications		177
Bibliography		190

I Introduction

Chapter 1

Introduction

In this chapter, the motivation of the thesis is introduced first. Then the research objectives of this work are outlined. Finally, the organization of the dissertation is presented.

1.1 Motivation

Cardiovascular disease is one of the major causes of death globally and this trend is projected to persist in the coming years [Mendis (2014)]. A number of heart diseases (hypertrophy, dilated cardio-myopathy, myocardial infarction diseases, *etc*), may be identified and localized by the analysis of cardiac motion and deformation. By comparing the quantified deformation values with the reference ones, myocardial lesions can be eventually detected. In order to quantify the cardiac motion and deformation, a number of imaging techniques have been developed in the past decades. Several modalities including ultrasound [Sheikh *et al.* (1991)], cine magnetic resonance (MR) imaging [Sakuma *et al.* (1993)], tagged MR [Axel and Dougherty (1989)a] and computed tomography [Ropers *et al.* (2003)] give access to cine loops of cardiac images over the heart cycle. Accordingly, a number of motion tracking methodologies were developed for post-processing these acquisitions [Reisner *et al.* (2004)] [Osman *et al.* (2000)] [Florack *et al.* (2007)] [Hor *et al.* (2011)].

Recently, there is a surge in the development of fast 3D cardiac imaging techniques. For example, the introduction of 2D matrix array transducer technology has made volumetric ultrasound imaging in clinical routine feasible [Mor-Avi *et al.* (2011)]. Also, on tagged MR, an accelerated CSPAMM acquisition technique was proposed where three sequences of tagged volumes were acquired in only three breath-hold of 18 heartbeats duration each

[[Rutz et al. \(2008\)](#)]. The advances on imaging techniques have stimulated research groups to develop fast and reliable 3D motion tracking algorithms adapted to each modality. Efficient 3D speckle tracking algorithms have been proposed in [[De Craene et al. \(2011\)](#)] [[Somphone et al. \(2013\)](#)] [[Heyde et al. \(2016\)a](#)]. Cine MR feature tracking [[Hor et al. \(2010\)](#)] [[Hor et al. \(2011\)](#)] [[Maret et al. \(2009\)](#)] was developed for the fast quantification of myocardial strains from cine MR sequences. However, for the recent 4D multi-channel tagged MR protocol [[Rutz et al. \(2008\)](#)], much fewer research efforts have been made to develop the corresponding post-processing tools [[Shi et al. \(2012\)](#)] [[De Craene et al. \(2011\)](#)]. An effective and fast quantification algorithm well adapted to this acquisition protocol is in strong demand to promote the use of this accelerated tagging acquisition in both research and clinics.

In fact, despite the recent achievements in both the 3D cardiac imaging technologies and the associated quantification solutions, their application to clinical practice is more or less held back by the lack of a solid validation. The 3D motion tracking algorithms must be thoroughly validated before being transferred to clinics. The quantitative validation based on segmental myocardial deformations is of great interest since strain is useful for the early detection of heart diseases. Several groups [[De Craene et al. \(2013\)](#)] [[Prakosa et al. \(2013\)](#)] [[Alessandrini et al. \(2015\)](#)] already worked towards this objective by generating synthetic echocardiography and cine MR sequences. Motion tracking algorithms were then evaluated on the synthetic data, *e.g.* the benchmarking of 3D speckle tracking presented in [[Alessandrini et al. \(2016\)](#)]. Currently, to the best of our knowledge, little work has been done for synthesizing 3D tagged MR. Moreover, most of the existing simulation strategies generated images of a *single* modality for the virtual patient. Indeed, generating synthetic sequences of *multiple* imaging modalities (ultrasound, cine MR, tagged MR) for the same given virtual subject is of significant importance. This would not only permit a more comprehensive validation of motion tracking algorithms by evaluating its performance across different modalities, but also be useful for comparing the established cardiac imaging modalities, *e.g.* comparing cine MR feature tracking [[Hor et al. \(2011\)](#)] against tagged MR harmonic phase tracking [[Osman et al. \(1999\)](#)] and 3D speckle tracking [[Somphone et al. \(2013\)](#)] using *dense* strain measures.

1.2 Objectives

In the above-described context, we summarize here the objectives of this work:

- we aim to develop a methodology that combines the benefits of the state-of-the-art algorithms for the quantification of myocardial motion and deformation from the recently introduced accelerated 3D CSPAMM tagged MR acquisitions [[Rutz et al. \(2008\)](#)].
- we aim to provide for the research community an open-access database consisting of synthetic multi-modal cardiac image sequences including simulated echocardiog-

raphy, cine MR and tagged MR acquisitions. One of the first applications of this synthetic database is to validate 3D cardiac motion tracking algorithms.

- we aim to show a preliminary benchmarking example using the simulated synthetic multi-modal cardiac image sequences.

1.3 Thesis organization

The dissertation is organized as follows.

In Chapter 1, the motivation and objectives of this work are introduced. The motivation behind this work is to develop a fast 3D motion and strain quantification method for post-processing the 3D tagging acquisitions [[Rutz et al. \(2008\)](#)]. Besides, we aim to generate multi-modal synthetic cardiac image sequences for validating cardiac motion tracking.

In Chapter 2, the state-of-the-art on cardiac motion tracking is introduced. Three most representative imaging modalities (echocardiography, cine MR and tagged MR) are presented in detailed subsections.

In Chapter 3, we introduce the different strategies used for validating 3D cardiac motion tracking algorithms. We concentrate on the generation of synthetic image sequences, which we consider as the most effective approach currently.

In Chapter 4, we present a novel 3D extension of the harmonic phase tracking [[Osman et al. \(1999\)](#)] for quantifying anatomically coherent cardiac deformations from 3D tagged MR acquisitions.

In Chapter 5, we propose a simulation pipeline for the generation of multi-modal synthetic cardiac image sequences for the same virtual patient. This pipeline aims at simulating a number of multi-modal virtual patients for validation purpose.

In Chapter 6, a preliminary benchmarking study is presented. The tracking method introduced in Chapter 4 is first extended to a generic algorithm and then compared against another generic motion tracking algorithm SparseDemons [[Somphone et al. \(2013\)](#)] using the synthetic database generated in Chapter 5.

In Chapter 7, the whole work is summarized, and perspective future work is discussed.

II Background

Chapter 2

Cardiac motion tracking

2.1 Introduction

Globally, cardiovascular diseases (CVD) are the number one cause of death and are expected to have an increasing prevalence in the coming years [Roth *et al.* (2015)]. An estimated 17.5 million people died from CVDs in 2012, representing 31% of all global deaths [Mendis (2014)]. Of these deaths, an estimated 7.4 million were due to coronary heart disease and 6.7 million were due to stroke. Assuming similar growth rates, by 2030 an estimated 23.6 million people will die from cardiovascular diseases in the world [Wang and Amini (2012)].

Heart disease, such as myocardial ischemia and ventricular dyssynchrony, may be identified and localized by the analysis of the cardiac motion and deformation. Early efforts used surgical implantation and tracking of radiopaque markers with X-ray imaging for quantifying the ventricular motion in canine hearts [Garrison *et al.* (1982)]. Such techniques are invasive and affect the regional motion pattern of the heart during the marker tracking process, thus not feasible clinically. With the advent of more advanced imaging techniques, non-invasive diagnosis techniques based on inspecting medical images were developed and have been widely used in clinical practice. Several modalities, such as echocardiography [Sheikh *et al.* (1991)], magnetic resonance (MR) imaging and cardiac computed tomography (CT) have been applied to cardiac function analysis [Mondillo *et al.* (2011)] [Osman *et al.* (1999)] [Tavakoli and Sahba (2014)]. From medical images acquired by these modalities, physicians can monitor and assess the progression of CVD so that effective procedures for the disease treatment can be developed accordingly.

So far, cardiac motion and strain imaging have been primarily based on echocardiog-

raphy and MR imaging. Cardiac CT has proven to be useful for obtaining a static segmentation at a high spatial resolution. It is also used for the segmentation of the coronary tree after contrast injection. Additionally, cardiac multi-detector computed tomography (MDCT) [Ropers *et al.* (2003)] is able to acquire dynamic images of the heart as a detailed source of information, it presents however several inherent limitations, if compared with echocardiography and MR imaging: 1) CT relies on ionizing radiation for delivering image contrast, which is harmful to human tissues; 2) the temporal resolution of MDCT is lower, hence hindering cardiac motion tracking since fewer frames are available within the same cardiac cycle; and 3) although the cardiac contour is prominent in CT images, the myocardial wall lacks a discernible pattern or "markers" that increases the difficulty for motion tracking [Tavakoli and Sahba (2014)]. As a result, cardiac CT is not as widely available as echocardiography and MR imaging for motion analysis. In this section, we therefore concentrate on cardiac motion tracking methods from echocardiography and cardiac MR.

Traditionally, cardiac deformation is assessed from medical images by visual inspections of an expert and each myocardial segment is then assigned a wall motion score. However, manual motion analysis similar to this is time-consuming and suffers from inter- and intra-observer variabilities. Automatic motion tracking softwares can help reducing the workload of the clinicians. Moreover, the medical conditions can be interpreted more objectively. Most of the motion tracking algorithms assess cardiac function through two categories of indexes: global and regional indexes. Global indexes include cavity volume, ejection fraction, cardiac output *etc*. They are important indexes that reveal the overall performance of the heart in terms of supplying oxygenated blood to the body. Regional indexes such as strain and left ventricle (LV) torsion may prove beneficial for the diagnosis of disease and evaluation of severity and the quantification of treatment effect [Wang and Amini (2012)]. Combining the global and regional analyses could lead to a reliable evaluation of the cardiac function.

Regarding the local motion tracking, echocardiography is one of the most common modality in clinics. The ultrasound is safe since no radiation is involved, real-time, portable and much cheaper compared to other imaging devices such as MR and CT. The speckle noises inherent to ultrasound imaging can be used as natural markers that move with the myocardium. The speckles remain locally stable during a few consecutive frames. Therefore, the underlying myocardial motion can be accurately recovered by tracking those speckles, both the global ejection fraction and local myocardial strains can be further derived from the tracking field. Recently, with the development of 2D matrix transducer technology, 3D echocardiography is becoming more and more common in clinical facilities [Mor-Avi *et al.* (2011)] [Alessandrini *et al.* (2015)]. Despite the reduced frame rate compared to 2D ultrasound, it still allows for an accurate quantification of cardiac motion [De Craene *et al.* (2013)]. Regarding the speckle tracking algorithms, a summarized description will be given later in Section 2.2. Cardiac cine MR [Sakuma *et al.* (1993)] is considered as a more advanced modality for assessing global ventricular functions in clinical routine. It has advantages over other modalities such as echocardiography and

tagged MR [Axel and Dougherty (1989)b] in that it provides clearer contrast between the myocardium and the blood pools. This facilitates the segmentation and the tracking of the borders of myocardium, *i.e.* the endocardium and the epicardium. From the trackings, global indexes such as left ventricle ejection fraction can be accurately calculated which allows an elementary assessment of cardiac function. It is more reproducible than echocardiography since it is easier to segment the myocardial borders. However, another characteristic of cardiac cine MR is that the images show nearly constant intensities within the myocardium, hampering somehow the quantification of local indexes such as motion and strain. Although reliable dense tracking field can still be computed by spatial regularizations (see Section 2.3), the absence of any local "markers" could reduce the tracking accuracy. Aside from ultrasound, cardiac tagged MR [Axel and Dougherty (1989)a] is another imaging technique able to quantify reliable local myocardial deformations. In this modality, a specific tagging preparation pulse is composited with conventional MR imaging in order to deliberately create markers (tags) by saturating the tissue magnetizations. Those tags will move alongside the myocardium over the whole sequence. Deformation fields can therefore be accurately reconstructed from tracking those virtual markers. Tagged MR is considered as the gold standard for estimating regional myocardial deformations since it provides the most detailed information about local motion. However, its use in clinical practice is held back by the long acquisition time and the limited spatial resolution for distinguishing tissues. For more details concerning cardiac tagged MR, the reader is referred to Section 2.4 of this chapter.

Despite the rapid developments in both imaging techniques and the associated motion tracking methodologies, the diagnosis and detection of heart diseases from quantifying the global/local indexes is generally limited to 2D. For instance, in clinical routine, dynamic cine MR loops on short-axis slices located at basal, mid and apical levels of the LV are acquired so as to evaluate the global ventricular functions. Accordingly, regional functions are usually assessed by 2D echocardiography or 2D tagged MR from which local deformation values are computed. Nonetheless, 2D cardiac motion tracking suffers from the out-of-plane motion. More specifically, only the motion's projection onto the imaging plane is captured. Both global and regional indexes are then computed from the projected tracking fields and hence may not represent the true deformations. For bypassing this issue, lots of efforts have been made to develop rapid 3D imaging techniques and the corresponding 3D motion tracking solutions. Quantifying motion and strain in 3D is able to capture the true deformation values. However, at the current stage, 3D motion tracking algorithms are rarely used in clinical practice since they have not been rigorously validated. Indeed, a thorough and comprehensive validation work is in demand. The utility of such 3D motion tracking algorithms relies heavily on the reliability and robustness of the quantified indexes, which determines directly their clinical value. The motion tracking needs to be validated both *qualitatively* (*i.e.* visually plausible trackings) and *quantitatively* (accurate global/local quantifications). However, validating motion tracking in 3D poses a number of technical challenges. To discuss the importance of validation in the context

of cardiac motion and deformation indexes, we outline the main existing strategies in a dedicated chapter (Chapter 3) along with our proposed contributions in the development of a multimodal framework (Chapter 5).

2.2 Echocardiography

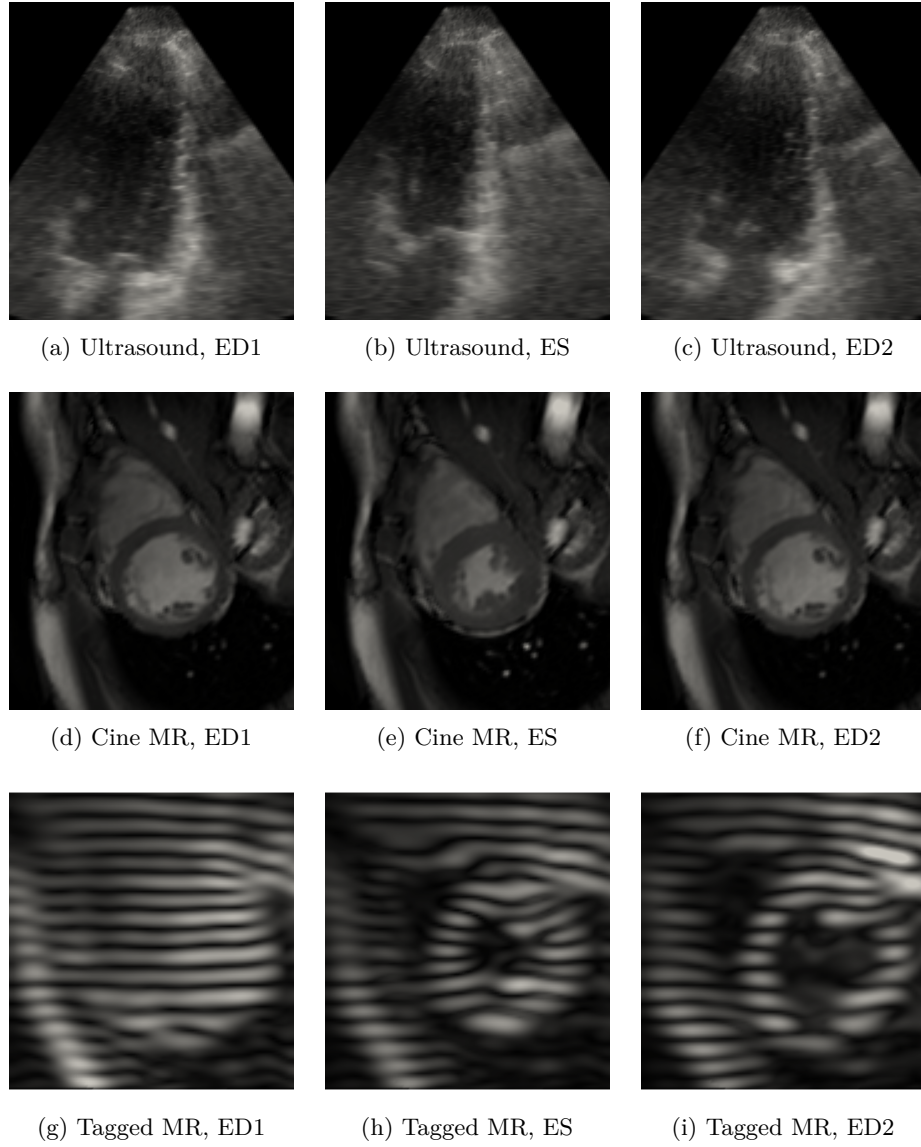


Figure 2.1: The three common imaging modalities used for assessing cardiac function.

Echocardiography is becoming more and more used in cardiac examinations. It has become one of the routine procedures for the diagnosis, management, and follow-up of patients with any suspected or known heart diseases. It can provide a lot of helpful information, from the anatomical details including the size and shape of the heart to the functional measures including the pumping capacity and regional myocardial deformations.

The combination of both the anatomical and the functional information helps clinicians diagnose the various pathological situations. In this thesis, we are most interested in the cardiac motion tracking from ultrasound images. We will give here a brief introduction about the characteristics of cardiac ultrasound and the existing motion tracking algorithms in the following.

2.2.1 Image characteristics

In the fields of cardiology and medical imaging, speckle tracking echocardiography (STE) is an echocardiographic imaging technique that analyzes the motion of tissues in the heart by using the naturally occurring speckle pattern in the myocardium when imaged by ultrasound insonification. 2D STE was introduced for estimating myocardial deformations [[O'Donnell et al. \(1994\)](#)] [[Reisner et al. \(2004\)](#)]. STE represents a noninvasive method of evaluating regional cardiac deformations, which is a valuable tool for the characterization and quantification of local myocardial deformations.

The speckle pattern is a mixture of interference patterns and natural acoustic reflections, refraction and scattering [[Reisner et al. \(2004\)](#)]. The pattern is generated randomly and each region of the myocardium has a unique speckle pattern that allows the region to be traced from one frame to the next. The speckles stay relatively stable, at least during several frames when the acquisition frame rate is high enough compared to the dynamic of the structure of interest. The movement of the kernel across the image can thus be tracked. The speckles are therefore used as natural acoustic markers for "tagging" the myocardial motion during the cardiac cycle. By adopting a frame-to-frame tracking approach, the complete LV wall motion throughout the sequence can be accurately recovered. In principle, speckle tracking can track in both the axial and lateral dimensions. However, the axial resolution of the ultrasound is far better than the lateral. The tracking ability is thus decreased in the lateral direction. Moreover, the lateral resolution decreases with imaging depth, hence further limiting the tracking ability.

Recently, the introduction of 2D matrix array transducer technology has made real-time 3D volumetric ultrasound imaging in clinical routine feasible [[Mor-Avi et al. \(2011\)](#)]. The emergence of this real-time volumetric imaging solves intrinsic shortcomings of the standard 2D modality, such as the presence of out-of-plane motion, problems in the optimal slice selection and the need of geometrical assumptions [[Alessandrini et al. \(2016\)](#)]. By tracking the myocardial motion truly in 3D, regional cardiac function can be evaluated. Consequently, lots of research efforts have been devoted to developing the matched 3D speckle tracking algorithms. We will introduce some of the most representative methods hereafter.

2.2.2 Speckle tracking

Over the last decade, several 3D speckle tracking techniques has been developed in order to quantify regional cardiac deformations in 3D. They can be roughly classified into

four categories. Note that here we only provide a brief introduction. A more detailed analysis of the state-of-the-art on 3D speckle tracking can be found in two recent publications [[De Craene *et al.* \(2013\)](#)] and [[Alessandrini *et al.* \(2016\)](#)].

Block matching

B-mode block matching Block matching algorithms such as [[Duan *et al.* \(2009\)a](#)] and [[Crosby *et al.* \(2009\)](#)] represent the conventional implementations on many existing commercial systems. In these approaches, myocardial tissue is divided in blocks that are tracked throughout the cardiac cycle. For each local block, an exhaustive search is performed over a predefined search window in order to find the most similar patch at the next frame. Similarity can be defined in several ways. For instance, in [[Duan *et al.* \(2009\)a](#)], the authors chose the normalized cross correlation. The independently tracked patch-wise displacements are then regularized after block matching by interpolation and filtering, aiming to ensure a smooth estimate of myocardial motion.

RF block matching The same concept was equally applied to the raw radiofrequency (RF) data (modulated signal derived at the first step of the beamforming process). In [[Lopata *et al.* \(2011\)](#)] and [[Chen *et al.* \(2005\)](#)], block matching was performed on the RF images. Both studies showed that reasonable cardiac deformations could be recovered. However, RF block matching can only handle small deformations [[Chen *et al.* \(2005\)](#)]. The current 3D echocardiographic commercial systems have a relatively low temporal resolution, leading to therefore relatively large deformations between subsequent frames. The applications of RF tracking to clinics remains an issue. Consequently, it still remains unclear whether RF speckle tracking is preferable to the conventional B-mode tracking for this particular task [[Alessandrini *et al.* \(2016\)](#)].

Optical flow

Intensity-based optical flow Optical flow has been applied for contour tracking in 3D ultrasound [[Duan *et al.* \(2006\)](#)]. By assuming that the intensity of a particular point in a moving pattern does not change over the image sequence, local motion vectors are solved either locally on independent image patches or globally using spatial smoothness terms as regularization. The demons algorithms represent a computationally efficient simplification of the optical flow problem [[Thirion \(1998\)](#)] [[Somphone *et al.* \(2013\)](#)]. Somphone *et al.* [[Somphone *et al.* \(2013\)](#)] developed a sparse implementation of the demons algorithms.

Phase-based optical flow Optical flow was applied not only to B-mode intensities but also to phase images [[Alessandrini *et al.* \(2012\)a](#)] [[Alessandrini *et al.* \(2013\)](#)]. Alessandrini *et al.* [[Alessandrini *et al.* \(2013\)](#)] chose to perform the optical flow tracking on monogenic phases computed from the ultrasound intensity images. They showed that the displacement estimated from the monogenic phase is robust to possible variations of the local

image energy. Large deformations were coped with by recursively applying the estimation in a pyramidal refinement scheme.

Elastic image registration

Elastic image registration provides an alternative method to compute a smooth dense deformation field from 3D cardiac ultrasound image sequences [De Craene *et al.* (2011)]. Cardiac motion fields were represented efficiently by a set of B-spline basis functions. Diffeomorphic Free-form deformation models were then used for registering echocardiographic images in time. Recently in [Heyde *et al.* (2016)a], an elastic registration model was proposed to register the ultrasound images resampled in an anatomical space. The ultrasound images were first resampled to an anatomical domain of the heart following the *radial*, *longitudinal* and *circumferential* directions. The resampled images were then registered by a classic free-form deformation algorithm which allowed the further derivation of local motion and strain fields.

Prior model-based tracking

All of the methods mentioned above tracked the cardiac motion without using any prior information. In fact, priors can be embedded in statistical or physical forms in order to improve the motion tracking accuracy [Leung *et al.* (2011)] [Papademetris *et al.* (2002)]. For instance, Leung *et al.* [Leung *et al.* (2011)] used a statistical model of cardiac motion for regularizing optical flow tracking results. Similarly, in [Papademetris *et al.* (2002)], the authors used a transversely isotropic linear elastic model for regularizing shape-based tracking *correspondences*.

2.3 Cardiac cine MR

In the field of MRI, cardiac cine MRI [Sakuma *et al.* (1993)] is considered as the reference modality for evaluating global heart function by quantifying global indexes such as ejection fraction. Cine studies are typically obtained by repeatedly imaging 2D slices through the cardiac cycle. Between 10 and 30 cardiac phases are usually acquired. To fully evaluate the entire heart, separate cine image sets at various locations must be obtained. For example, a standard cine study might include three sets of short-axis images (base, mid-ventricle, and apex). Retrospective ECG-gating [Fischer *et al.* (1999)] is performed so that imaging data can be assigned to the same phase of the cardiac cycle.

2.3.1 Image characteristics

The base pulse sequence used for acquiring cine MR image data is typically a balanced steady-state free precession (bSSFP) gradient echo method [Scheffler and Lehnhardt (2003)]. It generates high intra-vascular signal relative to other tissues due to the intrinsically high T2/T1 ratio of blood. This characteristic helps clinicians distinguish

the myocardium from the neighboring blood pools. Besides, the structure of the bSSFP sequence allows very short TR and TE values to be used, thus multiple echoes can be acquired during a single heart beat. Dynamic 2D slice loops can be acquired during the cardiac cycle.

Cardiac cine MR is widely used in clinical practice due to its high soft-tissue contrast, especially between the myocardium and the neighboring blood pools as shown in Fig. 2.1. The endocardium and epicardium can therefore be accurately segmented. The temporal resolution is also high enough to do motion tracking over the cardiac cycle. By tracking the endo and epi-cardial borders over the whole cycle, global indexes such as left ventricle ejection fraction is easily quantified. It is widely accepted as the reference modality for quantifying global cardiac function. However, as we can see in Fig. 2.1, inside the muscle, cine MR shows nearly spatially constant intensities. Different from cardiac ultrasound, there are no natural markers that "tags" the myocardium. To some extent, this increases the difficulty in quantifying local cardiac deformations from cine MR. However, with the help of spatial regularizations, regional myocardial deformations can still be recovered as demonstrated in several publications [[Shi et al. \(1999\)](#)] [[Lin and Duncan \(2004\)](#)]. Indeed, a major characteristic of cine MR lies in its clear endo- and epi-cardium contours. Cardiac cine MR is therefore commonly used for segmentation tasks. This currently falls outside the scope of this thesis. In the following subsections, we will mainly focus on the motion tracking from cardiac cine MR image sequences.

2.3.2 Motion tracking from cine MR

As mentioned above, the most commonly used features in cine MR are endocardial and epicardial contours. They are usually segmented at end-diastole and tracked throughout the image sequence. For motion analysis from cine MR, one strategy may be to first track sparse feature points and subsequently compute the myocardial deformations from the tracking field. The other strategy is to directly use existing image registration algorithms and register the whole sequence to a chosen reference time frame. Then, cardiac deformations can be further deduced from the recovered set of transformations. A comprehensive analysis of the state-of-the-art is available in [[Wang and Amini \(2012\)](#)]. We only briefly introduce some representative algorithms here.

Feature tracking

Hor *et al.* [[Hor et al. \(2010\)](#)] [[Hor et al. \(2011\)](#)] developed a feature tracking method applied to cardiac cine MR images. Endocardial and epicardial borders were manually drawn at the end-diastole frame. The myocardial border, as well as the columns of pixels radiating out from the endocardium, were then automatically propagated through the cardiac cycle by matching individual patterns that represent anatomical structures [[Hor et al. \(2011\)](#)]. These were identified by the method of maximum likelihood between the regions of interest of consecutive frames. Myocardial strains were then computed from the

tracking field. Maret *et al.* Similarly, [Maret *et al.* (2009)] tracked the myocardial borders from cine MR images and showed that displacement and strain in the radial and longitudinal direction could be used for the detection of transmural scar. Recently in [Moody *et al.* (2015)], myocardial strain quantified from cine MR feature tracking was compared with tagged MR quantification results. The authors claimed that sufficient agreement was found between the two imaging modalities and feature tracking was considered as potentially feasible and rapid alternative. Similarly in [Taylor *et al.* (2015)] and [Bogarapu *et al.* (2016)], cine MR was shown capable of obtaining normal values for myocardial strain measurements on healthy volunteers and detecting myocardial fibrosis in pediatric hypertrophic cardiomyopathy respectively.

Several other groups also tracked myocardial motion from cine MR images in a similar way. In [Queirós *et al.* (2014)], myocardial contours were first segmented by a B-spline explicit active surfaces technique, and then tracked throughout the heart cycle by an anatomically constrained optical flow method. Lin *et al.* [Lin and Duncan (2004)] proposed a generalized robust point matching framework to track the motion of left ventricle. The displacements of myocardial borders obtained by robust point matching were further regularized by the free-form deformation model. Shi *et al.* [Shi *et al.* (1999)] combined image-derived information (the tracked myocardial surfaces) and mechanical modeling of the myocardium and solved for deformations by finite-element models.

Registration-based methods

Others regarded the motion tracking as a non-rigid registration problem. They aimed to estimate appropriate non-linear transformation fields, from which cardiac motion and strain were further derived. Sundar *et al.* [Sundar *et al.* (2009)] used a 4D image registration method to estimate cardiac motion. An attribute vector for every point in the image was used to contain information about intensity, boundary, and geometric moment invariants. Perperidis *et al.* [Perperidis *et al.* (2005)] proposed two B-spline-based free-form deformation methods for the spatiotemporal alignment of cardiac cine MR image sequences. The two B-splines methods use the same transformation but differ in the order of the optimization process. One performed a combined optimization with spatial and temporal components. The other optimized each component separately. Cardiac deformations were then computed from the transformation field. Recently, Tsadok *et al.* [Tsadok *et al.* (2016)] applied non-rigid registration to cine MR images and observed that the regional longitudinal strain estimates correlated highly with tagged MR and STE.

2.4 Cardiac tagged MR

Tagged MR is a specific technique developed for recovering local tissue deformations [Axel and Dougherty (1989)a]. Tags are created non-invasively by modulating the longitudinal magnetization prior to the image acquisition. In cardiac applications, the

resulting tagging pattern moves with the myocardial and stays relatively stable during the whole heart cycle. This permits to track of myocardial deformations and to further evaluate regional cardiac functions.

2.4.1 Image characteristics

Tagging of myocardial tissue using MRI was first introduced by Zerhouni *et al.* [[Zerhouni *et al.* \(1988\)](#)]. The magnetization of the tissue is labeled or tagged by applying a spatially modulated saturation radiofrequency (RF) pulse before the actual MR imaging procedure. The tagging preparation sequence is played out at end-diastole upon detection of the ECG R-wave in planes perpendicular to the imaging plane. Since magnetization represents a characteristic tissue property, saturated regions are moving with the underlying tissue and displayed as black lines in the acquired images as shown in Fig. 2.1. By tracking these black lines, cardiac tissue can be tracked. Due to the T1 relaxation, the initially modulated magnetization tend to gradually return to its thermal equilibrium state. In the final image, this induces a progressive loss of contrast in the tags, known as *tag fading* [[Osman *et al.* \(2000\)](#)]. As a result, the tags are only visible during a limited time period. Nonetheless, at 1.5 T, the T1 relaxation time of healthy myocardium is about 850ms and therefore long enough to study cardiac contraction during the entire duration of a cardiac cycle. Since its invention in the late 1980s, tagged MR has undergone three major developments which we detail in the following sections.

Spatial Modulation of Magnetization (SPAMM)

Axel *et al.* [[Axel and Dougherty \(1989\)a](#)] first introduced an effective way to periodically modulate longitudinal magnetizations. As illustrated in Fig. 2.2, by applying two nonselective RF pulses separated by a dephasing gradient, periodic SPAtial Modulation of Magnetization (SPAMM) can be created. Explanations about this process are provided in Fig. 2.2 and the reader can also find more details in [[Rutz \(2008\)](#)]. At time point (d) in Fig. 2.2, the magnetization is flipped back to the longitudinal direction, all of the remaining transversal magnetizations decays fast with T2* since the myocardium has relatively small spin-spin relaxation times. In some cases, to ensure a complete removal of the transversal components, an additional spoiling is used in through-plane direction. After all these steps, a 1-1 sinusoidal modulation pattern of the magnetization is generated. The tag preparation sequence is then followed by a conventional MR imaging procedure, leading to images with spatially altered intensities, *i.e.* the tags.

Complementary Spatial Modulation of Magnetization (CSPAMM)

One major disadvantage of SPAMM is that the tag contrast deteriorates with time. At later cardiac phases, the tag fading is so prominent that it may hamper the motion tracking. Consequently, complementary SPAMM (CSPAMM) was introduced [[Fischer *et al.* \(1993\)](#)] in order to reduce the tag fading and improve the image quality at later

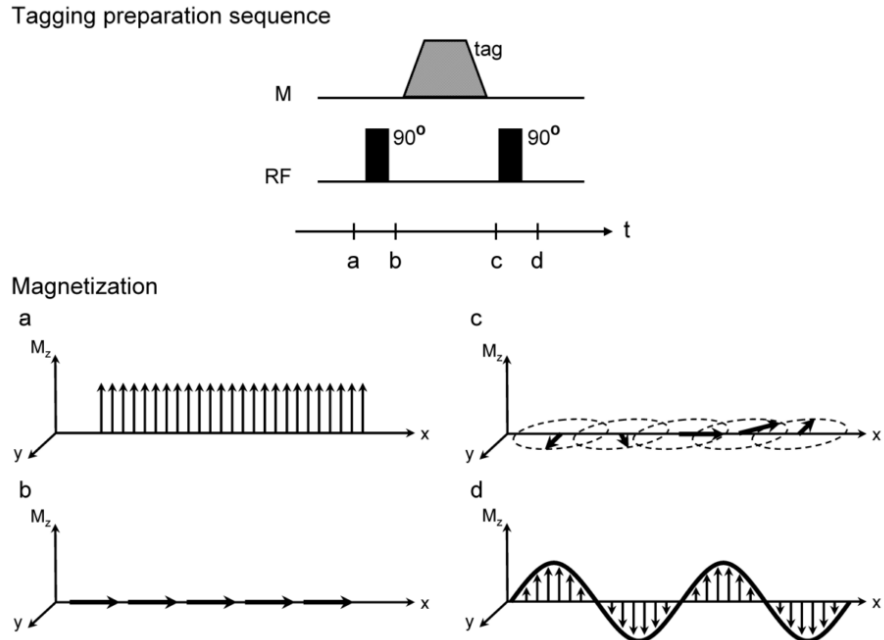


Figure 2.2: The tagging preparation sequence used in SPAMM. It consists of two RF block pulses interspersed by a dephasing gradient in measurement (M) direction. The states of the magnetization are shown for the time instants a,b,c and d in the sequence. The magnetization is flipped from the longitudinal axis (a) into the transversal plane (b), dephased along the x direction (c) and flipped back to the longitudinal direction, yielding a sinusoidal modulation of the longitudinal magnetization (d). The diagram is originally presented in [Rutz (2008)].

frames. With CSPAMM, an additional SPAMM dataset is acquired with inverted tagging modulation. By subtracting this complementary acquisition from the first scan, the DC signal component is canceled. Moreover, the authors [Fischer *et al.* (1993)] optimized the RF excitation angle of each frame so as to compensate for the tagging intensity attenuation resulting from longitudinal relaxation. All these efforts aimed to result in temporally constant myocardial tagging intensities. The emergence of CSPAMM significantly reduced the tag fading, but the acquisition time is doubled since two separate SPAMM acquisitions are needed. Actually, one major point that restricts tagged MR from wider clinical use is that the acquisition process is rather time-consuming and the patients are usually required to withstand a number of breath holds. As a consequence, a lot of research efforts have been dedicated to developing rapid tagging acquisition protocols in the last decade as described hereafter.

Accelerated CSPAMM

Ryf *et al.* [Ryf *et al.* (2005)] first proposed to combine a fast turbo-field echo-planar imaging (TFEPI) MR sequence with the tag preparation technique in order to reduce the acquisition time. TFEPI permits acquiring a dynamic 2D image sequence during a single cardiac cycle. The authors showed that although the image quality was decreased because

of shorter acquisition times, the acquired image sequence still allowed for reproducible accurate quantification of functional indexes [Ryf *et al.* (2005)]. Later on, Rutz *et al.* [Rutz *et al.* (2008)] extended the rapid 2D tagged MR acquisitions to 3D volumes. Smaller field of views enclosing sometimes merely the left ventricle were adopted in a bid to reduce maximally the acquisition time. Besides, the TFEPI is replaced by a more advanced segmented Echo-planar imaging MR sequence for accelerating the acquisition. As a result, three sequences of 3D CSPAMM volumes with orthogonal line tagging patterns were acquired in three breath-holds of 18 heartbeats duration each. The new tagging acquisition was shown sufficient to quantify accurately myocardial deformations [Rutz *et al.* (2008)]. The tagged MR images involved in this thesis were acquired using this recent acquisition protocol. However, this kind of tagging data shows a relatively moderate spatial resolution. For example, both the endocardium and the epicardium are blurred. Also, usually only the left ventricle and part of the right ventricle can be seen in the images due mainly to the reduced field-of-view.

2.4.2 Motion tracking from tagged MR

Since its introduction in the late 1980s, cardiac tagged MR has triggered the development of a wide spectrum of strain quantification methodologies. Some of them were specifically tailored for tagged MR. Some others are generic methodologies that were readily applied to tagged MR images.

Generic methods

Among generic methods, intensity-based registration by optical flow or Free Form Deformation (FFD) were successfully applied to tagged MR images. Chandrashekara *et al.* [Chandrashekara *et al.* (2004)] applied multilevel FFD to the post-processing of tagged MR. De Craene *et al.* [De Craene *et al.* (2011)] applied temporal diffeomorphic FFD to the analysis of tagged MR, resulting in a temporal regularization of the motion field. Shi *et al.* [Shi *et al.* (2012)] proposed a FFD-based tracking method that combines cine and tagged MR images to analyze cardiac deformation, with the possibility of adding incompressibility into the framework. Prince *et al.* [Prince and McVeigh (1992)] developed an optical flow method with considerations about compensating the tag fading effect. Florack *et al.* [Florack *et al.* (2007)] developed an optical flow method on phase images that automatically selects an optimal scale.

Generic registration methods are robust and have been applied to a large number of cardiac modalities. Most of the registration-based methods were applied to a grid tagged image combining all tagging acquisitions in a single sequence. However, they do not take advantage of separate directional encodings often performed in tagged acquisitions. Tagged MR images are acquired in several directions that provide different “channels” for recovering the motion field. This feature can potentially overcome the aperture problem inherent to monochannel optical flow or any parametric registration method. By analogy, this is

equivalent to reducing a color image to a black-and-white picture where any segmentation task will not exploit color differences between the objects in the scene.

Tagged MR-specific methods

All methods that exploit tagged MR specificities can be divided into four categories. These categories are rather separated, opening up the possibility of combining their respective advantages. Also, most of these methods were only applied to 2D tagged MR and adaptations to 3D are currently in an early stage [Wang *et al.* (2013)] [Rutz *et al.* (2008)], or focus on multiplanar [Pan *et al.* (2005)] [Liu *et al.* (2012)] rather than the volumetric acquisition protocol of Rutz *et al.* [Rutz *et al.* (2008)].

Detection-based methods A first option retained by Young *et al.* [Young *et al.* (1995)] and Amini *et al.* [Amini *et al.* (2001)] was to first detect the tag planes or intersections and then to track these extracted features. Amini *et al.* [Amini *et al.* (2001)] detected tag planes by B-spline surfaces and tracked sparse myocardial beads. Young *et al.* [Young *et al.* (1995)] used an active contour model to track the tag lines in images and then interpolated a 3D dense motion by a finite-element model. In [Young (1999)], the tagging stripes were detected by a Gaussian-shaped filter and matched by a line searching algorithm. The obtained sparse displacements were further regularized by a finite-element model defined in the local *radial*, *longitudinal* and *circumferential* directions. Chen *et al.* [Chen *et al.* (2010)] applied Gabor filters to detect tag line intersections which are further used to initialize a meshless deformable model.

HARP HARP [Osman *et al.* (1999)] is another tagged MR-specific method that became a reference in this modality. A first step in HARP is to compute phase images. They are computed by applying a band-pass filter in the Fourier domain. Back to the spatial domain, the tracking is then performed on phase (rather than intensity) images. The main rationale for substituting intensity by phase is to improve robustness against tag fading. The overall tracking procedure can be interpreted as an optical flow performed jointly on two “channels”, each channel corresponding to one tagging direction. Because the number of tagging directions equals the number of components of the displacement field, the aperture problem simply disappears. The estimation of HARP displacements was further improved when introducing the CSPAMM protocol, enabling the use of a wider k-space HARP filter [Kuijjer *et al.* (2001)]. However, unlike traditional optical flow algorithms, HARP does not integrate any spatial regularization. As strain is computed from the spatial derivatives of trajectories, one expects that outliers in the reconstructed motion field will yield high errors in the strain field.

The HARP community also proposed several strategies for addressing the limited capture range of tagged images. Indeed, the periodicity of tagged images prevents to recover displacements exceeding one-half of the tag spacing. Osman [Osman *et al.* (1999)] proposed

an initialization scheme by sorting the list of points to be tracked. Points with expected smaller motion are tracked first and the tracking result is used as initialization to neighboring points. This concept was further developed in [Liu and Prince (2010)] where the order is optimized through solving for the shortest path on a graph where each edge has a cost related to phase continuity between neighboring voxels in the image. However, the integration of an order to the point-wise tracking is somehow dangerous. Indeed, “tag jump” errors will be propagated to all subsequent points in the list.

SinMod The SinMod [Arts *et al.* (2010)] algorithm has recently emerged as an alternative to HARP. In the local environment of each pixel, the intensity distribution is modeled as a sinusoid wave orthogonal to the tagging direction. Then both the local frequency and the inter-frame phase shift are computed. The ratio of these two quantities gives an estimate of the displacement when combining the different tagging directions. SinMod was shown to be as fast as HARP and have advantage in accuracy and robustness to image noise. Yet, the ability of tracking large myocardial motion (superior than half tag spacing) remains to be further verified. Also, the absence of any spatial regularization makes strain estimates very sensitive to tracking errors when extracting spatial derivatives.

Gabor-based methods Qian *et al.* [Qian *et al.* (2011)] proposed to compute strain directly from the image without tracking the myocardial motion. The idea is to filter the intensity images through a Gabor filter bank for retrieving the local orientation and spacing of the tags. This gives a direct access to tissue deformation, without the need of computing displacements. This concept was further extended by Kause *et al.* in [Kause *et al.* (2014)] where the deformation gradient was directly evaluated from the frequency covector fields. The authors claim that it makes their strain estimate independent to any tracking result. However, they overlook that a tracking is always required for reporting strain evolution at all time points per material point.

2.5 Summary

In this chapter, we first introduced the clinical background of cardiac motion tracking. Tracking the cardiac deformations from medical images helps both the early detection and treatment planning of heart diseases. We gave a brief introduction about several common imaging modalities used for tracking the cardiac motion. Among them, cine MR is the reference for evaluating global cardiac function via indexes such as stroke volume and ejection fraction. The quantification algorithms developed for cine MR are briefly described earlier in this chapter. When it comes to assessing the regional function, echocardiography and tagged MR are the preferred modalities. Both rely on local myocardium markers for the tracking. In ultrasound, natural acoustic speckle noises were exploited as markers for the tracking. In tagged MR, bands of tissue are non-invasively marked by saturating the magnetization in selected directions prior to the acquisition. Tracking these markers

(speckles or tags) over the cardiac cycle allows accurately quantifying the underlying cardiac motion. Although a number of 3D quantification methods have been developed in recent years, their use for diagnosing regional cardiac functions in clinical routine is somehow held back by the lack of a solid validation. Both 3D speckle tracking and 3D motion tracking softwares developed for tagged MR need to be thoroughly validated before being transferred to clinics. The validation of cardiac motion tracking is itself a highly active field of research which we will introduce more in Chapter 3.

Chapter 3

The validation of cardiac motion tracking

3.1 Introduction

We have already introduced in Chapter 2 that detecting the diseases at an early stage would help reducing the mortality rate. In fact, the diagnosis of cardiovascular diseases has been much improved by the development of cardiac imaging techniques in recent years. Analyzing cardiac motion and strain from medical images reveals important patterns to analyze the extent of an infarct, dyssynchrony issues due to electrical disorders, abnormal filling patterns caused by impaired pressures and many more abnormalities. Important advances have been achieved in both ultrasound (US) and magnetic resonance (MR) technologies in recent decades. As for US, rapid 3D volumetric imaging is now feasible, thanks to the introduction of 2D matrix array transducer technology [[Mor-Avi et al. \(2011\)](#)]. Also, ultrasound is portable and non-invasive, being suitable for providing bed-side care to patients. Cardiac cine MR is widely used in clinical routine for evaluating global cardiac function since it provides clear contrast between the myocardium and the surrounding tissues. Aside from cine, tagging is the MR sequence that provides the most detailed information about local cardiac deformations [[Axel et al. \(2005\)](#)]. It is considered as the gold standard for quantifying local myocardial motion and strain. Nonetheless, its use in clinical practice is somewhat held back by the lack of reliable automatic post-processing tools, as well as its limited spatial resolution for distinguishing structures.

Despite all those developments of imaging techniques, the assessment of cardiac function generally relies on global measures, such as left ventricle (LV) ejection fraction (EF) and global longitudinal strain (GLS) [[Smiseth et al. \(2015\)](#)]. GLS quantified from speckle tracking echocardiography [[Blessberger and Binder \(2010\)](#)] is currently the best evaluated

strain parameter [Cheng *et al.* (2013)] [Shiino *et al.* (2016)]. Compared with global strains, regional strains are less reliable and reproducible as reported in [Shiino *et al.* (2016)] [Kleijn *et al.* (2012)] [Singh *et al.* (2010)]. Consequently, regional strain analysis is currently applied as a supplementary diagnosis method, but is still not ready for full clinical implementation in spite of their utility in a lot of applications [Smiseth *et al.* (2015)] [Pedrizzetti *et al.* (2016)]. One of the reasons is the fact that a well-established validation of regional strain imaging is still missing at the moment, despite the existence of a large number of dedicated quantification algorithms both in US [Somphone *et al.* (2013)] and tagged MR [Zhou *et al.* (2015)]. A comprehensive and thorough quantitative validation of these methods based on dense strain measurements would thus represent a major progress.

In order to validate cardiac motion tracking algorithms, one would first think of using manual ground-truth trackings generated by experts, similar to the strategy used for validating segmentation algorithms. However, unlike the cardiac segmentation which is usually performed at a single time frame where the experts are required to trace the heart contours, myocardial landmarks need to be tracked over the whole sequence of 3D volumes so as to generate the ground-truth. This is a tedious task and is prone to inter and intra-expert variabilities. Moreover, it is only feasible for a limited number of landmarks. Generating *densely* distributed landmarks would be difficult when considering the amount of work required. Consequently, most research groups turned to other more automatic alternatives which we introduce in the following sections.

3.2 Using dedicated imaging techniques as reference

One of the options is to rely on dedicated imaging devices capable of directly measuring myocardial displacements. For example, echocardiographic Doppler tissue imaging [Ho and Solomon (2006)] and the phase encoding DENSE MR [Aletras *et al.* (1999)] have been developed to directly measure the velocity or displacement fields for cardiac motion analysis. However, those methods are either not widely used in clinics (the case of DENSE MR) or give access only to limited components of the motion field (the case of tissue Doppler where merely the velocity in radial direction is available).

Others like [Duan *et al.* (2009)b] and [Yeon *et al.* (2001)] used sonomicrometry to directly measure the myocardial strains and compare motion tracking results against the measurements. However, sonomicrometry requires the implantation of piezoelectric crystals in the myocardium, hence too invasive for clinical use. As a consequence, most of the current validation studies based on sonomicrometry were performed on canine hearts. Yet human hearts are different and usually more complex, motion tracking algorithms validated on animals are not necessarily transferable to clinical applications. Moreover, the spatial resolution of the measured ground-truth deformations is proportional to the number of piezoelectric crystals placed in the heart. Usually, only a limited number of crystals are used. *Dense* ground-truth fields are therefore never available.

In addition, the multimodal registration is very challenging because the tissues are imaged differently. Also, the acquisitions suffer from the breathing artifacts and it is difficult to ensure the same cardiac phase is acquired. All these may challenge the validation.

3.3 Imaging physical phantoms

Several research groups built a physical heart model for validation purpose [Tobon-Gomez *et al.* (2011)a] [Boltz *et al.* (2010)]. The model has a geometry similar to the heart and is mechanically controlled. Most mechanical phantoms implement simple contraction and torsion motions that can be modulated and combined to generate different deformation patterns. Provided that the phantom is adapted to minimize imaging artifacts in MR and ultrasound, it can be dynamically imaged in these different modalities. Cardiac motion tracking algorithms can then be evaluated on these real image sequences. The groundtruth motion is controlled and thus accessible. Despite the various advantages of such physical phantoms, this strategy presents several limitations. First, in practice, having a dense ground truth motion field is actually rather difficult. We need to know material properties and model tissue deformations very accurately. Second, cardiac motion simulated by such physical phantoms are rarely as complex as the real human heart and it is not straightforward to simulate different levels of pathologies. We consider it vital to validate cardiac motion tracking algorithms on comprehensive cases including both healthy and pathological hearts. Second, we usually see only the heart in the acquired images. All the background structures are missing. Indeed, a realistic background with complex surrounding structures or imaging artifacts will challenge the motion tracking algorithms. For instance, all registration-based approaches suffer from the fact that the myocardium moves over the cardiac cycle while some of the neighboring structures are static, representing an inherent spatial motion discontinuity. Therefore, the lack of a complex background does reduce significantly the level of realism. Images acquired from the physical phantoms cannot fairly meet the real challenges faced by motion tracking algorithms.

3.4 Generating synthetic images

Besides the two alternatives presented above, another one relies on numerical simulations for validating cardiac motion tracking. Using synthetic cardiac images generated *in silico* could help evaluating the performance of motion tracking methods.

In fact, a number of research groups already made some initial attempts towards this objective. Synthetic US [Alessandrini *et al.* (2015)] [Prakosa *et al.* (2013)] [Glatard *et al.* (2013)], cine MR [Prakosa *et al.* (2013)] [Glatard *et al.* (2013)] and tagged MR [Clarysse *et al.* (2011)] images were generated. They all adopted computer-generated synthetic sequences for validating motion tracking for one specific image modality. The interest in using synthetic images has been well detailed in several studies [Alessandrini *et al.* (2015)] [Prakosa *et al.* (2013)]. Their main advantage is the straightforward possibility of

assessing the accuracy of algorithms by comparing their performance against the controlled (and thus known) ground-truth deformations. Also, it is convenient to simulate a variety of pathological situations by varying the parameters of the numerical model. However, their utility depends heavily on the realism of the simulated data. Lots of efforts have been made to improve the realism of cardiac synthetic images. We describe some of the representative realistic simulation work on each of the three main modalities used in cardiac applications (cine MR, tagged MR and US) hereafter.

3.4.1 Simulation of cine MR images

Tobon-Gomez *et al.* [Tobon-Gomez *et al.* (2011)b] and Wissmann *et al.* [Wissmann *et al.* (2014)] simulated cardiac cine MR image sequences based on the XCAT [Segars *et al.* (2010)] phantom. In [Tobon-Gomez *et al.* (2011)b], a tissue segmentation (or labeling) was performed where different tissue types were associated with relevant T1,T2 and proton density (PD) values obtained from the literature. The static T1, T2 and PD maps at end-diastole (ED) were then warped by cardiac motion obtained from the XCAT phantom. Finally, at each time frame, an MR simulator [Kwan *et al.* (1999)] was used to generate the cine MR images. Wissmann *et al.* [Wissmann *et al.* (2014)] directly simulated image intensities by signal equations instead of using an MR simulator. They claim that this choice facilitates the simulation of sampling strategies, trajectory optimization and post-processing methods [Wissmann *et al.* (2014)]. Haddad *et al.* [Haddad *et al.* (2007)] and Glatard *et al.* [Glatard *et al.* (2013)] also synthesized 3D+t cardiac cine MR images. They adopted a similar approach to that presented in [Tobon-Gomez *et al.* (2011)b] by combining a beating heart model with an MR simulator. The main difference is in the heart model, which is extracted from real acquisitions as described in [Haddad *et al.* (2005)].

Recently, Prakosa *et al.* [Prakosa *et al.* (2013)] developed a pipeline that combines an electromechanical model (E/M) of the heart with template acquisitions for generating realistic cine MR data. The E/M model has the benefit of relating the contraction law with its biophysical causes which allows for a more realistic incorporation of physiological and pathological conditions. The template cine MR sequence was registered to the first frame, yielding a quasi-static sequence. This sequence was then warped with the simulation results to create synthetic images. Synthetic images generated in some of the studies mentioned above are shown in Fig. 3.1.

3.4.2 Simulation of tagged MR images

Compared to cine MR, relatively little work has been done on simulating cardiac tagged MR. Crum *et al.* [Crum *et al.* (1997)] simulated the left ventricle (LV) in short-axis slices. They modeled the corresponding anatomy using a simple ring shape. Using a motion directly computed from a real cine MR sequence, the authors warped the initial simulated ED image to the rest of the sequence. The tagging pattern was simulated by applying a sinusoidal modulation function in the spatial domain. Later in [Crum *et al.* (1998)],

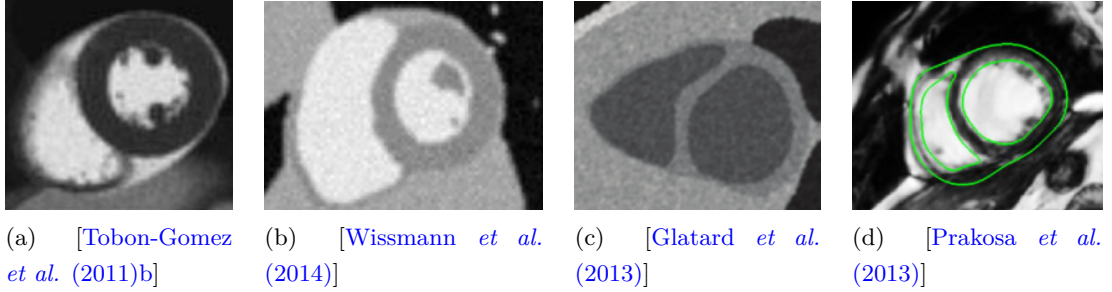


Figure 3.1: Several representative simulation results on synthetizing cardiac cine MR.

Crum *et al.* improved the generation of tag intensity profiles by using a frequency-domain model. Similarly, Waks *et al.* [Waks *et al.* (1996)] used a prolate sphere to mimic the LV geometry and a 13-parameter kinematic motion model. The model parameters were determined by a least-squares fit to the displacements of the implanted markers tracked from a dog heart acquisition.

Sermesant *et al.* [Sermesant *et al.* (2006)] segmented the myocardium from a real tagged MR image and further added tag lines to the binary mask. Finally, this image was warped by cardiac motions generated by the E/M model. Clarysse *et al.* [Clarysse *et al.* (2011)] warped a real short-axis tagged MR image by a simple kinematic mode-based heart motion model. However, the motion model was too simplistic to represent the complexity of true heart motion. We show in Fig. 3.2 some of the simulated tagged MR images.

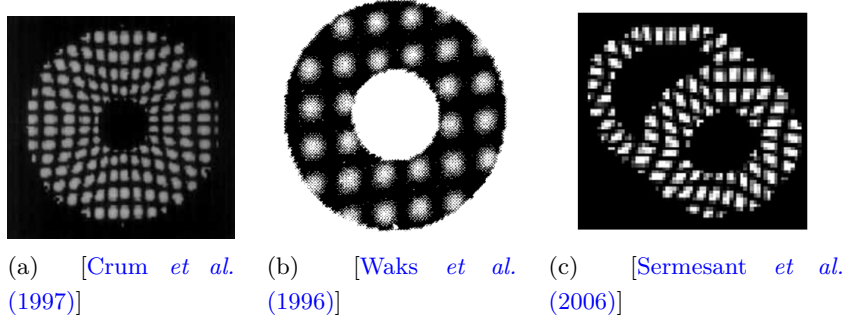


Figure 3.2: Several representative simulation results on synthetizing cardiac tagged MR.

In all of the methods mentioned above, myocardial intensities were assigned from merely one image at the end of diastole. This implies that no tag fading [Fischer *et al.* (1993)] is simulated. As commented in Section 2.4, tag fading refers to the phenomenon that the intensity of tags decays over time due to longitudinal relaxation. Tag fading poses the challenge for motion tracking since the tagging contrast is deteriorated at later cardiac phases. As a result, the CSPAMM sequence [Fischer *et al.* (1993)] was introduced so as to alleviate the tag fading by employing two specific techniques: 1) two sequences of SPAMM [Axel and Dougherty (1989)a] data that are 180 degrees out of phase were acquired and subtracted for removing the DC component [Fischer *et al.* (1993)]; and 2) RF

excitation angles (i.e. flip angles) were elaborately designed in order to mask the temporal intensity attenuation inherent to tagged MR [Ryf *et al.* (2005)]. The authors [Fischer *et al.* (1993)] [Ryf *et al.* (2005)] claimed that a constant myocardial tagging intensity over the cardiac cycle could thus be obtained in this way. However, this method relies on the assumption that the myocardium has spatially constant T_1 values, which is not realistic since spatial variations of T_1 inside the myocardium have already been reported in several studies such as [Reiter *et al.* (2013)] and [Tessa *et al.* (2015)]. Therefore, the myocardial tag fading always exists. When designing simulation strategies, it is important to have tag fading properly represented in synthetic images.

3.4.3 Simulation of echocardiographic images

As for the simulation of echocardiographic images, Alessandrini *et al.* has already given a rather comprehensive analysis in [Alessandrini *et al.* (2015)]. As a result, we provide here only a brief introduction about some of the most representative studies related to this thesis. [Suhling *et al.* (2005)] is among the first to generate synthetic cardiac US sequences for the validation of speckle tracking. An annular shape was used to represent a LV short-axis cross section in combination with a radial motion model used for simulating contraction and expansion. Alessandrini *et al.* [Alessandrini *et al.* (2012)b] combined a template US recording with a physical ultrasound simulator for generating the synthetic data. Cardiac motion in the template sequence was first tracked by image registration. The whole template sequence was then spatio-temporally aligned with the tracking results. As a final step, they used a physical ultrasound simulator to handle the generation of synthetic images so as to alleviate warping artifacts.

Recently, several groups used an electro-mechanical (EM) model for generating synthetic cardiac deformation fields [De Craene *et al.* (2013)] [Prakosa *et al.* (2013)] [Alessandrini *et al.* (2015)]. Although all of them used a similar E/M model, their image synthesis methodologies differed. Prakosa *et al.* [Prakosa *et al.* (2013)] combined the E/M model with template US recordings. Template sequences were warped towards the simulations generated by the E/M model. The resulting images showed realistic textures, but the warping artifacts reduced somehow the realism of the synthetic data. To alleviate warping artifacts, De Craene *et al.* [De Craene *et al.* (2013)] opted for using a physical ultrasound simulator for generating image data. However, they did not integrate any real acquisitions into the pipeline and the speckle model used was rather simplistic (i.e. high speckle intensity inside the muscle and low intensity outside), leading to unrealistic binary-like synthetic images. Recently, based on the two previous studies, Alessandrini *et al.* [Alessandrini *et al.* (2015)] combined the E/M model, the physical ultrasound simulator and the template US recordings into an unified pipeline. Their simulation pipeline combined the advantages of both [Prakosa *et al.* (2013)] and [De Craene *et al.* (2013)] and was able to produce realistic synthetic echocardiographic images. Some of the simulation results mentioned above are shown in Fig. 3.3.

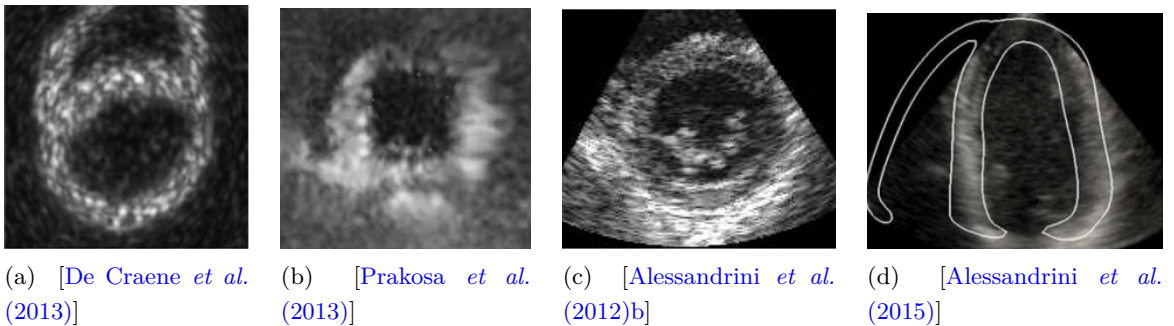


Figure 3.3: Several representative simulation results on synthetizing cardiac ultrasound.

3.5 Summary

In this chapter, we introduced some of the approaches used for validating cardiac motion tracking. Although cardiac motion or deformation directly measured by dedicated imaging techniques such as tissue Doppler imaging or DENSE MR could reveal valuable information about the ground-truth, their inherent limitations together with inaccuracies in matching different imaging modalities in space and time limit their validity as gold standard for validation purposes. Besides, manual landmark tracking is tedious and prone to inter and intra-expert variabilities. Manual tracking would also lead to high errors on deformation values. Another option is to design specific 3D+t physical heart models and perform the acquisition under routine cardiac imaging systems. It is then possible to evaluate the performance of motion tracking algorithms on the acquired images. However, the mechanically generated motion is rarely as complex as in a real heart and the acquired images lack realistic backgrounds. Both are important limitations to the use of physical phantoms for validating cardiac motion tracking algorithms.

Consequently, we opt for relying on realistic synthetic image sequences for the validation. A lot of research efforts have already been made in this field with realistic cardiac synthetic images being simulated for both ultrasound and MR modalities. The utility of such synthetic data for validation relies heavily on the level of realism of the simulated data. Both the image data and the ground-truth motion fields should stay close to reality. On one hand, the ground-truth deformations must possess mechanical properties in agreement with clinical references: i.e. both global indexes such as ejection fraction and regional motion and strains should be within the reference ranges published in the literature. On the other hand, the synthetic images should be realistic in terms of image quality and artifacts. Finally, motion underlying the synthetic images should be known exactly, within the myocardial tissue at least. For all these requirements to be satisfied, many aspects need to be taken into consideration when designing the simulation pipeline.

III Contributions

Chapter 4

3D harmonic phase tracking with anatomical regularization

This chapter is an extension of our paper "3D Harmonic Phase Tracking with Anatomical Regularization" published in *Medical Image Analysis* [[Zhou et al. \(2015\)](#)].

4.1 Introduction

The non-invasive quantification of local myocardial mechanics remains a central challenge for diagnosing heart diseases. Among motion and deformation indexes, strain is a prominent measure. Indeed, strain is less sensitive to tethering from surrounding segments, and is therefore preferred for detecting abnormal segments [[Voigt and Flachskampf \(2004\)](#)]. Tagged MR is a classical technique used to quantify regional myocardial deformation. It creates non-invasive markers that move with the myocardium along the cardiac cycle. Tracking these markers (tags) allows precise recovery of myocardial deformation. The introduction of CSPAMM [[Fischer et al. \(1993\)](#)] efficiently improved tag fading issues that were traditionally hampering the analysis of tagged MR data in diastole. Breathing artifacts producing unaligned slices have been corrected by the introduction of navigator-driven protocols [[Rutz et al. \(2008\)](#)] and the move to fully 3D acquisitions. Recently in [[Rutz et al. \(2008\)](#)], a rapid CSPAMM-based 3D protocol was proposed by performing three acquisitions sequentially with line tag preparation in each orthogonal direction. Each of these three acquisitions is performed in a single breath-hold of 18 heartbeats duration and retrospectively corrected for misalignment using a respiratory navigator.

The introduction of this accelerated 3D CSPAMM sequence calls for the associated

reliable and computationally efficient motion tracking solutions. In this chapter, we will introduce a novel 3D extension of the harmonic phase (HARP) tracking algorithm [[Osman et al. \(1999\)](#)]. We will describe the background and the proposed algorithm hereinafter.

4.1.1 The open question and our contributions

The extension and combination of 2D tagged MR quantification methods to the 3D protocol of Rutz *et al.* [[Rutz et al. \(2008\)](#)] remains an open challenge in the tagged MR community. Several attempts have been made for extending HARP to 3D. They are all based on interpolating 2D HARP results from sparse short- and long-axis images (SLIs). Pan *et al.* [[Pan et al. \(2005\)](#)] obtain 3D motion by Gaussian diffusing 2D motions from SLIs on a mesh model. Liang *et al.* [[Liang et al. \(2007\)](#)] use a nonuniform rational Bspline volumetric model to densely interpolate the 2D motions from SLIs. Liu *et al.* [[Liu et al. \(2012\)](#)] apply the divergence-free vector spline as the interpolation kernel. Recently, SinMod was also extended to volumetric tagged MR in a straightforward manner [[Wang et al. \(2013\)](#)], but without embedding any spatial regularization.

This calls for a novel method that integrates the benefits of available strategies in the literature. A detailed analysis of the state-of-the-art is already provided in Section 2.4 of Chapter 2. From registration-based approaches, regularization strategies have the potential to extract robustly motion fields from noisy image data. From tagged MR-specific techniques, extracting phase images and taking full benefit from the multi-channel nature of the input data are crucial aspects to preserve in the design of novel 3D tagged MR quantification tools. In this thesis, we developed a HARP-based method suitable for fast quantification of 3D *radial*, *longitudinal* and *circumferential* strains on volumetric tagged MR images [[Rutz et al. \(2008\)](#)]. Our main contributions are twofold.

First, we propose to add a spatial regularization step implemented in an anatomical space of coordinates to a straight extension of HARP to 3D. This regularization is performed on a volumetric mesh of the left ventricle (LV) to maintain a low computational cost. The volumetric mesh and anatomical coordinates follow the local directions (*radial*, *longitudinal* and *circumferential*). Local windows are defined on the LV myocardial domain, and HARP results are regularized by affine transformations in anatomical coordinates at a regional level. Heyde *et al.* [[Heyde et al. \(2013\)](#)] [[Heyde et al. \(2016a\)](#)] introduced the concept of anatomical regularization in ultrasound but implemented it by resampling the images and doing the tracking in anatomical coordinates. For this application, this would introduce non-linear distortions in the shape of the tags.

Second, we propose to enforce myocardial incompressibility by correcting strain values in the radial direction only. Indeed, this direction is by experience the most challenging to recover meaningful strains. This is likely due to the fact that the number of tags from endocardium to epicardium is small in the radial direction compared to circumferential and longitudinal directions. The divergence-free constraint is imposed at a regional level through the direct application of the divergence theorem.

Besides, we quantitatively compared two phase computation schemes: the original HARP phase and the Monogenic phase (MP) as introduced by [Alessandrini *et al.* (2012)a] to the field of tagged MR quantification. As earlier, the impact of using HARP vs. MP was evaluated on synthetic tagged MR images.

In addition to synthetic images, our method has been evaluated *in vivo* on healthy volunteers and patients. For healthy volunteers, we compare our accuracy against manually tracked trajectories on a public database [Tobon-Gomez *et al.* (2013)]. This evaluation includes the comparison to state-of-the-art tracking algorithms as available from [Tobon-Gomez *et al.* (2013)]. On clinical cases, we quantified the ability of our software to discriminate healthy from diseased myocardium by comparing our results between a control group and an ischemic group showing typical subendocardial late-enhancement MR.

4.2 Data Acquisition & Preprocessing

4.2.1 3D Tagged MR acquisition

The 3D tagged MR images were acquired on a Philips 1.5T Achieva System (Philips Healthcare, Best, The Netherlands) and a 32-channel cardiac coil. A survey scan was used to define the position and axis of the LV. The images were obtained using a 3D CSPAMM sequence [Rutz *et al.* (2008)] based on three volumetric datasets with sinusoidal line tagging preparation (tag distance=7 mm) in three orthogonal directions (3DTAG, GyroTools, Zurich, Swiss). The reader is referred to [Rutz *et al.* (2008)] for the details of the tag preparation pulse. For data acquisition, a modified hybrid multishot, segmented EPI sequence was employed (TR/TE= 7.0/3.2 ms), with ramped flip angles (19–25°) to prevent tag fading during the cardiac cycle. Images were acquired with a reduced field-of-view (108x108x108 mm) enclosing the LV. The acquisition matrix size was 28x14x14. The voxel size for each of the three datasets was 0.96x0.96x7.71mm. The number of reconstructed frames was 24, and the temporal resolution ranged from 30ms to 45ms. An echo-navigator technique was used to compensate for respiratory motion. As the three orthogonal sequences are aligned, the whole acquisition can be interpreted as a multi-channel sequence of 3D volumes where at each voxel, three intensities are available (one for each direction).

4.2.2 Segmentation of LV

LV segmentation was done manually. The LV was segmented at end-diastole only (last frame). Segmenting the first frame is not feasible because tissue and blood are both tagged and cannot be distinguished. For segmentation purposes, an untagged image was produced by calculating modulus for the complex image obtained from HARP bandpass filtering (described later in Sect. 4.3.3) on each channel. Untagged images from the 3 channels were then averaged to produce a single image with isotropic voxel resolution. A template mesh was first positioned on the untagged image by clicking landmarks: 1

landmark was placed in the apex, 4 in the basal planes and 1 at mid-level in the septum. The template mesh was rotated and scaled to match the set of input landmarks. The mesh was then converted to an implicit function and adjusted by adding pointwise penalties to the algorithm described in [Mory *et al.* (2012)].

4.2.3 Mesh model

The output of the segmentation is a closed surface mesh that encompasses LV endocardium and epicardium. The purpose of the resampling procedure (described later in Sect. 4.2.3) is twofold. First, the surface mesh is converted to a volumetric *dense* mesh that also contains an inner layer between endocardium and epicardium. Second, the LV domain is sampled regularly in *radial*, *longitudinal* and *circumferential* directions. This facilitates regularizing the displacement field on the mesh topology.

Resampling rules and directional indexes

The resampling is done by casting rays from the long axis to the endocardial and epicardial surfaces as described in Fig. 4.1. The mid part of the LV is discretized using a cylindrical sampling. The long axis is sampled uniformly. From each long axis point, N_c rays are then cast with equal angular binning in the plane orthogonal to the long axis. For each ray, the intersection with the surface mesh gives two points: one at endocardium and one at epicardium. The average of these two points produces the inner middle layer. Similarly, apical and basal parts are sampled in a spherical manner. Azimuth and elevation angles are binned uniformly (see Fig. 4.1a and 4.1b).

Following this discretization scheme, each point in the generated mesh can be associated to three indexes. First, each point is either endocardial, mid or epicardial. Second, each point is intercepted by a single ray in the *circumferential* direction. Finally, each ray is either casted from one source point on the long axis, being indexed from the sequential cylindrical discretization or angled with respect to the long axis, being indexed from the sequential spherical discretization (Fig. 4.1a). In this way, every node in the mesh is related to three indexes (m_r, m_l, m_c) where $m_d \in [1, N_d]$ and N_d ($d=r,l,c$) is the number of divisions in each of the three directions (*radial*, *longitudinal* or *circumferential*). Then the spatial coordinates of every node can be written as $\mathcal{P}(m_r, m_l, m_c)$.

In our experiments, $N_r = 3$, $N_l = 35$ and $N_c = 50$. As the number of tags is low in the radial direction, we chose to use only three radial layers. N_l and N_c were chosen to produce isotropic cells in the volumetric mesh, which implies similar cell resolutions in longitudinal and circumferential directions.

By convention, radial indexes are ordered from endocardium to epicardium, longitudinal indexes are ordered from apex to base, and circumferential indexes go counter-clockwise when looking from the apex.

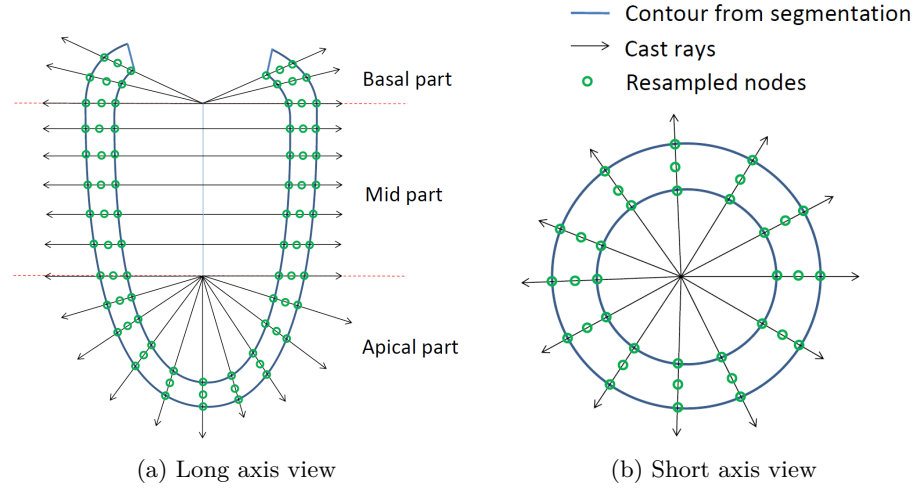


Figure 4.1: Resampling of LV surface mesh to volumetric dense mesh

Local directions

Based on the mapping \mathcal{P} (Sect. 4.2.3), local *radial*, *longitudinal* and *circumferential* directions $\hat{\mathbf{e}}_r(\mathbf{x})$, $\hat{\mathbf{e}}_l(\mathbf{x})$ and $\hat{\mathbf{e}}_c(\mathbf{x})$ can be computed by normalizing the edges of the volumetric mesh. However, this set of directions would not be orthogonal. As it will later be seen that the orthogonality assumption must be verified at all locations except the purely apical ones during the regularization procedure (Sect. 4.3.3), local directions were defined as follows.

For a non-apical mesh point \mathbf{x} whose directional indexes are (m_r, m_l, m_c) , its longitudinal direction can be computed as:

$$\begin{aligned} \mathbf{e}_l(\mathbf{x}) &= \mathcal{P}(m_r, m_l, m_c) - \mathcal{P}(m_r, m_l - 1, m_c) \text{ if } m_l > 1 \\ \hat{\mathbf{e}}_l(x) &= \frac{\mathbf{e}_l(x)}{\|\mathbf{e}_l(x)\|} \end{aligned} \quad (4.1)$$

Its circumferential direction $\hat{\mathbf{e}}_c(\mathbf{x})$ was then computed similarly but further corrected to be orthogonal to $\hat{\mathbf{e}}_l(\mathbf{x})$:

$$\hat{\mathbf{e}}_c(\mathbf{x}) = \frac{\mathbf{e}_c(\mathbf{x}) - (\mathbf{e}_c(\mathbf{x}) \cdot \hat{\mathbf{e}}_l(\mathbf{x}))\hat{\mathbf{e}}_l(\mathbf{x})}{\|\mathbf{e}_c(\mathbf{x}) - (\mathbf{e}_c(\mathbf{x}) \cdot \hat{\mathbf{e}}_l(\mathbf{x}))\hat{\mathbf{e}}_l(\mathbf{x})\|} \quad (4.2)$$

Finally, the radial direction $\hat{\mathbf{e}}_r(\mathbf{x})$ was obtained from the cross product between $\hat{\mathbf{e}}_c(\mathbf{x})$ and $\hat{\mathbf{e}}_l(\mathbf{x})$.

$$\hat{\mathbf{e}}_r(\mathbf{x}) = \hat{\mathbf{e}}_c(\mathbf{x}) \times \hat{\mathbf{e}}_l(\mathbf{x}) \quad \text{if } m_l > 1 \quad (4.3)$$

For purely apical points ($m_l = 1$), $\hat{\mathbf{e}}_c(\mathbf{x})$ has no definition due to the singularity on

the apex. $\hat{\mathbf{e}}_r(\mathbf{x})$ was defined in a similar manner by normalizing the edges in the radial direction. $\hat{\mathbf{e}}_l(\mathbf{x})$ was computed by taking the mean of its N_c nearest neighbors located in the same radial layer and normalizing the result.

Anatomical coordinates

Our goal is to map Cartesian (\mathbf{x}) to anatomical (r, l, c) coordinates while satisfying the following properties:

$$\begin{aligned} \forall \mathbf{x} \in \Omega, \quad \nabla r(\mathbf{x}) &= \hat{\mathbf{e}}_r(\mathbf{x}), \\ \nabla l(\mathbf{x}) &= \hat{\mathbf{e}}_l(\mathbf{x}), \\ \nabla c(\mathbf{x}) &= \frac{1}{\rho(\mathbf{x})} \hat{\mathbf{e}}_c(\mathbf{x}) \quad . \end{aligned} \quad (4.4)$$

where Ω is the LV myocardium domain, and $\rho(\mathbf{x})$ is the distance of point \mathbf{x} to the LV long axis.

For each direction $d \in \{r, l, c\}$, we start from a group of reference points $\{X_0^d\}$ where the anatomical coordinates are set to be zero. For longitudinal coordinates, the apex is taken as a reference point. In the circumferential direction, points located at the center of the local windows (described later in Sect. 4.3.3) are chosen as reference points. Finally, for the radial direction, $\{X_0^r\}$ is defined as the set of mid-layer points.

From $\{X_0^d\}$, the coordinates are obtained by curvilinear integration. Taking one direction $d \in \{r, l, c\}$, $d(\mathbf{x})$ is defined as

$$d(\mathbf{x}) = \begin{cases} \min_{\mathcal{C}_d(\mathbf{x})} \int_{\mathcal{C}_d(\mathbf{x})} \hat{\mathbf{e}}_d(\mathbf{s}) \cdot d\mathbf{s}, & \text{if } d = r, l \\ \min_{\mathcal{C}_d(\mathbf{x})} \int_{\mathcal{C}_d(\mathbf{x})} \frac{1}{\rho(\mathbf{s})} \hat{\mathbf{e}}_d(\mathbf{s}) \cdot d\mathbf{s}, & \text{if } d = c \end{cases} . \quad (4.5)$$

where $\mathcal{C}_d(\mathbf{x})$ is a geodesic path on the mesh starting at a node $\in X_0^d$.

The $r(\mathbf{x})$ and $l(\mathbf{x})$ coordinates are computed globally for the whole LV. However, practically, the $c^{(i)}(\mathbf{x})$ coordinate is defined locally for each window i (described later in Sect. 4.3.3) in order to ensure its continuity over the window domain. Examples of r, l over the whole myocardial domain and $c^{(i)}$ over the local window i are plotted in Fig. 4.2.

4.3 Tracking methodology

After the pre-processing step, the LV is tracked frame-by-frame backwardly. As a first step, the HARP tracking method is used to generate initial estimates of the motion field. HARP-based displacements are further regularized following a parametric motion model defined in an anatomical space of coordinates. Myocardial incompressibility is integrated as a *soft* constraint that helps retrieve robust radial strain estimations. For achieving fast convergence of the optimization, a window-weighted regression technique is used to decompose the complex global problem into simpler local ones. Also, a multiscale

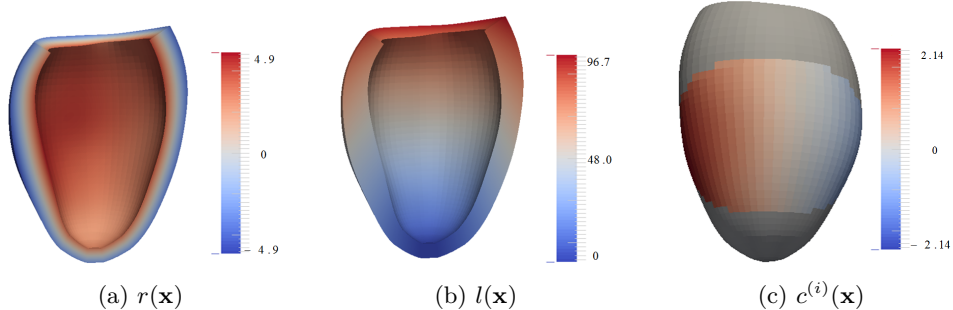


Figure 4.2: Anatomical coordinates $\{r, l, c^{(i)}\}$ defined on the LV volumetric mesh (in (c)), $c^{(i)}(x)$ has no definition in the surrounding grey region since it is beyond the range of the current window i

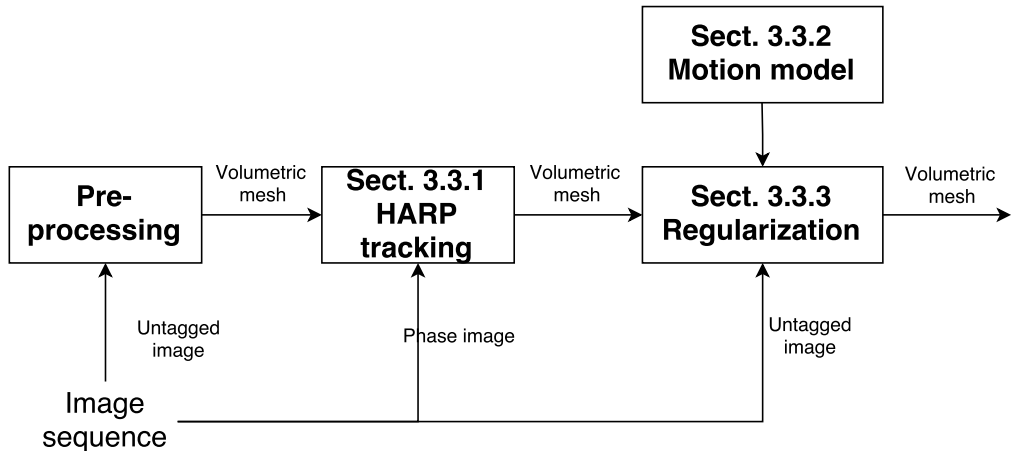


Figure 4.3: Pipeline of the proposed tracking method

framework was developed where strong regularization is imposed at first and gradually decreased.

4.3.1 HARP tracking

HARP [Osman *et al.* (1999)] estimates the displacements by first computing two phase image sequences and then performing a non-regularized optical flow on these two *channels*.

Phase computation

HARP [Osman *et al.* (1999)] pre-processes the original intensities and computes phase images. This pre-processing is meant to compensate for tag fading artifacts inherent to tagged MR images.

As a preliminary, it should be noted that the acquired 3D sequences do not have isotropic spacing (inter-slice thickness is about seven times the in-plane pixel spacing). Therefore, although the combination of the three channels can be seen as 3D (since the

three stacks are acquired in orthogonal directions), we opted for computing phase images in 2D slice by slice.

HARP phase is computed from the result of a bandpass filter in the frequency domain. As in our case, the tagging directions coincide with the m and n axes of each 2D slice, the 2D ellipsoid-shape bandpass filter $f_k(\omega)$ used in [Osman *et al.* (2000)] is therefore defined as

$$f_k(\omega) = \begin{cases} 1, & \text{if } \delta_k(\omega) \leq 1 \\ e^{-(\delta_k(\omega)-1)^2/(2\sigma_h^2)}, & \text{otherwise} \end{cases} \quad (4.6)$$

with

$$\delta_k(\omega) = \begin{cases} \sqrt{\frac{(\omega_m - \omega_0)^2}{(0.5\omega_0)^2} + \frac{\omega_n^2}{\omega_0^2}} & , \text{ if } m \text{ tagging direction} \\ \sqrt{\frac{(\omega_m)^2}{\omega_0^2} + \frac{(\omega_n - \omega_0)^2}{(0.5\omega_0)^2}} & , \text{ if } n \text{ tagging direction} \end{cases} \quad (4.7)$$

where $\omega = [\omega_m \ \omega_n]^T$, and ω_0 is the spatial tagging frequency. In essence, $f_k(\omega)$ is an elliptic-shape bandpass filter centered at the spatial tagging frequency, with a smooth transition around the ellipse border as shown in Fig. 4.4. In our experiments, we set σ_h to 0.05 as suggested in [Osman *et al.* (2000)]. It can be seen from Eq. 4.7 that the filter keeps positive frequencies only, around the first harmonic peak in the frequency domain [Osman *et al.* (1999)].

Back to the spatial domain, the phase $a_k(m, n)$ is then computed as

$$a_k(m, n) = \arg(\mathcal{F}^{-1}\{\mathcal{F}\{I_k(m, n)\}f_k(\omega)\}) \quad . \quad (4.8)$$

Since the 2D slices are sparsely distributed, the in-slice phase needs to be interpolated to 3D. In our experiments, the complex image $\mathcal{F}^{-1}\{\mathcal{F}\{I_k(m, n)\}f_k(\omega)\}$ was linearly interpolated before extracting the phase. This avoids artifacts related to phase wrapping discontinuities.

In this thesis, we compare the phase definition of HARP with the alternative brought by the monogenic signal theory [Alessandrini *et al.* (2013)] with a proposed bandpass filter. We opted for a symmetric ellipsoid-shape bandpass filter similar to the one used in HARP except that it consists of two ellipses centered at $\pm\omega_0$ and therefore is symmetric. This profile is obtained by modifying the $\delta_k(\omega)$ distance function introduced in Eq. 4.6 by:

$$\delta_k^{mono}(\omega) = \begin{cases} \sqrt{\frac{(|\omega_m| - \omega_0)^2}{(0.5\omega_0)^2} + \frac{\omega_n^2}{\omega_0^2}} & , \text{ if } m \text{ tagging direction} \\ \sqrt{\frac{(\omega_m)^2}{\omega_0^2} + \frac{(|\omega_n| - \omega_0)^2}{(0.5\omega_0)^2}} & , \text{ if } n \text{ tagging direction} \end{cases} \quad (4.9)$$

Replacing $\delta_k(\omega)$ by $\delta_k^{mono}(\omega)$ in Eq. 4.6 produces the bandpass filter as shown in Fig. 4.4e and 4.4f. Both phase definitions are compared experimentally in Sect. 4.5.1.

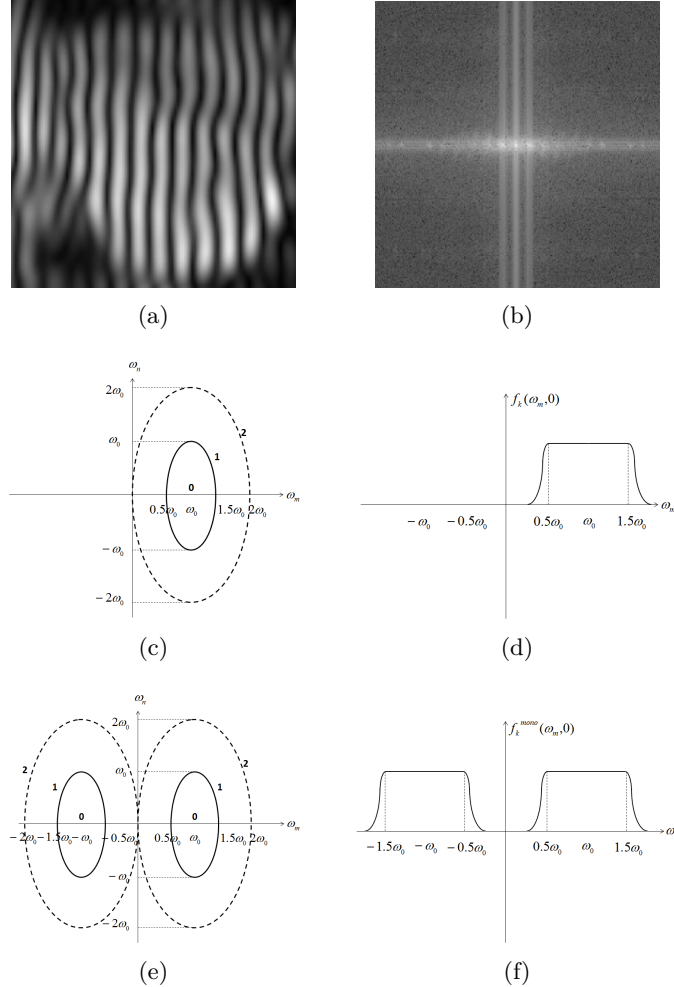


Figure 4.4: Bandpass filter used in HARP and MP with vertical line tagging (tagging direction in m -axis). ((a): $I_k(m, n)$; (b): $|\mathcal{F}\{I_k(m, n)\}|$; (c): isovales of $\delta_k(\omega)$ in HARP; (d): $f_k(\omega)$ along ω_m in HARP; (e): isovales of $\delta_k^{mono}(\omega)$ in MP; (f): $f_k^{mono}(\omega)$ along ω_m in MP)

Dense motion estimation

HARP tracking can be seen as a multi-channel optical flow on the true phases (phases without wrapping artifacts) [Osman *et al.* (1999)]. Here we denote the true phase by $\phi_k(\mathbf{x})$ with $k = 1, 2, 3$ in the 3D case where k indexes the channel number (tagging direction). The tracking of a material point from $t \rightarrow t-1$ can be solved iteratively by updating the displacement $\tilde{\mathbf{u}}_t$

$$\tilde{\mathbf{u}}_t \leftarrow \tilde{\mathbf{u}}_t + \mathbf{v}_t \quad (4.10)$$

where \mathbf{v}_t is computed by solving the following 3x3 linear system:

$$A \cdot \mathbf{v}_t = b \quad (4.11)$$

$$A = \begin{bmatrix} \nabla \phi_1^{t-1}(\mathbf{x} + \tilde{\mathbf{u}}_t)^T \\ \nabla \phi_2^{t-1}(\mathbf{x} + \tilde{\mathbf{u}}_t)^T \\ \nabla \phi_3^{t-1}(\mathbf{x} + \tilde{\mathbf{u}}_t)^T \end{bmatrix} \quad (4.12)$$

$$b = \begin{bmatrix} \phi_1^t(\mathbf{x}) - \phi_1^{t-1}(\mathbf{x} + \tilde{\mathbf{u}}_t) \\ \phi_2^t(\mathbf{x}) - \phi_2^{t-1}(\mathbf{x} + \tilde{\mathbf{u}}_t) \\ \phi_3^t(\mathbf{x}) - \phi_3^{t-1}(\mathbf{x} + \tilde{\mathbf{u}}_t) \end{bmatrix} \quad (4.13)$$

Spatial derivatives were corrected when the phase gets wrapped from $-\pi$ to π [Osman *et al.* (1999)]. Similarly, b was computed from the wrapped phases a_k as in [Osman *et al.* (1999)]. The details about their computation are provided in Appendix A.1.

4.3.2 Motion model

Let $\mathbf{u}_t^{(i)}(\mathbf{x})$ be a local parametric motion within a window i (described later in Sect. 4.3.3) from $t \rightarrow t-1$. As tracking aims at recovering both motion and deformation values, we opted for an affine transformation in the anatomical coordinates $\{r, l, c^{(i)}\}$ that combines translations, stretching (or shortening) and shearing. This 12-parameter model was defined in the anatomical system of coordinates introduced in Sect. 4.2.3 and 4.2.3:

$$\begin{aligned} \mathbf{u}_t^{(i)}(\mathbf{x}) &= L_r^{(i)}(\mathbf{x})\hat{\mathbf{e}}_r(\mathbf{x}) + L_l^{(i)}(\mathbf{x})\hat{\mathbf{e}}_l(\mathbf{x}) + L_c^{(i)}(\mathbf{x})\hat{\mathbf{e}}_c(\mathbf{x}) \\ \text{with } L_r^{(i)}(\mathbf{x}) &= a_{rr}^{(i)}r(\mathbf{x}) + a_{rl}^{(i)}l(\mathbf{x}) + a_{rc}^{(i)}c^{(i)}(\mathbf{x}) + b_r^{(i)} \\ L_l^{(i)}(\mathbf{x}) &= a_{lr}^{(i)}r(\mathbf{x}) + a_{ll}^{(i)}l(\mathbf{x}) + a_{lc}^{(i)}c^{(i)}(\mathbf{x}) + b_l^{(i)} \\ L_c^{(i)}(\mathbf{x}) &= (a_{cr}^{(i)}r(\mathbf{x}) + a_{cl}^{(i)}l(\mathbf{x}) + a_{cc}^{(i)}c^{(i)}(\mathbf{x}) + b_c^{(i)})\rho(\mathbf{x}) \end{aligned} \quad (4.14)$$

The set of zero-order $\{b_r^{(i)}, b_l^{(i)}, b_c^{(i)}\}$ (related to motion), first-order $\{a_{rr}^{(i)}, a_{ll}^{(i)}, a_{cc}^{(i)}\}$ (related to *radial, longitudinal and circumferential strains*) and first-order $\{a_{rl}^{(i)}, a_{rc}^{(i)}, a_{lr}^{(i)}, a_{lc}^{(i)}, a_{cr}^{(i)}, a_{cl}^{(i)}\}$ (related to shearing) parameters fully define the motion in the local window i .

The tracking accuracies between using the above motion model and a simplified one without the shearing elements $\{a_{rl}^{(i)}, a_{rc}^{(i)}, a_{lr}^{(i)}, a_{lc}^{(i)}, a_{cr}^{(i)}, a_{cl}^{(i)}\}$ will be further discussed in Sect. 4.5.1.

4.3.3 Regularization by window-weighted regression

Mcleod *et al.* [McLeod *et al.* (2013)] integrated local window functions defined in prolate spheroidal coordinates within the polyaffine registration framework. In this section, we will explain how we define the window functions similarly and further couple it with the motion model (Sect. 4.3.2) for regularizing HARP results.

The Partition of unity method

As introduced in [Makram-Ebeid and Somphone (2007)], a global regression problem can be simplified by solving a set of local ones with the help of the *Partition of unity* technique.

A partition of the LV domain is defined by a set of control points $\{\mathbf{x}_i\}$ and by window functions $\varphi^{(i)}(\mathbf{x})$ associated to each control point. The latter are assumed to satisfy the following conditions:

$$\begin{aligned} \arg \max_{\mathbf{x}} \varphi^{(i)}(\mathbf{x}) &= \mathbf{x}_i, \quad \forall i \\ \varphi^{(i)}(\mathbf{x}) &\geq 0, \quad \forall \mathbf{x} \in \Omega, \\ \sum_i \varphi^{(i)}(\mathbf{x}) &= 1 \quad \forall \mathbf{x} \in \Omega. \end{aligned} \tag{4.15}$$

where Ω is the LV myocardium. The computation of $\varphi^{(i)}(\mathbf{x})$ is described later in Sect. 4.3.3. The regularized displacement $\mathbf{u}_t(\mathbf{x})$ is computed as

$$\mathbf{u}_t(\mathbf{x}) = \sum_i \varphi^{(i)}(\mathbf{x}) \mathbf{u}_t^{(i)}(\mathbf{x}) \tag{4.16}$$

where $\mathbf{u}_t^{(i)}(\mathbf{x})$ is the motion model introduced in Sect. 4.3.2.

Under Eq. VF.8 and VF.9, if given certain measurement motion estimates $\tilde{\mathbf{u}}_t(\mathbf{x})$ (HARP tracking results in Sect. 4.3.1) and confidence weight $\tilde{w}_t(\mathbf{x})$ (described later in Sect. 4.3.3), the sum of the local errors $E^{(i)}$ then gives an upper bound to the global error E .

$$\begin{aligned} E &= \int_{\Omega} \tilde{w}_t(\mathbf{x}) \left\| \tilde{\mathbf{u}}_t(\mathbf{x}) - \sum_i \varphi^{(i)}(\mathbf{x}) \mathbf{u}_t^{(i)}(\mathbf{x}) \right\|^2 d\mathbf{x} \\ &\leq \sum_i \int_{\Omega} \tilde{w}_t(\mathbf{x}) \varphi^{(i)}(\mathbf{x}) \left\| \tilde{\mathbf{u}}_t(\mathbf{x}) - \mathbf{u}_t^{(i)}(\mathbf{x}) \right\|^2 d\mathbf{x} = \sum_i E^{(i)} \end{aligned} \tag{4.17}$$

The reader is referred to [Makram-Ebeid and Somphone (2007)] for further details. Bounding all $E^{(i)}$ to a small enough quantity also minimizes the global error, thus making it possible to decompose a global optimization problem into regional ones that are easier to solve.

Window functions

The LV domain was first divided into small windows as illustrated in Fig. 4.5. The purpose of this section is to define how $\varphi^{(i)}$ functions are defined for a given partition of the LV domain. This partition is obtained using a multi-resolution strategy as explained in Section 4.3.5.

Given a partition of the LV, control points were defined as the center of these windows. Window functions are centered at each control point and must decrease when the distance

to the control point increases. Since we opted for tracking a volumetric mesh and defined a system of coordinates on the mesh, the geodesic distance was chosen rather than the Cartesian one for computing the window function. Considering a standard Gaussian kernel involving the geodesic distance ξ between \mathbf{x} and the center of the window \mathbf{x}_i

$$g^{(i)}(\mathbf{x}) = \frac{1}{2\pi\sigma_i} e^{-\frac{\xi(\mathbf{x}, \mathbf{x}_i)^2}{2\sigma_i^2}} \quad (4.18)$$

To use a single σ parameter for various window sizes, we expressed σ_i as

$$\sigma_i = \sigma\chi_i \quad (4.19)$$

where χ_i is computed for each window by averaging its circumferential and longitudinal extents. In Eq. 4.19, σ is an auxiliary parameter named as *kernel bandpass*. It controls how neighboring windows will overlap for producing the final displacement estimate in Eq. VF.9. The influence of σ on the final tracking accuracy is further discussed in Sect. 4.5.1. Note that the σ parameter is normalized and can thus be used across several window resolutions (see Sect. 4.3.5).

Window functions are defined by normalizing $g^{(i)}$ values for summing to 1:

$$\varphi^{(i)}(\mathbf{x}) = \frac{g^{(i)}(\mathbf{x})}{\sum_j g^{(j)}(\mathbf{x})} \quad . \quad (4.20)$$

As seen in Sect. 4.2.3, $\hat{\mathbf{e}}_c(\mathbf{x})$ is not defined for purely apical points. Therefore these points should be excluded from the regularization process. This is done by setting all $\varphi^{(i)}(\mathbf{x})$ to 0 for those points.

Confidence weight

It was shown in Eq. 4.8 that the HARP phase is computed by taking the argument of the complex signal. In fact, computing its amplitude $|\mathcal{F}^{-1}\{\mathcal{F}\{I_k(m, n)\}f_k(\omega)\}|$ (note as \mathcal{M}_k) corresponds to untagging the original image [Osman *et al.* (1999)]. This information can be used as a confidence weight map $\tilde{w}_t(\mathbf{x})$: a high value of \mathcal{M}_k indicates a higher probability of belonging to the myocardium, hence an increased confidence in the HARP result $\tilde{\mathbf{u}}_t(\mathbf{x})$. In our implementation, the confidence weights $\tilde{w}_t(\mathbf{x})$ were obtained by averaging the three channels and taking the geometric mean over the two frames t and $t - 1$:

$$\tilde{w}_t(\mathbf{x}) = \sqrt{\frac{1}{3} \left(\sum_{k=1}^3 \mathcal{M}_k^t(\mathbf{x}) \right) \cdot \frac{1}{3} \left(\sum_{k=1}^3 \mathcal{M}_k^{t-1}(\mathbf{x} + \tilde{\mathbf{u}}_t(\mathbf{x})) \right)}, \quad (4.21)$$

Incompressibility constraint

Imposing a zero divergence is a classic way of enforcing incompressibility. This constraint can be imposed either as a soft (global) or hard (local) level. In our case, computing

the divergence locally would require complex spatial derivations of the $r(\mathbf{x})$, $l(\mathbf{x})$ and $c^{(i)}(\mathbf{x})$ functions. Therefore, we preferred to impose incompressibility within each window, enforcing the overall volume change to be zero. For doing so, we applied the divergence theorem. If $\partial S^{(i)}$ stands for the surface enclosing the window i , the outward flow of $\mathbf{u}_t^{(i)}(\mathbf{x})$ through $\partial S^{(i)}$ equals the volume integral of the divergence over that window. Therefore imposing myocardial incompressibility is equivalent to forcing the flow through $\partial S^{(i)}$ to be zero. For each local window i defined on the volumetric mesh, $\partial S^{(i)}$ consists of quadrilaterals. Each of the quadrilateral j can be represented by its center \mathbf{x}_j , its normal (pointing outward) \vec{n}_j and its area A_j . The flow of $\mathbf{u}_t^{(i)}(\mathbf{x})$ through $\partial S^{(i)}$ can then be written as

$$\begin{aligned} Q_t^{(i)} &= \sum_{j \in \partial S^{(i)}} \mathbf{u}_t^{(i)}(\mathbf{x}_j) \cdot A_j \vec{n}_j \\ &= \sum_{j \in \partial S^{(i)}} \sum_{d=r,l,c} L_d^{(i)}(\mathbf{x}_j) (\hat{\mathbf{e}}_d(\mathbf{x}_j) \cdot A_j \vec{n}_j) \end{aligned} \quad (4.22)$$

Because $L_d^{(i)}(\mathbf{x}_j)$ is linear in $\{b_d^{(i)}, a_{rd}^{(i)}, a_{ld}^{(i)}, a_{cd}^{(i)}\}$ ($d = r, l, c$), so is $Q_t^{(i)}$. Imposing $Q_t^{(i)} = 0$ amounts to add a linear equality constraint. In other words, a_{rr} can be written as a linear combination of all other parameters $\{b_r^{(i)}, b_l^{(i)}, b_c^{(i)}, a_{rl}^{(i)}, a_{rc}^{(i)}, a_{lr}^{(i)}, a_{ll}^{(i)}, a_{lc}^{(i)}, a_{cr}^{(i)}, a_{cl}^{(i)}, a_{cc}^{(i)}\}$.

Solving local system and reforming global motion

Let us show how, with the motion model defined in Sect. 4.3.2, we can obtain a quadratic form for the local $E^{(i)}$ errors. As $\{\hat{\mathbf{e}}_r(\mathbf{x}), \hat{\mathbf{e}}_l(\mathbf{x}), \hat{\mathbf{e}}_c(\mathbf{x})\}$ define an orthogonal basis, we can project HARP displacements $\tilde{\mathbf{u}}_t(\mathbf{x})$ on this basis:

$$\begin{aligned} \tilde{\mathbf{u}}_t(\mathbf{x}) &= \sum_{d=r,l,c} p_d(\mathbf{x}) \hat{\mathbf{e}}_d(\mathbf{x}) \\ \text{with } p_d(\mathbf{x}) &= \tilde{\mathbf{u}}_t(\mathbf{x}) \cdot \hat{\mathbf{e}}_d(\mathbf{x}) \end{aligned} \quad (4.23)$$

From Eq. 4.14 and VF.16, $E^{(i)}$ in Eq. VF.10 can be expanded as:

$$E^{(i)} = \int_{\Omega} \varphi^{(i)}(\mathbf{x}) \tilde{w}_t(\mathbf{x}) \left\| \sum_{d=r,l,c} \left(L_d^{(i)}(\mathbf{x}) - p_d(\mathbf{x}) \right) \hat{\mathbf{e}}_d(\mathbf{x}) \right\|^2 d\mathbf{x} \quad (4.24)$$

Using orthogonality between $\{\hat{\mathbf{e}}_r(\mathbf{x}), \hat{\mathbf{e}}_l(\mathbf{x}), \hat{\mathbf{e}}_c(\mathbf{x})\}$, it is easy to further obtain:

$$E^{(i)} = \int_{\Omega} \varphi^{(i)}(\mathbf{x}) \tilde{w}_t(\mathbf{x}) \sum_{d=r,l,c} \left(L_d^{(i)}(\mathbf{x}) - p_d(\mathbf{x}) \right)^2 d\mathbf{x} \quad (4.25)$$

Because $L_d^{(i)}(\mathbf{x})$ is linear in $b_d^{(i)}, a_{dr}^{(i)}, a_{dl}^{(i)}$ and $a_{dc}^{(i)}$ ($d = r, l, c$), $E^{(i)}$ is a quadratic form and can be minimized by solving a linear system. Since the radial strain is reported to be the most challenging to recover, we integrated the incompressibility constraint and in Eq. VF.18 we substituted $a_{rr}^{(i)}$ by the linear combination of $\{b_r^{(i)}, b_l^{(i)}, b_c^{(i)}, a_{rl}^{(i)}, a_{rc}^{(i)}, a_{lr}^{(i)}, a_{ll}^{(i)}, a_{lc}^{(i)}\}$,

$a_{cr}^{(i)}, a_{cl}^{(i)}, a_{cc}^{(i)}\}$. The minimization of $E^{(i)}$ then gives a 11x11 linear system which is solved by pseudo-inverse. As a final step, $a_{rr}^{(i)}$ was computed from the linear combination mentioned above. Once the local motions $\mathbf{u}_t^{(i)}(\mathbf{x})$ are computed, the global motion is reformed by Eq. VF.9.

4.3.4 Computing apex motion *a posteriori*

Since purely apical points do not take part in the regularization process (see Sect. 4.3.3), we need to compute their motions by other ways. For each of the N_r purely apical points, its displacement was computed by averaging the final motions $\mathbf{u}_t(\mathbf{x})$ of its N_c nearest neighbors located in the same radial layer.

4.3.5 Multi-resolution framework

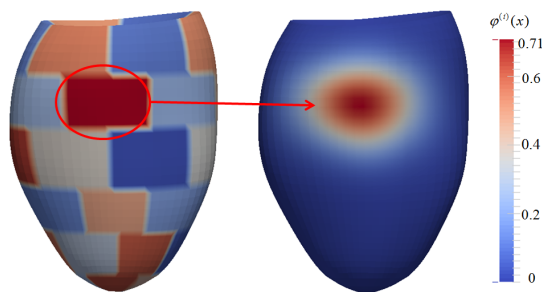


Figure 4.5: Definition of LV local windows and an example of the window function for the red-circled window

We need to define a partition of the LV domain at increasing levels of resolutions. For simplification purposes, we partitioned the LV using a single parameter: the number of divisions in the circumferential and longitudinal directions.

Additionally, to obtain a more homogeneous mix between windows, they were shifted by half their circumferential extent over contiguous longitudinal layers (see Fig. 4.5 for an illustration).

For improving the convergence of the motion and deformation coefficients, we started with 3 divisions in longitudinal and circumferential directions. This number was then doubled over the two next resolutions.

At each resolution, the HARP tracking (Sect. 4.3.1) was initialized with the result of the previous resolution before proceeding to the regularization described earlier in this Section.

The influence of the number of resolutions n on the final tracking accuracy is further discussed in Sect. 4.5.1.

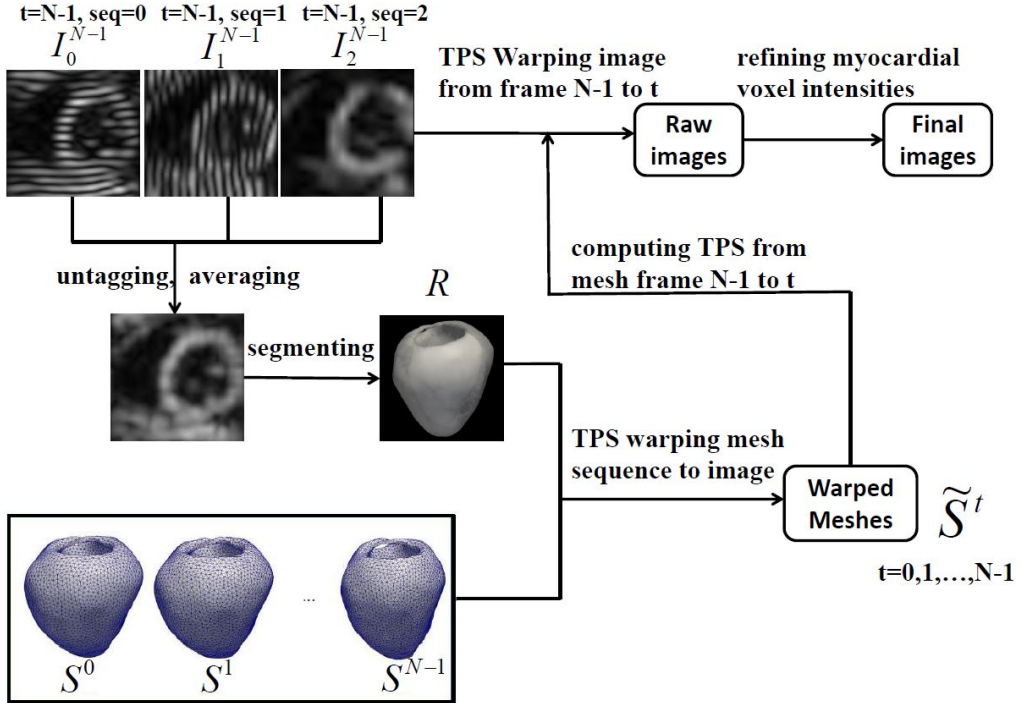


Figure 4.6: Pipeline for generating synthetic tagged MR sequence

4.4 Generation of synthetic images

For evaluating the impact of several parameters on tracking and strain accuracy, a simple strategy was implemented for generating synthetic images. The pipeline is shown in Fig. 4.6 and detailed in this Section. The required inputs are 1) one sequence of 3D+t tetrahedral LV meshes (noted as \mathcal{S}^t where t is the frame index) as made publicly available from [De Craene *et al.* (2013)]; and 2) three CSPAMM images with orthogonal tagging orientations (noted as I_k^{N-1} where N is the number of frames and $k \in \{1, 2, 3\}$), as made publicly available from [Tobon-Gomez *et al.* (2013)]. The LV meshes used here come from an electro-mechanical model [Marchesseau *et al.* (2013)] which takes into account fiber distribution. Fibers have a varying orientation from endocardium to epicardium that follows values published in the literature. The quasi incompressibility of the myocardial motion is ensured. However, on the simulation generated in [De Craene *et al.* (2013)], the apex was fixed using a hard constraint on displacements. This limits torsion on this simulation.

4.4.1 Registering LV meshes to real tagged MR images

We assume that the last frame in the image sequence and the last electro-mechanical mesh both correspond to the end of diastole. As described in Sect. 4.2.2, the untagged images were computed for the last frame and averaged to an isotropic volume. This volume was segmented by first extracting the surface of the last mesh of the electro-mechanical model as the template and manually position/deform it through the same segmentation

technique as in Sect. 4.2.2. The segmentation result will be noted as \mathcal{R} . A Thin plate spline (TPS) [Bookstein (1989)] transformation \mathcal{T} was then computed between the template and \mathcal{R} . This transformation was then applied to all meshes \mathcal{S}^t , creating a new sequence of tetrahedral LV meshes $\tilde{\mathcal{S}}^t = \mathcal{T}(\mathcal{S}^t)$.

4.4.2 Warping real tagged MR images by forces computed from meshes

Synthetic images were obtained by deforming the last frame images \mathcal{I}_k^{N-1} to match the sequence of $\tilde{\mathcal{S}}^t$ meshes. This was done in two steps. First, a TPS transformation $\mathcal{T}' : \tilde{\mathcal{S}}^{N-1} \mapsto \tilde{\mathcal{S}}^t$ was computed for extending displacements defined at the mesh nodes only to the whole volume and warping the \mathcal{I}_k^{N-1} image. Second, this image was corrected inside the myocardial for removing TPS-induced artifacts as follows. For every voxel in \mathcal{I}_k^t , we checked if it belonged to the myocardial domain $\tilde{\mathcal{S}}^t$. If it did, we found the corresponding tetrahedral cell and the barycentric coordinates of the voxel within that cell. We then interpolated the intensity of \mathcal{I}_k^{N-1} for the same cell and barycentric coordinates. This intensity was used instead of the one obtained through TPS warping. This myocardial intensity correction procedure ensures that the motion represented in the synthetic sequence matches the ground-truth $\tilde{\mathcal{S}}^t$ mesh sequence.

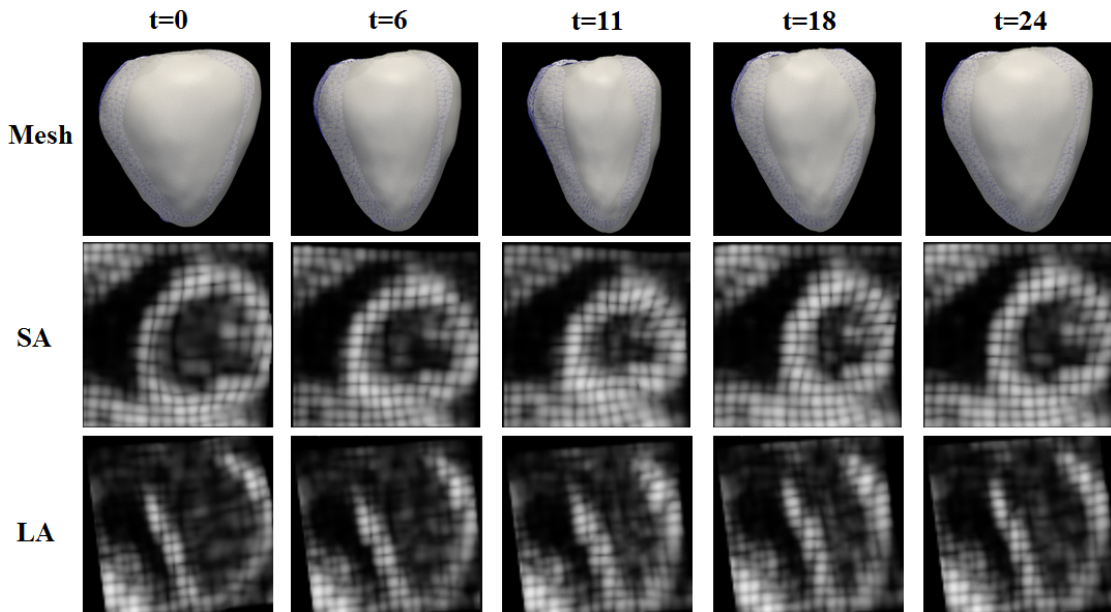


Figure 4.7: Ground truth meshes and short- and long-axis slices of synthetic tagged MR images (3 sequences of tagged MR images with line tagging patterns are multiplied for better visualization)

4.5 Results

4.5.1 Synthetic images

A synthetic tagged MR image sequence was generated for a normal geometry using the approach described in Sect. 4.4. Fig. 4.7 shows the ground truth meshes and the synthetic images. The grid pattern was obtained by multiplying the three input channels (with orthogonal line tagging pattern) in a single image after resampling. This resampled image is used for visualization only and not for processing.

The tetrahedral simulation mesh at the last frame was resampled to a hexahedral mesh as described in Sect. 4.2.3. Over this procedure, special attention was paid to have all nodes of the resampled mesh within the elements of the original mesh. Using barycentric coordinates of the simulation meshes, node displacements can be interpolated at all times on the resampled mesh, hence providing ground truth displacement values. After propagating the last mesh through tracking, measured displacements can be compared to ground truth for quantifying tracking accuracy.

Ground truth strain values were computed on the set of resampled meshes. Our mesh model makes the computation of 1D engineering strain trivial since all edges are following *radial*, *longitudinal* and *circumferential* directions. Relative length changes were computed for each hexahedral cell according to

$$\epsilon_d = \frac{1}{4} \sum_{j=1}^4 \frac{l_{dj}^t}{l_{dj}^0} - 1 \quad (4.26)$$

where l_{dj}^t is the length of edge j in the d direction (being either *radial*, *longitudinal* or *circumferential*) at time t . Strain values were then averaged per AHA segment for all cells belonging to that segment. Similarly to tracking accuracy, strain accuracy was measured by doing the same computation on tracked meshes and comparing ground truth with measured values.

Tracking and strain accuracies on the synthetic sequence were used as a reference for tuning key parameters, comparing the two phase computation techniques (HARP and MP) and discussing the influence of shearing elements. Fig. 4.8 and Fig. 4.9-4.11 show the evolution of motion and strain errors when spanning different n (Sect. 4.3.5) and σ (Sect. 4.3.3) values.

Tuning the regularization parameters

From Fig. 4.8, 4.9, 4.10 and 4.11, it can be seen that for both HARP and MP, setting either $n = 3$ and $\sigma = 0.2$, or $n = 3$ and $\sigma = 0.3$ outperform other configurations with tracking errors below 1.5 mm. When also considering strain accuracy, $n = 3$ and $\sigma = 0.3$ is the best choice on the synthetic data. Bland Altman plots of *radial*, *longitudinal* and *circumferential* strains of this case are shown in Fig. 4.12.

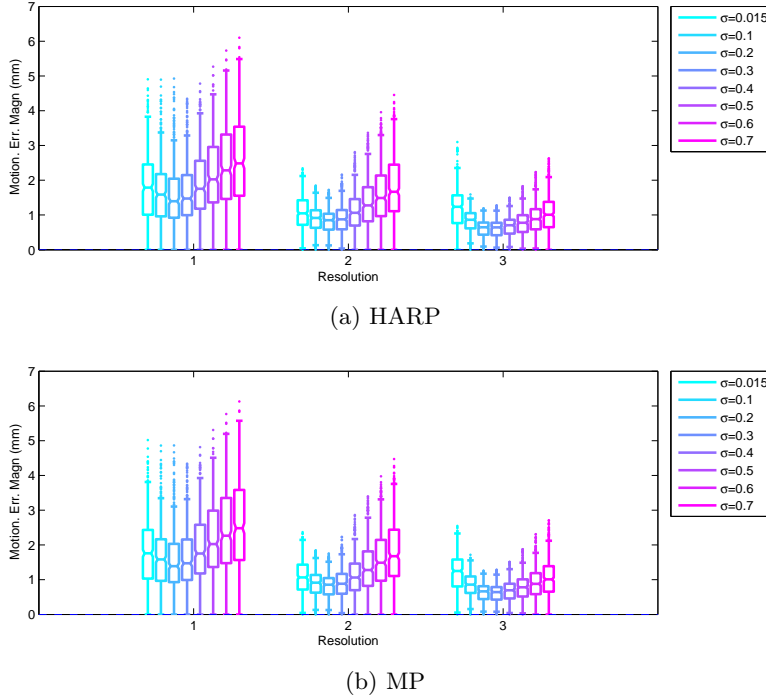


Figure 4.8: Quartile plots showing the evolution of tracking accuracy with the number of resolutions n and the kernel bandwidth σ when using HARP (a) and MP (b) on synthetic images (each data point represents the motion error of certain AHA segment at certain time frame).

Comparison of HARP and MP

Fig. 4.13 summarizes the comparison between MP and HARP in terms of tracking and strain accuracies. One can see that both phase computation methods give very similar results. We computed the point-wise end-systolic motion and strain accuracies when using HARP and MP, and applied the two sample t-test [Cressie and Whitford (1986)] on them. The returned p-values are all above 0.05 when comparing motion, radial, longitudinal and circumferential strain accuracies. Therefore no significant differences were found between HARP and MP.

Influence of the shearing elements in the motion model

In our previously defined motion model (Sect. 4.3.2), $\{a_{rl}^{(i)}, a_{rc}^{(i)}, a_{lr}^{(i)}, a_{lc}^{(i)}, a_{cr}^{(i)}, a_{cl}^{(i)}\}$ are parameters related to shearing. To understand the role they play in the tracking, we also considered the use of a simplified model where all shearing coefficients are set to zero. With this 6-parameter motion model, we regenerated the tracking on synthetic images. The magnitude of displacement errors are compared to those obtained by the original model (Eq. 4.14) in Fig. 4.14. As seen from Fig. 4.14, both the median and the dispersion of the displacement errors are reduced when taking into account the shearing

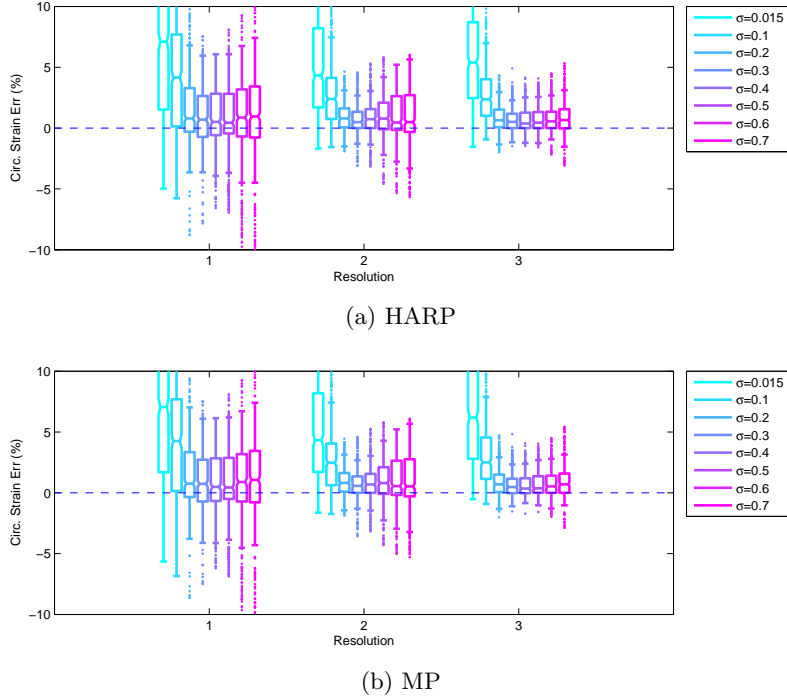


Figure 4.9: Quartile plots showing the evolution of circumferential strain accuracy with the number of resolutions n and the kernel bandwidth σ when using HARP (a) and MP (b) on synthetic images (each data point represents the circ. strain error of certain AHA segment at certain time frame).

elements. This result is further confirmed by two statistical tests. Applying the Levene's test [Miller Jr (1997)] to these two datasets of displacement errors returns a p-value below 0.05, rejecting the null hypothesis that their variances are equal. Also, the Wilcoxon signed-rank [Woolson (2007)] test on these two datasets reveals that their median values are statistically different.

4.5.2 Volunteer data sets

This section compares quantitatively our method to other state-of-the-art tagged MR algorithms. For doing so, we used the data provided by [Tobon-Gomez *et al.* (2013)] to compare our tracking accuracy using manually tracked landmarks located in the basal, mid and apical myocardium. In total, 15 volunteer datasets were used for the evaluation. The 12 landmarks were warped forwardly in time by computing barycentric coordinates in the first frame and propagating them through the sequence of volumetric meshes. This could slightly penalize our method in this evaluation as image-based tracking was performed backward in time. Fig. 4.15 shows box plots of motion tracking accuracy for all the 15 volunteers at end-systole. It can be seen that our method matches accuracies obtained using MEVIS and UPF algorithms while having less outliers. However, it should be noted, that the computation time of our method is in the range of minutes while UPF and MEVIS are in the range of hours as reported in [Tobon-Gomez *et al.* (2013)] for this same dataset.

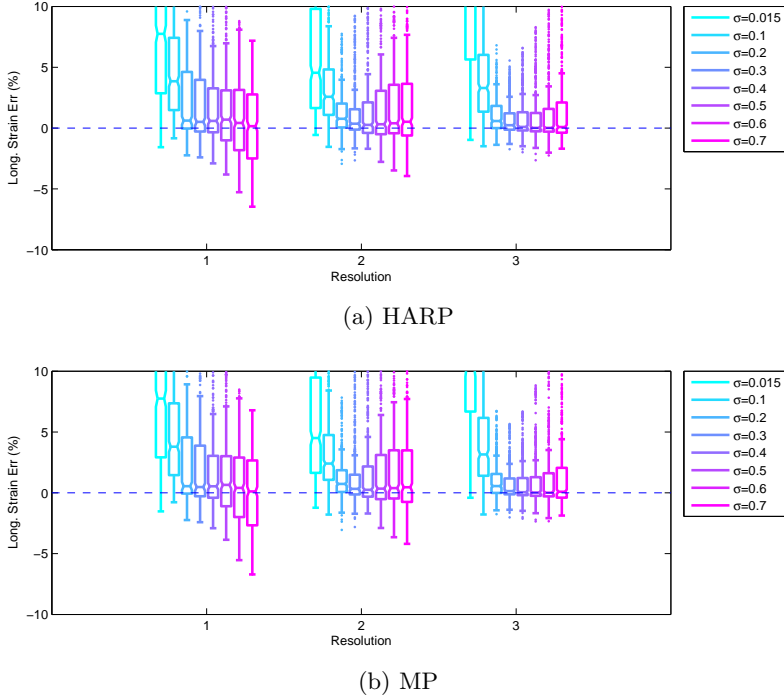


Figure 4.10: Quartile plots showing the evolution of longitudinal strain accuracy with the number of resolutions n and the kernel bandwidth σ when using HARP (a) and MP (b) on synthetic images (each data point represents the long. strain error of certain AHA segment at certain time frame).

4.5.3 Patient data sets

In this paper, we show quantification results for four patients showing grading levels of fibrosis confirmed by late gadolinium-enhanced MR images. The patient datasets were acquired at GIP Cyceron. All patients gave an informed consent and the study was approved by the regional ethics committee (CPP Nord Ouest III). For comparison purposes, we also quantified three healthy volunteers acquired at the same institution and enrolled in the same study. Fig. 4.16 plots the dispersion of end-systolic circumferential strain values for the volunteers (v1 to v5) and the four patients (p1 to p4). The two first volunteers were taken from [Tobon-Gomez *et al.* (2013)] while the others were scanned at Caen-CHU/Cyceron. The four patients were ordered by the number of segments where transmural fibrosis was visible on late-enhancement MR. It is expected that for diseased cases with grading levels of infarction, more segments with abnormally low deformation values will coexist with segments overcompensating for infarcted segments. Therefore, the overall dispersion of strain values should increase for more extreme cases of infarction. Fig. 4.16 shows that this tendency can be observed in our database: the circ. strain dispersion increases from healthy volunteers (v1-v5) to patients (p1-p4) classified by de-

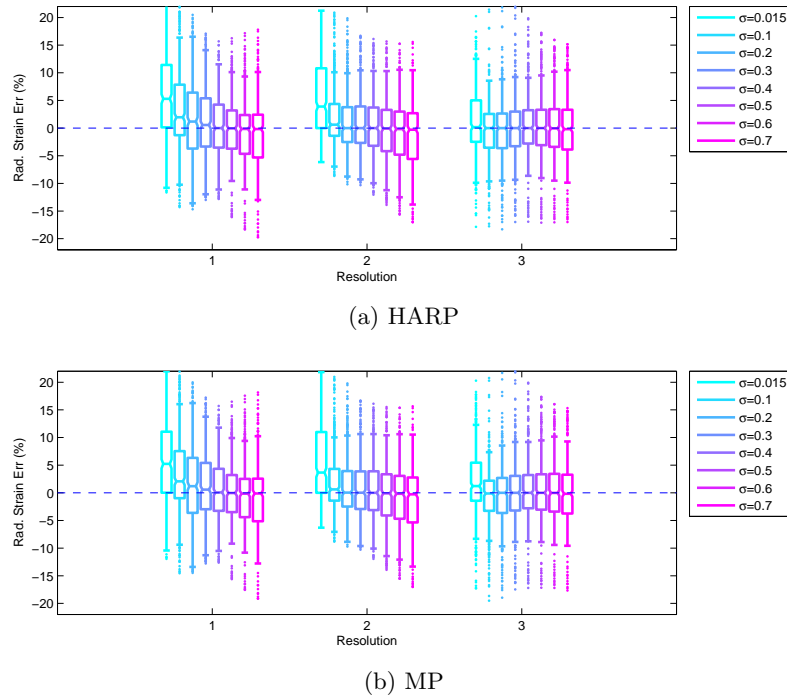


Figure 4.11: Quartile plots showing the evolution of radial strain accuracy with the number of resolutions n and the kernel bandwidth σ when using HARP (a) and MP (b) on synthetic images (each data point represents the rad. strain error of certain AHA segment at certain time frame).

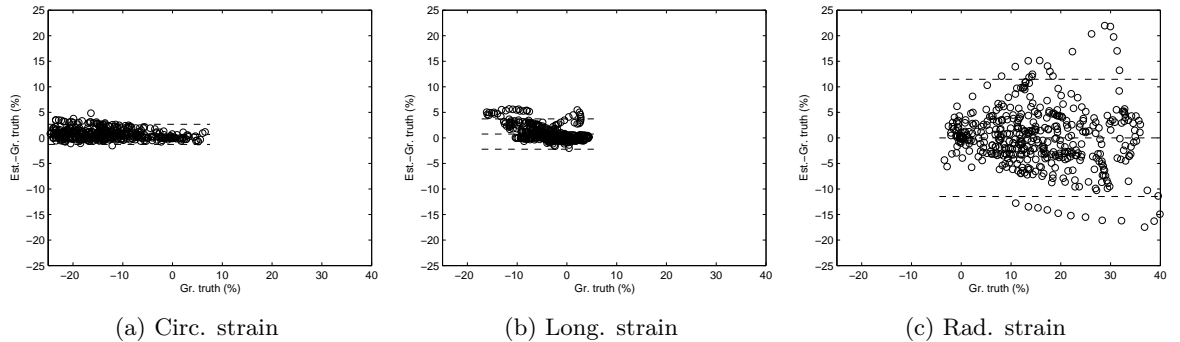


Figure 4.12: Bland Altman plots on Circ. Long. and Rad. strains when $n = 3$ and $\sigma = 0.3$ using MP on synthetic images (each data point represents the strain of certain AHA segment at certain time frame)

gree of fibrosis. Also, the median circ. strain decreases from volunteers (around -20%) to patients (around -15%). We took the example of circumferential strain as we observed this component to be more robust when image quality is lower. Indeed, the four patients we report here showed very different image qualities, mainly depending on their ability to hold their breath over all acquisitions in a similar manner.

To look at strain at a more detailed level, in Fig. 4.17 we plot for the second patient p2 end-systolic circumferential strain as a colormap and display circ. strain curves at a seg-

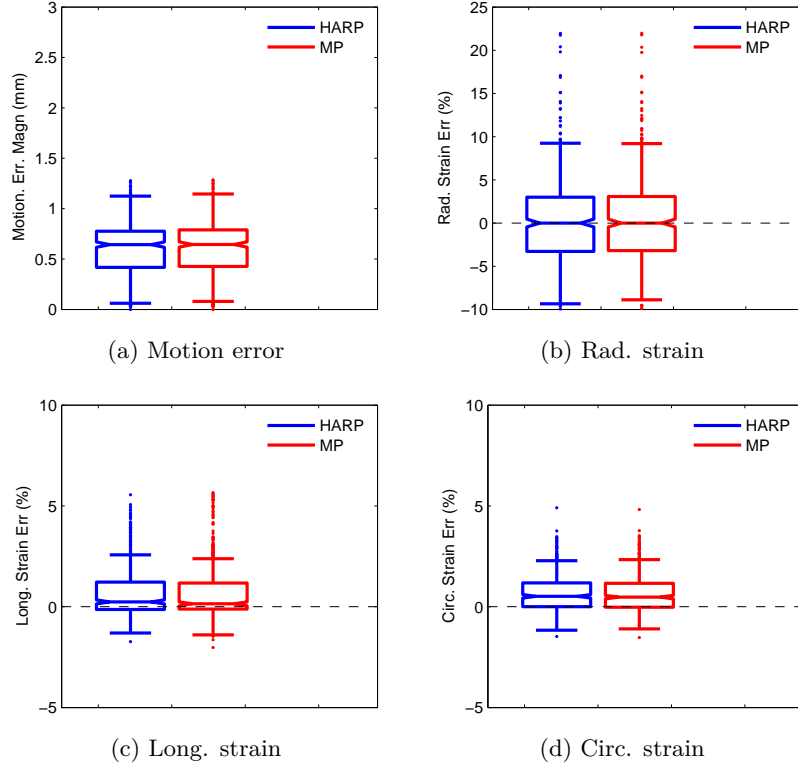


Figure 4.13: Comparisons of HARP and MP with respect to end-systolic tracking, rad. strain, long. strain and circ. strain accuracies for $n = 3$ and $\sigma = 0.3$ on synthetic images (each data point represents the motion, rad. strain, long. strain or circ. strain errors of certain AHA segment at the end-systole).

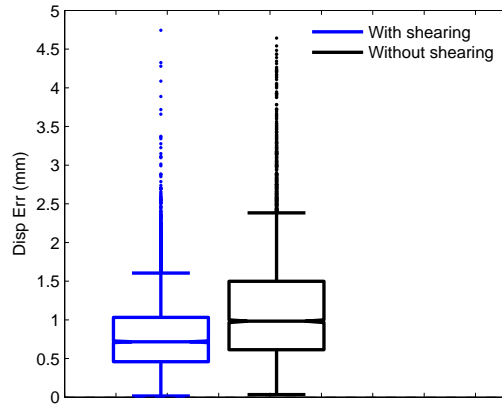


Figure 4.14: End-systolic motion error magnitudes with/without shearing elements using MP (parameters $n = 3, \sigma = 0.3$) on synthetic images (The data points represent the motion error magnitudes of all mesh points at end-systole)

mental level. This patient had myocardial fibrosis at the entire inferior wall, basal and mid levels of the inferolateral wall, and basal inferoseptal wall (different degrees of fibrosis at AHA segments 3,4,5,10,11,15). Fig. 4.17a(left) and Fig. 4.17b(left) show a clear difference

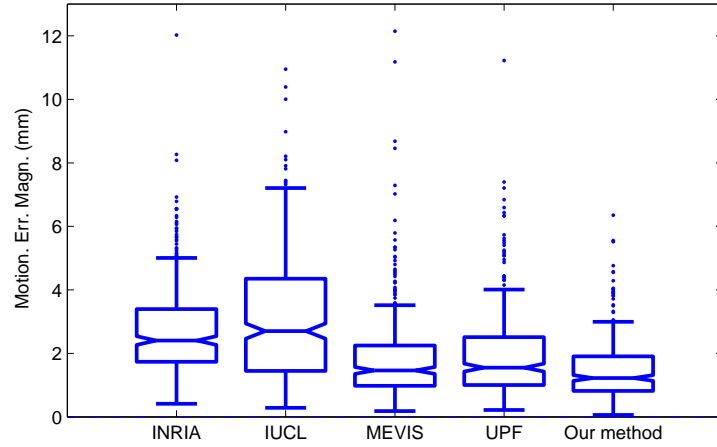


Figure 4.15: Motion tracking accuracy using MP (parameters $n = 3, \sigma = 0.3$) on volunteer data sets compared to four other state-of-art methods: INRIA, IUCL, MEVIS and UPF (for details of these methods please refer to [Tobon-Gomez *et al.* (2013)]).

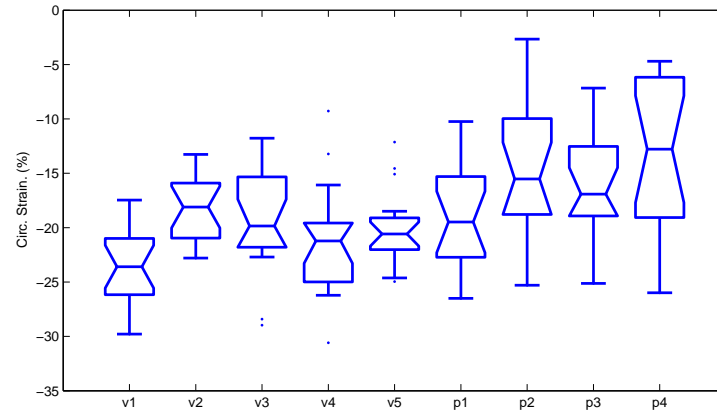
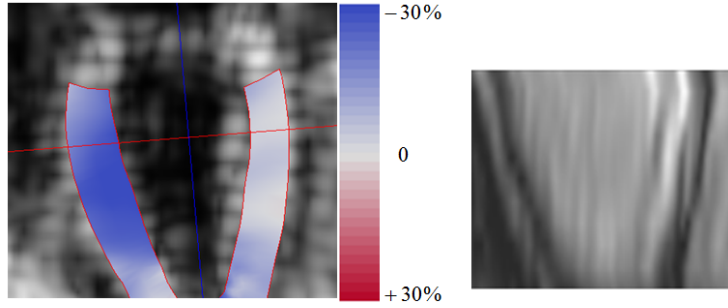
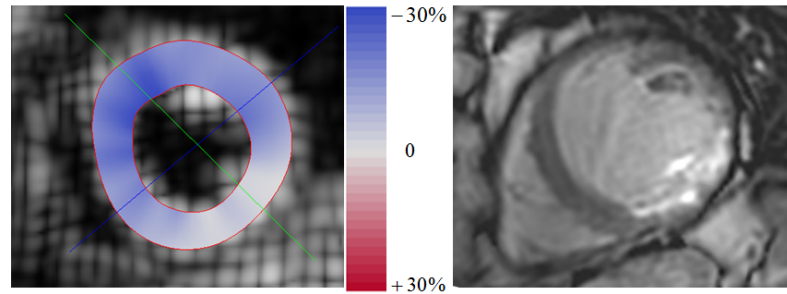


Figure 4.16: End-systolic Circ. strain at AHA 17 segment level, v1 and v2 are healthy volunteers from Sect. 4.5.2, v3,v4,v5 are healthy volunteers from GIP Cyceron, and p1, p2, p3, p4 are patients from GIP Cyceron increasingly classified by the myocardial fibrosis degree (results obtained using MP)

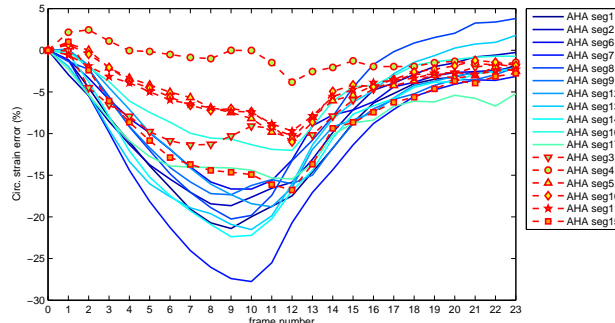
of circ. strain values between the inferior wall (infarcted) and the anterior wall (normal). This is coherent with the results by late-enhancement MR, as shown in Fig. 4.17a(right) and Fig. 4.17b(right) where high gray levels indicate the existence of fibrosis. A clear correlation could be seen between the low deformation regions and the infarcted areas (those with brighter image intensities). However, here the observed correlation is quite qualitative and limited because the two modalities were merely manually aligned. Indeed, these two kinds of images had different spatial resolutions, making their registration a difficult task. Besides, from the strain curves in Fig. 4.17c infarcted segments can be easily distinguished from the healthy ones.



(a) End-systolic Circ. strain colormap displayed on a LA slice and late-enhancement MR image of the same location



(b) End-systolic Circ. strain colormap displayed on a mid-level SA slice and late-enhancement MR image of the same location



(c) Circ. strain evolution of 17 AHA segs

Figure 4.17: Circ. strain plotted as a colormap {(a),(b)} and over time {(c)} for patient p2 in Fig. 4.16. This patient had fibrosis at the entire inferior wall, part of the inferolateral wall and part of the inferoseptal wall (corresponding to AHA segments 3,4,5,10,11,15). The colormap is shown at end of systole. Circ. strain curves are shown for all 17 segments: solid lines display normal segments while curves with markers show segments with fibrosis (results obtained using MP)

4.6 Discussion

The concept of anatomical regularization applied to cardiac motion tracking was directly or implicitly introduced in several previous publications [Young and Axel (1992), Young (1999), McLeod *et al.* (2013), Heyde *et al.* (2013), Heyde *et al.* (2016)a, Pan *et al.* (2005)]. We here discuss the differences between those methods and the proposed one.

Young *et al.* [Young and Axel (1992), Young (1999)] employed a finite-element model for regularizing the sparse image-based displacements. The variation of the deformation gradient tensor in *radial*, *longitudinal* and *circumferential* directions was used as the penalty term. The model was recently used to improve registration of a generic template to patient specific biventricular geometry [Gilbert *et al.* (2014)]. Although the mesh is defined in anatomical coordinates, the projection of sparse input displacements on the mesh is done in Cartesian coordinates. Our approach differs by projecting displacements in anatomical coordinates which we supposed to be more appropriate for the proposed regularization scheme.

McLeod *et al.* [McLeod *et al.* (2013)] used an affine regional approximation of displacements. Affine transformations were mixed through weight functions that are following anatomy. However, the affine transformations were defined in the Cartesian space, rather than exploiting the anatomical system of coordinates. We preferred to use anatomical coordinates for both defining window functions and the transformation model. This allows to regularize and constrain the motion field in the system used for reporting strain values. In our model, first order parameters are directly linked to *radial*, *longitudinal* and *circumferential* strains. Pan *et al.* [Pan *et al.* (2005)] interpolated 2D HARP displacements by a Gaussian kernel defined using the geodesic distance on the mesh. This is quite similar to our window function. However, as mentioned above, we differ in not only defining window functions that are following the anatomy, but also regularizing and constraining HARP displacements in anatomical coordinates. Besides, we processed the recent 3D CSPAMM data introduced in [Rutz *et al.* (2008)]. Compared with the tagging data used in both [Pan *et al.* (2005)] and [Young (1999)], each volume has more slices and images have better in-plane resolution.

Heyde *et al.* [Heyde *et al.* (2013), Heyde *et al.* (2016)a] performed the tracking of ultrasound images in anatomical coordinates. However, this was achieved by resampling all images in this space prior to the tracking. Such a resampling would introduce non-linear distortion in image intensities. Also, it would modify the spectrum of tagged MR images, modifying the band-pass nature of the signal. This would violate HARP assumptions. Thus, we preferred to use anatomical coordinates in the representation of the transformation.

This study has several technical limitations that are listed and discussed hereafter. First, the method is dependent of the segmentation of the LV done on the last frame as it serves both for defining the set of points to track and a local coordinate system used for regularization. This limitation also exists in the original HARP algorithm and in any method using an LV mask as region of interest. Second, we assumed the phase images to be available as 3D information while each image stack has a low inter-slice spatial resolution. However, each stack has a higher voxel spacing in a different dimension, hence reducing the overall impact of this low resolution. Also, since the local windows have a full transmural extent, the motion model will not capture the increase in circumferential shortening and radial thickening occurring from epicardium to endocardium [Clark *et al.*

(1991), Rademakers *et al.* (1994)]. Such a choice is justified by the limits of the acquisition scheme where the number of tags is low from endocardium to epicardium, making the information contained in the radial direction too poor for capturing radial deformation. Admittedly, defining multiple windows from endocardium to epicardium would allow to quantify transmural changes in deformation thanks to the good tagging resolution in the circumferential direction. Transmural changes in circumferential strain would then propagate to radial strain with the incompressibility constraint. This would require a more detailed validation and is currently left to future work.

Besides, our method depends on HARP accuracy and could be prone to tag jumps. We observed that tag jumps mostly occur in the longitudinal direction and that the multiscale strategy helps limiting tag jumps. Furthermore, at the end of systole, the myocardial incompressibility does not hold anymore due mainly to blood being squeezed out of the myocardium. The myocardial volume conservation is therefore an approximation (of about 8%) at the end of systole. Nonetheless, as explained earlier in this section, image intensities only will not suffice to capture the radial deformation. The incompressibility constraint was therefore used to help estimating the radial deformation, rather than as a hard constraint influencing all the deformation components. Moreover, using engineering strains as obtained from length changes in the volumetric mesh edges neglects shear-induced rotations. However, note that this approximation is standard in clinical echocardiography as reported by [Voigt *et al.* (2014)]. It results from applying 1D concepts, that are more intuitive to the clinician. In addition, for simplifying the parameter tuning, σ was set to be homogeneous for all resolutions. Nonetheless, σ is multiplied by the window extent to obtain σ_i (Eq. 4.19). As the window extent decreases with the resolution, so does σ_i . Finally, the tagged images were not apodized before computing the Fourier transform. As a result, some artifacts (the vertical lines) appear in Fig. 4.4b. However, those artifacts' influence on the tracking is rather limited because most of them will be filtered out by the bandpass filter (Fig. 4.4c, 4.4e). Nonetheless, a study of the apodization's impact on the tracking would help to determine its benefits. It is currently left for future work.

There are also several limitations with respect to the validation. We performed a comparison to the state-of-the-art on a reduced number of cases and landmarks, benchmarking tracking accuracy only. Besides the relatively limited number of methods present in this evaluation, we also see the need for a tagged MR validation framework yielding dense ground truth displacement *and* strain values. Clearly, comparing the accuracy on displacements only overlooks many challenges related to strain, including the impact of the regularization method on strain accuracy and sensitivity. Besides, our strategy for generating synthetic images was too simplistic for being representative of challenges inherent to clinical images. Images were produced through warping of a single frame, ignoring artifacts induced by valve motion or tag contrast variations over the cardiac cycle. Moreover, regarding simulation aspects, an electromechanical simulation should be done specifically on the patient geometry. Also, MR simulators would likely be more realistic than simple image warping. Finally, the experiments performed in this paper are preliminary and only

aim at demonstrating the applicability of our method to process clinical images. Image quality for patient datasets was found to be more heterogeneous than volunteer data. Evaluating the clinical impact of 3D tagged MR in general - and this method in particular - requires a thorough study on the correlation between the low deformation regions quantified by our method with the fibrosis areas revealed by late-enhancement MR. The interaction mechanisms between the fibrosed and the surrounding contracting regions need to be further studied on a larger patient population, taking into account the different tissue properties.

4.7 Summary

In this chapter, we introduced a novel algorithm that extends HARP to handle 3D tagged MR data. While doing so, we proposed an original regularization method done in an anatomical space of coordinates. HARP results were regularized according to a windows-weighted regression method that maintains a low computational complexity. Our implementation performs LV tracking and strain computation in less than a minute, a time range compatible with clinical practice requirements. The algorithm was evaluated at three levels: on synthetic, healthy volunteers and patient data. On healthy volunteers, tracking accuracy was found to be similar to the best candidates of a recent benchmark. Strain accuracy was evaluated on synthetic data (as no public data for strain was available), showing low bias and strain errors under 5 percents (excluding outliers) for longitudinal and circumferential strains. As reported in the literature, radial strain was found to be more challenging but had the second and third quartiles of strain errors in the $(-5\%, 5\%)$ range, thanks to an implementation of the incompressibility constraint that solely corrects this strain component. Our method was shown to be applicable to clinical data by first correlating strain dispersion with the extent of transmural fibrosis. Lower deformation values were also observed inside and around the infarcted region. In synthetic data, we also compared the effectiveness of tracking the HARP phase and MP, although no significant differences were found between them. As future work, we will develop a more elaborated validation framework for the validation of tagged MR tracking algorithms by extending our pipeline for the generation of synthetic images.

Chapter 5

Multi-modal simulation of virtual patients

This chapter is an extension of our paper "A Framework for the Generation of Realistic Synthetic Cardiac Ultrasound and Magnetic Resonance Imaging Sequences from the same Virtual Patients" submitted to *Special Issue on Simulation and Synthesis in Medical Imaging, IEEE Transactions on Medical Imaging*.

5.1 Introduction

Despite recent developments in both the fast 3D cardiac imaging techniques [Alessandrini *et al.* (2015)] [Rutz *et al.* (2008)] and the associated local deformation quantification solutions such as [Heyde *et al.* (2016)a] [Somphone *et al.* (2013)] [Zhou *et al.* (2015)], the assessment of cardiac function is generally limited to global measures (e.g., ejection fraction, stroke volume, global longitudinal strain) [Smiseth *et al.* (2015)] [Alessandrini *et al.* (2015)]. Regional strains are less reliable and reproducible as reported in [Shiino *et al.* (2016)] [Kleijn *et al.* (2012)] [Singh *et al.* (2010)]. 3D regional strain analysis has not been rigorously validated. Indeed, as mentioned in chapter 3, unlike cardiac segmentation which is usually validated against manually traced contours, 3D cardiac motion tracking cannot be validated similarly since landmarks should be manually tracked in 3D volumes throughout the cardiac cycle which is tedious and challenging task for experts. Moreover, it is prone to inter- and intra-expert variabilities. Apart from manual validation, one can resort to several imaging modalities such as tissue Doppler [Ho and Solomon (2006)] and the DENSE MR [Aletras *et al.* (1999)]. Those imaging techniques provide a direct access to the ground-truth velocity or displacements. However, they suffer from some inherent limitations: tissue Doppler imaging can only measures the velocity in the radial direc-

tion while DENSE MR is rarely used in clinical practice. Another alternative is to image physical heart phantoms. The ground-truth motion is controlled by mechanical devices, hence known. Nonetheless, the simulated cardiac motion is rarely as complex as real cases. Besides, the lack of a realistic background with artifacts/noises cannot fairly represent the challenges faced by cardiac motion tracking algorithms.

Under such circumstances, in chapter 3, we reached a conclusion that among the several existing validation strategies, adopting computer-generated synthetic cardiac image sequences with simulated ground-truth motion fields may be the most convenient and feasible solution for the time being. In this thesis, instead of simulating a single modality, we opted for generating multimodal images for the same virtual subject. This allows for a direct comparison of different imaging modalities. For instance, there is currently increasing research interest in investigating whether cine MR feature tracking (CMR-FT) [Hor *et al.* (2011)] can quantify strain values similar to classical techniques applied on tagged MR [Moody *et al.* (2015)] and US data [Onishi *et al.* (2013)]. Although the corresponding studies showed a close correlation between CMR-FT results and the ones obtained from tagged MR and US, it is still not clear which modality outperformed the others, in which aspects and to which extent. Thus, providing the research community with a multimodal synthetic cardiac database is of great value in pushing forward not only the validation within a single modality but also the cross-modality comparison. The application of such synthetic sequences is highly dependent on the level of realism of the simulations. Both the simulated ground-truth cardiac motion and the corresponding synthetic image should be realistic. Moreover, the simulation should include a considerable range of cardiac situations: from healthy to various pathological hearts including ischemia and dyssynchrony.

In this chapter, we will introduce a novel image simulation pipeline that allows the generation of multi-modal (ultrasound, cine and tagged MR) synthetic cardiac image sequences for the same virtual subject. This work extends the pipeline initially proposed in [Alessandrini *et al.* (2015)] for US simulation to the MR modality in order to simulate multi-modal virtual patients. The proposed simulation pipeline consists of three main elements: i) the use of real clinical recordings to extract relevant information to improve the realism of the generated images; ii) the involvement of an electro-mechanical (E/M) model of the heart [Marchesseau *et al.* (2013)] to generate healthy and pathological synthetic motion field used as reference; iii) the use of physical simulation environments to model image formation with the possibility to introduce complex effects such as tag fading for tagged MR. The proposed extended pipeline was used to create a database of 18 virtual patients including healthy and various pathological cases, *i.e.* ischemia and dyssynchrony. For each patient, benchmark sequences of 3D US, cine and tagged MR were generated. We generated a total of 90 synthetic sequences representing 2700 image volumes. The synthetic sequences along with the corresponding reference motion fields are made publicly

available via an open-access database¹. The novelties are the following :

- The combination of an E/M model with an MR physical simulator to introduce the possibility of interacting with the image formation process to introduce complex effects such as tag fading;
- The use of multimodal template sequences from the same patient to extract the most relevant information from each modality (e.g. anatomical structures from cine and motion estimation from tagged MR) in order to generate both cine and tagged MR synthetic sequences;
- The introduction of a novel combinative warping strategy, with the goal of reducing motion artifacts that may occur in myocardium regions;
- The contribution of the first unified framework which allows the generation of multimodal (US, cine and tagged MR) realistic synthetic sequences for the same virtual patient.
- The use of a novel strategy based on a Gaussian weighting function to generate smooth interface between the myocardium and the surrounding structures.

The remainder of this chapter is organized as follows. In Section 5.2, the proposed generic pipeline is described. The quality of the simulated sequences for MR modalities is then investigated in Section 5.3. A discussion part is provided in Section 5.4 while concluding remarks are given in Section 5.5.

5.2 Methodology

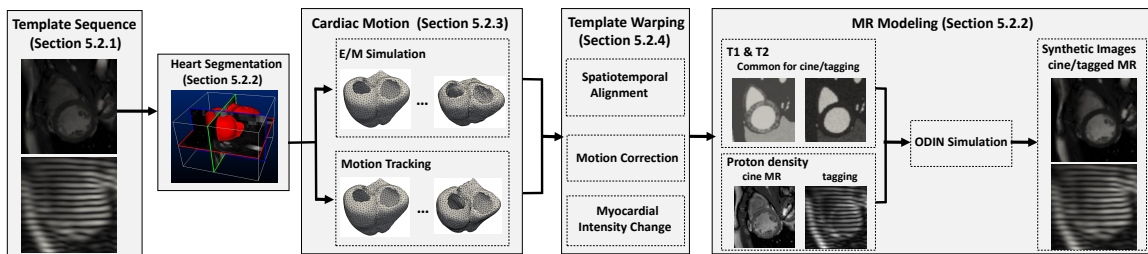


Figure 5.1: Proposed pipeline for the simulation of realistic cardiac cine and tagged MR sequences.

We extend in this section the ultrasound pipeline initially developed in [Alessandrini *et al.* (2015)] to the generation of synthetic MR sequences. The interest is to derive a generic framework which can be used to simulate multimodal cardiac sequences for the virtual patient. Since much of the innovations presented in this work reside on the MR aspects, we mainly focus in this section on the different steps we introduced to simulate

¹<http://humanheart-project.creatis.insa-lyon.fr/multimodalityStraus.html>

realistic cine and tagged MR sequences. It is worth pointing out that the same pipeline was also used in this thesis to generate synthetic US images, as shown in Section 5.3 (only the “MR Modeling” block has to be replaced by the one proposed in [[Alessandrini *et al.* \(2015\)](#)]).

A schematic view of the pipeline extended to MR is shown in Fig. 5.1. Each block specifies the number of the section where it is described in detail. Briefly, real acquisitions (cine/tagged MR) are used as template sequences (Sect. 5.2.1) for deriving realistic textures. The first step is to segment the right ventricle (RV) and the left ventricle (LV) on the first frame of cine MR template sequence (Sect. 5.2.2). The E/M model is then applied to the segmented 3D geometry to simulate one cardiac cycle (Sect. 5.2.3). For each frame of the simulated sequence, cine or tagged MR images are generated from a physical simulator which takes relaxation times T_1 and T_2 and proton density maps as inputs (Sect. 5.2.2). To achieve realistic texture, proton density maps are derived from the template recordings. This requires a dedicated spatio-temporal alignment between the simulations and the template recordings (Sect. 5.2.4). As such, the pipeline will generate synthetic cine and tagged MR sequences with a fully controlled deformation field and with a texture visually similar to the one of the corresponding template recording.

5.2.1 Template image sequences

3D template recordings used in this study come from the open access database provided in [[Tobon-Gomez *et al.* \(2013\)](#)]. For each volunteer, one US, one cine MR and three tagged MR sequences were acquired. The MR datasets were acquired using a 3T Philips Achieva System (Philips Healthcare, Best, The Netherlands). The MR sequences processed by the participants were cine steady state free precession (SSFP) [[Scheffler and Lehnhardt \(2003\)](#)] and 3D tagged MR (3DTAG) [[Rutz *et al.* \(2008\)](#)]. Cine MR images were acquired during breath-holds of approximately 15 seconds and were gated to the vector ECG. 3DTAG datasets were obtained with three sequential breath-hold acquisitions in each orthogonal directions. Since MR images were acquired in the same patient coordinate system, cine and tagged MR sequences are naturally aligned in space. A set of 24 manual landmarks identifying the same keypoints in all the modalities allows the derivation of a rigid transformation to pass from MR to US coordinates. These landmarks are evenly distributed over the LV, with 8 landmarks at each of the three ventricular levels (basal, midventricular, apical) [[Tobon-Gomez *et al.* \(2013\)](#)]. The tagged MR sequence was acquired by the accelerated CSPAMM [[Rutz *et al.* \(2008\)](#)]. The three tagging acquisitions have orthogonal line tag orientations. All the acquisitions represent one cardiac cycle. The US template has a spatial resolution of $0.82 \times 0.83 \times 0.73 \text{ mm}^3$ while the cine and tagged MR have spatial resolutions of $1.25 \times 1.25 \times 8.08 \text{ mm}^3$ and $0.96 \times 0.96 \times 7.71 \text{ mm}^3$.

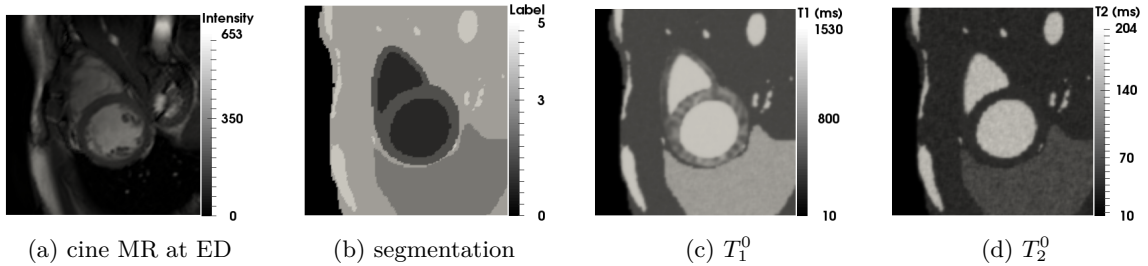


Figure 5.2: Illustration of the different steps involved to simulate the initial T_1 and T_2 maps relative to the first frame (ED).

5.2.2 MR modeling

We used the ODIN simulator [Jochimsen *et al.* (2006)] to generate both cine and tagged MR images. ODIN is a physical simulator which allows either the selection or the design of specific MR sequences. To simulate one 3D image, ODIN requires T_1 , T_2 and proton density maps as inputs. In this study, we used the same T_1 and T_2 maps to generate both cine and tagged MR sequences for each virtual patient, only the proton density maps were computed separately for each modality and for each time instant of the simulated sequence. The first step of the proposed MR pipeline is the computation of the initial T_1 and T_2 maps for the first frame. We first describe how these initial maps were generated. We then give details on the way they were extended to all time frames.

Heart segmentation

Because we assign different T_1/T_2 values per structure, we first need to segment the initial template image into different classes, *i.e.* myocardium, blood, lung and air. Since cine MR provides the best image contrast and since all the template modalities can easily be mapped, it represents a natural choice to extract the heart geometry. We first used the VP2HF segmentation pipeline proposed in [Groth *et al.* (2012)] to segment the myocardium and the underlying blood pools. We then segmented the lung and the air outside the body manually. Finally, the remaining unlabeled pixels were classified by thresholding: high intensity pixels belonging to blood and the rest to muscles. Fig. 5.2b shows a typical segmentation result obtained by using such procedure.

Initial T_1 and T_2 maps

We assigned T_1 and T_2 maps using published reference mean and standard deviation values (denoted as u and σ) available from [Tobon-Gomez *et al.* (2011)b]. At each pixel location, T_1 and T_2 values were randomly sampled from Gaussian distributions, yielding initial static maps denoted as T_1^0 and T_2^0 (see Fig. 5.2c and 5.2d). The relevant u and σ values used in this study are listed in Table 5.1. Moreover, since the myocardium is our region of interest, a dedicated strategy was applied to better control its underlying texture.

Table 5.1: T_1 and T_2 reference values attached to each label of the segmented cine MR image.

Label	Class	T1 (ms)		T2 (ms)	
		<i>u</i>	σ	<i>u</i>	σ
0	Air	0	0	0	0
1	Blood	1516	21	189	26
2	Myocardium	982	46	54	12
3	Lung	1199	117	79	29
4	Other (low)	549	52	49	20
5	Other (high)	1516	21	189	26

Indeed, since tagged MR intensity changes contain strong T_1 information, it is possible to deduce relevant local and structural T_1 values from image intensities. In particular, temporal intensity changes of the CSPAMM tagged MR sequence can be described as follows [Fischer *et al.* (1993)] [Wang *et al.* (2011)]:

$$I_{tag}^n = I_{tag}^0 \exp\left\{-\frac{n\Delta t}{T_1}\right\} \frac{\sin(\alpha_n)}{\sin(\alpha_0)} \prod_{j=0}^{n-1} \cos(\alpha_j), \quad \forall n \geq 1 \quad (5.1)$$

where Δt is the temporal resolution, n is the frame index and I_{tag}^n is the tagging intensities of the material point at frame n . α_n corresponds to the RF flip angle at frame n . They were computed by the method described in Appendix B.1. Eq. (5.1) thus gives access to T_1 information from the intensity changes of the tagged MR template sequence. In order to accurately estimate the T_1 map of the myocardium, the following procedure was repeated for all pixels belonging to this region. For a given point at ED, we tracked it through the entire tagged MR template sequence (this step is later described in Section 5.2.3). This gives a sequence of intensities I_{tag}^n for all time instants. The corresponding T_1 value was then estimated from linear least square minimization problem:

$$\arg \min_{T_1} \sum_n \left(\log \left(\frac{I_{tag}^n \sin(\alpha_0)}{I_{tag}^0 \sin(\alpha_n) \prod_{j=0}^{n-1} \cos(\alpha_j)} \right) T_1 + n\Delta t \right)^2 \quad (5.2)$$

Since there are three template sequences of tagged MR images per subject (Section 5.2.1), we derived three different T_1 values for the same myocardium point. A median filtering was then applied for removing possible outliers, yielding the final T_1^0 myocardial map as shown in Fig. 5.2c.

Dynamic T_1 and T_2 maps

Since each frame of the simulated sequences was generated independently, the initial T_1^0 and T_2^0 maps previously described had to be extended over time. This was achieved by a dedicated warping strategy described in Section 5.2.4. The corresponding dynamic maps are denoted as T_1^k and T_2^k , with k indexing the simulation frame.

Proton density maps

For each simulation frame, we further computed the proton density map from the corresponding template recordings. This ensures the generation of a texture visually similar to the one of the underlying template. To this aim, one needs to spatially and temporally align each frame of the simulated sequence with its counterpart in the template sequence. This was achieved by a dedicated warping strategy detailed in Section 5.2.4. The outputs of this step correspond to a set of warped templates denoted as \tilde{I}_{cine}^k and \tilde{I}_{tag}^k and aligned with each simulation frame k .

Cardiac cine MR images were acquired using the balanced steady state free precession (bSSFP) MR sequence [Scheffler and Lehnhardt (2003)]. The proton density map ρ_{cine}^k of frame k can then be computed from the corresponding warped template [Scheffler and Lehnhardt (2003)]:

$$\rho_{cine}^k = \tilde{I}_{cine}^k \sqrt{T_1^k / T_2^k} \quad (5.3)$$

For tagged MR, the characteristics of the CSPAMM sequence provide the following ρ_{tag}^k map [Wang *et al.* (2011)]:

$$\rho_{tag}^k = \tilde{I}_{tag}^k \exp^{\frac{TE}{T_2^*}} / \sin(\alpha_k^s) \quad (5.4)$$

where α_k^s corresponds to the simulated RF flip angle. It was computed by Eq. ?? using the temporal resolution of the simulations. TE is the echo time here set to 21 ms. T_2^* corresponds to the effective spin-spin relaxation times and are here approximated by the relaxation time T_2 [Haase (1990)]. We thus assume $T_2^* = T_2^k$ in the sequel.

ODIN simulation

Each frame k of the simulated sequences was independently generated from ODIN by using the T_1^k , T_2^k and ρ_{mod}^k maps derived above (with $mod = cine$ or tag) as inputs. For the sake of simplicity, we decided to use the same resolution for those maps and the generated output MR images. Moreover, since we wanted to reproduce as close as possible the template recordings, we used the image properties (origin, spacing, size and axis orientations) of the template cine and tagged MR as reference. This defines the pixel positions of the simulated images for each modality. The T_1^k , T_2^k and ρ_{mod}^k maps were thus interpolated to those pixel positions before being passed on to ODIN. We used

respectively the *odinfisp* and *odinepi* MR sequences available under ODIN for simulating cine and tagged MR images. Indeed, these sequences are consistent with the corresponding real acquisition protocol, *i.e.* the bSSFP for cine sequence [Tobon-Gomez *et al.* (2013)] and the EPI for tagged sequence [Rutz *et al.* (2008)].

5.2.3 Cardiac motion

As commented in Section 5.2.2, the first frame of the template cine MR sequence was segmented into different classes including myocardium region (LV and RV). From this mask, a volumetric mesh (both LV and RV) was generated using [Alessandrini *et al.* (2015)] and propagated to all further simulation and template image time frames as described hereinafter.

E/M simulation

From the myocardial mask of the first frame, a tetrahedral mesh was generated using the CGAL meshing software and passed to the E/M simulator which generated as output a sequence of volumetric meshes \mathcal{S}_k . The E/M simulator applies the Bestel-Clement-Sorine model which estimates the electrical activation and the resulting mechanical contraction [Marchesseau *et al.* (2013)] and is implemented in the SOFA framework². This model was chosen for its realistic properties and it complies with the four cardiac phases (isovolumic contraction, ejection, passive and active filling). Cardiac fiber orientations were estimated with a rule-based method (elevation angle between -70° to +70°) in order to model the E/M anisotropy. It has already shown its efficiency in the generation of realistic US image sequences [Alessandrini *et al.* (2015)]. A number of biophysical parameters such as the local myocardial contractility, stiffness and conduction governs the E/M equations. By varying those parameters, both normal and pathological cardiac motion fields can be simulated. For each patient, we generated in this study one healthy, one dyssynchrony (LBBB) and four realistic ischemic hearts. For the dyssynchrony, only the right endocardium was initially activated. For the ischemia, varying scar locations with random and realistic shapes were simulated [Duchateau *et al.* (2016)] in parts of the LV where arterial occlusion can occur: one for the Left Anterior Descending artery (LAD), one for the Left Circumflex (LCX), and two for Right Coronary Artery (RCA). Fig. 5.14 shows an example of the simulated ischemia regions and the associated strain maps.

Motion Tracking

Since the cine and tagged MR were acquired under the same coordinate system, we used the tagged MR sequence to perform the tracking. The LV and RV of the first E/M model mesh \mathcal{S}_0 (the E/M model and the template are naturally aligned at the first frame)

²<https://www.sofa-framework.org/>

were extracted and processed separately by two state-of-the-art algorithms in order to maximize the tracking accuracy. The LV border was tracked using the HarpAR algorithm given its good reliability in estimating LV radial deformations [Zhou *et al.* (2015)]. The sparse Demons algorithm was then selected to perform RV tracking given its good tracking accuracy and its low computational cost [Somphone *et al.* (2013)]. To avoid possible discontinuities at the LV/RV border since they were tracked independently, we refined the RV displacements by a simple method described in Appendix B.2. The final output of this procedure corresponds to a unique sequence of segmented meshes \mathcal{R}_t attached to both cine and tagged MR.

5.2.4 Template warping

As described in Section 5.2.2, a spatio-temporal alignment between the template sequences and each simulation frame is needed to derive the proton density maps. We developed a novel warping framework to tackle this problem. Similar to [Alessandrini *et al.* (2015)], we used two different strategies to deal with the myocardium and the surrounding structures (named as background in the sequel), however we introduce the following innovative aspects: *i*) we developed a dedicated strategy to ensure smooth transition at the interface between the myocardium and the background; *ii*) we introduced a model to handle temporal myocardial intensity changes over the cardiac cycle. Each step of the proposed procedure is detailed hereunder.

Generic transformation model

Similar to [Alessandrini *et al.* (2015)], we used myocardial landmark points extracted from the two sequences of meshes \mathcal{S}_k and \mathcal{R}_t to compute displacement fields. However, we also involved in this study static background landmarks (denoted as \mathcal{B}) to alleviate unphysiological warpings of the surrounding structures. These landmarks were detected from the cine MR template sequence. In particular, for each pixel position, we computed the variation of cine MR intensity over the whole sequence and we kept the points with the smallest variation and with a minimal spacing of 5 mm. For each simulation, the number of static background landmarks was fixed to 200.

The goal of the introduced generic model was to compute a global transformation to efficiently match a source space (represented by the heart mesh \mathcal{M}_0) with a target space (represented by the heart mesh \mathcal{M}_1) where \mathcal{M}_0 and \mathcal{M}_1 share the same number of points. In both spaces, we assumed the presence of the same static background landmarks \mathcal{B} . The transformation maps one pixel \mathbf{x} of the source space to a corresponding position \mathbf{y} in the target space. As stated above, different transformation strategies were applied to the myocardium and the background.

Regarding the myocardial points, since they all lie inside the volumetric mesh \mathcal{M}_0 , the corresponding transformation was directly computed from the two volumetric meshes

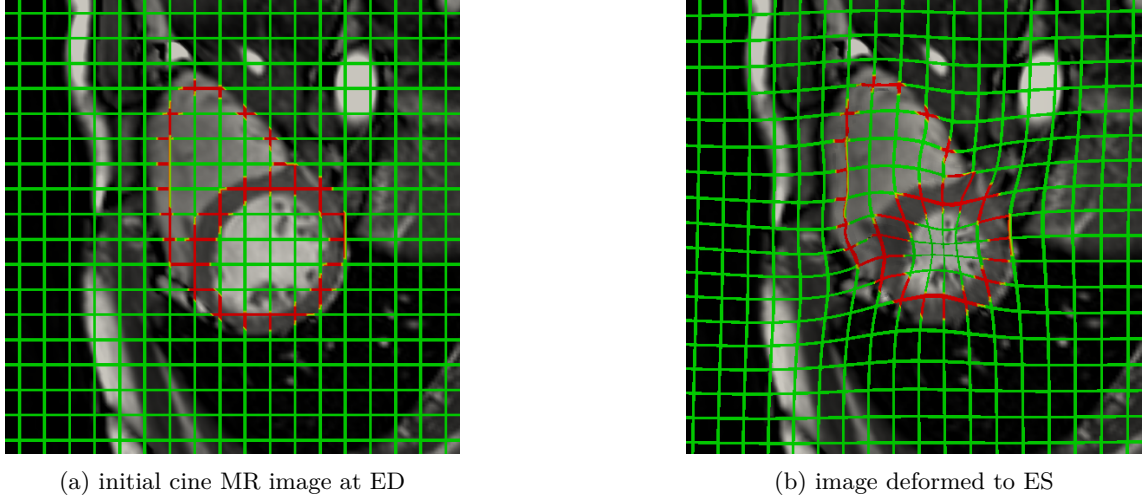


Figure 5.3: Illustration of the use of the generic transformation model. The ED cine MR image was warped to ES by the generic transformation. The grid superimposed on the image shows the corresponding deformation. The myocardium and the background are shown in red and green respectively. The generic transformation was computed from the ED/ES simulation meshes and the static background points.

$\mathcal{M}_0 \rightarrow \mathcal{M}_1$. The barycentric coordinates of \mathbf{x} in mesh \mathcal{M}_0 were evaluated. From these barycentric coordinates and the node positions of the target mesh \mathcal{M}_1 , we computed the absolute coordinates. This gave the matched position \mathbf{y} . This procedure is denoted as $\mathbf{y} = MESH_{\{\mathcal{M}_0 \rightarrow \mathcal{M}_1\}}(\mathbf{x})$.

Concerning the background points, we used the TPS algorithm to model the underlying transformation. We randomly selected a fraction of mesh points (800 points in all the simulations) which, together with the static landmarks, were used to parameterize the TPS algorithm. This procedure is denoted as $\mathbf{y} = TPS_{\{\mathcal{M}_0, \mathcal{B} \rightarrow \mathcal{M}_1, \mathcal{B}\}}(\mathbf{x})$. The overall transformation can thus be written as:

$$\begin{aligned} & \mathcal{T}_{\{\mathcal{M}_0, \mathcal{B} \rightarrow \mathcal{M}_1, \mathcal{B}\}}(\mathbf{x}) \\ &= \begin{cases} MESH_{\{\mathcal{M}_0 \rightarrow \mathcal{M}_1\}}(\mathbf{x}), & \text{if } \mathbf{x} \in \text{Myocardium} \\ TPS_{\{\mathcal{M}_0, \mathcal{B} \rightarrow \mathcal{M}_1, \mathcal{B}\}}(\mathbf{x}), & \text{otherwise} \end{cases} \end{aligned} \quad (5.5)$$

Fig. 5.3 shows an example of the use of the generic transformation defined by Eq. 5.5 to derive a deformation map between two time instances.

Temporal alignment

Temporal alignment was performed by linearly stretching/shrinking the time axis of the template recording in order to match relevant cardiac events used as temporal landmarks in the simulation sequence. In this paper, ED and ES time events were chosen as landmarks. Each frame k of the simulation was matched to a cardiac time (ms) in the template

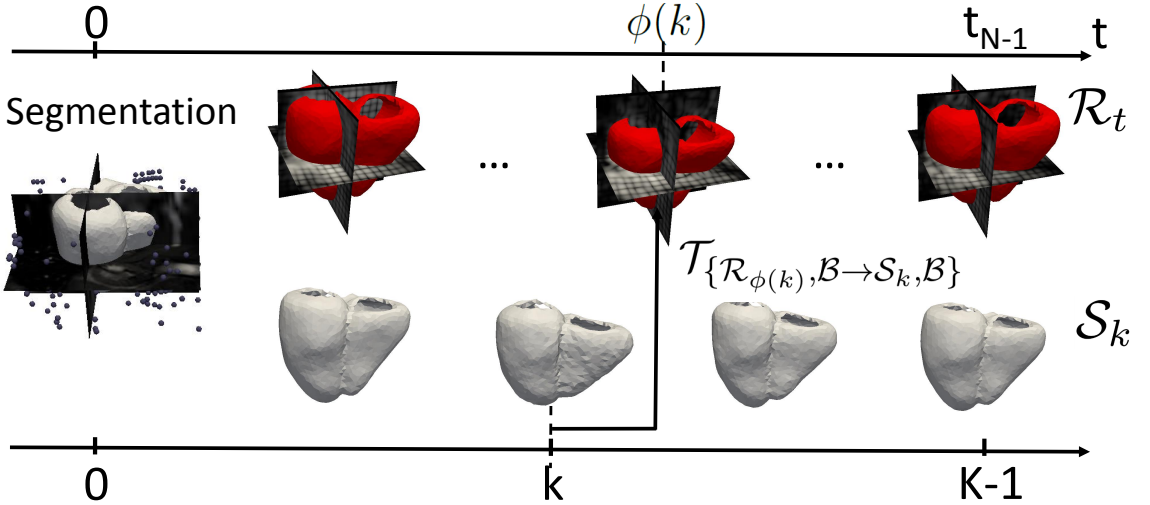


Figure 5.4: Illustration of the spatio-temporal alignment used for template warping. The segmentation mesh at time zero is first tracked in the template sequence, leading to a sequence of meshes plotted in red color (the upper row). Then, the E/M model is used for simulating myocardial motion fields, starting from the same segmentation mesh. This generates another sequence of meshes plotted in white color as is shown at the bottom row of the figure. For the temporal alignment, each simulation frame k is matched to the cardiac time $\phi(k)$ in the template sequence. The spatial alignment further deforms the template image of time $\phi(k)$ towards the simulation mesh S_k . The deformation field is computed using both the tracking mesh R_t , the simulation mesh S_k and the static background points B shown as black dots at time zero.

sequence by the ϕ operator defined as:

$$\phi(k) = \begin{cases} \frac{t^{es}}{k^{es}}k, & \text{if } k \leq k^{es} \\ t^{es} + \frac{k-k^{es}}{K-k^{es}}(t^{max} - t^{es}), & \text{otherwise.} \end{cases} \quad (5.6)$$

K is the number of simulated frames and k^{es} corresponds to the ES frame index. Similarly, t^{max} is the template cardiac cycle while t^{es} refers to the template ES timing. Both the template cine and tagged MR sequences were resampled to cardiac timings $\phi(k)$, with $k \in [0, K - 1]$. In each template sequence, the two frames with the cardiac times closest to $\phi(k)$ were found. These two images were then linearly interpolated to $\phi(k)$, producing template sequences temporally aligned with the simulation frames and denoted as \hat{I}_{mod}^k .

Spatial alignment

After temporal synchronization, spatial alignment was needed to align the resampled images \hat{I}_{mod}^k with the corresponding E/M geometry S_k . To this aim, the generic transfor-

mation introduced in Section 5.2.4 was used, yielding to the following expression:

$$\hat{I}_{mod}^k = \hat{I}_{mod}^k \circ \mathcal{T}_{\{\mathcal{R}_{\phi(k)}, \mathcal{B} \rightarrow \mathcal{S}_k, \mathcal{B}\}} \quad (5.7)$$

where \hat{I}_{mod}^k is the warped template image aligned both in time and space with the corresponding simulation mesh \mathcal{S}_k . The whole spatio-temporal alignment procedure is illustrated in Fig. 5.4.

Motion Correction

The warped template sequences \hat{I}_{mod}^k rely on motion tracking which may introduce artifacts in the synthetic images by adding an apparent residual motion to the true motion given by the E/M model. Contrary to [Prakosa *et al.* (2013)], we introduced in this study a dedicated strategy that corrects the myocardial motion in the warped sequences. To ensure a coherence with the E/M model, the myocardial intensities of each frame of the simulated sequences were sampled from the first template images. This was achieved by deforming I_{mod}^0 to all simulation frames, yielding a complementary warped template sequence \bar{I}_{mod}^k expressed as:

$$\bar{I}_{mod}^k = I_{mod}^0 \circ \mathcal{T}_{\{\mathcal{S}_0, \mathcal{B} \rightarrow \mathcal{S}_k, \mathcal{B}\}} \quad (5.8)$$

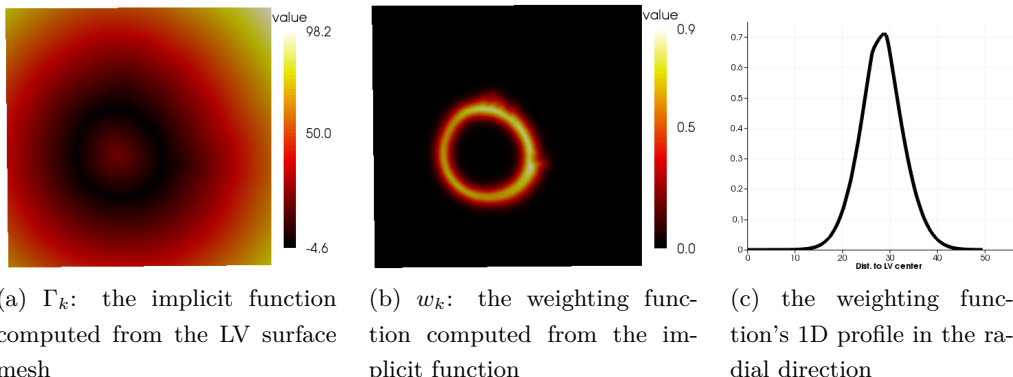


Figure 5.5: The computation of the Gaussian shaped weighting function.

This warped sequence was used to provide myocardial intensities while the warped sequence \hat{I}_{mod}^k was used to get background intensities. In order to ensure a smooth interface between these two regions, we computed a Gaussian shaped weighting function centered at the myocardium for each simulation frame. For each simulation mesh \mathcal{S}_k we extracted the LV myocardial surface and further converted it to an implicit function denoted as Γ_k . This function equals to 0 at the endo- and epicardium borders, is negative inside the myocardium and positive outside as is shown in Fig. 5.5. Its minimal value is denoted as

τ_k^{min} . The weighting function was then defined as follows:

$$w_k(\mathbf{x}) = \exp\left\{-\frac{(\Gamma_k(\mathbf{x}) - \tau_k^{min})^2}{2\sigma^2}\right\} \quad (5.9)$$

where σ controls the transmural profile of the weighting function and was set to 5 in all the simulations. Fig. 5.5 shows an example of the computed implicit function and the associated Gaussian weighting. The warped template sequences with myocardial motion correction were then computed as follows:

$$\mathcal{IM}_{mod}^k = w_k \bar{I}_{mod}^k + (1 - w_k) \hat{I}_{mod}^k \quad (5.10)$$

Eq. (5.10) reveals that most of the myocardial intensities are assigned from the first template frame, ensuring coherent myocardial motion with the E/M model. The background intensities are principally retrieved from the spatiotemporally aligned template sequence, preserving the realistic nature of the surrounding structures.

Myocardial intensity changes

The warped template sequences \mathcal{IM}_{mod}^k involved constant myocardium intensities over the cardiac cycle, which is too simplistic. We thus developed dedicated strategies for each modality to integrate myocardial temporal intensity changes in the simulated sequences.

Regarding tagged MR, Eq. (5.1) reveals that tagging intensity changes depend on T_1 relaxation and the RF flip angle. We thus used the static T_1^0 map together with the simulated RF flip angles α_k^s (α_k^s was computed by the method described in Appendix B.1) to reproduce myocardial intensity variations for each simulated frame k as follows:

$$\Delta\mathcal{IM}_{tag}^k = I_{tag}^0 \left(\exp\left\{-\frac{k\Delta t^s}{T_1^0}\right\} \frac{\sin(\alpha_k^s)}{\sin(\alpha_0^s)} \prod_{j=0}^{k-1} \cos(\alpha_j^s) - 1 \right) \quad (5.11)$$

where Δt^s corresponds to the simulated temporal resolution, while $\Delta\mathcal{IM}_{tag}^k$ corresponds to a non-warped sequence characterizing the temporal intensity changes at each pixel location.

Concerning cine MR, it can be observed that myocardial intensities increase from ED to ES and gradually decrease to their initial values at the end of the cardiac cycle. We assume that the intensity varies linearly during these two phases. The intensity change was defined as a percentage of the initial intensity. This percentage equals to 0 at ED, ξ at ES and changes linearly in between as follows:

$$\lambda_\xi(t) = \begin{cases} \frac{t}{t^{es}} \xi, & \text{if } t \leq t^{es} \\ \frac{t^{max}-t}{t^{max}-t^{es}} \xi, & \text{otherwise} \end{cases} \quad (5.12)$$

where t^{es} and t^{max} were introduced in Section 5.2.4. The ξ parameter was automatically computed from the template cine MR sequence for all myocardial points. In particular, for a given myocardial point \mathbf{x}_i , we first retrieved the corresponding intensity values for all time instants thanks to the protocol described in Section 5.2.3. These intensities are denoted as $I_{cine}^n(\mathbf{x}_i)$ in the sequel, where n corresponds to the cardiac cine MR frame instant. Each ξ value related to a myocardial point \mathbf{x}_i was computed by fitting a linear model:

$$\arg \min_{\xi} \sum_n \left(I_{cine}^n(\mathbf{x}_i) - (1 + \lambda_{\xi}(t_n)) I_{cine}^0(\mathbf{x}_i) \right)^2 \quad (5.13)$$

Since Eq. (5.13) has a quadratic form with respect to ξ , its resolution is straightforward. For the points outside the myocardium, ξ was set to 0, meaning that their intensity does not vary over time. Finally, the intensity variations for each simulated frame k was computed as:

$$\Delta \mathcal{IM}_{cine}^k = \lambda_{\xi}(\phi(k)) \cdot I_{cine}^0 \quad (5.14)$$

where $\phi(k)$ is the temporal alignment introduced in Section 5.2.4 and I_{cine}^0 is the first template cine MR image.

The myocardial intensity variations $\Delta \mathcal{IM}_{mod}^k$ were finally added to the previously generated warping images \mathcal{IM}_{mod}^k . Since the intensity variation maps were computed in static (*i.e.* without the integration of any motion), they had to be deformed before summation. The final warped template sequences with motion correction and integrating myocardial intensity changes were computed as follows:

$$\tilde{I}_{mod}^k = \mathcal{IM}_{mod}^k + w_k (\Delta \mathcal{IM}_{mod}^k \circ \mathcal{T}_{\{\mathcal{S}_0, \mathcal{B} \rightarrow \mathcal{S}_k, \mathcal{B}\}}) \quad (5.15)$$

where w_k is the weighting function given by Eq. (5.9). \tilde{I}_{cine}^k and \tilde{I}_{tag}^k are therefore the final warped template cine/tagging sequences used to compute the effective proton density maps, as described in Section 5.2.2.

5.2.5 US simulation

As stated at the beginning of this Section, the same general pipeline (Fig. 5.1) was applied to simulate US sequences. Since the MR and US coordinate systems can easily be matched thanks to the manual landmarks described in Section 5.2.1, the same initial mesh segmented from the first frame of the cine template was exploited. Only the "MR Modeling" block was replaced by the one proposed in [Alessandrini *et al.* (2015)] (block C in the paper). The underlying tasks allow the derivation of a 3D scatter map with backscattering amplitudes computed from the corresponding US template. From this map, an ultrasound volume was simulated by convolution with the spatially variant point spread function of the simulated imaging system. COLE [Gao *et al.* (2009)] was adopted as ultrasound simulation environment due to its good compromise between computational efficiency and accuracy. The properties of the synthetic probe were set so to match as

close as possible the ones of the transducer used in the acquisition of the template. More details related to the ultrasound simulation modeling can be found in [Alessandrini *et al.* (2015)]. Contrary to [Alessandrini *et al.* (2015)], the derived US pipeline allows an explicit management of the transition between the myocardium and the surrounding structures, as further illustrated in Section 5.3.

5.3 Result

We used in this study three volunteers from [Tobon-Gomez *et al.* (2013)]. For each volunteer, we simulated one healthy and five pathological cases (Section 5.2.3), yielding an open access database composed of 18 virtual patients. For each patient, five synthetic sequences were generated (one cine MR, three tagged MR and one US). All the simulations were launched from the virtual imaging platform VIP³ [Glatard *et al.* (2013)] which allows the execution of applications such as ODIN as a web service and benefits from the EGI⁴ computing power. The generation of one full 3D sequence took around 6 hours on VIP.

5.3.1 Image properties: qualitative assessment

The proposed generic pipeline allows the simulation of multimodality volumes visually similar to real template recordings, as illustrated by Fig. 5.6, 5.7 and 5.8. In Fig. 5.6, we show the three dynamic 2D slices located at the basal, mid and apical regions of the LV. Fig. 5.7 illustrates the three channels of tagged MR simulated in this study. As for the US images, the conventional short-axis, 2-chamber and 4-chamber views are displayed in Fig. 5.8. Global deformation values were in clinical ranges (See Section 5.3.3). To give the readers a straightforward visual comparison between the template and the simulation, we show in Fig. 5.10 and Fig. 5.11 the ultrasound and MR simulations corresponding to the LCX pathology. The simulated images were shown alongside the templates. We observe that the simulations have image textures visually similar to the templates.

Fig. 5.9 also reveals the efficiency of the Gaussian weighting function introduced in Section 5.2.4 to deal with the interface between the myocardium and the surrounding structures. Indeed, the proposed scheme allows a smooth transition between the different structures in this region while preserving a consistent motion inside the myocardium with the E/M model.

5.3.2 Image properties: quantitative assessment

Since the US simulation is based on the same scatter modeling as the one used in [Alessandrini *et al.* (2015)], the same image property is expected. We thus concentrate in this section on the MR image characteristics. In particular, the level of realism was assessed quantitatively by measuring the intensity distribution inside the myocardium

³<https://vip.creatis.insa-lyon.fr>

⁴<https://www.egi.eu>

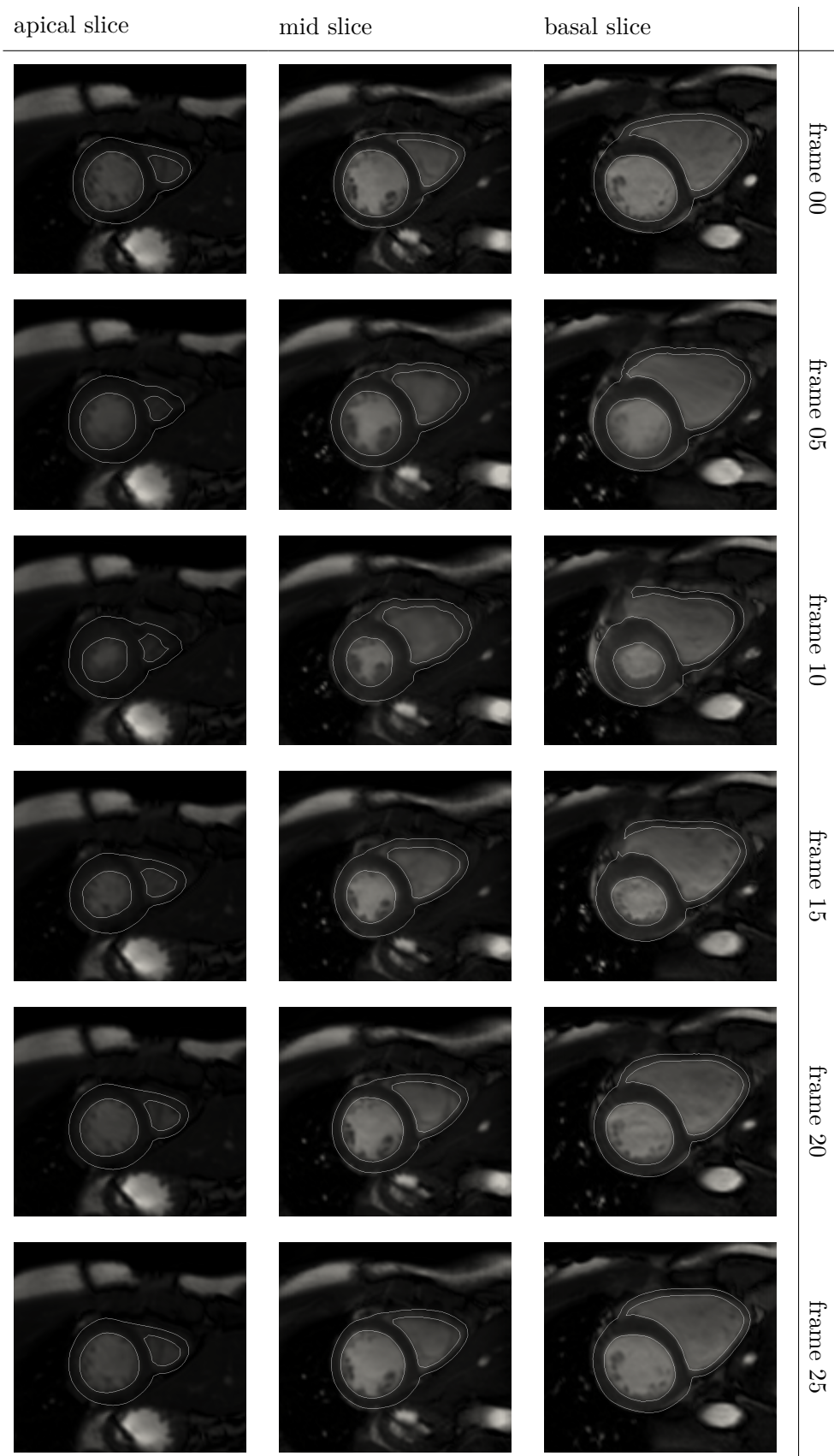


Figure 5.6: Simulated cine MR images. Three slices located at basal, mid and apical regions of the left ventricle are shown. The mesh contour is superposed on the images.

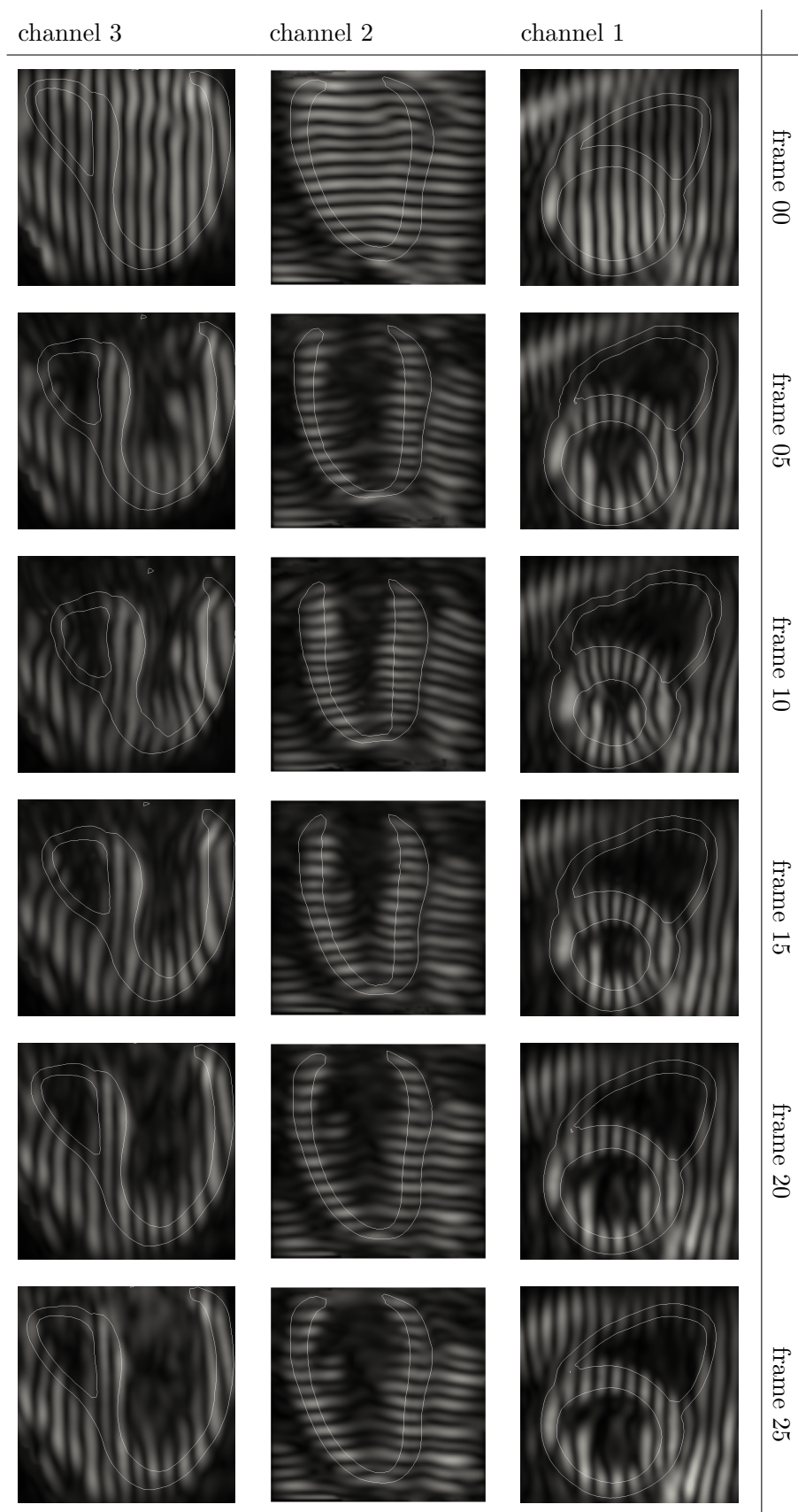


Figure 5.7: Simulated tagged MR images. Three channels with orthogonal tag orientations are simulated. The mesh contour is superposed on the images.

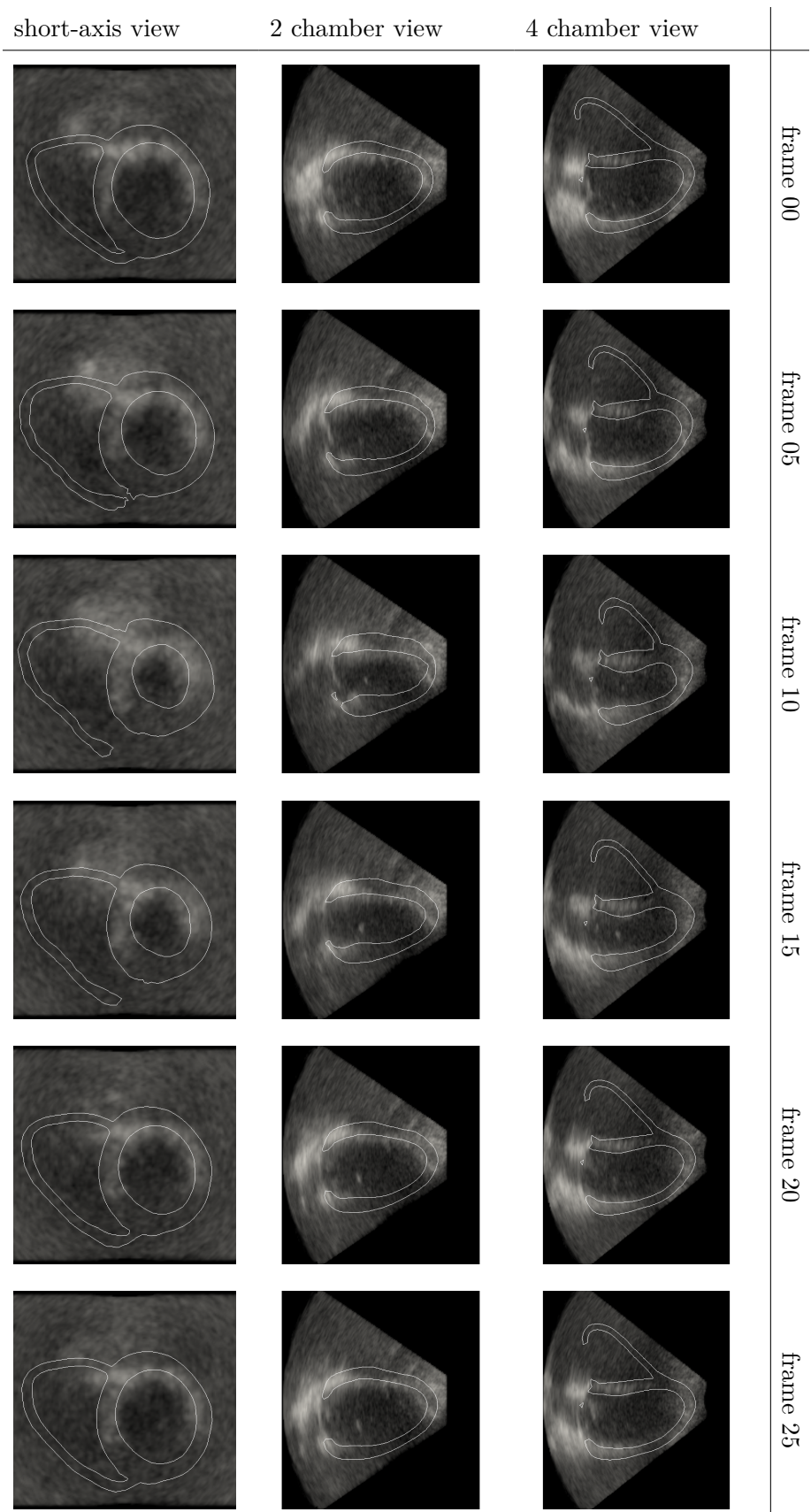


Figure 5.8: Simulated ultrasound images. The 4-chamber, 2-chamber and short-axis views are shown. The mesh contour is superposed on the images.

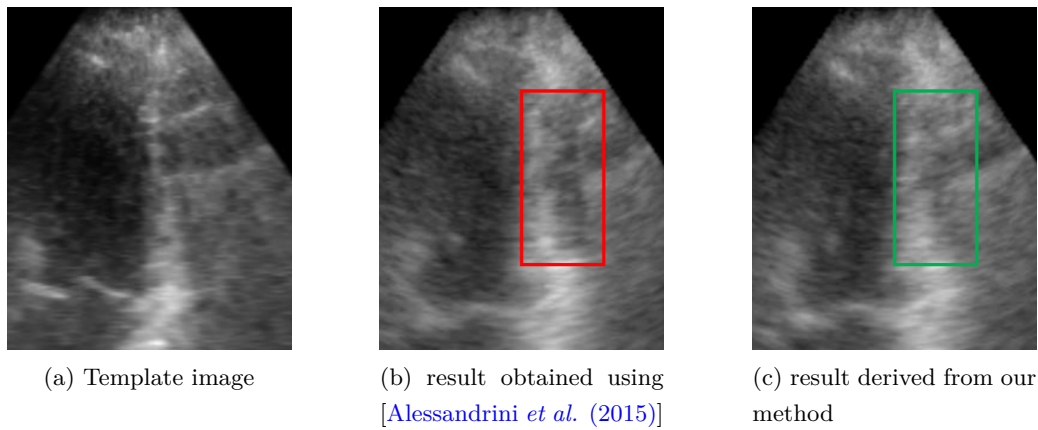


Figure 5.9: Illustration of the interest of the proposed method to better handle the interface between myocardium and the surrounding structures. a) template image at ES; b) simulated image using [Alessandrini *et al.* (2015)]; c) simulated image using our approach.

since it is the feature commonly exploited for the analysis of MR cardiac datasets. The myocardial histograms at end diastole (ED) and end systole (ES) for both a simulated cine MR sequence and its corresponding template are reported on the left side of Fig. 5.12. The analysis first demonstrated that the computed histograms showed very similar shapes at ED. This is consistent with the fact that ED corresponds to the reference time in the proposed pipeline from which T1, T2 and proton density maps were directly computed from the corresponding template frame. This result is further confirmed by two statistical tests. Both the Wilcoxon signed-rank test and the Levene's test returned p-value greater than 0.05, meaning that the median and variance of the myocardial intensities are statistically similar. At ES, the histograms are still in a good agreement, even if some slight difference may be observed. Similarly, we applied the same statistic tests on the myocardial intensities. The Wilcoxon signed-rank test returned a p-value greater than 0.05, revealing that the template and the simulation have similar median values. However, the Levene's test returned a p-value below 0.05, meaning that the variances are statistically different. This is coherent with what we see from the histograms. They are due to the fact that intensities of the T1 and T2 maps were not updated over the cardiac cycle, only warping strategies were performed. Moreover, the myocardial intensity changes were embedded through the proton density maps which was modeled through a simple linear fit in the case of cine MR. Nevertheless, the similarity of the distributions validates the proposed strategy to handle the myocardial intensity changes while preserving the motion derived from the E/M model. The myocardial histograms of tagged MR simulations are also shown in Fig. 5.12. Results show that the exact same observations can also be made for this modality.

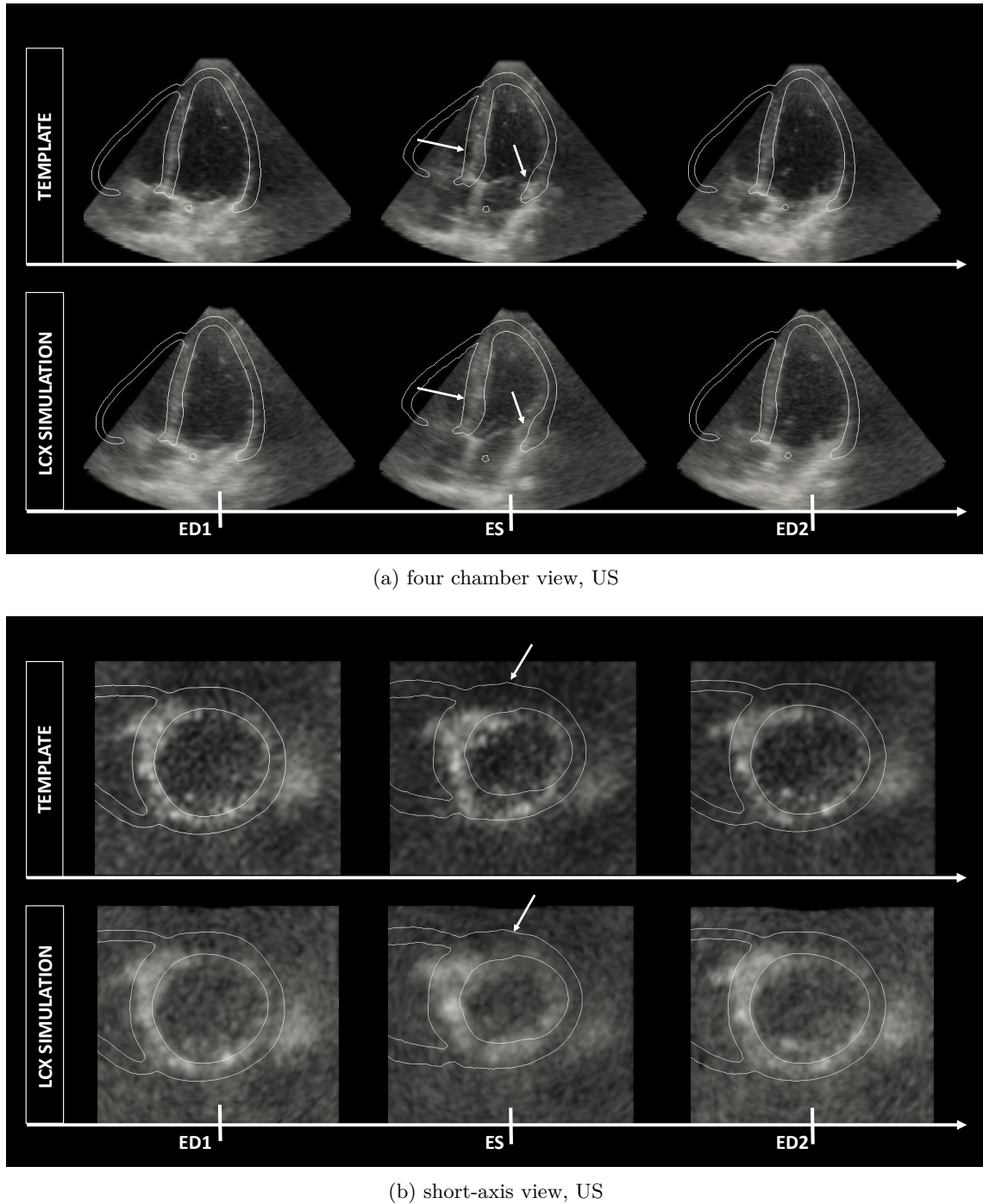
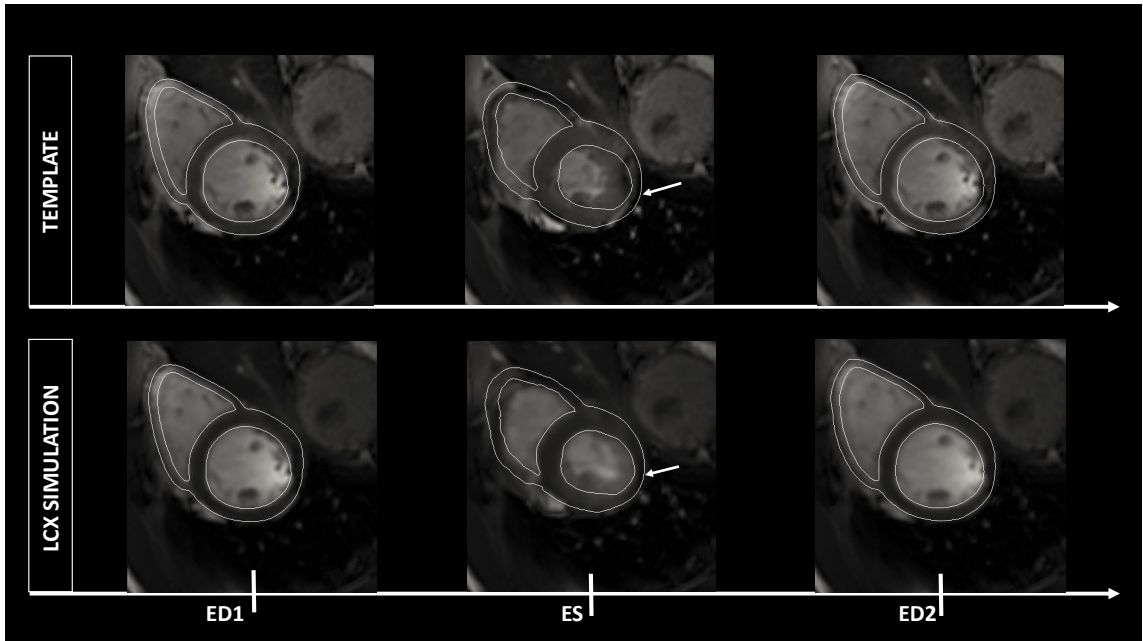
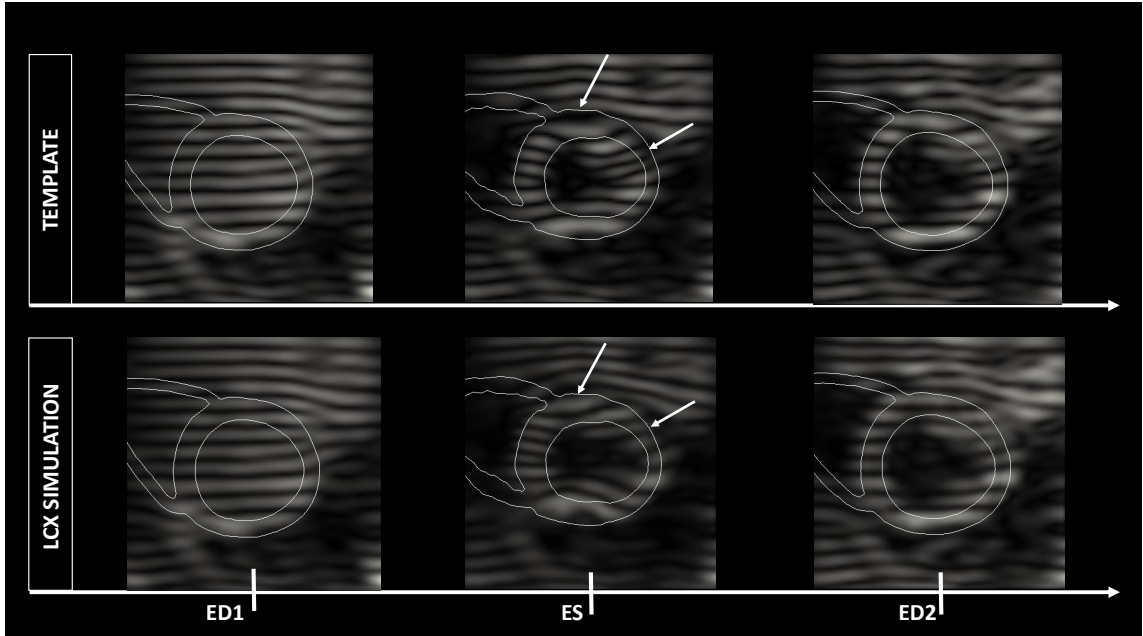


Figure 5.10: Template US recording (top row) and LCX simulation (bottom row) at matched time instants for an apical four chamber (a) and a short axis (b) slice. The E/M meshes (i.e. ground truth segmentation of the LCX simulation) are superimposed to both sequences as white contours. Template, simulation and, therefore, E/M geometry are aligned by construction at time zero (i.e. at ED1). From then on, the simulation runs independently of the template recording and, therefore, the E/M geometry no longer provides a valid segmentation of the latter. In the figure, this is particularly evident at regions marked by the white arrows. This is a consequence of the fact that, as due to the simulated ischemia, contraction in the E/M simulation is reduced as compared to the template.



(a) short-axis view, Cine MR



(b) short-axis view, Tagged MR

Figure 5.11: Template MR recording (top row) and LCX simulation (bottom row) at matched time instants for a short-axis cine MR slice (a) and a short-axis tagged MR slice (b). The E/M meshes (i.e. ground truth segmentation of the LCX simulation) are superimposed to both sequences as white contours. Template, simulation and, therefore, E/M geometry are aligned by construction at time zero (i.e. at ED1). From then on, the simulation runs independently of the template recording and, therefore, the E/M geometry no longer provides a valid segmentation of the latter. In the figure, this is particularly evident at regions marked by the white arrows. This is a consequence of the fact that, as due to the simulated ischemia, contraction in the E/M simulation is reduced as compared to the template.

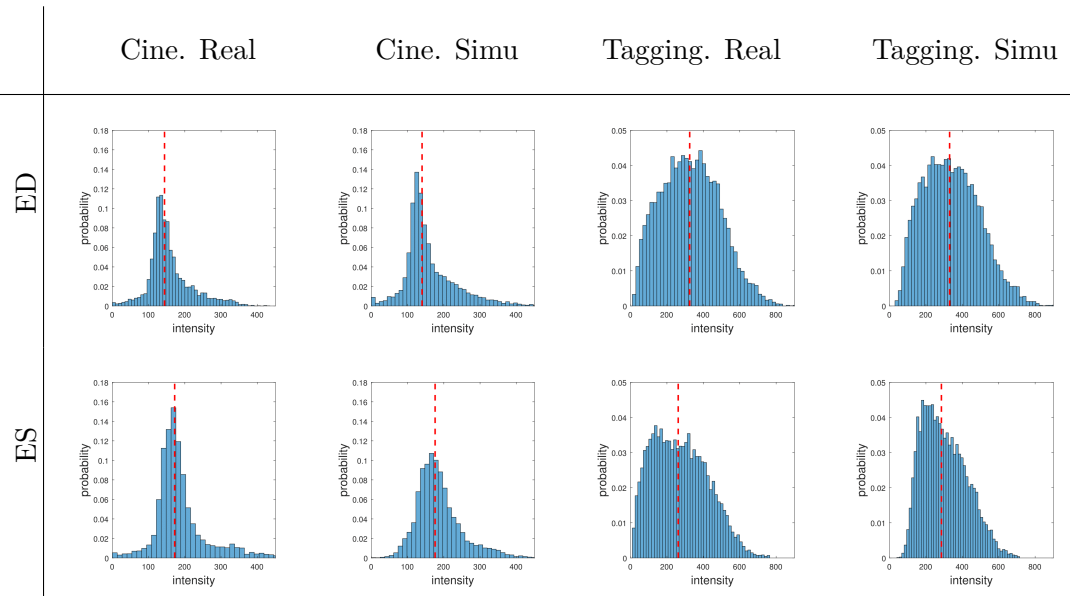


Figure 5.12: Histograms of myocardial intensities in both real and simulated MR data. Red dashed lines mark median intensities. Cine MR results are shown on the left side and tagged MR shown on the right side.

5.3.3 Mechanical properties

Global indices

Table 5.2 displays the LV volumes at ED and ES along with the corresponding EF for the healthy and pathological cases. Those values were computed from the simulated meshes \mathcal{S}_k used as benchmark for the proposed database. For the healthy case, the LV volumes present values around 104 mL at ED and 50 mL at ES, which is in agreement with the reference range published in [EchoNoRMAL *et al.* (2015)] when combining all ethnic groups, all ages and both sexes for analysis. In dyssynchrony, the ES volumes slightly increase to values around 53 mL, revealing a reduced blood output. This tendency is clearer for ischemic cases where ES volumes are above 60 mL. Regarding the EF, the values are around 52% for healthy cases and concentrated around 40% for ischemic cases. The EF of the healthy cases are rather close to but slightly below the reference values from the literature (above 60%) [Aquaro *et al.* (2017)].

Table 5.2: Average LV volumes at ED/ES and the corresponding EF distributed among the virtual population.

	Healthy	LBBB	LCX	LAD	RCA	RCA2
ED (mL)	104.0	104.0	104.0	104.0	104.0	104.0
ES (mL)	49.6	52.8	65.7	60.9	60.3	63.4
EF (%)	52.3	49.2	36.8	41.4	42.0	39.0

Strain Curves

We provide in Fig. 5.13 the full set of regional strain (radial, longitudinal and circumferential) curves at the basal, mid and apical levels of the LV for one healthy and four pathological cases. The color map used for displaying the strain curves is further shown in Fig. A.1 (Appendix B.3). The regional strain curves were computed using Engineering strain as in [[Alessandrini et al. \(2015\)](#)]. Their properties are in accordance with the ones described in the literature. For instance, in the LBBB case, the ES timings differ between the septum (AHA n° 2,3,8,9,14) and the lateral wall (AHA n° 5,6,11,12,16). The septum is activated slightly before the lateral wall, meaning the myocardium contracts asynchronously. Besides, ischemic cases show wide disparities between healthy and pathological segments. Reduced deformation values are observed for those infarcted AHA segments.

For the ischemic cases, we also provided the ground truth infarction areas projected onto the AHA segments in Fig. 5.14. We see a clear consistency between the strain maps and the groundtruth affected regions. This validates the accuracy of the simulated ischemia.

In addition, we show in Fig. 5.15 the global circumferential strain (GCS) for the 18 virtual patients simulated in this thesis. We observe that pathological cases display reduced circumferential deformations compared to healthy ones.

5.4 Discussion

We introduced in this chapter a generic framework allowing the generation of realistic multimodal cardiac synthetic sequences for the same virtual patient. Based on our previous work described in [[Alessandrini et al. \(2015\)](#)], the main novelties of the proposed technique are twofold: i) we extended the pipeline originally developed for US to MR simulation; ii) we developed a dedicated scheme to better handle the transition between the myocardium and the surrounding structures. To the best of our knowledge, this is the first time that such a multimodality simulation framework is proposed.

It is widely acknowledged that multimodality raises many issues in cardiac imaging, beyond the mapping of all information in a common reference space. Indeed, different modalities were reported to provide significant differences for the quantification of volumes and ejection fraction values [[Jenkins et al. \(2009\)](#)]. Offering to the community a consolidated dataset, on the basis of which generic or modality-specific algorithms can be quantitatively compared, is a step forward towards understanding whether reported differences between modalities originate from the processing, the difference in image quality or can only be explained by more fundamental differences in the physics of imaging the same complex tissue through different modalities. By construction, our simulation method ensures that the synthetic MR and US sequences are generated from the same patient. The E/M simulations generated in the MR system of coordinates were brought

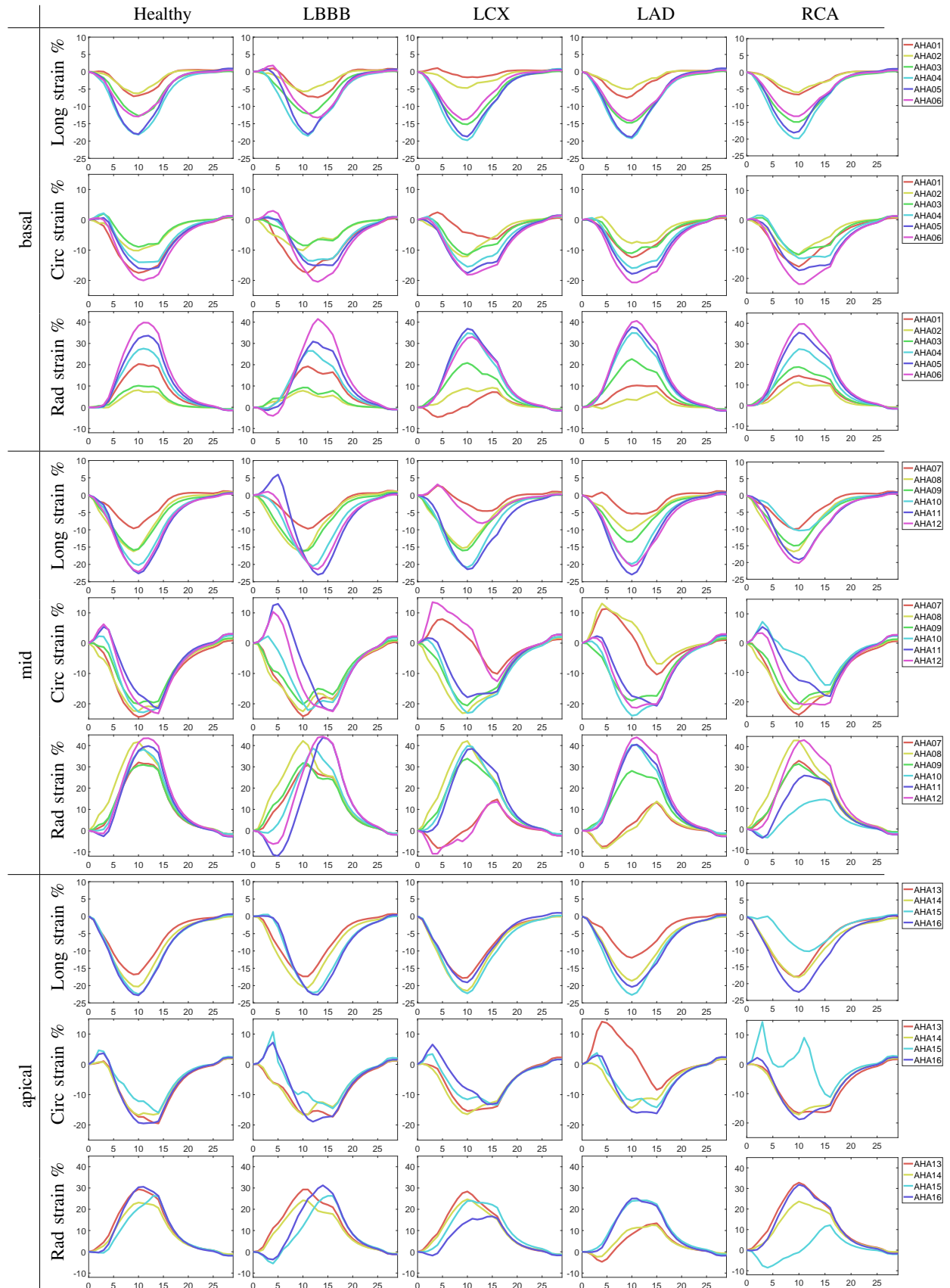


Figure 5.13: Regional strain curves at basal, mid and apical levels of the LV. We show one healthy, one dynssynchrony (LBBB) and three infarcted hearts (LCX, LAD, RCA).

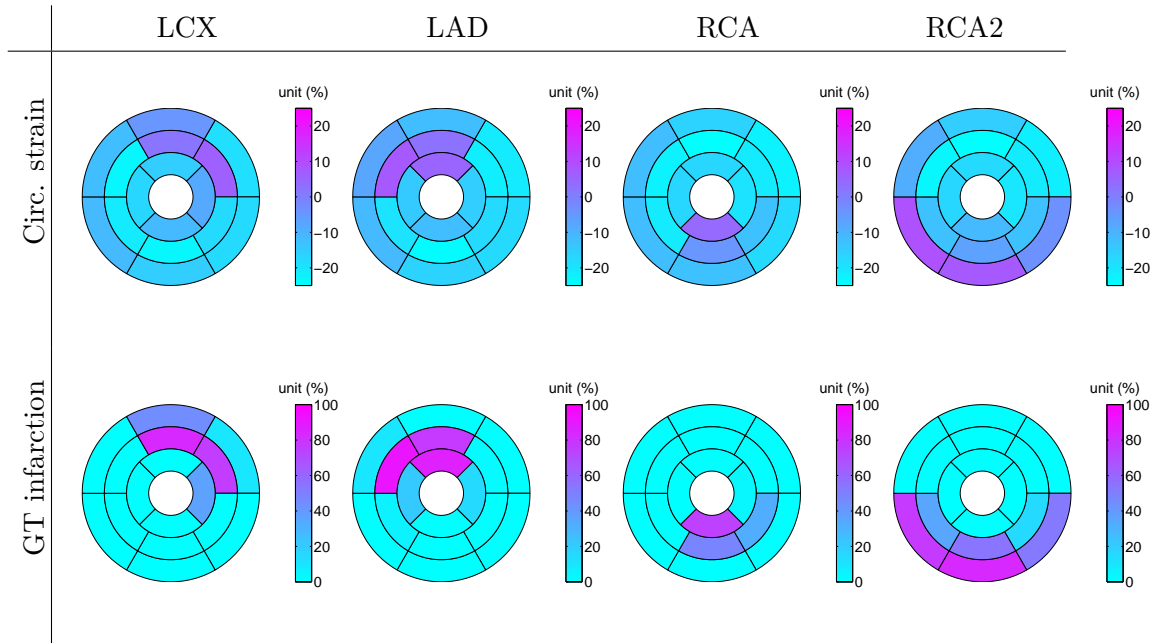


Figure 5.14: Bullseye displays on end-systolic circumferential strain maps (upper row) and the groundtruth infarction regions (lower row) corresponding to the four ischemic cases simulated in this thesis.

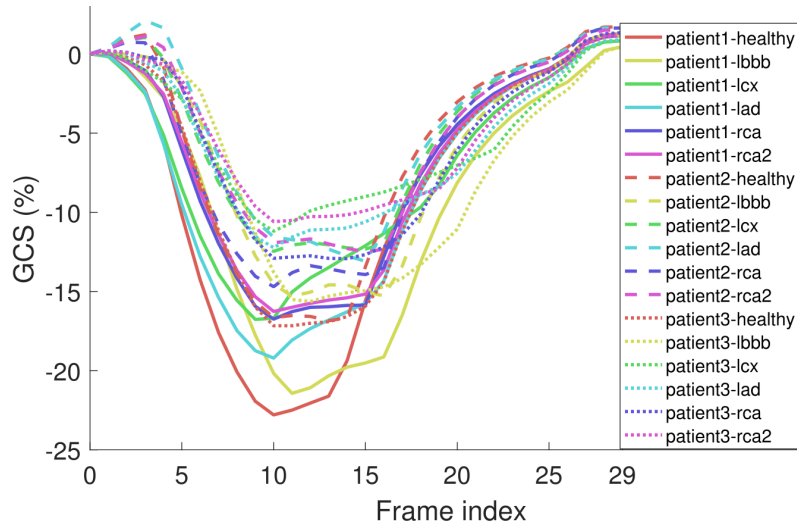


Figure 5.15: Global circumferential strain curves corresponding to the 18 simulated virtual patients.

to the US system by a simple rigid transformation composed of translation and rotation. The interest of such rigid transformation resides in the fact that it will not introduce any local myocardium deformation. The deformation patterns represented in the US and MR sequences are therefore the same, allowing a straightforward cross-modality comparison. However, this rigid transformation is sensitive to the accuracy of the 24 manual landmarks introduced in Section 5.2.1. The manual tracing should thus be carefully performed in order to minimize the potential impact on the US simulations.

By combining warpings of the whole template sequence and of the first frame only to each simulation mesh, we obtained a realistic background while guaranteeing that no registration error can introduce artifacts inside the myocardium. This is a fundamental difference with all registration-based methods such as [Prakosa *et al.* (2013)] where the error on displacements gets composed with the true displacement field, making any derived benchmark affected by such artifacts inside the myocardium. Moreover, we introduced an efficient Gaussian weighting function to deal with the interface between the myocardium and the background. Such a scheme guarantees a smooth transition between the different structures around the myocardium and thus avoids potential artifacts as it may appear for instance from the pipeline developed in [Alessandrini *et al.* (2015)] (Fig. 5.9).

Despite the advantages, we also acknowledge a number of limitations and simplifications. First, the realism of the computed relaxation times T_1 and T_2 could be improved to account for the temporal variations of these quantities as reported in [Reiter *et al.* (2013)]. The corresponding spatial distribution we used was kept simple (average reference values + Gaussian noise for the background region). Also, the myocardial T_1 values we computed from real tagging templates should be compared against real T_1 mapping acquisitions to validate this process. Additionally, when computing the proton density for tagged MR simulation, we assumed the effective spin-spin relaxation time T_2^* to equal the theoretical T_2 value. This assumption simplifies the simulation method and since they have close values, it should not significantly impact the simulation results. It should be emphasized however that our modeling strategy was aimed at optimizing the realism of the generated images rather than rigorously following the underlying physics. With this in mind, the derivations of most MR parameters we made from real MR images ensure a high level of realism of the simulated images as shown in Fig. 5.6 and 5.7.

We put a lot of effort in this paper to make sure that tracking errors would not introduce any artifacts inside the myocardium. However, it is worth mentioning that the quality of the simulated data remains sensitive to the tracking accuracy. Since the background is taken from a frame of the template sequence, tracking errors will appear as a residual motion applied to the background, resulting in possible tag line fractures occurring at the myocardium/background interface, although the use of a Gaussian weighting function is expected to limit such unrealistic artifacts. An accurate tracking is therefore required for producing high quality simulation data, which we ensured by using high quality images from carefully selected healthy subjects [Tobon-Gomez *et al.* (2013)].

Finally, the median longitudinal strain corresponding to the cardiac deformations gen-

erated by the E/M model is around 15%, which is still lower than reference clinical values. This has already been discussed in [[Alessandrini *et al.* \(2015\)](#)] and remains one of the major limitations of the E/M model. Compared to [[Alessandrini *et al.* \(2015\)](#)], the simulations generated in this paper already show increased longitudinal deformations thanks to a thorough parameter tuning process. Further improvement of the longitudinal strain as well as the reduction of the dispersion of GCS and the increase of the EF remains the object of future work.

5.5 Summary

In this chapter, we developed a generic pipeline for simulating 3D synthetic cardiac cine MR, tagged MR and US image sequences. The groundtruth cardiac motion fields were generated by an electro-mechanical model. Template acquisitions were deformed into the simulation space by a novel warping technique which ensures that i) motion in the synthetic images matches the E/M model and ii) transitions at the myocardium/background interface are smooth. Both MR and US images were generated by relevant physical simulators. We analyzed the image properties both qualitatively and quantitatively. In total, we simulated 18 virtual subjects representing 90 synthetic sequences which are made publicly available via an open-access database. In the following chapter, we will present an preliminary example of using this synthetic database to compare the performance of cardiac motion tracking algorithms.

Chapter 6

A generic HarpAR algorithm and a preliminary benchmarking study

6.1 Introduction

In Chapter 4, we presented a 3D extension of the HARP tracking algorithm specifically designed for the recent rapid 3D tagging acquisitions [Rutz *et al.* (2008)]. The developed algorithm makes use of the multi-channel nature of the tagged MR acquisition and combined the point-wise optical flow tracking with an anatomical motion model in order to obtain spatially smooth myocardial deformations. The proposed method 3D HARP tracking with Anatomical Regularization (HarpAR) was validated on one synthetic sequence, fifteen healthy volunteers and four patients. Nevertheless, the validation on real data was mostly confined to qualitative measures. For instance, we showed that the disparity of the estimated regional strain values is more significant on patients than on healthy hearts. On healthy volunteers, only sparse landmark tracking errors (rather than *dense* error maps) were evaluated. No regional strain quantification accuracy was assessed since the ground-truth deformation fields were not available in real data. The validation of HarpAR against the ground-truth *strain* maps is important since HarpAR is aimed at quantifying accurate local radial, longitudinal and radial strains, thanks to the proposed anatomical regularization model.

In Chapter 5, we introduced a novel simulation pipeline that is capable of generating realistic 4D synthetic US and MR (cine and tagging) image sequences for the same virtual subject. In total, 18 virtual subjects of various conditions (healthy or pathological) were

simulated. Each virtual patient has one dataset of synthetic 4D CSPAMM tagged MR, one sequence of multi-planar cine MR and one sequence of 3D ultrasound. A direct application of this simulated database is to validate and compare the performance of different motion tracking algorithms. Since the ground-truth motion is controlled and thus known, regional strain errors can be precisely evaluated. In this chapter, we will introduce a generic motion tracking algorithm derived from HarpAR and evaluate its performance on both motion and strain quantification against another fast motion tracking method called SparseDemons [[Somphone et al. \(2013\)](#)]. This chapter is organized as follows: first, we present a phase-based registration algorithm (Section 6.2) which is a direct extension of HarpAR. Then in Section 6.3, we propose a generalized version of HarpAR (named as gHarpAR) and further show a preliminary benchmarking example by comparing its performance against the SparseDemons based on the results on the synthetic database generated in Chapter 5. Note that due to the limited time, this benchmarking study remains quite preliminary and needs to be improved in the future. It is merely one of the first attempts to show the application of the simulated 18 virtual patients for validating cardiac motion tracking algorithms.

6.2 Phase-based registration of tagged MR images

6.2.1 Introduction

The quantification of local myocardial motion and strain remains a central challenge for diagnosing heart diseases. As explained in Chapter 2, tagged MR is the current reference imaging modality used to quantify regional myocardial deformation.

Recently in [[Rutz et al. \(2008\)](#)], a fast 3D CSPAMM acquisition was developed. A segmented EPI sequence and a small field-of-view (FOV) were employed so as to reduce the acquisition time. As a result, three sequences with line tagging can be acquired during only three breath-holds of 18 heartbeats duration each. The three tagged MR sequences were aligned using a navigator echo technique. The emergence of this 3D tagging acquisition protocol calls for a well-adapted fast quantification method. As a result, in Chapter 4, an algorithm that combines HARP tracking and an **A**natomical **R**egularization (HarpAR) framework was presented. In a first step, a point-wise motion tracking based on the extension of the HARP framework in 3D was proposed. The resulting field was then regularized by the introduction of a new parametric anatomical model in order to quantify strain accurately.

In this section, we propose an unified formulation in order to quantify motion field and strain at once, which would lead to a reduction of cumulative errors. The performance of the proposed method is compared to the original HarpAR on both synthetic data and healthy volunteers.

6.2.2 Preprocessing

The reader is referred to [Rutz *et al.* (2008)] for a full description of the acquisition of the tagged MR data used in this study. The data consists of three sequences with orthogonal tagging directions. In the sequel, the sequence ID is identified by the indice k ($k = 0, 1, 2$).

As described in Chapter 4, the preprocessing is composed of five procedures: 1) the segmentation of the left ventricle (LV); 2) the mesh resampling, along with the definitions of local anatomical directions (radial, longitudinal and circumferential); 3) the partition of LV into local windows and the definitions of window functions; 4) the computation of the distance maps in anatomical directions and finally 5) the computation of the HARP phase and amplitude images.

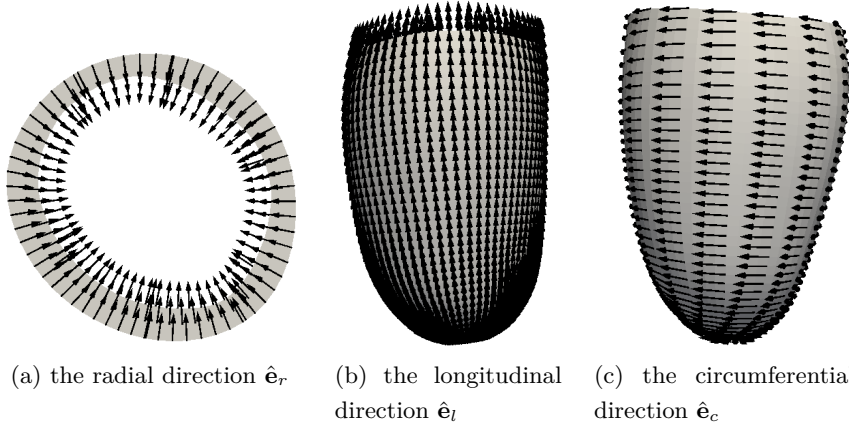


Figure 6.1: An illustration of the local anatomical directions of the left ventricle. The radial, longitudinal and circumferential directions are denoted as $\hat{\mathbf{e}}_r$, $\hat{\mathbf{e}}_l$ and $\hat{\mathbf{e}}_c$ respectively.

Step 1) and 2) aim to segment the LV and further resample the LV following the anatomical directions with the help of user-clicked landmarks (one at apex, four points at the base and one at the septum). Fig. 6.1 shows an example of the segmentation and the local radial, longitudinal and circumferential directions $\{\hat{\mathbf{e}}_r, \hat{\mathbf{e}}_l, \hat{\mathbf{e}}_c\}$.

Step 3) aims to divide the LV myocardium into local windows and define Gaussian shaped window functions. In Fig. 6.2, we show the partition of the LV and an example of the window function used in our framework. Regarding the details about the computation of the window function, the reader is referred to Sect. 4.3.3 of Chapter 4.

In step 4), we propose to compute the anatomical distance maps $\{r^{(i)}, l^{(i)}, c^{(i)}\}$ locally for each window i . $r^{(i)}$, $l^{(i)}$ and $c^{(i)}$ are defined as the distances to the window center in the radial, longitudinal and circumferential directions respectively. They were computed by curvilinear integrations as is described in Chapter 4. An example of the computed anatomical distance maps is shown in Fig. 6.3.

Finally, in Step 5), the image intensities are filtered by the HARP bandpass filters so as to produce the phase images (denoted as $\tilde{A}_k^t(\mathbf{x})$) and the corresponding amplitude

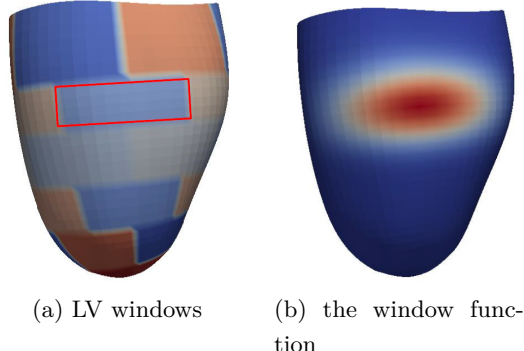


Figure 6.2: Local LV windows and the associated Gaussian shaped window function.

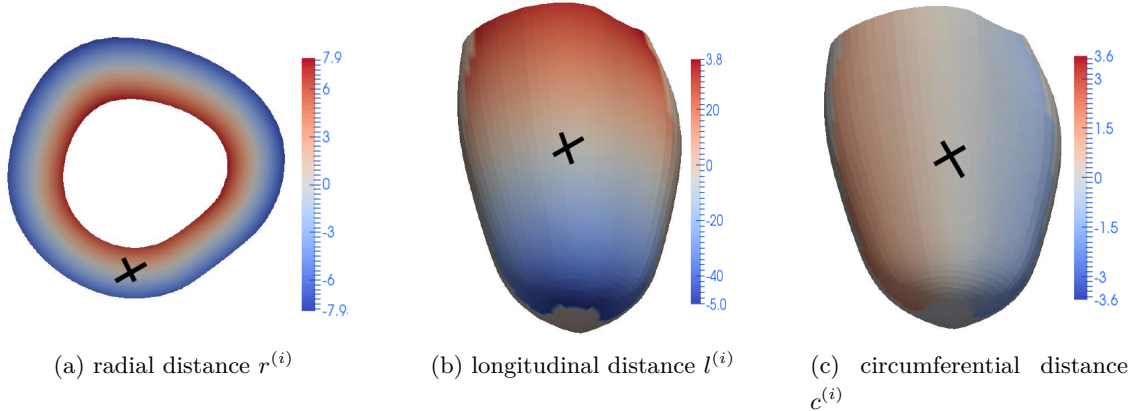


Figure 6.3: Computation of the distance maps $\{r^{(i)}, l^{(i)}, c^{(i)}\}$ in the radial, longitudinal and circumferential directions corresponding to a local window i . The window center is marked by the cross.

images (denoted as $\mathcal{M}_k^t(\mathbf{x})$) where k indicates the channel as mentioned before.

6.2.3 Methodology

In this section, we will introduce the anatomical deformation model defined using the anatomical directions and the local distance maps. Then, we formulate the motion tracking as a registration problem and finally we propose a multiscale framework in order to help recovering larger LV wall motions.

Myocardial motion tracking is regarded as a sequence of frame-to-frame registration problems. We chose to adopt a frame-to-frame strategy conducted backward in time since the myocardium was segmented at the last frame. The reason is the difficulty in distinguishing the myocardium at the first frame where both the myocardium and the background are tagged. We introduce the motion model used to represent the cardiac motion field from time t to $t - 1$ in the following.

Anatomical deformation model

We have already described in Chapter 4 the full details about the anatomical motion model. The LV myocardium domain is partitioned into windows. Gaussian-shaped window functions $\varphi^{(i)}(\mathbf{x})$ are then defined while satisfying the *partition-of-unity* properties [Makram-Ebeid and Somphone (2007)] (i.e. $\forall \mathbf{x}, \forall i, \varphi^{(i)}(\mathbf{x}) \geq 0; \forall \mathbf{x}, \sum_i \varphi^{(i)}(\mathbf{x}) = 1$). Inside each window i , the myocardial motion from $t \rightarrow t - 1$ is constrained to fit an affine transformation in this anatomical space $\{r^{(i)}, l^{(i)}, c^{(i)}\}$:

$$\mathbf{u}_t^{(i)}(\mathbf{x}) = L_r^{(i)}(\mathbf{x})\hat{\mathbf{e}}_r(\mathbf{x}) + L_l^{(i)}(\mathbf{x})\hat{\mathbf{e}}_l(\mathbf{x}) + L_c^{(i)}(\mathbf{x})\rho(\mathbf{x})\hat{\mathbf{e}}_c(\mathbf{x}) \quad (6.1)$$

$$L_d^{(i)}(\mathbf{x}) = a_{dr}^{(i)}r^{(i)}(\mathbf{x}) + a_{dl}^{(i)}l^{(i)}(\mathbf{x}) + a_{dc}^{(i)}c^{(i)}(\mathbf{x}) + b_d^{(i)} \quad (d = r, l, c) \quad (6.2)$$

where $\hat{\mathbf{e}}_d(\mathbf{x})$ (with $d = r, l, c$) are the *radial*, *longitudinal* and *circumferential* directions. $\rho(x)$ is the distance to the long axis of LV. $a_{mn}^{(i)}$ ($m, n = r, l, c$) and $b_m^{(i)}$ ($m = r, l, c$) are the parameters that define the motion. In Eq. 6.2, since $a_{dd}^{(i)}$ ($d=r,l,c$) is multiplied with the corresponding local distance map $d^{(i)}$, it represents in fact the stretch/shortening following the anatomical direction. $b_d^{(i)}$ are zero-order parameters representing the translations. The remaining parameters contribute to the shearing.

Enforcing myocardial incompressibility at the window level allows substituting $a_{rr}^{(i)}$ by the linear combination of all other parameters, resulting in a 11-parameter model per window. For this, the reader can find more details in Sect. 4.3.3 of Chapter 4.

The final motion from $t \rightarrow t - 1$ is obtained by mixing all local motions weighted by the window functions:

$$\mathbf{u}_t(\mathbf{x}) = \sum_i \varphi^{(i)}(\mathbf{x})\mathbf{u}_t^{(i)}(\mathbf{x}) \quad (6.3)$$

This gives a motion model with $11 \times \mathcal{N}$ parameters (\mathcal{N} being the window number). Estimating these parameters allows obtaining both anatomically coherent myocardial motions (i.e. locally affine) and meaningful deformations.

Unlike in Chapter 4 where the motion tracking is separated into two consecutive phases: 1) point-wise HARP tracking and 2) fitting the HARP results to the parametric model, here we propose to adjust the model parameters at once by minimizing a global energy based on phase similarity. This strategy avoids the introduction and accumulation of HARP tracking errors and we thus anticipate to obtain slightly better results. We describe the registration framework in the following section.

Phase-based registration

For the motion tracking from $t \rightarrow t - 1$, if given an initial estimate of the displacement $\mathbf{u}(\mathbf{x})$, the key idea is to find an optimal incremental displacement field $\mathbf{v}(\mathbf{x}) =$

$\sum_i \varphi^{(i)}(\mathbf{x}) \mathbf{v}^{(i)}(\mathbf{x})$ by minimizing an energy E defined as follows:

$$E(\mathbf{v}; \mathbf{u}) = \int_{\Omega} \sum_{k=0}^2 \omega_k(\mathbf{x}) \left(\mathcal{A}_k^t(\mathbf{x}) - \mathcal{A}_k^{t-1}(\mathbf{x} + \mathbf{u}(\mathbf{x}) + \mathbf{v}(\mathbf{x})) \right)^2 d\mathbf{x} \quad (6.4)$$

with $\omega_k(\mathbf{x}) = \sqrt{\mathcal{M}_k^t(\mathbf{x}) \mathcal{M}_k^{t-1}(\mathbf{x} + \mathbf{u}(\mathbf{x}))}$

where \mathcal{A}_k^t and \mathcal{A}_k^{t-1} are unwrapped phase images. Applying first-order approximations on \mathcal{A}_k^{t-1} gives:

$$E(\mathbf{v}; \mathbf{u}) \approx \int_{\Omega} \sum_{k=0}^2 \omega_k(\mathbf{x}) \left(\xi_k(\mathbf{x}) - \boldsymbol{\eta}_k(\mathbf{x}) \cdot \mathbf{v}(\mathbf{x}) \right)^2 d\mathbf{x} \quad (6.5)$$

with $\xi_k(\mathbf{x}) = \mathcal{A}_k^t(\mathbf{x}) - \mathcal{A}_k^{t-1}(\mathbf{x} + \mathbf{u}(\mathbf{x}))$

$\boldsymbol{\eta}_k(\mathbf{x}) = \nabla \mathcal{A}_k^{t-1}(\mathbf{x} + \mathbf{u}(\mathbf{x}))$

ξ_k and $\boldsymbol{\eta}_k$ are computed from the wrapped phases denoted as \tilde{A}_k^t and \tilde{A}_k^{t-1} by the method described in [Osman *et al.* (1999)]. Regarding this, more details can also be found in Appendix A.1. Based on the *partition-of-unity* properties of $\varphi^{(i)}$, it is easy to prove that the global energy E is upbounded by the sum of local energies:

$$\begin{aligned} E(\mathbf{v}; \mathbf{u}) &\approx \\ &\int_{\Omega} \sum_{k=0}^2 \omega_k(\mathbf{x}) \left(\sum_i \varphi^{(i)}(\mathbf{x}) \left(\xi_k(\mathbf{x}) - \boldsymbol{\eta}_k(\mathbf{x}) \cdot \mathbf{v}^{(i)}(\mathbf{x}) \right) \right)^2 d\mathbf{x} \\ &\leq \sum_i \int_{\Omega} \varphi^{(i)}(\mathbf{x}) \sum_{k=0}^2 \omega_k(\mathbf{x}) \left(\xi_k(\mathbf{x}) - \boldsymbol{\eta}_k(\mathbf{x}) \cdot \mathbf{v}^{(i)}(\mathbf{x}) \right)^2 d\mathbf{x} \\ &= \sum_i E^{(i)}(\mathbf{v}^{(i)}; \mathbf{u}) \end{aligned} \quad (6.6)$$

This means that minimizing the local energies $E^{(i)}(\mathbf{v}^{(i)}; \mathbf{u})$ also minimizes the global energy $E(\mathbf{v}; \mathbf{u})$. The reader is referred to [Makram-Ebeid and Somphone (2007)] for a more detailed proof. The global optimization problem is therefore decomposed into a set of local ones at a lower computational cost. As $v^{(i)}$ is linear with respect to its parameters, $E^{(i)}$ is a quadratic form and is minimized by solving a linear system.

Multi-scale framework

For capturing large myocardial motion, a multi-scale framework detailed in Sect. 4.3.5 of Chapter 4 is used. We adopt three scales with gradually increased window numbers (i.e. smaller windows). The motion field is refined each time passing from the current scale to the next. Within each scale, the procedure described in Sect. 6.2.3 is iterated

until convergence.

Algorithm 1: The proposed algorithm

```

Set  $n = 0$ ,  $\mathbf{u}_0 = 0$ 
for each scale  $s$  do
    Compute  $\varphi^{(i)}$ 
    repeat
        for each window  $i$  do
             $\mathbf{v}_n^{(i)} = \text{argmin}_{\mathbf{v}^{(i)}} E^{(i)}(\mathbf{v}^{(i)}; \mathbf{u}_n)$ 
        end
         $\mathbf{v}_n = \sum_i \varphi^{(i)} \mathbf{v}_n^{(i)}$ 
         $\mathbf{u}_{n+1} = \mathbf{u}_n + \mathbf{v}_n$ 
         $n = n + 1$ 
    until  $\|\mathbf{v}_n\| < \delta$ ;
end

```

6.2.4 Results

On 18 virtual patients simulated in Chapter 5

The proposed algorithm was compared with HarpAR on the 18 synthetic tagged MR datasets simulated in Chapter 5. For each dataset, the left ventricle of the first simulation mesh was resampled to the anatomical mesh model described in Section 6.2.2. When performing the resampling, special attention was paid to ensure the resampled mesh was located within the tetrahedral cells of the simulation mesh. This facilitates the interpolation of the ground-truth motion on the resampled mesh nodes. The resampled mesh was then tracked by both HarpAR and the proposed algorithm. From the tracking results, we computed regional motion and strain values at the AHA segmental level and calculated the quantification errors. The tracking errors from all time instants of the 18 sequences were combined and displayed as boxplots in Fig. 6.4. From the figure, we see that the proposed method shows slightly reduced motion and longitudinal strain errors compared to HarpAR. This is further confirmed by the RMSE computation: for HarpAR, RMSE on motion and long. strain are respectively 1.26mm and 2.13%. Yet those values obtained by the proposed phase-based registration method are respectively 1.05mm/1.71%.

On healthy volunteers

We used the volunteer data available from [Tobon-Gomez *et al.* (2013)] to evaluate the performance of the proposed method by comparing the tracking accuracy to HarpAR and another state-of-the-art method referred to as MEVIS in [Tobon-Gomez *et al.* (2013)]. Each volunteer data has 24 manually tracked landmarks located in the basal, mid and apical myocardium. These landmarks were warped forwardly in time by computing barycentric coordinates in the first frame and propagating them throughout the sequence of volumetric meshes.

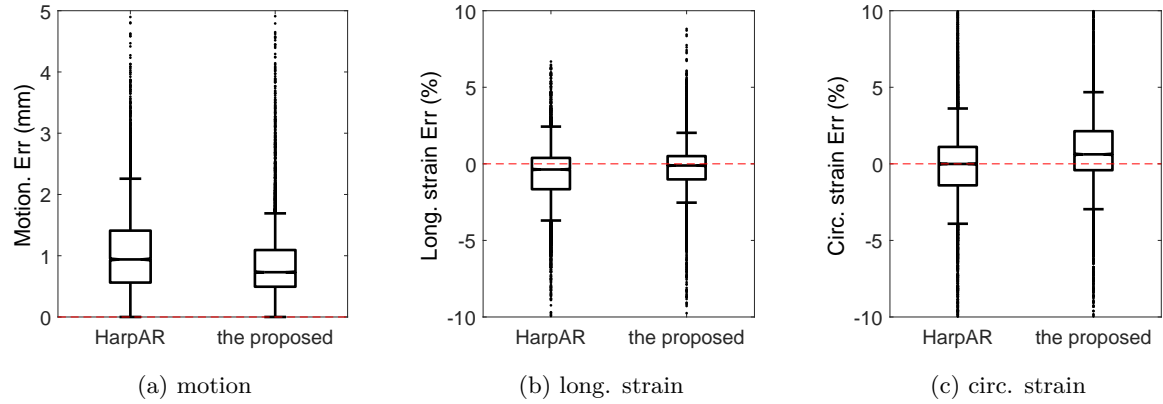


Figure 6.4: Comparison between motion and strain quantification accuracies of HarpAR and the proposed algorithm on the 18 synthetic tagged MR datasets simulated in Chapter 5. Both the motion and strain are computed at the segmental AHA level. For each metric (motion or strain), regional errors from all time frames of the 18 sequences are combined and shown as boxplots.

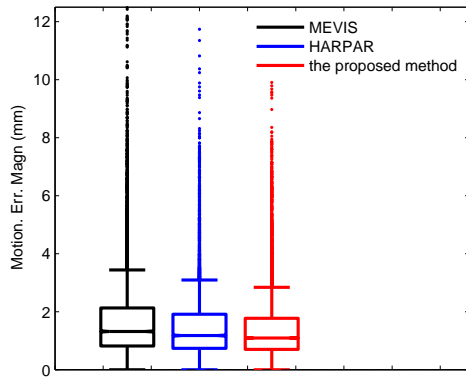


Figure 6.5: Volunteer data landmark tracking errors using MEVIS ([Tobon-Gomez *et al.* (2013)]), HARPAR and the proposed method.

Fig. 6.5 shows boxplots of landmark tracking accuracy for all the 15 volunteers and for all the cardiac phases. From Fig. 6.5, it appears that both the median and the dispersion of the tracking errors are reduced when comparing the proposed method to the two others. This result is further confirmed by two statistical tests. Both the Levene's test and the Wilcoxon signed-rank test returned p-values below 0.05, revealing that neither the variance nor the median are the same.

6.2.5 Conclusion and discussion

In this section, we presented an extension of the HarpAR algorithm for the quantification of cardiac motion and deformation from tagged MR image sequences. The proposed algorithm is formulated in a conventional phase-based registration framework. The param-

eters of the motion model were optimized using a phase-based SSD metric. The proposed method was compared to the HarpAR algorithm previously introduced in Chapter 4. On the 18 realistic synthetic image sequences generated in Chapter 5, the proposed method marginally improved the accuracy of both motion and strain estimates. On volunteer data, the proposed method achieved better results regarding the median and variance of the landmark tracking errors. Moreover, the proposed method is formulated in a classic image registration framework and would allow the integration of additional regularization terms that might help improving the accuracy. One limitation of the algorithm is that the window sizes in the multi-scale framework were adapted to the tag spacing of 7 mm. If the tag grid resolution changes, one should modify the scales accordingly.

6.3 A generalized version of HarpAR: the gHarpAR

In Section 6.2, the previously introduced anatomical motion model has been integrated within a standard image registration framework. The parameters of the motion model were optimized to minimize the frame-to-frame dissimilarities between phase images. The proposed registration method was tested on both synthetic and real tagged MR images and results proved that it improved both the motion and strain quantification accuracy, compared to the original HarpAR algorithm presented in Chapter 4.

Actually, the same concept can be extended to intensity-based registration so as to quantify also the ultrasound and the cine MR images. In this section, we propose a generalized version of the HarpAR algorithm (named as gHarpAR) and show a preliminary benchmarking example using the multi-modal synthetic image sequences simulated in Chapter 5.

6.3.1 The generic anatomical registration algorithm gHarpAR

The mathematical formulation

As described in Section 6.2, cardiac motion tracking can be formulated as a registration problem. The tracking of the motion from *ref* time to frame *t* is equivalent to solving for the parameters of \mathbf{u} that minimizes the total energy defined as follows:

$$\underset{\mathbf{u}}{\operatorname{argmin}} \int_{\Omega} \sum_{k=0}^{K-1} w_k(\mathbf{x}) \left(I_k^{ref}(\mathbf{x}) - I_k^t(\mathbf{x} + \mathbf{u}(\mathbf{x})) \right)^2 d\mathbf{x} \quad (6.7)$$

Where \mathbf{u} represents the myocardial motion field from *ref* to *t*. It is defined on the anatomical model of the LV and has $11 \times \mathcal{N}$ parameters (\mathcal{N} being the number of windows) as is described in Section 6.2.3. Ω represents the myocardium domain. k indexes the channel of the imaging sequence and K is the total number of channels. This is aimed to deal with the multi-channel acquisitions such as the tagged MR data used in this thesis. Both the echocardiography and the cine MR acquisitions consist of only one channel, hence $K = 1$. I_k^t refers to the k -th channel of the image information which can be either intensity or

phase. I_k^{ref} is the information at *ref* time. Finally, w_k is the confidence weight map of the k -th channel. It can be used to incorporate the weight of each specific spatial location into the registration.

The multi-resolution framework

In order to help recovering large LV wall deformations, the registration is implemented under a multi-resolution framework as is described in Section 6.2.3. Three resolutions with increasing numbers of LV windows (thus smaller local window size) are computed (Section 6.2.3). The myocardial displacement is refined when passing the current resolution to the next. Within each resolution, the incremental motion is calculated using the window weighted regression technique as is detailed in Section 6.2.3. The window weighted regression is chosen since it allows the decomposition of a global optimization problem into local ones that are computationally cheaper to solve.

The frame-to-frame tracking

We have introduced the computation of the motion field from time *ref* to *t*. We opt for adopting a frame-to-frame tracking strategy. The tracking of the myocardial motion over the whole cardiac cycle is then regarded as a succession of frame-to-frame registration problems which are solved by the algorithm described above.

The implementations on different modalities

The generic algorithm gHarpAR presented in Section 6.3.1 needs to be implemented according to the specific cardiac imaging modality. For instance, we need to decide which kind of information (intensity or phase) to employ in Eq. 6.7. For tagged MR, the myocardial intensity decreases over time due to the tag fading. The HARP phase is then preferred over the original image intensity for the motion tracking. Tracking the phase achieved slightly better accuracy than tracking the intensity as it will be shown later in Section 6.3.2. Besides, in Eq. 6.7, K is set to 3 since there are three channels of tagged MR. Also, as is described in Section 6.2.3, the untagged image computed from the amplitude image was used as the confidence weight w_k where k denotes the channel ID.

When it comes to cardiac US or cine MR, only one acquisition channel is available, hence $K = 1$. In addition, it is natural to assume that for a given material point, the image intensity stays stable between neighboring time frames. We opted for tracking the motion directly from the intensity images. The confidence weight w_k is set as a constant map equals to 1 for all pixel positions.

6.3.2 Results on the simulated virtual patients

We have introduced the multi-modal implementations of the proposed gHarpAR algorithm. Its performance on quantifying myocardial motion and strain from tagged MR

images has already been evaluated in Section 6.2.4. We are interested to see whether the same accuracy can be obtained on the other two imaging modalities: US and cine MR. As a result, the gHarpAR was applied to the 18 virtual patients simulated in Chapter 5. We show the quantification accuracies in this section. Another generic motion tracking algorithm SparseDemons [[Somphone et al. \(2013\)](#)] was also used to process the same synthetic database. A comparison of how the two algorithms perform in terms of tracking accuracy is provided hereafter.

Comparing gHarpAR and SparseDemons across different modalities

Thanks to the synthetic data generated in Chapter 5, for a given generic motion tracking algorithm, we can now evaluate its performance across the three cardiac imaging modalities (US, cine and tagged MR). This would help to better understand the properties of each modality, especially the associated ability in quantifying local myocardial deformations. Besides, those generic motion tracking algorithms can be more fairly evaluated, not only based on a single given imaging modality. Quantification accuracies can be computed for all the three modalities. First of all, we explain how the tracking of synthetic sequences was generated.

For each virtual patient, in the MR coordinate system, we resampled the LV of the first simulation mesh in the *radial*, *longitudinal* and *circumferential* directions by the method introduced in Sect. 4.2.3 of Chapter 4. The resampled mesh has three layers in the radial direction: endocardium, epicardium and a mid-myocardium layer. As in the previous validation experiments (Section 6.2.4), special efforts were made to ensure the resampled mesh is inside the original simulation mesh. We show in Fig. 6.6 an example that illustrates the resampling results. Since the mesh is resampled in the MR space, as mentioned in Section 5.2.1, a rigid transformation built upon 24 manually chosen landmarks is then used to bring the resampled mesh to the US system of coordinates. For each imaging modality (US, cine or tagged MR), the corresponding resampled mesh was then tracked by both the gHarpAR and the SparseDemons algorithms. Note that since SparseDemons cannot handle multi-channel data, the three channels of the tagged MR image were multiplied to create a single sequence of tagging grids. To obtain the ground-truth motion of the resampled mesh points, the resampled mesh was warped over the sequence by forces computed from the simulation meshes. It was convenient to compute the warping forces since the resampled mesh was inside the volumetric simulation mesh.

In total, 18 virtual patients were tracked, yielding 54 tracked mesh sequences corresponding to each algorithm. We now need to compute the regional tracking errors for each AHA segment. Similar to [[Alessandrini et al. \(2015\)](#)] and [[Zhou et al. \(2015\)](#)], we opted for using the Engineering strains since it describes the myocardial stretch/shortening in the anatomical directions that are clinically relevant. As a result, for each cardiac phase, local motion and strains (radial, longitudinal and circumferential) errors were calculated and then averaged within each AHA segment. The regional strain and motion errors from

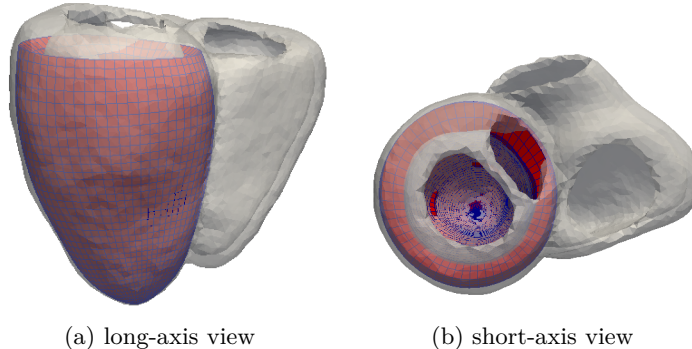


Figure 6.6: The resampling of the first simulation mesh into a new LV mesh defined following the radial, longitudinal and circumferential directions. The resampled mesh is shown in red color. The simulation mesh is shown in white with adjusted opacity level.

all time instants and all virtual patients were combined and displayed as boxplots in Fig. 6.7. We observe that globally, motion and strains quantified from tagged MR and US show smaller errors than cine MR. This is because unlike tagged MR or US, there are no markers in the myocardium in cine MR. The myocardium shows almost homogeneous intensities. This hinders the fine estimation of motion and strain. For instance, from Fig. 6.7 we see that the median motion errors of SparseDemons tracking are below 1mm on both tagged MR and US, yet for cine MR, this value increases to somewhere around 2mm.

Between the gHarpAR and SparseDemons algorithms, we observe that the two algorithms reached similar motion and strain accuracies on tagged MR whereas on radial strain gHarpAR recovered much more accurate deformation values. On cine MR, it is clear that SparseDemons outperformed gHarpAR on both motion and all the three strains. On US, SparseDemons gave more accurate motion, longitudinal and circumferential strain estimations while gHarpAR performed better on radial strain thanks to the imposed radial regularization introduced in Chapter 4.

In order to give a more straightforward analysis on motion and strain accuracies, we calculated the corresponding root mean square errors (RMSE) in Fig. ???. We can see that across different modalities, the tendency is that both motion and strain accuracies are improved when comparing US and tagged MR results to cine MR.

Besides, from the results on tagged MR, we observe that SparseDemons slightly outperformed gHarpAR regarding motion accuracy, but shows bigger errors on longitudinal and circumferential strains. Moreover, on radial strain, the RMSE obtained by SparseDemons is almost twice that of gHarpAR. This confirms the interest of the specific radial regularization technique developed for the gHarpAR algorithm [Zhou *et al.* (2015)]. The above analyses are further supported by the Levene's test performed on the boxplots shown in Fig. 6.7. On both the motion and three strain errors on tagged MR, the Levene's test returned p-value below 0.05, rejecting the null hypothesis that gHarpAR and SparseDemons quantification errors (both motion and strain) have equal variances. Combined with a

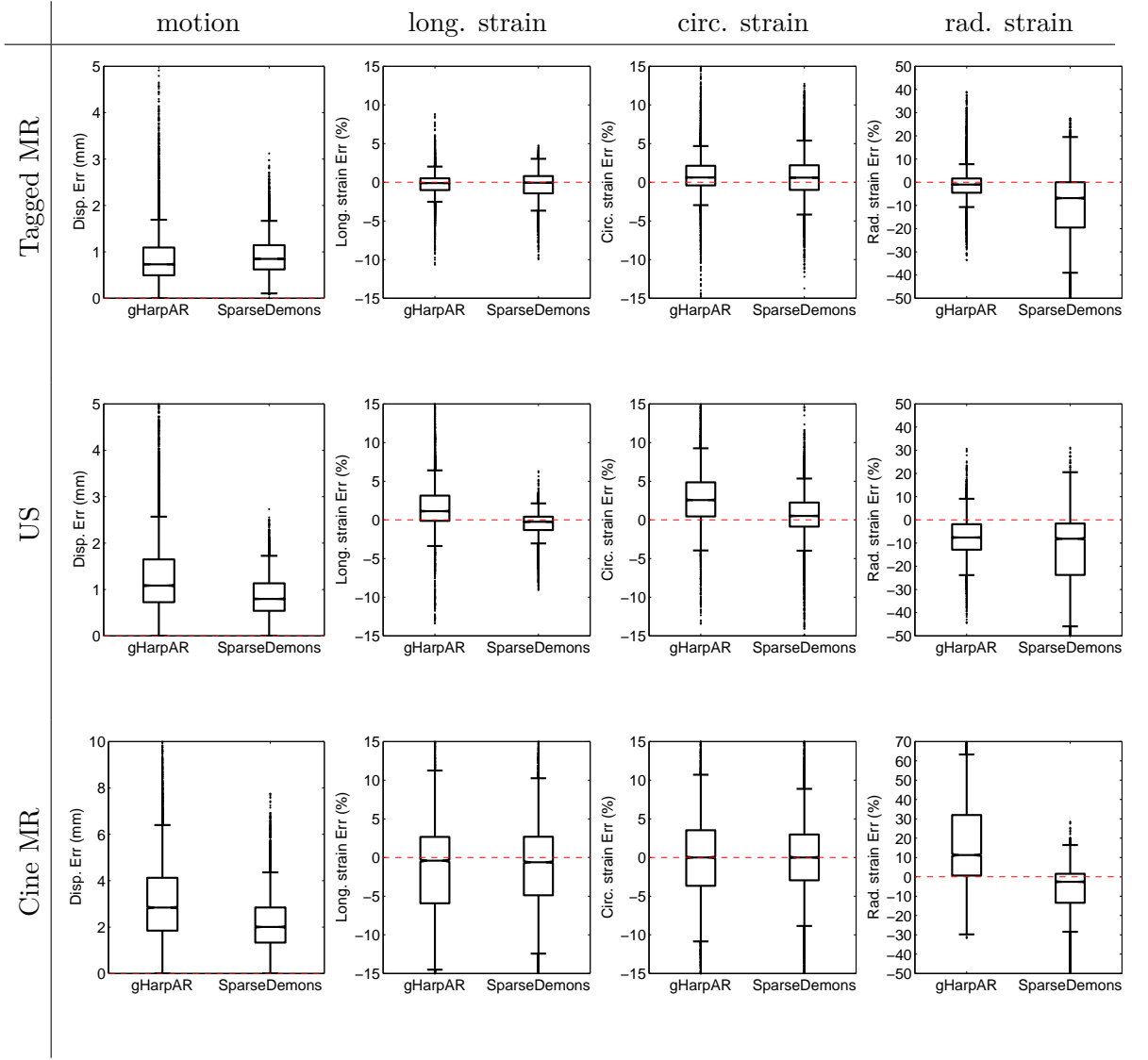


Figure 6.7: The local motion and strain quantification errors obtained by two generic cardiac motion tracking algorithms: gHarpAR and SparseDemons. Both algorithms were run on the 18 virtual patients simulated in Chapter 5. The point-wise motion and strain errors were averaged inside each AHA segment. The regional quantification errors from all time frames and all virtual patients were combined and shown as boxplots.

careful visual inspection of Fig. 6.7, we observe that SparseDemons gave smaller variance on motion error while the dispersion is bigger on both longitudinal and circumferential strain errors.

All in all, based on the information revealed by Fig. 6.7 and 6.8, we consider that for cine MR, SparseDemons is a better choice for quantifying cardiac motion. But for tagged MR, gHarpAR is preferred over SparseDemons due to the much improved radial strain accuracy. When it comes to US images, if one is most interested in recovering reliable radial deformations, gHarpAR should be considered. Otherwise, we would recommend SparseDemons since it showed better accuracies on the displacement and the other strain

components.

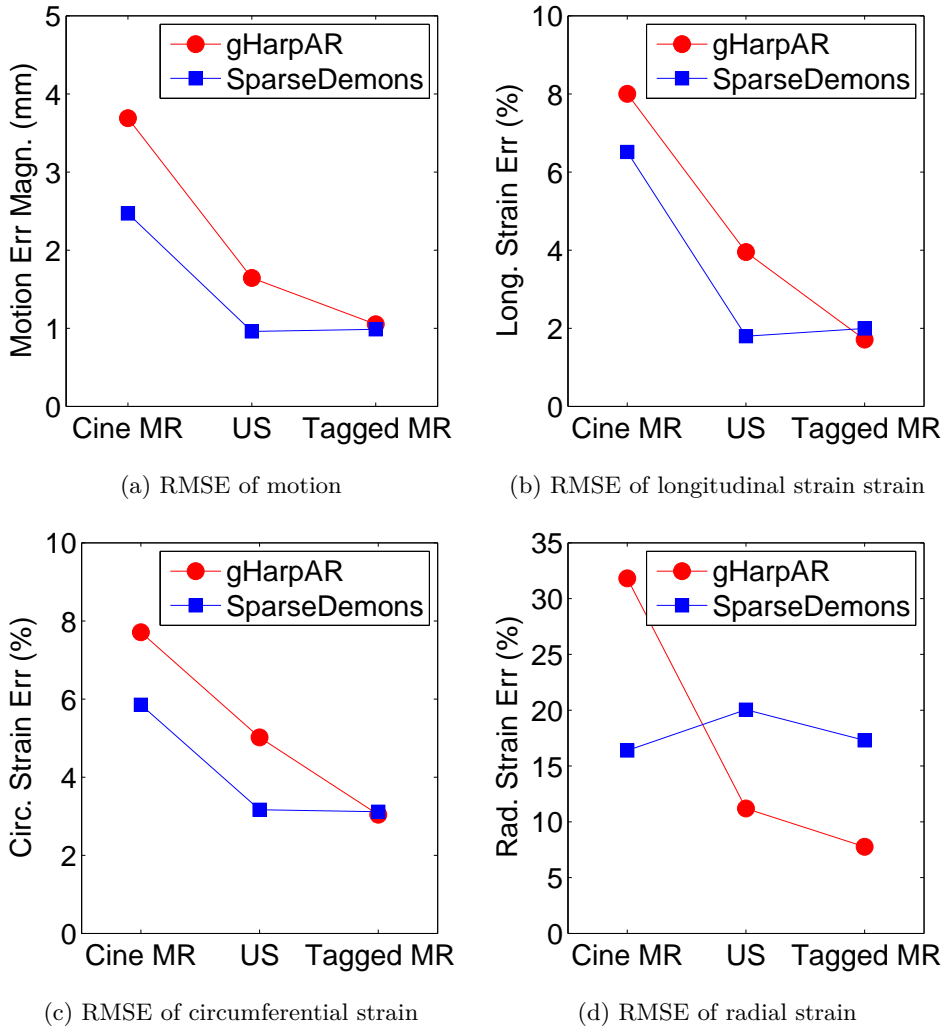


Figure 6.8: The root mean square errors computed on regional motion and strains obtained by two generic cardiac motion tracking algorithms: gHarpAR and SparseDemons. The x-axis represents the modality. From left to right: cine MR, US and tagged MR.

Comparing gHarpAR between using the HARP phase and using the intensity

We have shown earlier in this section that gHarpAR outperformed SparseDemons in quantifying tagged MR images. However, as mentioned in Section 6.3.1, gHarpAR registered the HARP phase while SparseDemons tracked the intensity image. Tracking the phase is anticipated to perform better as the phase is less sensitive to tag fading than intensity. This would have biased the comparison between the two algorithms. To figure out whether improved performance of HarpAR comes simply from the fact that it employs HARP phase (rather than intensity) for tracking or from the algorithm itself, we replaced the HARP phase by the original tagged MR intensity (i.e. the I in Eq. 6.7 now becomes the intensity) and re-executed gHarpAR on the 18 synthetic tagged MR datasets. The results

were compared with the old ones based on HARP phase. We would like to emphasize that the two versions of gHarpAR have exactly the same parameters and configurations, they only differ in the information used for tracking: one uses the HARP phase and the other the image intensity.

The quantification accuracies by both methods are shown in Fig. 6.9 alongside the SparseDemons results. From the boxplots, we observe that using either the phase or the intensity achieved quite similar accuracies on motion, longitudinal and radial strains. Yet on circumferential strain, the phase-based gHarpAR showed better accuracy in terms of both the median and the variance of the strain errors. To verify this, we applied the Levene's test and the Wilcoxon signed rank test on the two samples. Both returned p-values below 0.05, meaning that neither the variance nor the median are equal. This confirms the result observed from the boxplots.

Generally speaking, the intensity-based gHarpAR showed a tracking performance comparable to the phase-based registration. This is due to the fact that the tracking was always performed between two neighboring frames. Although the variation of myocardial intensity is non-negligible between the beginning and the end of the heart cycle, tag intensities are in similar ranges between two frames. This explains why switching from phase to intensities does not significantly impact the tracking. As a result, only slightly deteriorated circumferential strain accuracy is observed. In addition, In Fig. 6.9, the tracking results of SparseDemons are shown once again in order to give a visual comparison between the intensity-based gHarpAR and the SparseDemons. Since phase- and intensity-based gHarpAR have similar performance on tagged MR data and we already showed earlier that phase-based gHarpAR slightly outperformed SparseDemons when processing tagged MR images, we consider the same conclusion can be drawn for intensity-based gHarpAR as it can be observed from Fig. 6.9. The better accuracy on strain estimation originates therefore from the algorithm itself, more precisely from the anatomical regularization especially the specific radial regularization brought by imposing myocardial incompressibility.

6.3.3 Conclusion and discussion

In this section, we showed that the phase-based registration using the anatomical motion model originally developed for tagged MR can be extended to handle also the ultrasound and the cine MR images. The same anatomical regularization concept can be extended to the general case. We proposed therefore a generic motion tracking framework named as gHarpAR and evaluated it on synthetic US, tagged and cine MR image sequences generated previously in Chapter 5. Since the synthetic database is comprehensive in terms of both pathology and modality, a fair comparison can be made between cardiac motion tracking algorithms. We evaluated the gHarpAR against the SparseDemons algorithms using this synthetic database. Based on motion and strain quantification accuracies, we found that the gHarpAR is better suited for quantifying tagged MR. Moreover, we further confirmed that the more accurate strains obtained by gHarpAR come from the algorithm

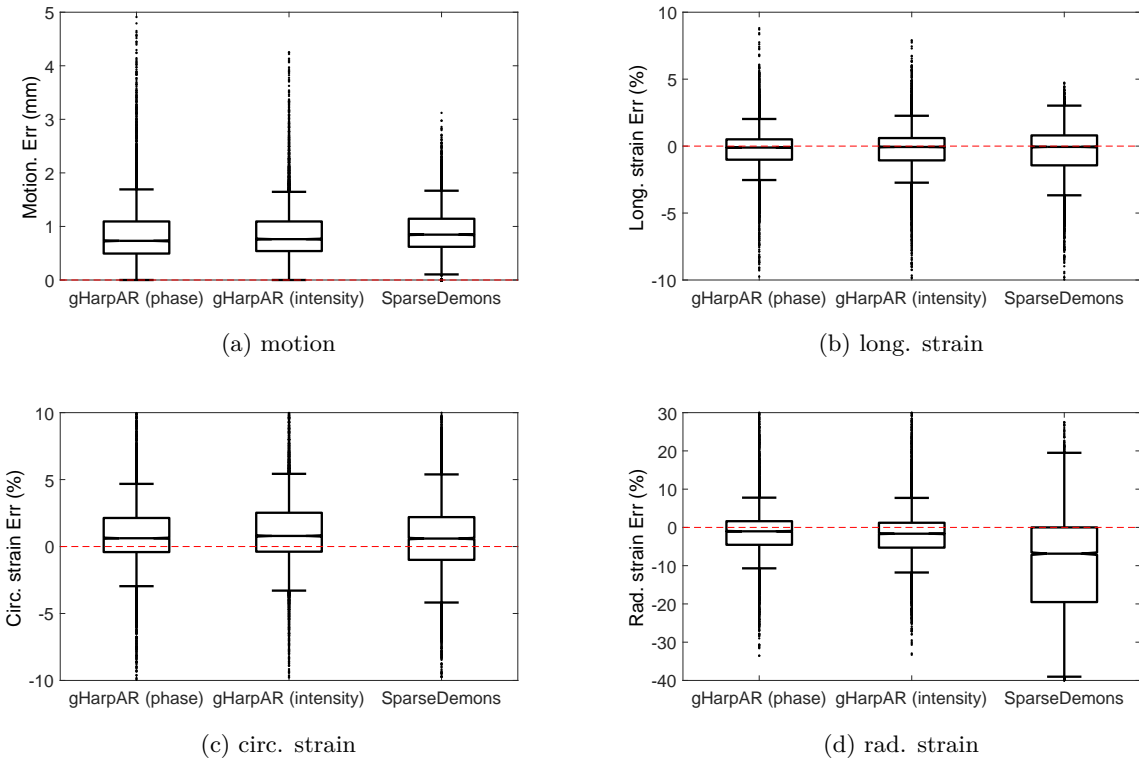


Figure 6.9: Tracking accuracies of gHarpAR using the HARP phase or directly the image intensity. Besides, we show the SparseDemons tracking results alongside. All the tracking results were obtained on the 18 synthetic tagged MR datasets generated in Chapter 5. The motion and strain errors were computed at the AHA segmental level. Quantification errors from all time frames and all the sequences were combined and shown as boxplots.

itself (e.g. the anatomical regularization), rather than the fact of using the HARP phase. As for cine MR, SparseDemons is preferred over gHarpAR since it achieved better accuracies on both motion and strain. When it comes to US, thanks to the specific radial regularization, gHarpAR obtained more accurate radial strains. However, SparseDemons has many advantages over gHarpAR on other strain components and the motion.

From the experiments conducted on synthetic data, we observe that a given motion tracking algorithm may perform inconsistently across different modalities. Differences on the quantified myocardial deformation errors were observed among US, cine and tagged MR images for both SparseDemons and gHarpAR (Fig. 6.8). The reason behind those observed disparities remains still unknown at the current stage. Whether those differences result from the post-processing, the different image contrasts or the fundamental physical basis, *etc* remains an open question. This is one of the future research axes. In addition, it would be interesting to evaluate also accuracies on the global indexes such as ejection fraction and stroke volume and compare different motion tracking algorithms' performance in evaluating global cardiac function. However, due to the limited time and resources, this fell outside the scope of this thesis and is worth investigating in future work.

Aside from the inter-modality differences, we also find that for a given imaging modality, different post-processing algorithms may produce quite different tracking results. For example, as we observe in Fig. 6.8, when quantifying the cine MR, gHarpAR yielded more than 50% bigger quantification errors on both motion and the three strain components than SparseDemons. This is possibly because in cine MR, no local "markers" exist inside the myocardium, hence the tracking of the middle myocardium points relies heavily on the regularization. Unlike gHarpAR, SparseDemons utilizes a spatially wider regularization beyond the myocardial domain. Therefore, the information coming from outside the myocardium also contributes to the tracking. Besides, it makes the tracking less sensitive to the segmentation performed at end-diastole. All these may explain why SparseDemons obtained better quantification accuracies on cine MR.

Contrary to cine MR, tagged MR provides the most detailed information about the local myocardial motion, thanks to the tags. Moreover, instead of acquiring a single channel which is the case of most cardiac imaging modalities including cine MR and US, three channels of line tagging with orthogonal tag orientations are acquired. The abundant information somewhat reduces the dependency of the tracking accuracy on the regularization. Therefore, gHarpAR recovered more accurate local deformations than SparseDemons. In particular, it greatly improved radial strain accuracy due to the radial regularization used. Indeed, cardiac motion tracking algorithms should be chosen according to the characteristics of the specific imaging modality in order to obtain more reliable quantification results.

6.4 Summary

In this chapter, we first introduced an extension of the previously developed HarpAR algorithm in order to better formulate it in a classic phase-based image registration framework. The original HarpAR tracks the cardiac motion by a two-step method consisting of a point-wise optical flow and a regularization *a posteriori* using an anatomical model. Reformulating it in an unified one-step image registration approach would lead to a reduction of cumulative errors. This was confirmed by our experiments on both synthetic and real data. The recently simulated synthetic tagged MR image sequences introduced in Chapter 5 were used for comparing the performance of the original two-step method HarpAR and the proposed unifying phase-based registration. Results revealed that the phase-based registration obtained better motion and longitudinal strain accuracies.

The second part of this chapter is dedicated to showing a preliminary benchmarking example using the 18 virtual patients simulated in Chapter 5. As a first step, the phase-based registration was generalized to a common framework named as gHarpAR. The generic motion tracking algorithm gHarpAR was then compared against another generic tracking solution SparseDemons initially developed for speckle tracking. Local motion and strain errors at the AHA segmental level were evaluated for all of the three modalities (US, cine MR and tagged MR). From the results, we concluded that gHarpAR

is well suited for processing images with more detailed local information such as tagged MR and that SparseDemons should be preferred for cine MR since it imposes a stronger spatial regularization which helps tracking middle myocardial points despite the lack of markers. Besides, the results showed that except for cine MR, gHarpAR obtained more accurate radial strain values, thanks primarily to the specific radial regularization described in Chapter 4. Finally, we would like to address that our main goal here is to show that the simulated virtual patients could be used for a cross-modality validation of 3D cardiac motion tracking algorithms, rather than judging which algorithm is more powerful. Besides, the benchmarking example presented here is rather simplistic and preliminary. A more comprehensive and thorough benchmarking study remains the objective of future work.

IV Conclusions and Perspectives

Chapter 7

Conclusions and Perspectives

7.1 Conclusions

The goals of this thesis were to propose a fast 3D motion and strain quantification algorithm for the post-processing of the recently accelerated CSPAMM tagged MR acquisitions [[Rutz et al. \(2008\)](#)] and to develop a novel simulation pipeline for generating realistic multi-modal synthetic cardiac sequences (ultrasound, cine MR, tagged MR) for validating our tracking algorithm in a multi-modal context.

First of all, we proposed a novel 3D extension of the famous harmonic phase tracking method. The point-wise phase-based optical flow tracking was combined with an anatomical regularization model in order to estimate spatially smooth and anatomically coherent myocardial motions. In particular, special efforts were made to ensure a reasonable radial strain estimate by enforcing myocardial incompressibility. The model was optimized by a window-weighted regression technique, which reduced the computation complexity by decomposing one global system into local ones that were computationally easier to solve. We tuned the model parameters based on tracking results on a synthetic tagged MR dataset. The proposed HarpAR algorithm was further evaluated on both healthy volunteers and patients with different levels of ischemia.

Second, we proposed a novel multi-modal simulation pipeline for generating realistic synthetic cardiac ultrasound, cine and tagged MR image sequences for the same virtual subject. Template ultrasound and MR acquisitions, the electro-mechanical model and physical US or MR simulators were combined in the framework. The heart geometry was segmented from the real cine MR images. The electro-mechanical model was used for simulating ground-truth myocardial deformation fields including both healthy and pathological

hearts. The template sequences were registered to the simulations by a novel warping technique aimed at ensuring a motion pattern consistent with the electro-mechanical model. Also, a Gaussian weighting function was proposed to alleviate the intensity transitions observed at the interface between the myocardium and the background. Finally, backscattering amplitudes and effective proton densities were derived from the warped templates respectively for ultrasound and MR simulations so as to exploit the corresponding physical simulators for generating image data. In total, we simulated 18 virtual patients (3 healthy, 3 dyssynchrony and 12 ischemia), each with one synthetic 3D cine MR sequence, one synthetic 3D echocardiography sequence and three channels of synthetic 3D tagged MR.

Finally, we showed a preliminary benchmarking study using the simulated images. We aimed to compare the performance of two motion tracking methods based on regional motion and strain accuracies. The HarpAR algorithm initially developed for handling the 3D tagged MR data was generalized, leading to a generic motion tracking algorithm named as gHarpAR. It was compared against another generic algorithm SparseDemons in terms of tracking and strain accuracies on all of the three modalities (US, cine MR, tagged MR). The results showed that SparseDemons outperformed gHarpAR in processing the cine MR images. This is because the myocardium is not marked in cine MR, a stronger regularization is therefore required. Since SparseDemons imposes a stronger regularization beyond the myocardial domain, it achieved better accuracies. On tagged MR, both methods obtained similar accuracies on motion and two strain components (circumferential and longitudinal). However, gHarpAR quantified much more accurately radial strains, thanks to the specific myocardial incompressibility constraint imposed at a window level. Based on the experiments, we realize that cardiac motion tracking solutions should be designed according to the specific image characteristics of the given modality, *e.g.* the quantification of myocardial deformation from cine MR would require an algorithm with a much stronger spatial regularization, compared to tagged MR and ultrasound.

7.2 Perspectives

In this thesis, our major contributions are two-fold: 1) we developed a fast 3D motion tracking algorithm for quantifying the multi-channel 3D acquisitions of tagged MR; and 2) we proposed a novel simulation pipeline for the generation of synthetic multi-modal (US, cine MR, tagged MR) image sequences for the same virtual subject. Both the tracking and the simulation are highly active research fields and there are still a lot of open questions to be further investigated.

First, for the motion tracking from tagged MR, despite adopting a multi-resolution framework aimed at handling large cardiac motions, *tag jumping* errors [Osman *et al.* (1999)] could still occur. From our experience, *tag jumps* usually take place at the lateral wall of the basal left ventricle where the longitudinal displacement between two neighboring frames could be relatively significant. Once the displacement is larger than one half of the

tag spacing, the tracking is likely to output errors of the order of the tag spacing. Although *tag jumping* is a widely acknowledged issue, there have been few relevant studies addressing this problem. It would be interesting to design specific techniques for correcting *tag jumps*. For us, it is one research topic worth pursuing research in tagged MR.

Second, as for the cardiac simulation and image synthesis, we simulated 18 virtual patients with synthetic multi-modal image sequences. Due to the limited time, we presented only a preliminary benchmarking study. A more detailed evaluation needs to be done in the future. Moreover, we only compared the performance based on synthetic images with a given level of quality close to the templates used. It would be more fair to assess the performance of motion tracking using a range of synthetic sequences with different levels of image quality as presented in a recent study [Heyde *et al.* (2016)b]. More specifically, by varying the parameters of the physical simulators involved in the pipeline, various artifacts and noises can be modeled, yielding synthetic images that cover a wide range of qualities. Benchmarking cardiac motion tracking across the full quality spectrum remains the objective of future work.

Finally, the simulated multi-modal virtual patients could be used for comparing the recently developed cine MR feature tracking against the conventional tagged MR quantification and the 3D speckle tracking. Recently, there is increasing research interest in investigating whether cine MR feature tracking can achieve strain estimates similar to those derived from tagged MR. On real patients, [Hor *et al.* (2010)] [Moody *et al.* (2013)] [Moody *et al.* (2015)] reported respectively that circumferential strain, longitudinal strain and systolic/diastolic global strain and strain rate measures calculated from cine MR feature tracking correlated highly with results derived from tagged MR. Similarly in [Onishi *et al.* (2013)], the authors showed that measurements of radial dyssynchrony computed from cine MR feature tracking showed reasonable agreement with those from speckle tracking echocardiography on patient data. However, all of the above studies merely showed that cine MR feature tracking quantified similar deformation values to tagged MR or speckle tracking echocardiography by showing the correlation between both results. Which modality outperformed the other, in which aspects and to which extent, is still unclear. We think it would be of great value to conduct a truly quantitative comparison using the simulated multi-modal synthetic sequences. This would allow evaluating cine MR feature tracking at a much more detailed level.

Résumé en français

Chapter 8

Résumé en français

I. Introduction

Chapitre 1. Introduction

1.1 Motivation

Les maladies cardiovasculaires sont parmi les principales causes de décès dans le monde et cette tendance devrait persister dans les années à venir [Mendis (2014)]. Un certain nombre de maladies cardiaques (hypertrophie, cardiomyopathie dilatée, infarctus du myocarde, etc) peuvent être identifiées et localisées par l'analyse du mouvement cardiaque et de la déformation cardiaque. En comparant les valeurs de déformation quantifiées avec celles de référence, les lésions myocardiques peuvent éventuellement être détectées. Afin de quantifier le mouvement et la déformation, un certain nombre de techniques d'imagerie ont été développées au cours des dernières décennies. Plusieurs modalités incluant l'échographie [Sheikh *et al.* (1991)], l'imagerie par résonance magnétique (IRM) cine [Sakuma *et al.* (1993)], l'IRM marquée [Axel and Dougherty (1989)a] et la tomodensitométrie [Ropers *et al.* (2003)] donnent accès aux images acquises au cours du cycle cardiaque. En conséquence, un certain nombre de méthodologies de suivi de mouvements ont été développées pour le post-traitement de ces acquisitions [Reisner *et al.* (2004)] [Osman *et al.* (2000)] [Florack *et al.* (2007)] [Hor *et al.* (2011)]. Ces dernières années, nous pouvons constater une augmentation du développement de techniques rapides d'imagerie cardiaque 3D. Par exemple, l'introduction de la technologie des transducteurs matriciels 2D a rendu possible l'imagerie par ultrasons volumétriques [Mor-Avi *et al.* (2011)]. De plus, en IRM marquée, une technique d'acquisition CSPAMM accélérée a été proposée où trois séquences de volumes ont été acquises dans un temps très rapide [Rutz *et al.* (2008)].

Les progrès réalisés sur les techniques d'imagerie ont stimulé les groupes de recherche à développer des algorithmes de suivi de mouvements adaptés à chaque modalité. Des algorithmes de suivi 3D ont été proposés dans [De Craene *et al.* (2011)] [Somphone *et al.* (2013)] [Heyde *et al.* (2016)a]. Le suivi des caractéristiques d'IRM cine [Hor *et al.* (2010)] [Hor *et al.* (2011)] [Maret *et al.* (2009)] a été développé pour la quantifica-

tion rapide de déformations myocardiques à partir des séquences d'IRM cine. Cependant, en ce qui concerne le protocole 4D IRM marquée à plusieurs canaux [Rutz *et al.* (2008)], beaucoup moins d'efforts de recherche ont été faits pour développer des outils de post-traitement correspondants [Shi *et al.* (2012)] [De Craene *et al.* (2011)]. Un algorithme de quantification efficace et rapide, bien adapté à ce protocole d'acquisition, est nécessaire afin de promouvoir l'utilisation de cette acquisition dans les recherches et les centres cliniques. En fait, malgré les réalisations récentes dans les technologies d'imagerie cardiaque 3D et les solutions de quantification associées, leur application en routine clinique est freinée par l'absence d'une validation solide. Des algorithmes du suivi de mouvements 3D doivent être soigneusement validés avant d'être transférés en routine clinique. La validation quantitative basée sur la déformation myocardique présente un grand intérêt car la déformation est utile pour la détection précoce des maladies cardiaques. Plusieurs groupes [De Craene *et al.* (2013)] [Prakosa *et al.* (2013)] [Alessandrini *et al.* (2015)] ont déjà travaillé pour cet objectif en générant des séquences d'IRM cine et échocardiographiques. Des algorithmes de suivi de mouvements ont ensuite été évalués sur des données synthétiques, par exemple à partir de l'analyse du suivi du speckle 3D [Alessandrini *et al.* (2016)]. Actuellement, peu de travaux ont été faits pour la synthèse en IRM marquée 3D. De plus, la plupart des stratégies de simulation existantes ont généré des images synthétiques pour une modalité d'imagerie donnée pour un même patient virtuel. Cependant, être capable de simuler des séquences synthétiques multimodales (échographie, IRM cine et IRM marquée) pour un même patient virtuel présenterait de nombreux avantages. Cela permettrait une validation plus complète des algorithmes de suivi de mouvements. Une telle base de données est utile afin de comparer la performance des différents algorithmes en fonction de la modalité utilisée.

1.2 Objectif

Dans ce contexte, les objectifs de cette thèse sont les suivants:

- Développement d'une méthodologie qui combine les avantages des algorithmes pour la quantification du mouvement et de la déformation cardiaques à partir des acquisitions de CSPAMM accéléré [Rutz *et al.* (2008)].
- Développement d'une base de données libre d'accès de séquences synthétiques d'images cardiaques multi-modales (échocardiographie, IRM cine et IRM marquée). L'une des premières applications de cette base de données synthétiques est de valider des algorithmes 3D de suivi de mouvements cardiaques.
- Réalisation d'une première étude de validation multimodale de la performance d'algorithmes de suivi de mouvement et de déformation à partir des séquences synthétiques générées.

II. Contexte

Chapitre 2. Suivi de mouvements cardiaques

Les maladies cardiovasculaires constituent la première cause de décès et devraient connaître une augmentation croissante dans les années à venir [Roth *et al.* (2015)]. On estime que 17,5 millions de personnes sont mortes de maladies cardiovasculaires en 2012, ce qui représente 31% de tous les décès dans le monde [Mendis (2014)]. En supposant des taux de croissance semblables, d'ici 2030, environ 23,6 millions de personnes mourront des maladies cardiovasculaires dans le monde [Wang and Amini (2012)].

Les maladies cardiaques, telles que l'ischémie myocardique et la dyssynchronie ventriculaire, peuvent être identifiées et localisées par l'analyse du mouvement et de la déformation cardiaque. Les premiers efforts ont utilisé l'implantation chirurgicale et le suivi des marqueurs radio-opaques avec l'imagerie par rayons X pour quantifier le mouvement ventriculaire dans des cœurs de chien [Garrison *et al.* (1982)]. De telles techniques sont invasives et affectent le motif de mouvement régional du cœur pendant le processus de suivi des marqueurs, ce qui n'est pas réalisable cliniquement. Avec l'avènement des techniques d'imagerie plus avancées, les techniques de diagnostic non invasives basées sur l'inspection d'images médicales ont été développées et ont été largement utilisées en routine clinique. Plusieurs modalités, comme l'échocardiographie [Sheikh *et al.* (1991)], l'imagerie par résonance magnétique et la tomographie cardiaque (CT) ont été appliquées à l'analyse de la fonction cardiaque [Mondillo *et al.* (2011)] [Osman *et al.* (1999)] [Tavakoli and Sahba (2014)]. À partir des images médicales acquises au travers de ces modalités, les médecins peuvent surveiller et évaluer la progression des maladies cardiovasculaires afin que des procédures efficaces pour le traitement de la maladie puissent être développées en conséquence.

Classiquement, la déformation cardiaque est évaluée à partir des images médicales par des inspections visuelles d'un expert, permettant d'attribuer un score de mouvement de la paroi à chaque segment myocardique. Cependant, une analyse manuelle du mouvement prend beaucoup de temps et est sujet à de la variabilité inter- et intra- observateur. Les logiciels de suivi automatique de mouvements peuvent réduire la charge de travail des cliniciens. De plus, les conditions médicales peuvent être interprétées plus objectivement. La plupart des algorithmes de suivi de mouvement évaluent la fonction cardiaque au travers de deux types d'indices: les indices globaux et les indices régionaux. Les indices globaux comprennent le volume de la cavité, la fraction d'éjection, etc. Ce sont des indices importants qui révèlent la performance du cœur en termes de transport de sang oxygéné au corps. Les indices régionaux, tels que la déformation et la torsion du ventricule gauche (VG) peuvent s'avérer bénéfiques pour le diagnostic de maladies [Wang and Amini (2012)]. La combinaison des analyses globales et régionales pourrait conduire à une évaluation plus fiable de la fonction cardiaque.

En ce qui concerne le suivi de mouvements, l'échocardiographie est l'une des modalités les plus utilisées en routine clinique. L'échographie est sûre car elle n'émet aucun rayonnement nausif pour le corps, temps réel, portable et beaucoup moins cher par rapport à l'IRM et à l'imagerie CT. Le bruit de speckle inhérent à l'imagerie par ultrasons peuvent être utilisés comme marqueurs naturels qui se déplacent avec le myocarde. Le motif de speckle demeure stables localement pendant quelques images successifs du cycle cardiaque. Par conséquent, le mouvement sous-jacent du myocarde peut être suivi de façon précise. La fraction d'éjection et les déformations locales du myocarde peuvent être dérivées du champ de mouvement. Récemment, avec le développement de la technologie

de transducteurs matriciels 2D, l'échocardiographie 3D devient de plus en plus fréquente dans les établissements cliniques [Alessandrini *et al.* (2015)]. Malgré la résolution temporelle réduite par rapport à l'échographie 2D, cette imagerie permet quand même une quantification des mouvements cardiaques [De Craene *et al.* (2013)]. L'IRM cine [Sakuma *et al.* (1993)] est considérée comme une modalité plus avancée pour évaluer les fonctions ventriculaires globales dans la routine clinique. Cette modalité présente des avantages par rapport à d'autres modalités telles que l'échocardiographie et l'IRM marquée [Axel and Dougherty (1989)a] en ce sens qu'elle fournit un contraste plus clair entre le myocarde et le sang. Ceci facilite la segmentation et le suivi des frontières du myocarde, c'est-à-dire l'endocarde et l'épicarde. Les indices globaux tels que la fraction d'éjection du ventricule gauche peuvent être calculés avec précision ce qui permet une évaluation élémentaire de la fonction cardiaque. Il est plus reproductible que l'échocardiographie car les tissus présentent un meilleur contraste et sont donc naturellement plus facile à segmenter. Cependant, une autre caractéristique de cette modalité est que les intensités des pixels dans le myocarde est quasi constante, rendant difficile la quantification des indices locaux tels que le mouvement et la déformation. À part l'échographie, l'IRM marquée [Axel and Dougherty (1989)a] est une autre technique d'imagerie capable de quantifier les déformations locales. Dans cette modalité, une préparation de tagging est composée avec l'imagerie MR conventionnelle afin de créer des marqueurs (tags) en saturant les aimantations tissulaires. Les tags générés se déplacent en suivant le mouvement du myocarde sur toute la séquence. Les champs de déformation peuvent donc être reconstruits à partir du suivi de ces marqueurs virtuels. L'IRM marquée est considérée comme l'imagerie de référence pour l'estimation de déformations régionales car elle fournit l'information la plus riche sur le mouvement local. Cependant, son utilisation en clinique est freinée par le long temps d'acquisition et la résolution spatiale limitée pour distinguer les tissus.

Malgré l'évolution rapide des techniques d'imagerie et des méthodes de suivi de mouvements associées, le diagnostic et la détection des maladies cardiaques par quantification d'indices globaux et/ou locaux est généralement limité au 2D. Ainsi, le suivi des différentes structures souffre des mouvements hors-plan. Plus précisément, seule la projection du mouvement sur le plan image est capturé. Les indices globaux et régionaux sont ensuite calculés à partir des projections du mouvement et ne peuvent donc pas représenter les vraies déformations. Pour contourner ce problème, de nombreux efforts ont été faits pour développer des techniques d'imagerie 3D. La quantification du mouvement et de la déformation en 3D est capable de capturer les vraies valeurs de déformations. Cependant, à l'heure actuelle, les algorithmes du suivi du mouvement 3D sont rarement utilisés en routine clinique à cause d'un manque de validations rigoureuses. L'utilité de ces algorithmes de suivi de mouvements repose fortement sur la fiabilité et la robustesse de l'estimation des indices quantifiés. Pour discuter de l'importance de la validation dans le contexte des mouvements cardiaques et des indices de déformations, nous décrirons les principales stratégies existantes dans un chapitre dédié (Chapitre 3) ainsi que nos contributions proposées pour l'élaboration d'un cadre multimodal pour la validation (Chapitre 5).

2.1 Echocardiographie

L'échocardiographie est la modalité d'imagerie la plus utilisée en routine clinique pour le suivi et le diagnostic de maladies cardio-vasculaires. Cette modalité permet d'extraire à la fois des informations anatomiques (taille et forme du cœur) et des informations fonctionnelles (déformation régionales). La combinaison de ces deux sources d'informations fournit une aide précieuse aux cliniciens afin de diagnostiquer d'éventuelles pathologies car-

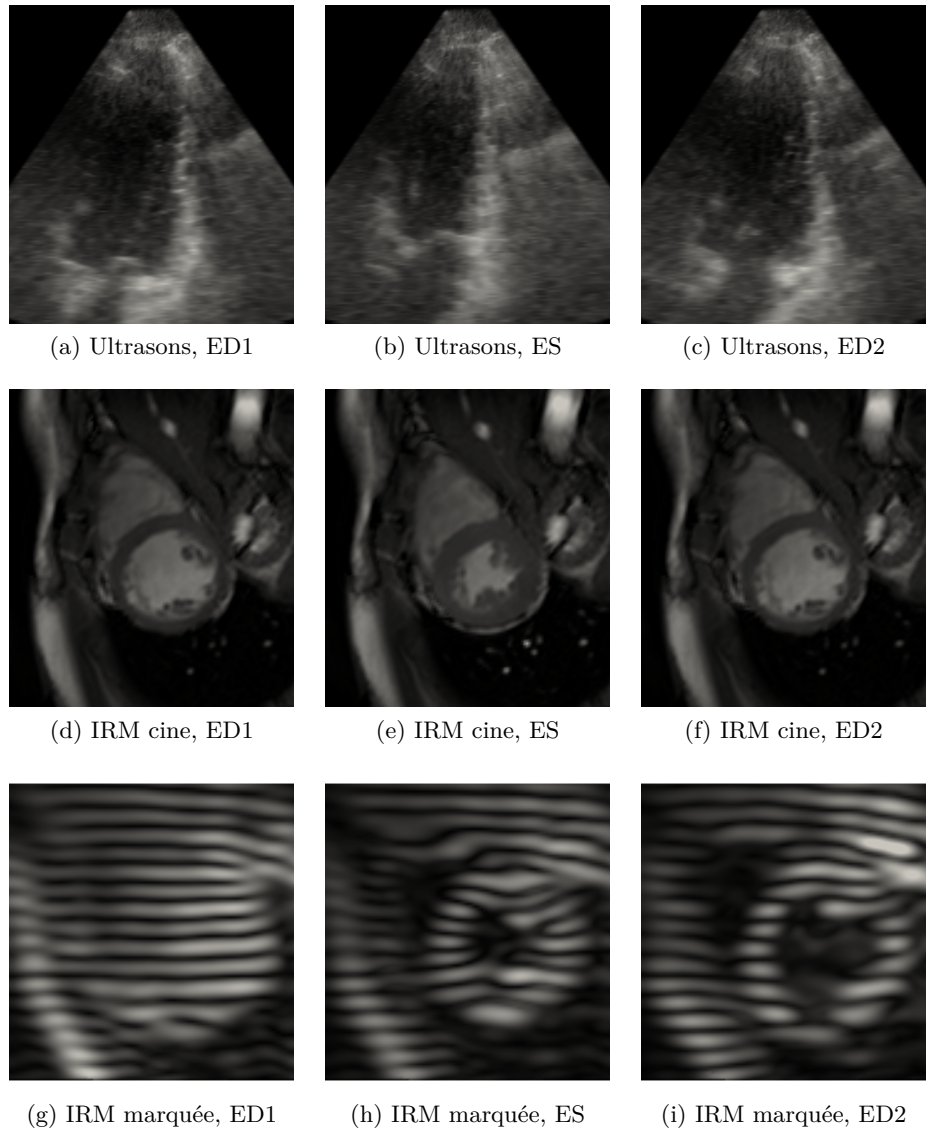


Figure VF.1: Les trois modalités d'imagerie utilisées pour évaluer la fonction cardiaque.

diaques. Dans la section suivante, nous donnons une description synthétique de l'imagerie échocardiographique ainsi que des algorithmes de suivi de mouvement adaptés à cette modalité.

2.1.1 Caractéristique des images

En échocardiographie, les techniques de speckle tracking (STE) sont des méthodes basées sur le suivi du motif de speckle au cours de la déformation du myocarde. Cette technique a d'abord été appliquée en 2D pour l'estimation des déformations du myocarde [O'Donnell *et al.* (1994)] [Reisner *et al.* (2004)]. La STE représente une méthode non invasive d'évaluation des déformations cardiaques régionales, outil précieux pour la caractérisation et la quantification des déformations locales du myocarde.

Le motif de speckle provient de la sommation aléatoire d'interférences accoustiques dues à des phénomènes de réflexions, réfraction et de diffusion [Reisner *et al.* (2004)].

Ainsi, chaque région du myocarde possède un motif de speckle unique qui peut être suivi au cours du mouvement. Le motif de speckle peut donc être vu comme un marqueur accoustique naturel permettant d'estimer les indices globaux et locaux du myocarde.

Récemment, l'introduction de la technologie de transducteurs matriciels 2D a rendu possible l'imagerie volumétrique 3D en temps réel [Alessandrini *et al.* (2015)]. L'émergence de cette imagerie volumétrique résout les défauts intrinsèques de la modalité 2D standard, comme la présence d'un mouvement hors plan, les problèmes de sélection optimale des coupes et le besoin d'hypothèses géométriques [Alessandrini *et al.* (2016)]. En suivant le mouvement du myocarde en 3D, la fonction cardiaque régionale peut être évaluée. En conséquence, beaucoup d'efforts de recherche ont été consacrés ces dernières années au développement des algorithmes de suivi du speckle en 3D. Nous présentons quelques-unes des méthodes les plus représentatives dans le paragraphe ci-dessous.

2.1.2 Suivi du speckle

Au cours de la dernière décennie, plusieurs techniques de suivi 3D ont été développées afin de quantifier des déformations cardiaques régionales en 3D. Ces méthodes peuvent être classées en quatre catégories. Nous ne présentons dans cette partie qu'une description synthétique de ces méthodes. Une analyse plus détaillée de l'état de l'art sur le suivi du speckle en imagerie US 3D est fournie dans les deux publications récentes [De Craene *et al.* (2013)] et [Alessandrini *et al.* (2016)].

Block matching

Block matching en mode B Les algorithmes de Block matching tels que [Duan *et al.* (2009)b] et [Crosby *et al.* (2009)] représentent les implémentations classiques sur de nombreux systèmes commerciaux. Dans ces approches, le tissu myocardique est divisé en blocs qui sont suivis tout au long du cycle cardiaque. Pour chaque bloc local, une recherche exhaustive est effectuée sur une fenêtre de recherche prédéfinie afin de trouver le patch le plus semblable dans l'image suivante. La similitude peut être définie de plusieurs manières. Par exemple, dans [Duan *et al.* (2009)b], les auteurs ont choisi la corrélation croisée normalisée. Les déplacements en patchs indépendamment suivis sont ensuite régularisés par l'interpolation et le filtrage, afin d'assurer une estimation régulière du mouvement myocardique.

Block matching en RF Le même concept a été appliqué aux données brutes dite de radiofréquence (RF) (signal modulé obtenu directement en sortie de la sonde avant des étapes de post-traitements). Dans [Lopata *et al.* (2011)] et [Chen *et al.* (2005)], la méthode de Block matching a été appliquée sur des images RF. Les deux études ont montré que les déformations cardiaques raisonnables pouvaient être estimées. Cependant, l'application du block matching à partir des images RF ne peut traiter que des déformations de l'ordre de la longueur d'ondes (quelques dixièmes de millimètre) [Chen *et al.* (2005)]. Les systèmes commerciaux 3D échocardiographiques actuels ont une résolution temporelle relativement faible ce qui entraîne donc des déformations relativement importantes entre deux volumes consécutifs. Les applications des méthodes basées sur l'image RF en routine clinique ne sont donc pas encore d'actualité.

Flux optique

Flux optique basé sur l'intensité Le flux optique a été appliqué au suivi de contours en échographie 3D [Duan *et al.* (2006)]. En supposant que l'intensité d'un point particulier d'un motif en mouvement ne change pas au cours de la séquence d'images, les vecteurs

de mouvement locaux sont résolus soit localement sur des patchs d'image indépendants, soit globalement en utilisant des termes de fluidité spatiale en tant que régularisation. Les algorithmes des démons représentent une simplification du problème du flux optique [Thirion (1998)] [Somphone *et al.* (2013)].

Flux optique basé sur la phase Le flux optique a été appliqué non seulement aux intensités en mode B mais aussi aux images de phases [Alessandrini *et al.* (2012)a] [Alessandrini *et al.* (2013)]. Alessandrini et al. [Alessandrini *et al.* (2013)] ont choisi d'effectuer le suivi du flux optique sur des phases monogéniques calculées à partir des images d'intensité ultrasonores. Ils ont montré que le déplacement estimé à partir de la phase monogénique était robuste aux variations possibles d'énergie locale. De grandes déformations ont été estimées en appliquant de façon récursive la méthode d'estimation de mouvements dans un schéma de raffinement pyramidal.

Recalage élastique

Le recalage élastique d'images fournit une autre méthode pour calculer un champ de déformation lisse et dense à partir des séquences d'images ultrasonores cardiaques 3D [De Craene *et al.* (2011)] [Heyde *et al.* (2016)a]. Le champ de mouvement cardiaque est efficacement représenté par un ensemble de fonctions de base B-spline. Les modèles de déformation difféomorphique sont ensuite utilisés pour recaler les images échocardio-graphiques dans le temps.

2.2 IRM cine cardiaque

L'IRM cine cardiaque [Sakuma *et al.* (1993)] est considérée comme la modalité de référence pour évaluer la fonction cardiaque globale en quantifiant des indices tels que la fraction d'éjection. Les études d'IRM cine sont généralement effectuées en 2D (visualisation d'un plan de coupe 2D au cours du cycle cardiaque). Les méthodes dites ECG gating rétrospective [Fischer *et al.* (1993)] sont réalisées afin d'affecter une image acquise à la phase du cycle cardiaque correspondante.

2.2.1 Caractéristique des images

La séquence d'impulsions de base utilisée pour acquérir des données d'IRM cine est typiquement une méthode d'écho en gradient en état d'équilibre (bSSFP) [Scheffler and Lehnhardt (2003)]. Cette technique génère un signal intra-vasculaire élevé par rapport à d'autres tissus en raison du rapport T2/T1 intrinsèquement élevé du sang. Cette caractéristique permet aux cliniciens de distinguer le myocarde des tissus voisins. De plus, la structure de la séquence bSSFP permet d'utiliser des valeurs TR et TE très petites, de sorte que de multiples échos peuvent être acquis pendant une seule période cardiaque.

L'IRM cardiaque est utilisée en clinique en raison de son contraste élevé des tissus mous. L'endocarde et l'épicarde peuvent être segmentés avec précision. La résolution temporelle est également suffisamment élevée pour effectuer un suivi de mouvements au cours du cycle cardiaque. En suivant les frontières du myocarde, les indices globaux tels que la fraction d'éjection du ventricule gauche sont facilement quantifiés. Cette imagerie est largement acceptée en tant que modalité de référence pour la quantification de la fonction cardiaque globale. Cependant, comme nous pouvons le voir dans la Fig. VF.1, à l'intérieur du muscle, l'IRM cine produit des intensités pratiquement constantes. Contrairement à l'échographie, l'IRM cine ne produit pas de marqueur naturel permettant de suivre des régions à l'intérieur du myocarde. Dans une certaine mesure, cela augmente la

difficulté à quantifier les déformations cardiaques locales. Cependant, à l'aide des régularisations spatiales, des déformations régionales du myocarde peuvent cependant être estimées comme cela a été démontré dans plusieurs publications [[Shi et al. \(1999\)](#)] [[Lin and Duncan \(2004\)](#)]. Dans les paragraphes suivants, nous décrivons brièvement l'état de l'art en suivi de mouvement à partir des séquences IRM cine.

2.2.2 Suivi de mouvements cardiaques à partir des images IRM cine

Comme mentionné ci-dessus, les caractéristiques les plus couramment utilisées en IRM cine sont des contours endocardiques et épicardiques. Ils sont segmentés à la fin de la diastole et suivis au cours du cycle cardiaque. Pour l'analyse de mouvements à partir de l'IRM cine, une stratégie peut consister à parcourir d'abord des points de caractéristiques et ensuite à calculer des déformations myocardiques. L'autre stratégie consiste à utiliser directement les algorithmes de recalage afin de recaler toutes les images de la séquence à une référence. Ensuite, les déformations cardiaques peuvent être déduites à partir de la transformation estimée.

Feature tracking

Hor et al. [[Hor et al. \(2010\)](#)] [[Hor et al. \(2011\)](#)] ont développé une méthode de suivi des caractéristiques d'IRM cine. Les bordures endocardiques et épicardiques sont tout d'abord tracés manuellement en fin diastole. Les frontières myocardiques sont alors propagées automatiquement au travers du cycle cardiaque en faisant correspondre les motifs qui représentent des structures anatomiques [[Hor et al. \(2011\)](#)]. Les déformations myocardiques sont ensuite calculées à partir du champ de mouvement estimé. De même, Maret *et al.* [[Maret et al. \(2009\)](#)] ont proposé de suivre les frontières du myocarde à partir des images IRM cine. Ils ont montré que le déplacement et la déformation dans les directions radiales et longitudinales peuvent être utilisés pour détecter des lésions transmurales du myocarde. Dans [[Moody et al. \(2015\)](#)], les auteurs ont comparé la déformation quantifiée à partir d'IRM cine avec des résultats estimés à partir d'IRM marquée. Ces auteurs ont montré que les méthodes fournissent des résultats corrélés à partir de modalités d'imagerie différentes.

Méthodes basées sur le recalage Certaines méthodes considèrent le suivi de mouvement comme un problème de recalage non rigide. Les algorithmes correspondant sont basés sur l'estimation des champs de transformation non linéaire. Perperidis *et al.* [[Perperidis et al. \(2005\)](#)] ont proposé deux méthodes de déformation libre basées sur les fonctions de base de B-spline pour recaler des images IRM cine cardiaques. Tsadok *et al.* [[Tsadok et al. \(2016\)](#)] ont appliqué le recalage non rigide aux images IRM cine et ont observé que les estimations de la déformation longitudinale étaient fortement corrélées avec les résultats obtenus à partir d'IRM marquée et d'échographie.

2.3 IRM marquée cardiaque

L'IRM marquée est une technique spécifique pour estimer des déformations locales du tissu [[Axel and Dougherty \(1989\)a](#)]. Dans les applications cardiaques, le motif de tagging se déplace avec le myocarde et reste localement stable pendant le cycle cardiaque. Cela permet la quantification des déformations myocardiques et l'évaluation des fonctions cardiaques locales.

2.3.1 Caractéristique des images

Le tissu est marqué en appliquant une impulsion de radiofréquence spatialement modulée avant la procédure d'imagerie IRM [Zerhouni *et al.* (1988)]. Comme l'aimantation représente une propriété caractéristique du tissu, les régions saturées se déplacent avec le tissu sous-jacent et s'affichent sous la forme de lignes plus sombres dans les images acquises (Fig. VF.1).

2.3.2 Suivi de mouvements à partir des images IRM marquées

Depuis son introduction dans les années 1980, l'IRM marquée cardiaque a stimulé le développement de méthodes de quantification de déformation. Certaines d'entre elles ont été spécialement conçues pour l'IRM marquée. D'autres correspondent à des méthodologies génériques qui ont été appliquées aux images d'IRM marquées.

Méthodes génériques

Parmi ces méthodes génériques, le recalage basé sur l'intensité par flux optique ou par la technique dite Free Form Deformation (FFD) a été appliqué aux images IRM marquées. Chandrashekara *et al.* [Chandrashekara *et al.* (2004)] ont appliqué le FFD multiniveau au post-traitement des images d'IRM marquée. De Craene *et al.* [De Craene *et al.* (2011)] ont appliqué le FFD temporelle difféomorphique à l'analyse d'IRM marquée, ce qui donne lieu à une régularisation temporelle du champ de mouvement. Prince *et al.* [Prince and McVeigh (1992)] ont développé une méthode de flux optique avec la compensation de l'effet de tag fading. Florack *et al.* [Florack *et al.* (2007)] ont développé une méthode de flux optique appliquée aux images de phase qui sélectionne automatiquement une échelle optimale.

Les méthodes de recalage génériques sont robustes et ont été appliquées à beaucoup de modalités cardiaques. La plupart des méthodes basées sur le recalage ont été appliquées à une grille de tags obtenue en combinant toutes les acquisitions d'IRM marquée en une seule séquence. Cependant, ils ne profitent pas de l'encodage directionnel des acquisitions d'IRM marquées. Des images d'IRM marquées sont acquises dans plusieurs directions qui fournissent différents canaux. Cette caractéristique peut potentiellement surmonter le problème d'ouverture (aperture) du flux optique monocanal.

Méthodes spécifiques développées pour l'IRM marquée

Toutes les méthodes qui exploitent les spécificités de l'IRM marquée peuvent être classifiées en quatre catégories. Ces catégories sont plutôt séparées, ouvrant ainsi la possibilité de combiner leurs avantages respectifs. De plus, la plupart de ces méthodes ont été appliquées seulement à l'IRM marquée 2D. L'adaptation à la 3D est actuellement à un stade préliminaire ou s'est concentrée sur l'acquisition multiplanaire [Liu *et al.* (2012)]. Peu d'approches traitent les images acquises par le protocole d'acquisition volumétrique proposé par Rutz *et al.* [Rutz *et al.* (2008)].

Méthodes basées sur la détection

Une première approche proposée par Young *et al.* [Young (1999)] et Amini *et al.* [Amini *et al.* (2001)] consiste à détecter d'abord les plans de tag, puis de suivre ces caractéristiques extraites. Amini *et al.* [Amini *et al.* (2001)] ont détecté des plans de tag par des surfaces de B-spline. Young *et al.* [Young *et al.* (1995)] ont utilisé un modèle de contour actif pour suivre les lignes de tags dans les images puis pour interpoler un mouvement 3D par un

modèle d'éléments finis. Dans [Young (1999)], les bandes de tags ont été détectées par un filtre gaussien et suivies par un algorithme de recherche de ligne. Les déplacements obtenus ont été régularisés par un modèle d'éléments finis défini dans les directions radiales, longitudinales et circonférentielles. Chen et al. [Chen et al. (2010)] ont appliqué des filtres de Gabor pour détecter des intersections de tags qui sont utilisées pour initialiser un modèle déformable.

HARP

HARP [Osman et al. (1999)] est une autre méthode d'IRM spécifique qui est devenue une référence dans cette modalité. Une première étape dans HARP est de calculer des images de phase. Elles sont calculées en appliquant un filtre passe-bande dans le domaine de Fourier. Dans le domaine spatial, le suivi est alors effectué sur des images de phase. La raison principale pour substituer l'intensité par la phase est d'améliorer la robustesse par rapport au tag fading. Le suivi peut être interprété comme un flux optique réalisé conjointement sur deux "canaux", chaque canal correspondant à un sens de marquage. Comme le nombre de directions de marquage est égal au nombre de composantes du champ de déplacement, le problème d'ouverture disparaît simplement. Cependant, contrairement aux algorithmes traditionnels du flux optique, HARP n'intègre aucune régularisation spatiale. Comme la déformation est calculée à partir des dérivées spatiales du champ de mouvement, les valeurs aberrantes de mouvement vont produire des erreurs élevées sur la déformation.

SinMod

La méthode SinMod [Arts et al. (2010)] a récemment émergé comme une alternative à HARP. Dans l'environnement local de chaque pixel, la distribution d'intensité est modélisée comme une onde sinusoïdale. Ensuite, la fréquence locale et le déphasage entre deux images consécutives sont calculés. Le rapport des deux valeurs donne une estimation de déplacement dans la direction de marquage. Il a été montré que la méthode SinMod était aussi rapide que HARP et surpassait HARP dans la précision de l'estimation et la robustesse au bruit d'image. Cependant, la capacité de suivre un grand mouvement myocardique (supérieur à la moitié de l'espacement de tags) reste à vérifier. De plus, l'absence de régularisation spatiale rend l'estimation de déformation très sensible aux erreurs de suivi.

Méthodes de Gabor

Qian et al. [Qian et al. (2011)] ont proposé de calculer la déformation directement à partir des images sans faire le suivi de mouvements. L'idée est de filtrer les images d'intensité au travers d'un banc de filtres Gabor pour estimer l'orientation locale et la fréquence locale. Cela donne accès à la déformation du tissu, sans avoir besoin de calculer les déplacements. Ce concept a été étendu par Kause et al. Dans [Kause et al. (2014)] où le gradient de déformation a été directement évalué à partir du champ de vecteurs fréquentiels. Les auteurs affirment que ceci rend leur technique d'estimation de déformation indépendante à tout résultat de suivi. Cependant, ils négligent le fait qu'un suivi reste nécessaire pour montrer l'évolution de déformation d'un point matériel au cours du cycle cardiaque.

2.4 Résumé

Dans ce chapitre, nous avons présenté le contexte clinique du suivi de mouvements cardiaques. Le suivi de déformations cardiaques à partir des images médicales aide à la fois la détection et la planification du traitement des maladies cardiaques. Nous avons fait une brève introduction sur plusieurs modalités d'imagerie. Parmi elles, l'IRM cine est la référence pour évaluer la fonction cardiaque globale via des indices tels que le volume

du ventricule et la fraction d'éjection. Lorsqu'il s'agit d'évaluer la fonction régionale, l'échocardiographie et l'IRM marquée sont les deux modalités préférées. Les deux se basent sur des marqueurs locaux pour suivre le mouvement du myocarde. Le suivi des marqueurs (speckles ou tags) dans le cycle cardiaque permet d'estimer le mouvement cardiaque sous-jacent. Bien qu'un certain nombre de méthodes de quantification 3D aient été développées ces dernières années, leur utilisation en routine clinique est freinée par l'absence d'une validation solide. Les logiciels du suivi de mouvements développés pour l'IRM marquée doivent être validés avant d'être transférés en clinique. La validation du suivi de mouvements cardiaques est elle-même un domaine de recherche très actif que nous introduisons dans le chapitre 3.

Chapitre 3. Validation du suivi de mouvements cardiaques

3.1 Introduction

Nous avons déjà introduit dans le chapitre 2 que la détection des maladies à un stade précoce contribuerait à réduire le taux de mortalité. En fait, le diagnostic des maladies cardiovasculaires a été beaucoup amélioré par le développement des techniques d'imagerie cardiaque ces dernières années. L'analyse du mouvement et de la déformation cardiaque à partir d'images médicales révèle des informations importantes pour analyser l'étendue d'infarctus, les problèmes de dyssynchronie, les problèmes de remplissage anormal causés par des pressions altérées *etc.* Des progrès importants ont été réalisés en échographie (US) et imagerie par résonance magnétique (IRM) au cours des dernières décennies. En ce qui concerne l'US, l'imagerie volumétrique 3D est désormais possible, grâce à l'introduction de la technologie de transducteurs matriciels 2D [Mor-Avi *et al.* (2011)]. L'IRM cine cardiaque est utilisée en routine clinique pour évaluer la fonction cardiaque globale. L'IRM marquée est la séquence IRM qui fournit l'information la plus détaillée sur la déformation locale du tissu [Axel *et al.* (2005)]. Elle est considérée comme la modalité d'imagerie de référence pour la quantification du mouvement et de la déformation. Néanmoins, son utilisation en routine clinique est freinée par le manque d'outils de post-traitement fiables, ainsi que par sa résolution spatiale limitée pour distinguer des structures fines.

Malgré ces développements en imagerie, l'évaluation de la fonction cardiaque est généralement limitée aux mesures globales, telles que la fraction d'éjection (FE) et le volume du ventricule [Alessandrini *et al.* (2015)]. Les index locaux tels que la déformation régionale sont rarement utilisés malgré leur utilité pour la détection précoce des maladies cardiaques [De Craene *et al.* (2013)]. Ceci s'explique par le fait qu'il manque une validation solide en ce moment, malgré l'existence d'un grand nombre d'algorithmes de suivi de mouvements développés en US [Alessandrini *et al.* (2016)], en IRM cine [Maret *et al.* (2009)] et en IRM marquée [Zhou *et al.* (2015)]. Une validation quantitative de ces méthodes basée sur les mesures de déformation représenterait donc un progrès majeur.

Afin de valider les algorithmes de suivi de mouvements, on peut d'abord penser à l'utilisation de vérités terrain générées manuellement par les experts, de manière similaire à la stratégie utilisée pour valider les algorithmes de segmentation. Cependant, contrairement à la segmentation cardiaque qui est généralement effectuée à un seul instant où les experts tracent les contours du cœur, les repères myocardiques doivent être suivis au cours de tout le cycle cardiaque afin de générer des trajectoires de référence pour la validation. Cette tâche est fastidieuse et est sujette aux variabilités inter et intra-expert. Par conséquent, la plupart des groupes de recherche se sont tournés vers d'autres alternatives plus automatiques que nous présentons dans les sections suivantes.

3.2 Utilisation des techniques d'imagerie comme référence

Une première option est de se baser sur des méthodes d'imagerie dédiées qui sont capables de mesurer directement les déplacements myocardiques. Par exemple, l'imagerie tissulaire Doppler [Ho and Solomon (2006)] et la DENSE MR [Aletras *et al.* (1999)] a été développé pour mesurer directement la vitesse et le déplacement. Cependant, ces méthodes ne sont pas largement utilisées en clinique (pour le cas du DENSE MR) ou ne donnent accès qu'à des composantes limitées du champ de mouvement (pour le cas du Doppler tissulaire où seule la vitesse dans la direction du champs ultrasonore est disponible).

D'autres études comme [Duan *et al.* (2009)b] et [Yeon *et al.* (2001)] ont utilisé la sonomicrométrie pour mesurer directement les déformations du myocarde. Cependant, la

sonomicrométrie nécessite l'implantation de cristaux piézoélectriques dans le myocarde, et est donc trop invasive pour une utilisation clinique. De plus, la résolution spatiale des déformations mesurées est proportionnelle au nombre de cristaux piézoélectriques installés dans le cœur. Normalement, on n'utilise qu'un nombre limité de cristaux. Un champ dense de la vérité de terrain n'est donc jamais disponible. De plus, le recalage multimodal est très difficile parce que les tissus sont imagés différemment. Tout cela pose un défi pour la validation.

3.3 Imagerie des fantômes physiques

Plusieurs groupes de recherche ont construit un modèle du cœur physique pour la validation [[Tobon-Gomez et al. \(2011\)a](#)] [[Boltz et al. \(2010\)](#)]. Le modèle a une géométrie similaire au cœur et est mécaniquement contrôlé. La plupart des fantômes mécaniques simulent des mouvements simples (contraction et torsion). Les mouvements sont modulés et combinés pour générer différents motifs de déformation. Le fantôme peut être imaginé par différentes modalités d'imagerie. Les algorithmes de suivi de mouvements cardiaques sont évalués en utilisant ces acquisitions réelles. La vérité de terrain est contrôlée et donc accessible. Malgré les divers avantages de ces fantômes physiques, cette stratégie présente plusieurs limitations. Premièrement, dans la pratique, avoir un champ dense de mouvement pour la vérité de terrain est assez difficile. Nous devons connaître les propriétés des matériaux et modéliser des déformations tissulaires de manière très précise. Deuxièmement, le mouvement cardiaque simulé par ces fantômes physiques est rarement aussi complexe que le cœur réel. De plus, il n'est pas simple de simuler différents niveaux de pathologies. Finalement, nous ne voyons généralement que le cœur dans les images acquises. Toutes les structures d'arrière-plan sont manquantes. En effet, une texture réaliste avec des structures d'arrière-plan et les artefacts d'imagerie pose un défi pour les algorithmes de suivi de mouvements. Les images acquises à partir des fantômes physiques ne peuvent donc pas répondre aux véritables défis auxquels sont confrontés les algorithmes de suivi.

3.4 Génération d'images synthétiques

Outre les deux alternatives présentées ci-dessus, une autre repose sur les simulations numériques pour valider le suivi de mouvements cardiaques. L'utilisation des images synthétiques peut aider à évaluer la performance des méthodes du suivi de mouvements. En fait, un certain nombre de groupes de recherche ont déjà travaillé pour atteindre cet objectif. Les séquences synthétique d'US [[Alessandrini et al. \(2015\)](#)] [[Prakosa et al. \(2013\)](#)] [[Glatard et al. \(2013\)](#)], d'IRM cine [[Prakosa et al. \(2013\)](#)] [[Glatard et al. \(2013\)](#)] et d'IRM marquée [[Clarysse et al. \(2011\)](#)] ont été générées. Ces travaux sont tous basés sur la simulation d'images synthétiques pour une modalité d'imagerie spécifique. L'intérêt d'utiliser des images synthétiques a été bien détaillé dans plusieurs études [[Alessandrini et al. \(2015\)](#)] [[Prakosa et al. \(2013\)](#)]. Leur principal avantage est la possibilité directe d'évaluer la précision des algorithmes en comparant leur performance à la vérité de terrain. Cependant, l'utilité de ces séquences synthétiques dépend du niveau de réalisme des simulations. Beaucoup d'efforts ont été faits pour améliorer le réalisme des images synthétiques cardiaques.

3.4.1 Simulation des images IRM cine

Tobon-Gomez et al. [Tobon-Gomez *et al.* (2011)b] et Wissmann et al. [Wissmann *et al.* (2014)] ont simulé des séquences d’images IRM cine en utilisant le fantôme XCAT [Segars *et al.* (2010)]. Dans [Tobon-Gomez *et al.* (2011)b], une segmentation tissulaire (ou étiquetage) a été réalisée. Les différents types de tissus sont associés à des valeurs de T1, T2 et densité de protons (PD) obtenues à partir de la littérature. Les cartes statiques T1, T2 et PD à la fin de la diastole (ED) ont ensuite été déformées par le mouvement cardiaque du fantôme XCAT. Enfin, à chaque instant, un simulateur d’IRM [Kwan *et al.* (1999)] a été utilisé pour générer des images IRM cine. Wissmann et al. [Wissmann *et al.* (2014)] ont simulé directement les intensités d’image par les équations de signal. Ils affirment que ce choix facilite la simulation des stratégies d’échantillonnage, l’optimisation de la trajectoire et les méthodes de post-traitement [Wissmann *et al.* (2014)]. Haddad et al. [Haddad *et al.* (2007)] et Glatard et al. [Glatard *et al.* (2013)] ont également synthétisé des images IRM cardiaques. Ils ont adopté une approche similaire à celle présentée dans [Tobon-Gomez *et al.* (2011)b] se basant sur la combinaison d’un modèle de mouvement avec un simulateur IRM. La principale différence réside dans le modèle, qui est extrait des acquisitions réelles comme décrit dans [Haddad *et al.* (2005)]. Prakosa et al. [Prakosa *et al.* (2013)] a développé un pipeline qui combine un modèle électromécanique (E/M) du cœur avec des acquisitions de modèle pour générer les images IRM cine. La séquence IRM cine a été recalée à un instant de référence, donnant une séquence quasi-statique. Cette séquence a ensuite été déformée par la simulation E/M pour créer des images synthétiques. Les images synthétiques générées dans certaines des études mentionnées ci-dessus sont montrées dans la Fig. VF.2.

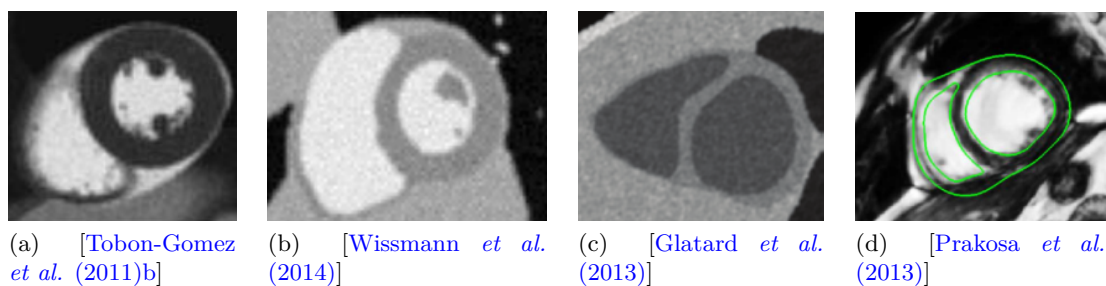


Figure VF.2: Quelques résultats représentatifs en simulation d’images IRM cine.

3.4.2 Simulation des images IRM marquées

Par rapport à l’IRM cine, relativement peu de travaux ont été faits pour la simulation d’IRM marquée cardiaque. Crum et al. [Crum *et al.* (1997)] ont simulé le ventricule gauche dans des coupes à axe court. Ils ont modélisé l’anatomie correspondante en utilisant une forme d’anneau. En utilisant un mouvement calculé à partir d’une séquence d’IRM cine, les auteurs ont déformé la première image à tous les instants du cycle cardiaque. Le modèle de marquage a été simulé en appliquant une fonction de modulation sinusoïdale dans le domaine spatial. Plus tard dans [Crum *et al.* (1998)], les auteurs ont amélioré la génération de profils d’intensité par un modèle de domaine fréquentiel. De même, Waks et al. [Waks *et al.* (1996)] ont utilisé un système de coordonnées sphéroïde/prolate pour simuler la géométrie de ventricule et un modèle de 13 paramètres pour simuler le mouvement. Les paramètres du modèle ont été déterminés par une optimisation au sens

des moindres carrés. Sermesant et al. [Sermesant *et al.* (2006)] ont segmenté le myocarde à partir d'une image réelle d'IRM marquée et ajouté les lignes de tags au masque binaire. Enfin, cette image a été déformée par les mouvements cardiaques générés par le modèle E/M. Clarysse et al. [Clarysse *et al.* (2011)] ont déformé une image IRM marquée (axe court) par un modèle de mouvement cardiaque. Cependant, le modèle de mouvement était trop simpliste pour représenter la complexité du vrai mouvement du cœur. Nous montrons dans la Fig. VF.3 quelques-unes des images simulées.

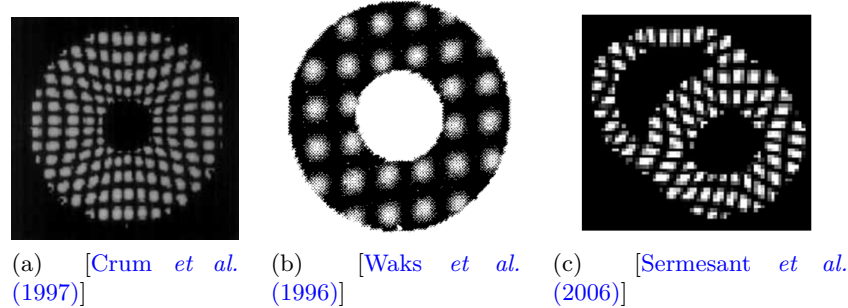


Figure VF.3: Quelques résultats représentatifs en simulation d'images IRM marquées.

3.4.3 Simulation des images ultrasonores

Quant à la simulation des images échocardiographiques, Alessandrini et al. [Alessandrini *et al.* (2015)] ont déjà donné une analyse assez complète. En conséquence, nous ne présentons ici qu'une brève introduction sur certaines des études les plus représentatives liées à cette thèse. Alessandrini et al. [Alessandrini *et al.* (2012)b] ont combiné une séquence type avec un simulateur physique d'US pour générer des données synthétiques. Le mouvement cardiaque dans la séquence type a d'abord été suivi par le recalage d'image. La séquence type est alors alignée spatio-temporellement avec un modèle de mouvement. Dans une dernière étape, ils ont utilisé un simulateur physique d'US pour gérer des images synthétiques afin d'atténuer les artefacts de recalage d'images. Prakosa et al. [Prakosa *et al.* (2013)] ont aussi combiné un modèle E/M avec quelques séquences type. Les séquences type ont été alignées avec les simulations générées par le modèle E/M. Les images produites présentent des textures réalistes, mais les artefacts introduits par le recalage réduisent le réalisme des données synthétiques. Pour atténuer les artefacts de recalage, De Craene et al. [De Craene *et al.* (2013)] ont utilisé un simulateur physique d'US. Cependant, ils n'intègrent aucune acquisition réelle dans le pipeline et le modèle de speckle utilisé est simpliste (c'est-à-dire une intensité speckle élevée à l'intérieur du muscle et une faible intensité à l'extérieur), conduisant à des images synthétiques binaires qui ne sont pas suffisamment réalistes. Alessandrini et al. [Alessandrini *et al.* (2015)] ont combiné le modèle E/M, le simulateur physique d'US et des séquences de modèle dans un pipeline unifié. Leur pipeline de simulation a combiné les avantages des deux travaux [Prakosa *et al.* (2013)] et [De Craene *et al.* (2013)]. Ils ont réussi à produire des images réalisistes. Certains des résultats de simulation mentionnés ci-dessus sont montrés dans la Fig. VF.4.

3.5 Résumé

Dans ce chapitre, nous avons présenté certaines des approches utilisées pour valider le suivi de mouvements cardiaques. Bien que le mouvement mesuré par les techniques

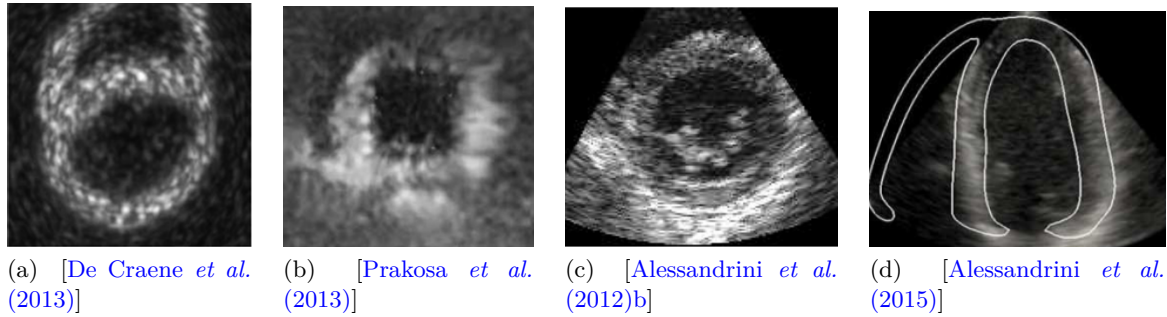


Figure VF.4: Quelques résultats représentatifs en simulation d'images ultrasonores.

d'imagerie dédiée telles que l'imagerie Doppler tissulaire ou l'imagerie DENSE MR révèlent des informations précieuses sur la vérité terrain, leurs limitations intrinsèques ainsi que les inexacititudes du recalage des différentes modalités d'imagerie limitent leur utilisation pour la validation. Suivre des repères manuellement est fastidieux et sujet aux variabilités inter et intra-expert. Une autre option consiste à concevoir des modèles du cœur physiques spécifiques et acquérir des images à l'aide de plusieurs modalités. Il est alors possible d'évaluer la performance des algorithmes de suivi de mouvements sur les images acquises. Cependant, le mouvement généré est rarement aussi complexe que le cœur réel et les images acquises ne simulent pas les organes environnants, pouvant poser un défi aux algorithmes de suivi. Par conséquent, nous choisissons de nous reposer sur des séquences d'images synthétiques pour la validation. De nombreux travaux de recherche ont déjà été réalisés dans ce domaine avec des images synthétiques réalistes simulées en US et IRM. L'utilité de telles données synthétiques repose fortement sur le niveau de réalisme des images. Les données et les champs de mouvement de la vérité de terrain doivent être proches des acquisitions réelles. De plus, le mouvement sous-jacent aux images synthétiques doit être connu exactement, au moins dans le myocarde. Pour que toutes ces exigences soient satisfaites, de nombreux aspects doivent être pris en considération lors de la conception des pipelines de simulation.

III. Contribution

Chapitre 4. Suivi de phase harmonique 3D avec la régularisation anatomique

Ce chapitre est une extension de notre article "3D Harmonic Phase Tracking with Anatomical Regularization" publié dans *Medical Image Analysis* [[Zhou et al. \(2015\)](#)].

4.1 Introduction

La quantification non invasive de la déformation myocardique reste un défi pour le diagnostic des maladies cardiaques. Parmi les index, la déformation est une mesure importante. En effet, la déformation est moins sensible à l'influence des segments environnants et est donc préférée pour détecter des segments anormaux [[Voigt and Flachskampf \(2004\)](#)]. L'IRM marquée est une modalité d'imagerie utilisée pour quantifier la déformation régionale du myocarde. Elle crée les marqueurs qui se déplacent avec le myocarde le long du cycle cardiaque. Le suivi de ces marqueurs permet une estimation précise de la déformation myocardique. Dernièrement, dans [[Rutz et al. \(2008\)](#)], un protocole de CSPAMM 4D a été proposé en réalisant trois acquisitions séquentiellement avec la préparation de tags dans les directions orthogonales. Chacune de ces trois acquisitions est effectuée alors que le patient retient sa respiration. Le désalignement temporel est rétrospectivement corrigé à l'aide d'un navigateur respiratoire. L'introduction de cette séquence de CSPAMM 4D accélérée nécessite des solutions de suivi de mouvements fiables. Dans ce chapitre, nous allons présenter une nouvelle extension 3D de l'algorithme de suivi de la phase harmonique (HARP) [[Osman et al. \(1999\)](#)].

4.2 La question ouverte et nos contributions

L'extension et la combinaison des méthodes de quantification d'IRM marquée 2D au protocole 3D proposé par Rutz *et al.* [[Rutz et al. \(2008\)](#)] reste un défi non résolu dans la communauté d'IRM marquée. Plusieurs tentatives ont été faites pour étendre HARP à la 3D. Elles sont toutes basées sur l'interpolation des résultats de HARP 2D à partir d'images acquises dans les coupes de court et long axe. Pan *et al.* [[Pan et al. \(2005\)](#)] ont obtenu un mouvement 3D en étendant des mouvements 2D à la 3D grâce à un modèle de maillage. Liang *et al.* [[Liang et al. \(2007\)](#)] utilisent un modèle volumétrique (bspline non uniforme) pour interpoler des mouvements. Liu *et al.* [[Liu et al. \(2012\)](#)] appliquent la Spline vectorielle comme noyau d'interpolation. Dernièrement, SimMod a également été étendu à l'IRM marquée [[Wang et al. \(2013\)](#)], mais sans intégrer de régularisation spatiale.

Ce contexte motive l'introduction d'une nouvelle méthode qui intègre les avantages des stratégies disponibles dans la littérature. Une analyse détaillée de l'état de l'art est déjà fournie dans le Chapitre 2. Des approches basées sur le recalage ont le potentiel d'extraire des champs de mouvement robustes à partir de données bruitées. À partir des techniques d'IRM spécifiques, extraire les images de phase vectorielle sans réduire la phase à une quantité scalaire est primordial pour quantifier la déformation 3D. Dans cette thèse, nous avons développé une méthode HARP adaptée pour une quantification rapide des déformations 3D *radiales*, *longitudinales* et *circonférentielles* à partir des images IRM marquées volumétriques [[Rutz et al. \(2008\)](#)]. Nos principales contributions sont les suivantes:

Premièrement, nous proposons d'ajouter une étape de régularisation spatiale à la méthode de HARP 3D. Cette régularisation est réalisée sur un maillage volumétrique du ven-

tricule gauche (VG) pour maintenir un faible coût de calcul. Les coordonnées anatomiques suivent les directions locales (*radiales*, *longitudinales* et *circonférentielles*). Les résultats de HARP 3D sont régularisés par des transformations affines définies en coordonnées anatomiques. Heyde *et al.* [Heyde *et al.* (2013)] [Heyde *et al.* (2016a)] ont introduit le concept de régularisation anatomique en échographie, mais l'ont implémenté en rééchantillonnant des images et en effectuant le suivi dans ces images rééchantillonées. Pour cette application, ceci introduira des distorsions non linéaires dans la forme des tags.

Deuxièmement, nous proposons d'imposer l'incompressibilité du myocarde pour corriger la déformation radiale. En effet, cette direction est par expérience la plus difficile à estimer. Ceci est probablement dû au fait que le nombre de tags est réduit dans la direction transmurale. La contrainte que nous proposons est imposée au niveau régional par l'application directe du théorème de la divergence.

4.3 Prétraitement

4.3.1 Segmentation de VG

La segmentation a été effectuée manuellement. Le VG a été segmenté uniquement à l'instant ED (dernière image). Segmenter la première image n'est pas possible parce que le tissu et le sang sont tous marqués et ne peuvent donc pas être distingués. Pour la segmentation, une image non marquée a été produite en calculant le module de l'image complexe obtenue à partir du filtrage passe-bande de HARP [Osman *et al.* (1999)]. Un maillage a été positionné pour la première fois sur l'image non marquée en cliquant sur les repères: 1 repère dans l'apex, 4 dans le plan de la base et 1 au milieu du septum. Le maillage de référence a été tourné et mis à l'échelle pour correspondre aux repères d'entrée. Le maillage a ensuite été converti en une fonction implicite et ajusté en ajoutant des pénalités ponctuelles par l'algorithme LiverMorph [Mory *et al.* (2012)].

4.3.2 Modèle de maillage

La procédure de segmentation décrite ci-dessus donne un maillage de surface fermée qui comprend l'endocarde et l'épicardium. Le maillage de surface est converti en un maillage volumétrique qui contient également une couche interne entre l'endocarde et l'épicardium. Le domaine du VG est échantillonné régulièrement dans les directions *radiales*, *longitudinales* et *circonférentielles*. Cela facilite la régularisation du champ de déplacement sur la topologie de maillage.

Règles de rééchantillonnage Le rééchantillonnage s'effectue en lancant des rayons depuis l'axe long de VG vers les surfaces endocardiques et épicaïques comme montré dans la Fig. VF.5. Le centre de VG est discréteisé en utilisant un échantillonnage cylindrique. L'axe longitudinal est échantillonné uniformément. À partir de chaque point du long axe, N_c rayons sont ensuite émis pour une répartition uniforme d'angles dans le plan orthogonal au long axe. Pour chaque rayon, l'intersection avec le maillage de surface donne deux points: un à l'endocarde et un à l'épicarde. La moyenne de ces deux points produit la couche médiane. De même, les parties apicale et basale sont échantillonnées de façon sphérique. Les angles d'azimut et d'élévation sont définis uniformément sur le VG (Fig. VF.5a et VF.5b).

Suivant ce schéma de discréteisation, chaque point du maillage peut être associé à trois indices. Tout d'abord, chaque point est soit endocardique, soit mid, soit épicaïque.

Deuxièmement, chaque point est intercepté par un rayon unique dans la direction *circonférentielle*. Enfin, chaque rayon est soit indexé à partir de la discréétisation cylindrique séquentielle ou angulaire par rapport à l'axe long (Fig. VF.5a). De cette façon, chaque noeud du maillage est lié à trois indices (m_r, m_l, m_c) où $m_d \in [1, N_d]$ et N_d ($d = r, l, c$) est le nombre de divisions dans chacune des trois directions (*radiale*, *longitudinale* ou *circonférentielle*). Ensuite, les coordonnées spatiales de chaque noeud peuvent être écris comme $\mathcal{P}(m_r, m_l, m_c)$.

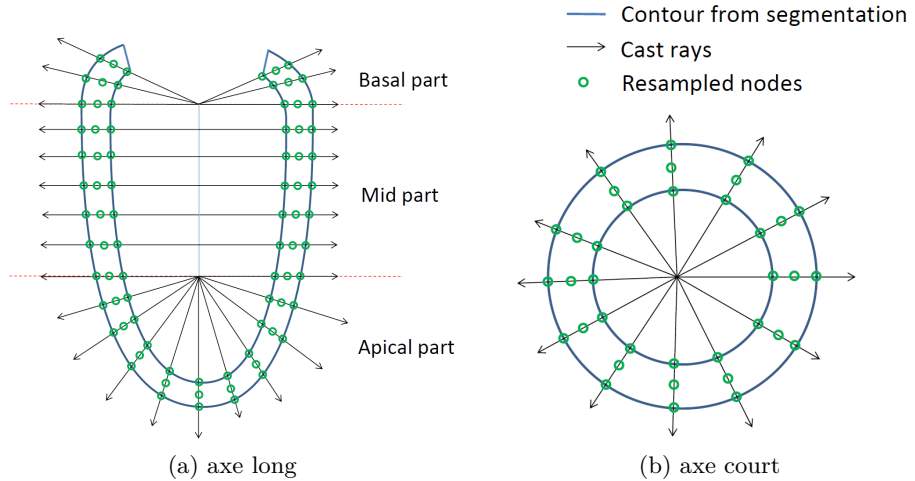


Figure VF.5: Rééchantillonnage du maillage de surface au maillage volumétrique.

Coordonnées anatomiques À partir de \mathcal{P} , les directions locales *radiales*, *longitudinales* et *circonférentielles* $\hat{\mathbf{e}}_r(\mathbf{x})$, $\hat{\mathbf{e}}_l(\mathbf{x})$ et $\hat{\mathbf{e}}_c(\mathbf{x})$ peuvent être calculées en normalisant les bords du maillage volumétrique. Les coordonnées Cartesiennes (\mathbf{x}) peuvent être liées aux coordonnées anatomiques (r, l, c) en satisfaisant les propriétés suivantes:

$$\begin{aligned} \forall \mathbf{x} \in \Omega, \quad \nabla r(\mathbf{x}) &= \hat{\mathbf{e}}_r(\mathbf{x}), \\ \nabla l(\mathbf{x}) &= \hat{\mathbf{e}}_l(\mathbf{x}), \\ \nabla c(\mathbf{x}) &= \frac{1}{\rho(\mathbf{x})} \hat{\mathbf{e}}_c(\mathbf{x}) . \end{aligned} \quad (\text{VF.1})$$

où Ω est le domaine du myocarde, et $\rho(\mathbf{x})$ est la distance du point \mathbf{x} à l'axe long de VG.

Pour chaque direction $d \in \{r, l, c\}$, nous commençons par un groupe de points de référence $\{X_0^d\}$ où les coordonnées anatomiques sont définies comme étant nulles. Pour les coordonnées longitudinales, l'apex est pris comme point de référence. Dans la direction circonférentielle, les points situés au centre des fenêtres locales (Session 4.4.3) sont choisis comme points de référence. Enfin, pour la direction radiale, $\{X_0^r\}$ est défini comme l'ensemble des points de la couche médiane.

Depuis $\{X_0^d\}$, les coordonnées sont obtenues par intégration curviligne. Prenant une direction $d \in \{r, l, c\}$, $d(\mathbf{x})$ est défini comme

$$d(\mathbf{x}) = \begin{cases} \min_{\mathcal{C}_d(\mathbf{x})} \int_{\mathcal{C}_d(\mathbf{x})} \hat{\mathbf{e}}_d(\mathbf{s}) \cdot d\mathbf{s}, & \text{if } d = r, l \\ \min_{\mathcal{C}_d(\mathbf{x})} \int_{\mathcal{C}_d(\mathbf{x})} \frac{1}{\rho(\mathbf{s})} \hat{\mathbf{e}}_d(\mathbf{s}) \cdot d\mathbf{s}, & \text{if } d = c \end{cases} . \quad (\text{VF.2})$$

où $\mathcal{C}_d(\mathbf{x})$ est un chemin géodésique défini sur le maillage en commençant par un noeud

$$\in X_0^d.$$

Les coordonnées $r(\mathbf{x})$ et $l(\mathbf{x})$ sont calculées globalement pour le VG. Toutefois, les coordonnées $c^{(i)}(\mathbf{x})$ sont définies localement pour chaque fenêtre i (Sect. 4.4.3) afin d'assurer sa continuité dans la domaine de fenêtre. Exemples de r, l et $c^{(i)}$ sont montrés dans la Fig. VF.6.

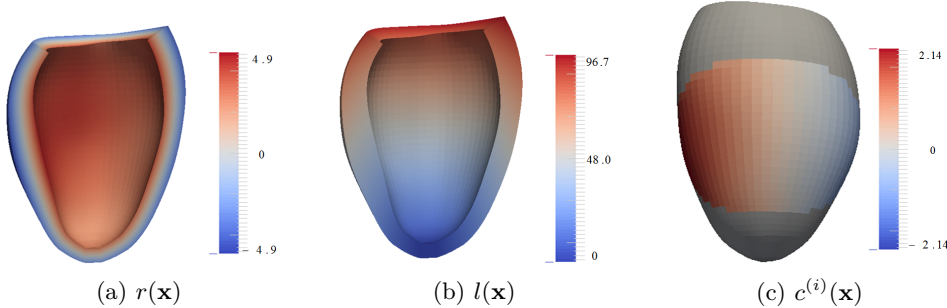


Figure VF.6: Coordonnées anatomiques $\{r, l, c^{(i)}\}$ définies sur le VG (dans (c), $c^{(i)}(\mathbf{x})$ n'a pas de définition dans la région en gris comme elle est à l'extérieur de la fenêtre actuelle).

4.4 Méthodologie de suivi

Après l'étape de prétraitement, le VG est suivi de l'image actuelle à l'image suivante. Dans un premier temps, la méthode HARP est utilisée pour générer une estimation initiale du champ de mouvement. Les déplacements obtenus par la méthode HARP sont régularisés par un modèle de mouvement paramétrique défini dans un espace anatomique de coordonnées. L'incompressibilité du myocarde est intégrée comme une contrainte faible qui permet d'estimer des déformations radiales d'une manière robuste. Pour aboutir à une convergence rapide de l'optimisation, une technique de régression pondérée par fenêtre est utilisée pour décomposer le problème global en un nombre de problèmes locaux. De plus, un cadre multirésolution a été développé où une forte régularisation est imposée au début et diminue progressivement.

4.4.1 Le suivi par la méthode de HARP

La méthode HARP [Osman *et al.* (1999)] estime le déplacement en calculant d'abord deux séquences d'images de phase, puis en effectuant un flux optique non régularisé sur ces deux canaux. HARP prétraite les intensités originales et calcule les images de phase par la méthode décrite dans [Osman *et al.* (1999)]. Ce prétraitement est destiné à compenser les artefacts de tag fading qui sont inhérents aux images d'IRM marquées.

Estimation du champ de mouvement dense Le suivi par HARP peut être considéré comme un flux optique multicanal sur les images de phases vraies (les phases sans artefacts de repli de phase) [Osman *et al.* (1999)]. Ici nous désignons la phase vraie par $\phi_k(\mathbf{x})$ avec $k = 1, 2, 3$. k indexe le numéro de canal (la direction de marquage). Le suivi d'un point matériel de l'instant $t \rightarrow t-1$ peut être résolu itérativement en mettant à jour le déplacement $\tilde{\mathbf{u}}_t$

$$\tilde{\mathbf{u}}_t \leftarrow \tilde{\mathbf{u}}_t + \mathbf{v}_t \quad (\text{VF.3})$$

Où \mathbf{v}_t est calculé en résolvant le système linéaire 3x3 suivant:

$$A \cdot \mathbf{v}_t = b \quad (\text{VF.4})$$

$$A = \begin{bmatrix} \nabla \phi_1^{t-1}(\mathbf{x} + \tilde{\mathbf{u}}_t)^T \\ \nabla \phi_2^{t-1}(\mathbf{x} + \tilde{\mathbf{u}}_t)^T \\ \nabla \phi_3^{t-1}(\mathbf{x} + \tilde{\mathbf{u}}_t)^T \end{bmatrix} \quad (\text{VF.5})$$

$$b = \begin{bmatrix} \phi_1^t(\mathbf{x}) - \phi_1^{t-1}(\mathbf{x} + \tilde{\mathbf{u}}_t) \\ \phi_2^t(\mathbf{x}) - \phi_2^{t-1}(\mathbf{x} + \tilde{\mathbf{u}}_t) \\ \phi_3^t(\mathbf{x}) - \phi_3^{t-1}(\mathbf{x} + \tilde{\mathbf{u}}_t) \end{bmatrix} \quad (\text{VF.6})$$

Les dérivées spatiales ont été corrigées lorsque la phase est replée de $-\pi$ à π par la méthode décrite dans [Osman et al. (1999)]. De même, b a été calculé à partir des phases repliées a_k [Osman et al. (1999)].

4.4.2 Modèle de mouvement

$\mathbf{u}_t^{(i)}(\mathbf{x})$ est un mouvement paramétrique local dans une fenêtre i (décrit plus loin dans la section 4.4.3) de l'instant $t \rightarrow t-1$. Nous optons pour une transformation affine définie dans les coordonnées anatomiques $\{r, l, c^{(i)}\}$ qui combine les translations, l'étirement (ou le raccourcissement) et le cisaillement. Ce modèle a 12 paramètres par fenêtre.

$$\begin{aligned} \mathbf{u}_t^{(i)}(\mathbf{x}) &= L_r^{(i)}(\mathbf{x})\hat{\mathbf{e}}_r(\mathbf{x}) + L_l^{(i)}(\mathbf{x})\hat{\mathbf{e}}_l(\mathbf{x}) + L_c^{(i)}(\mathbf{x})\hat{\mathbf{e}}_c(\mathbf{x}) \\ \text{avec } L_r^{(i)}(\mathbf{x}) &= a_{rr}^{(i)}r(\mathbf{x}) + a_{rl}^{(i)}l(\mathbf{x}) + a_{rc}^{(i)}c^{(i)}(\mathbf{x}) + b_r^{(i)} \\ L_l^{(i)}(\mathbf{x}) &= a_{lr}^{(i)}r(\mathbf{x}) + a_{ll}^{(i)}l(\mathbf{x}) + a_{lc}^{(i)}c^{(i)}(\mathbf{x}) + b_l^{(i)} \\ L_c^{(i)}(\mathbf{x}) &= (a_{cr}^{(i)}r(\mathbf{x}) + a_{cl}^{(i)}l(\mathbf{x}) + a_{cc}^{(i)}c^{(i)}(\mathbf{x}) + b_c^{(i)})\rho(\mathbf{x}) \end{aligned} \quad (\text{VF.7})$$

$\{b_r^{(i)}, b_l^{(i)}, b_c^{(i)}\}$ sont les paramètres d'ordre zéro liés au mouvement. $\{a_{rr}^{(i)}, a_{ll}^{(i)}, a_{cc}^{(i)}\}$ sont liés aux déformations *radiales, longitudinales et circonférentielles*. $\{a_{rl}^{(i)}, a_{rc}^{(i)}, a_{lr}^{(i)}, a_{lc}^{(i)}, a_{cr}^{(i)}, a_{cl}^{(i)}\}$ sont liés au cisaillement.

4.4.3 Régularisation par la régression pondérée par fenêtres

Mcleod et al. [McLeod et al. (2013)] ont intégré les fonctions de fenêtre locales définies dans les coordonnées sphéroïdales dans le cadre du recalage polyaffine. Dans cette section, nous expliquerons comment définir la fonction de fenêtre de manière similaire et la coupler avec le modèle de mouvement pour régulariser les résultats de suivi de HARP 3D.

La méthode de la partition de l'unité Comme présenté dans [Makram-Ebeid and Somphone (2007)], un problème de régression globale peut être simplifié en résolvant un ensemble de problèmes locaux en utilisant la technique de *partition de l'unité*.

Une partition du domaine VG est définie par un ensemble de points de contrôle $\{\mathbf{x}_i\}$ et par les fonctions de fenêtre $\varphi^{(i)}(\mathbf{X})$ associé à chaque point de contrôle. On suppose que

ces derniers satisfont aux conditions suivantes:

$$\begin{aligned} \arg \max_{\mathbf{x}} \varphi^{(i)}(\mathbf{x}) &= \mathbf{x}_i, \quad \forall i \\ \varphi^{(i)}(\mathbf{x}) &\geq 0, \quad \forall \mathbf{x} \in \Omega, \\ \sum_i \varphi^{(i)}(\mathbf{x}) &= 1 \quad \forall \mathbf{x} \in \Omega. \end{aligned} \tag{VF.8}$$

Où Ω est le domaine du myocarde. Le calcul de $\varphi^{(i)}(\mathbf{x})$ est décrit plus tard dans Sect. 4.4.3. Le déplacement régularisé $\mathbf{u}_t(\mathbf{x})$ est calculé comme

$$\mathbf{u}_t(\mathbf{x}) = \sum_i \varphi^{(i)}(\mathbf{x}) \mathbf{u}_t^{(i)}(\mathbf{x}) \tag{VF.9}$$

Où $\mathbf{u}_t^{(i)}(\mathbf{x})$ est le modèle de mouvement (Sect. 4.4.2).

Si nous avons certaines estimations initiales de mouvement $\tilde{\mathbf{u}}_t(\mathbf{x})$ (actuellement les résultats du suivi de HARP) et les poids de confiance $\tilde{w}_t(\mathbf{x})$ que nous décrirons plus tard dans la section 4.4.3), La somme des erreurs locales $E^{(i)}$ donne une borne supérieure à l'erreur globale E :

$$\begin{aligned} E &= \int_{\Omega} \tilde{w}_t(\mathbf{x}) \left\| \tilde{\mathbf{u}}_t(\mathbf{x}) - \sum_i \varphi^{(i)}(\mathbf{x}) \mathbf{u}_t^{(i)}(\mathbf{x}) \right\|^2 d\mathbf{x} \\ &\leq \sum_i \int_{\Omega} \tilde{w}_t(\mathbf{x}) \varphi^{(i)}(\mathbf{x}) \left\| \tilde{\mathbf{u}}_t(\mathbf{x}) - \mathbf{u}_t^{(i)}(\mathbf{x}) \right\|^2 d\mathbf{x} = \sum_i E^{(i)} \end{aligned} \tag{VF.10}$$

Le lecteur peut trouver plus de détails dans [Makram-Ebeid and Somphone (2007)]. Le fait de limiter chaque terme $E^{(i)}$ à une quantité suffisamment petite minimise également l'erreur globale, permettant ainsi de décomposer un problème d'optimisation globale en un nombre de problèmes régionaux plus simples à résoudre.

Fonction de fenêtre Le domaine du VG a d'abord été divisé en petites fenêtres comme illustré dans la Fig. VF.7. Le but de cette section est de définir les fonctions $\varphi^{(i)}$ pour une partition donnée du domaine de VG. Cette partition est obtenue en utilisant une stratégie multi-résolution qui sera expliquée dans la section 4.4.4.

Compte tenu d'une partition de VG, les points de contrôle ont été définis comme le centre de ces fenêtres. Les fonctions de fenêtre sont centrées à chaque point de contrôle et doivent diminuer lorsque la distance au point de contrôle augmente. Puisque nous avons choisi de suivre un maillage volumétrique, la distance géodésique a été choisie pour calculer la fonction de fenêtre. Nous utilisons un noyau gaussien pour définir la fonction de fenêtre, en impliquant la distance géodésique ξ entre \mathbf{x} et le centre de la fenêtre \mathbf{x}_i :

$$g^{(i)}(\mathbf{x}) = \frac{1}{2\pi\sigma_i^2} e^{-\frac{\xi(\mathbf{x}, \mathbf{x}_i)^2}{2\sigma_i^2}} \tag{VF.11}$$

Afin d'utiliser un unique σ pour différentes tailles de fenêtres, nous exprimons σ_i comme

$$\sigma_i = \sigma \chi_i \tag{VF.12}$$

Où χ_i est calculé pour chaque fenêtre en moyennant le support de cette fenêtre dans les directions circonférentielle et longitudinale. Dans l'équation VF.12, σ est un paramètre auxiliaire dit *kernel bandpass*. Il contrôle la façon dont les fenêtres se chevauchent pour

produire l'estimation du déplacement final dans l'équation VF.9. Le paramètre σ est normalisé et peut donc être utilisé dans plusieurs résolutions de fenêtre. Les fonctions de fenêtre sont définies en normalisant les valeurs de $g^{(i)}$ pour que leur somme soit 1:

$$\varphi^{(i)}(\mathbf{x}) = \frac{g^{(i)}(\mathbf{x})}{\sum_j g^{(j)}(\mathbf{x})} . \quad (\text{VF.13})$$

Poids de confiance La phase de HARP est calculée en prenant l'argument du signal complexe [Osman *et al.* (1999)]. En fait, son amplitude (noté comme \mathcal{M}_k) correspond à l'image non marquée [Osman *et al.* (1999)]. Cette information peut être utilisée comme une pondération, donnant une mesure de confiance $\tilde{w}_t(\mathbf{x})$: une valeur élevée de \mathcal{M}_k indique une plus grande probabilité d'appartenir au myocarde, d'où une confiance accrue dans les résultats du suivi de HARP $\tilde{\mathbf{u}}_t(\mathbf{x})$. Dans notre expérience, les poids $\tilde{w}_t(\mathbf{x})$ ont été obtenus en calculant la moyenne des trois canaux sur les deux images de l'instant t et $t - 1$:

$$\tilde{w}_t(\mathbf{x}) = \sqrt{\frac{1}{3} \left(\sum_{k=1}^3 \mathcal{M}_k^t(\mathbf{x}) \right) \cdot \frac{1}{3} \left(\sum_{k=1}^3 \mathcal{M}_k^{t-1}(\mathbf{x} + \tilde{\mathbf{u}}_t(\mathbf{x})) \right)}, \quad (\text{VF.14})$$

Contrainte d'incompressibilité Imposer une divergence nulle est un moyen classique d'imposer l'incompressibilité du myocarde. Cette contrainte peut être imposée au niveau global ou local. Dans notre cas, le calcul de la divergence locale nécessite des dérivés spatiales complexes de $r(\mathbf{x}), l(\mathbf{x})$ et $c^{(i)}(\mathbf{x})$. Par conséquent, nous optons pour imposer une incompressibilité locale au niveau des fenêtres, en imposant que le changement de volume global soit nul. Pour ce faire, nous appliquons le théorème de divergence. Si $\partial S^{(i)}$ représente la surface entourant la fenêtre i , le flux extérieur de $\mathbf{u}_t^{(i)}(\mathbf{x})$ à $\partial S^{(i)}$ est équivalent à l'intégrale de volume de la divergence du champ de mouvement sur cette fenêtre. Par conséquent, imposer l'incompressibilité de myocarde est équivalent à forcer le flux qui traverse $\partial S^{(i)}$ à zéro. Pour chaque fenêtre locale i , $\partial S^{(i)}$ est composé des quadrillatères. Chacun des quadrillatères j peut être représenté par son centre \mathbf{x}_j , sa normale (pointant vers l'extérieur) \mathbf{n}_j et sa superficie A_j . Le flux de $\mathbf{u}_t^{(i)}(\mathbf{x})$ à $\partial S^{(i)}$ est écrit comme:

$$\begin{aligned} Q_t^{(i)} &= \sum_{j \in \partial S^{(i)}} \mathbf{u}_t^{(i)}(\mathbf{x}_j) \cdot A_j \vec{n}_j \\ &= \sum_{j \in \partial S^{(i)}} \sum_{d=r,l,c} L_d^{(i)}(\mathbf{x}_j) (\hat{\mathbf{e}}_d(\mathbf{x}_j) \cdot A_j \vec{n}_j) \end{aligned} \quad (\text{VF.15})$$

Puisque $L_d^{(i)}(\mathbf{x}_j)$ est linéaire par rapport à $\{b_d^{(i)}, a_{rd}^{(i)}, a_{ld}^{(i)}, a_{cd}^{(i)}\}$ ($d = r, l, c$), donc est $Q_t^{(i)}$. Imposer $Q_t^{(i)} = 0$ est équivalent à ajouter une contrainte d'égalité linéaire au problème d'optimisation. a_{rr} peut être écrit comme une combinaison linéaire de tous les autres paramètres $\{b_r^{(i)}, b_l^{(i)}, b_c^{(i)}, a_{rl}^{(i)}, a_{rc}^{(i)}, a_{lr}^{(i)}, a_{ll}^{(i)}, a_{lc}^{(i)}, a_{cr}^{(i)}, a_{cl}^{(i)}, a_{cc}^{(i)}\}$.

Résoudre le système local et calculer le mouvement global Nous montrons comment, avec le modèle de mouvement défini dans Sect. 4.4.2, nous pouvons obtenir une forme quadratique pour les erreurs locales $E^{(i)}$ (l'équation VF.10). Comme $\{\hat{\mathbf{e}}_r(\mathbf{x}), \hat{\mathbf{e}}_l(\mathbf{x}), \hat{\mathbf{e}}_c(\mathbf{x})\}$ définit une base orthogonale, nous pouvons projeter des déplacements de HARP $\tilde{\mathbf{u}}_t(\mathbf{x})$ dans

cette base:

$$\tilde{\mathbf{u}}_t(\mathbf{x}) = \sum_{d=r,l,c} p_d(\mathbf{x}) \hat{\mathbf{e}}_d(\mathbf{x}) \quad (\text{VF.16})$$

avec $p_d(\mathbf{x}) = \tilde{\mathbf{u}}_t(\mathbf{x}) \cdot \hat{\mathbf{e}}_d(\mathbf{x})$

Par l'équation VF.7 et VF.16, $E^{(i)}$ dans l'équation VF.10 peut être exprimé comme suivant:

$$E^{(i)} = \int_{\Omega} \varphi^{(i)}(\mathbf{x}) \tilde{w}_t(\mathbf{x}) \left\| \sum_{d=r,l,c} \left(L_d^{(i)}(\mathbf{x}) - p_d(\mathbf{x}) \right) \hat{\mathbf{e}}_d(\mathbf{x}) \right\|^2 d\mathbf{x} \quad (\text{VF.17})$$

En utilisant l'orthogonalité entre $\{\hat{\mathbf{e}}_r(\mathbf{x}), \hat{\mathbf{e}}_l(\mathbf{x}), \hat{\mathbf{e}}_c(\mathbf{x})\}$, il est facile d'obtenir:

$$E^{(i)} = \int_{\Omega} \varphi^{(i)}(\mathbf{x}) \tilde{w}_t(\mathbf{x}) \sum_{d=r,l,c} \left(L_d^{(i)}(\mathbf{x}) - p_d(\mathbf{x}) \right)^2 d\mathbf{x} \quad (\text{VF.18})$$

Puisque $L_d^{(i)}(\mathbf{x})$ est linéaire par rapport à $b_d^{(i)}, a_{dr}^{(i)}, a_{dl}^{(i)}$ et $a_{dc}^{(i)}$ ($d = r, l, c$), $E^{(i)}$ est une forme quadratique et peut être minimisée en résolvant un système linéaire. Étant donné que la déformation radiale est la plus difficile à estimer, nous avons intégré la contrainte d'incompressibilité et dans l'équation VF.18 nous avons substitué $a_{rr}^{(i)}$ par la combinaison linéaire de $\{b_r^{(i)}, b_l^{(i)}, b_c^{(i)}, a_{rl}^{(i)}, a_{rc}^{(i)}, a_{lr}^{(i)}, a_{lc}^{(i)}, a_{ll}^{(i)}, a_{lc}^{(i)}, a_{cr}^{(i)}, a_{cl}^{(i)}, a_{cc}^{(i)}\}$. La minimisation de $E^{(i)}$ donne alors un système linéaire de taille 11x11. Ce système est résolu par la technique de pseudo-inverse. En dernière étape, $a_{rr}^{(i)}$ est calculé à partir de la combinaison linéaire mentionnée ci-dessus. Une fois les mouvements locaux $\mathbf{u}_t^{(i)}(\mathbf{x})$ sont calculés, le mouvement global est obtenu par l'équation VF.9.

4.4.4 Cadre de multirésolution

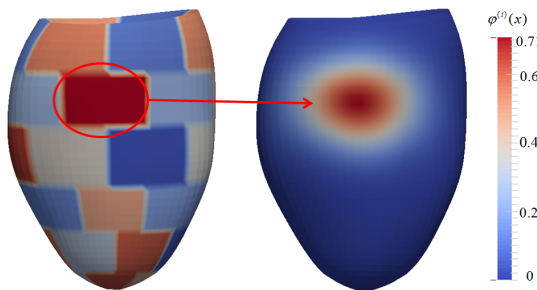


Figure VF.7: Définition des fenêtres locales de VG et un exemple de la fonction de fenêtre.

Nous devons définir une partition du domaine de VG à des niveaux croissants de résolutions. À des fins de simplification, nous avons divisé le VG en utilisant un seul paramètre: le nombre de divisions dans les directions circonférentielle et longitudinale. De plus, pour obtenir un mélange plus homogène entre les fenêtres, elles ont été décalées de la moitié de leur étendue circonférentielle sur des couches longitudinales contiguës (voir Fig. VF.7 pour une illustration). Pour améliorer la convergence des paramètres de mouvement et de déformation, nous avons commencé avec 3 divisions dans les directions longitudinales et circonférentielles. Ce nombre a ensuite été doublé sur les deux prochaines résolutions.

À chaque résolution, le suivi de HARP a été initialisé avec le résultat de la résolution précédente avant de procéder à la régularisation anatomique.

4.5 Génération d'images synthétiques

Pour évaluer l'impact de plusieurs paramètres sur le suivi et la déformation, une stratégie simple a été utilisée pour générer des images synthétiques. Les entrées sont 1) une séquence de maillages tétraédriques du VG (notée comme \mathcal{S}^t) accessible publiquement depuis [De Craene *et al.* (2013)]; et 2) trois images IRM marquées avec des orientations orthogonales de tag (notées comme \mathcal{I}_k^{N-1} où N est le nombre d'instants et $k \in \{1, 2, 3\}$ est le numéro de canal) rendues public à partir de [Tobon-Gomez *et al.* (2013)]. Les maillages utilisés ici proviennent d'un modèle électromécanique [Marchesseau *et al.* (2013)] qui prend en compte la distribution des fibres.

4.5.1 Recaler les maillages de VG aux images réelles d'IRM marquée

Nous supposons que la dernière image de la séquence et le dernier maillage électromécanique correspondent à la fin de la diastole. Cette dernière image a été segmentée en extrayant d'abord la surface du dernier maillage du modèle électromécanique et le positionner et déformer manuellement en utilisant la même technique de segmentation (Sect. 4.3). Le résultat de la segmentation est notée comme \mathcal{R} . Une transformation par thin-plate spline (TPS) [Bookstein (1989)] \mathcal{T} a ensuite été calculée entre le modèle électromécanique et \mathcal{R} . Cette transformation est ensuite appliquée à tous les maillages \mathcal{S}^t , produisant une nouvelle séquence de maillages de VG notée comme $\tilde{\mathcal{S}}^t = \mathcal{T}(\mathcal{S}^t)$.

4.5.2 Déformer les images réelles par les maillages

Les images synthétiques ont été obtenues en déformant les dernières images \mathcal{I}_k^{N-1} par la séquence de $\tilde{\mathcal{S}}^t$. Cela a été fait en deux étapes. Tout d'abord, une transformation TPS $\mathcal{T}' : \tilde{\mathcal{S}}^{N-1} \mapsto \tilde{\mathcal{S}}^t$ a été calculée pour étendre les déplacements définis sur les nœuds de maillage uniquement au volume entier et déformer l'image \mathcal{I}_k^{N-1} . Deuxièmement, cette image a été corrigée à l'intérieur du myocarde pour éliminer les artefacts induits par le TPS. Pour chaque pixel myocardique dans \mathcal{I}_k^t , nous trouvons la cellule tétraédrique correspondante et calculons les coordonnées barycentriques du pixel à l'intérieur de cette cellule. Nous avons ensuite interpolé l'intensité de \mathcal{I}_k^{N-1} pour les mêmes coordonnées cellulaire et barycentrique. Cette intensité a été utilisée à la place de celle obtenue par la déformation de TPS.

4.6 Résultats

4.6.1 Images synthétiques

Les précisions de suivi et de déformation sur la séquence synthétique ont été utilisées comme référence pour régler les paramètres. Fig. VF.9 montre l'évolution des erreurs de mouvement et de déformation en couvrant différents valeurs de n (Sect. 4.4.4) et σ (Sect. 4.4.3). Nous pouvons voir que le paramètre $n = 3$ et $\sigma = 0.2$, ou $n = 3$ et $\sigma = 0.3$ surpassent les autres configurations avec erreurs de suivi inférieures à 1,5 mm. En considérant également la précision sur la déformation, $n = 3$ et $\sigma = 0,3$ est le meilleur choix. Nous montrons le *Bland Altman plot* sur les déformations *radiales*, *longitudinales* et *circonférentielles* dans la Fig. VF.10.

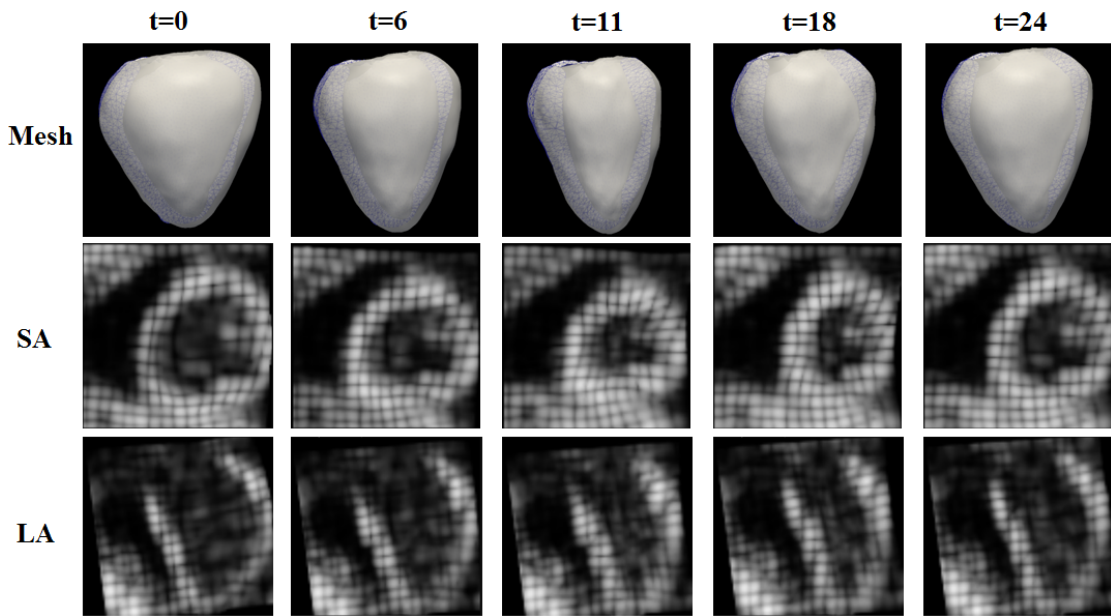


Figure VF.8: Les maillages de la vérité du terrain et les coupes d’axes courts et longs d’images IRM marquées synthétiques.

4.6.2 Volontaires sains

Cette section compare quantitativement notre méthode à d’autres algorithmes de suivi de mouvements en IRM marquée. Pour ce faire, nous avons utilisé les données fournies par [Tobon-Gomez *et al.* (2013)] pour comparer la précision de suivi. Au total, 15 volontaires ont été utilisés pour l’évaluation. L’erreur de suivi est interpolée sur les 24 repères. Fig. VF.11 montre les erreurs de mouvement pour tous les 15 volontaires. On peut voir que notre méthode donne une précision similaire à celles obtenues par les algorithmes de MEVIS et de l’UPF tout en présentant moins de valeurs aberrantes. Cependant, il convient de noter que le temps de calcul de notre méthode se situe dans un ordre de grandeur de quelques minutes tandis que les algorithmes UPF et MEVIS se situent dans un ordre de grandeur de plusieurs heures comme indiquée dans [Tobon-Gomez *et al.* (2013)].

4.6.3 Données de patients

Dans cette section, nous montrons des résultats de quantification pour quatre patients présentant de la fibrose confirmée par l’imagerie d’IRM à rehaussement tardif. Les données de patients ont été acquises au GIP Cyceron. À des fins de comparaison, nous avons également quantifié trois volontaires sains acquis dans la même institution. Fig. VF.12 montre la dispersion des valeurs de déformation circonférentielle pour les volontaires (v1 à v5) et les quatre patients (p1 à p4). Les deux premiers volontaires ont été publiés par [Tobon-Gomez *et al.* (2013)] tandis que les autres ont été scannés au CHU de Caen/Cyceron. Les quatre patients sont ordonnés par le nombre de segments où la fibrose transmurale était visible en imagerie à rehaussement tardif. La dispersion globale des valeurs de déformation devrait augmenter pour les cas d’infarctus les plus sévères. Fig. VF.12 montre que cette tendance peut être observée dans notre résultat: la dispersion des déformations circ. augmente des volontaires sains (v1-v5) aux patients (p1-p4) classés par le degré de fibrose. De plus, la déformation circ. diminue chez les patients (environ -15% pour le médian).

Pour regarder la déformation locale à un niveau plus détaillé, dans la Fig. VF.13, nous

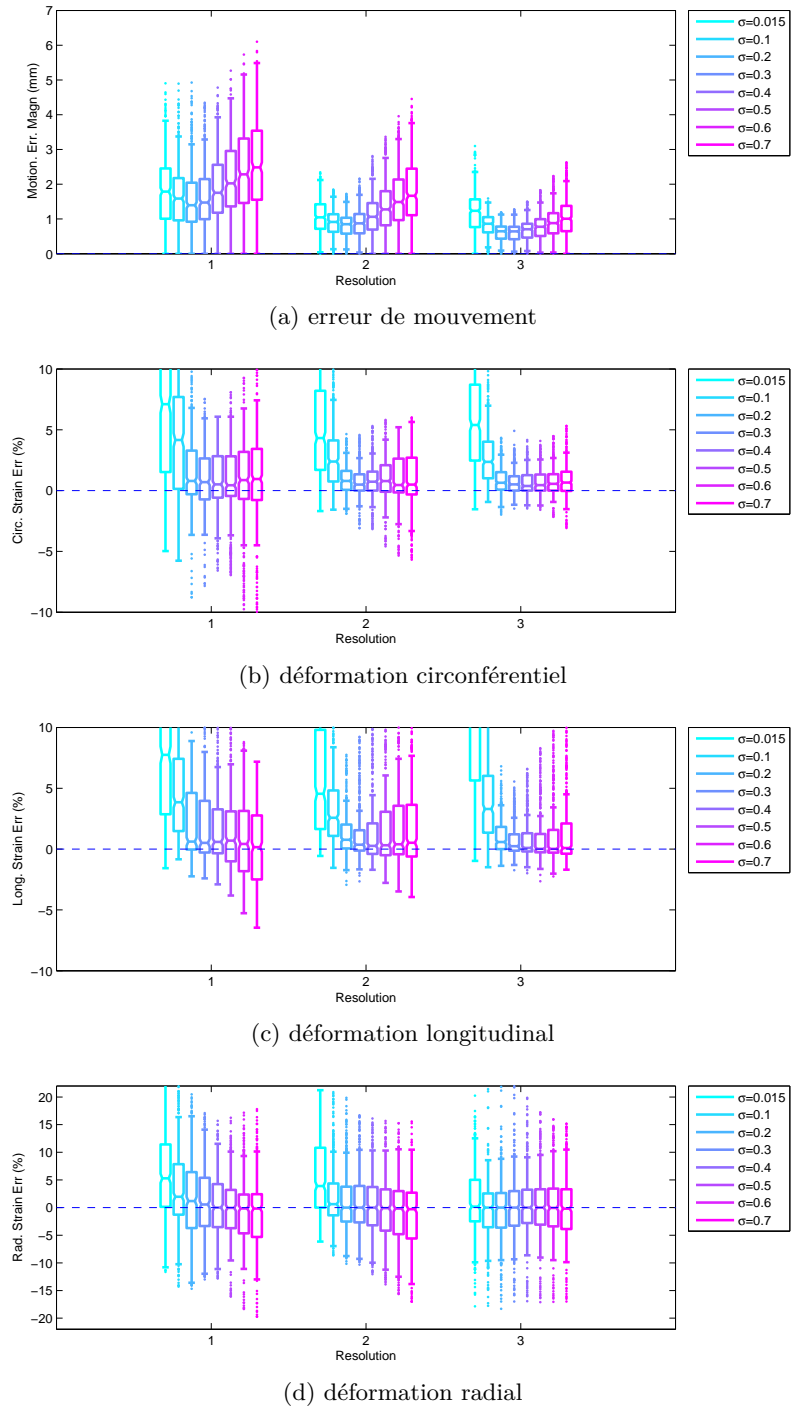


Figure VF.9: Les diagrammes de quartile montrant l'évolution de la précision du suivi en fonction des paramètres: le nombre de résolutions n et la bande passante σ .

montrons la carte de déformation circonférentielle à la fin de la systole pour le patient p2. Nous affichons aussi les courbes de déformation circ. au niveau des segments AHA. Ce patient a une fibrose myocardique dans l'ensemble de la paroi inférieure, des niveaux basals et moyens de la paroi inférolatérale et de la paroi inféroseptale basale (différents degrés de fibrose dans les segments AHA 3,4,5,10,11,15). Fig. VF.13a et Fig. VF.13b

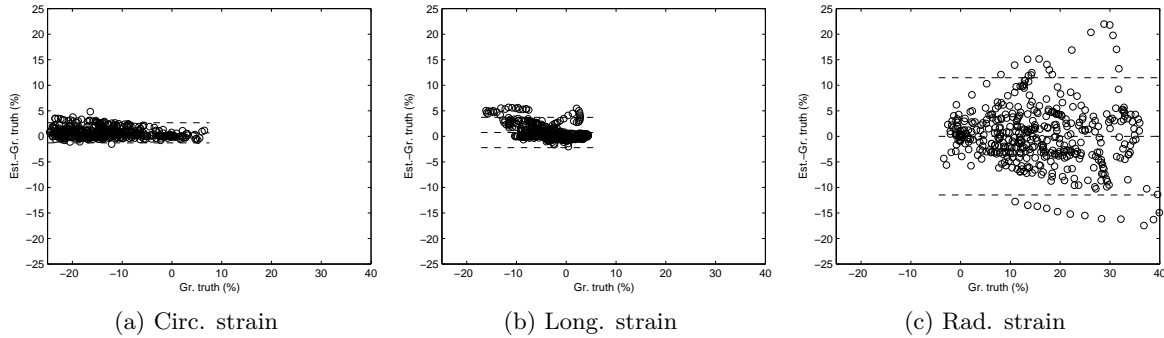


Figure VF.10: Bland Altman sur l'erreur de strain Circ. Long. et Rad. lorsque $n = 3$ et $\sigma = 0, 3$. (Chaque point de données représente le strain de certains segments AHA à certains instant cardiaque)

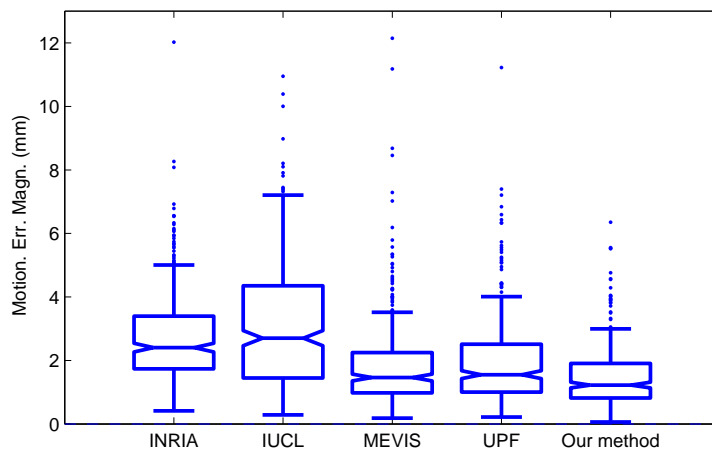


Figure VF.11: La précision du suivi de mouvements (paramètres $n = 3, \sigma = 0.3$) sur les 15 volontaires. Notre méthode est comparée à quatre autres méthodes de l'état de l'art: INRIA, IUCL, MEVIS and UPF (pour les détails de ces méthodes, se référer à [Tobon-Gomez *et al.* (2013)]).

montre une différence claire de déformation circ. entre la paroi inférieure (infarctée) et la paroi antérieure (normale). Ceci est cohérent avec les résultats d'IRM à rehaussement tardif, comme le montre les figures VF.13a VF.13b où les niveaux de gris élevés indiquent l'existence de fibrose. Une corrélation claire est observée entre les régions de faible déformation et les zones infarcies (celles ayant des intensités d'image plus brillantes). Cependant, ici, la corrélation observée est assez qualitative et limitée car les deux modalités étaient alignées manuellement. En effet, ces deux types d'images avaient des résolutions spatiales différentes, rendant leur recalage difficile. De plus, à partir des courbes de déformations (Fig. VF.13c), on peut facilement distinguer les segments sains.

4.7 Résumé

Dans cette section, nous avons introduit un nouvel algorithme qui étend la méthode HARP pour quantifier des données d'IRM marquée. Nous proposons une méthode de régularisation réalisée dans un espace de coordonnées anatomiques. Les résultats du suivi de HARP ont été régularisés par une méthode de régression pondérée par fenêtre qui main-

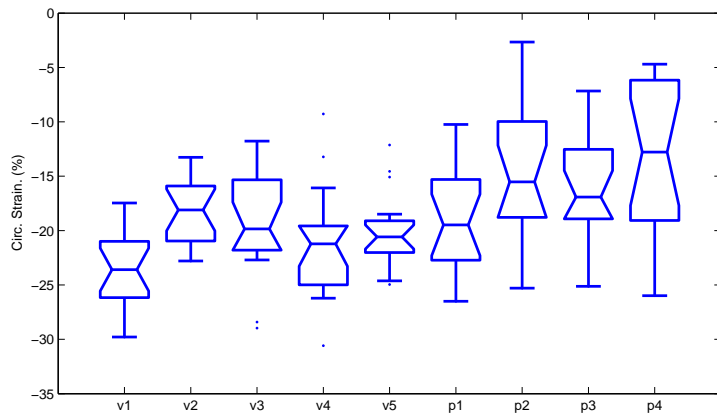
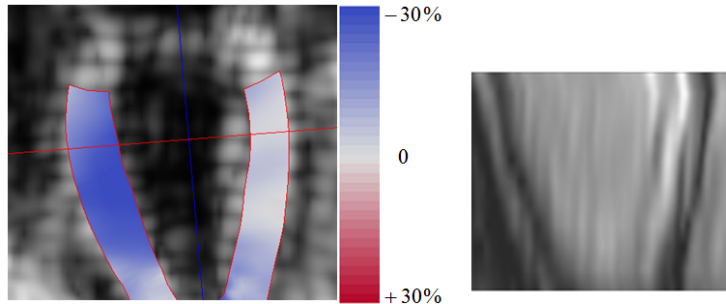
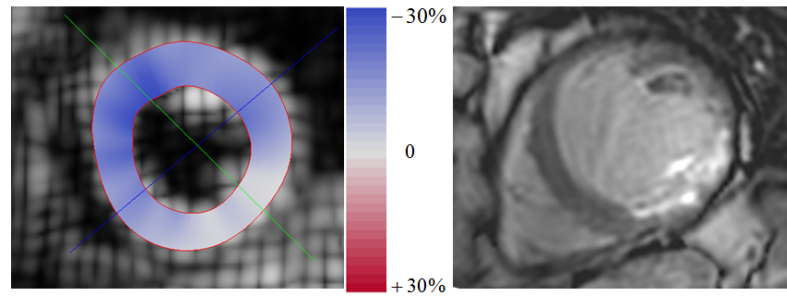


Figure VF.12: La déformation Circ. au niveau des segments AHA, v1 et v2 sont deux volontaires sains obtenus à partir de [Tobon-Gomez *et al.* (2013)], v3,v4,v5 sont trois volontaires sains acquis chez GIP Cyceron, et p1, p2, p3, p4 sont quatre patients acquis à GIP Cyceron. Ils sont classés par le degré de la fibrose myocardique.

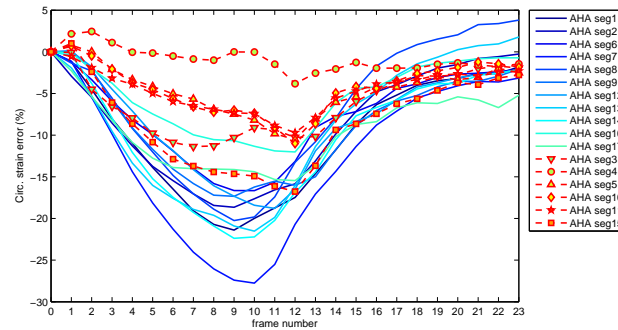
tient une faible complexité de calcul. L’algorithme proposé a été évalué à trois niveaux: sur des séquences synthétiques, des volontaires sains et des données de patients. Sur les volontaires, la précision du suivi s’est révélée comparable aux meilleurs résultats d’une évaluation récente. La précision de la déformation a été évaluée sur les données synthétiques, présentant des erreurs de déformations inférieures à 5 % (à l’exclusion des valeurs aberrantes) sur les déformations longitudinale et circonférentielle. La déformation radiale est plus difficile à estimer, mais nous avons le deuxième et le troisième quartiles d’erreurs de la déformation radiale dans la gamme ($-5\%, 5\%$), grâce à la contrainte d’incompressibilité du myocarde. On a montré que notre méthode était applicable aux données cliniques en corrélant d’abord la dispersion de déformation avec le degré de la fibrose transmurale. Des valeurs de déformations plus faibles ont également été observées à l’intérieur et autour de la région affectée. De plus, la carte de déformation est corrélée avec les résultats d’IRM à rehaussement tardif.



(a) La déformation circonférentielle en fin systole. La carte de déformation affichée sur une coupe grand axe et une image IRM à rehaussement tardif au même endroit



(b) La déformation circonférentielle en fin systole. La carte de déformation affichée sur une coupe petit axe et une image IRM à rehaussement tardif au même endroit



(c) l'évolution temporelle de la déformation circonférentielle

Figure VF.13: La carte de la déformation circonférentielle en couleur (a)(b) et les courbes de déformation (c) pour le patient p2 dans la Fig. VF.12. Ce patient a une fibrose dans l'ensemble de la paroi inférieure, une partie de la paroi inferolatérale et une partie de la paroi inferoseptique (correspondant aux segments AHA 3,4,5,10,11,15). La carte de déformation est affichée à la fin de la systole. Dans les courbes de déformations: les lignes solides affichent des segments normaux tandis que les courbes avec marqueurs montrent des segments avec une fibrose.

Chapitre 5. Simulation multimodale des patients virtuels

Ce chapitre est une extension de notre article "A generic framework for the generation of realistic cardiac magnetic resonance and ultrasound imaging sequences of the same virtual patients" soumis à *Special Issue on Simulation and Synthesis in Medical Imaging, IEEE Transactions on Medical Imaging*.

5.1 Introduction

Dans ce chapitre, nous allons présenter un nouveau pipeline de simulation qui permet de générer des séquences d'images synthétiques cardiaques multimodales (US, IRM cine et IRM marquée) pour le même sujet virtuel. Ce travail étend le pipeline initialement proposé par [Alessandrini *et al.* (2015)] pour la simulation d'US. Le pipeline de simulation que nous proposons se compose de trois éléments principaux: i) l'utilisation d'acquisitions réelles pour extraire des informations pertinentes afin d'améliorer le réalisme des images générées; ii) l'utilisation d'un modèle E/M du cœur [Marchesseau *et al.* (2013)] pour générer des champs de mouvement synthétique (sain et pathologiques) utilisés comme référence; iii) l'utilisation des simulateurs physiques pour modéliser la formation d'image. Le pipeline a été utilisé pour créer une base de données de 18 patients virtuels. Pour chaque patient, des séquences d'US 3D, d'IRM cine 3D et d'IRM marquée 3D ont été générées. Nous avons généré un total de 90 séquences synthétiques représentant 2700 volumes. Des séquences synthétiques ainsi que des champs de mouvement de référence correspondants sont mis à la disposition du public via une base de données en libre accès¹. Les nouveautés de ce travail sont les suivantes:

- La combinaison d'un modèle E/M avec un simulateur physique d'IRM pour modéliser la formation d'image;
- L'utilisation des séquences d'acquisitions multimodales à partir du même patient pour extraire l'information la plus pertinente de chaque modalité (par exemple, les structures anatomiques de l'IRM cine et de l'estimation de mouvement à partir de l'IRM marquée);
- L'introduction d'une nouvelle stratégie de recalage pour réduire des artefacts de mouvement dans le myocarde;
- L'introduction du premier cadre uniifié qui permet la génération des séquences synthétiques multimodales (US, IRM cine et IRM marquée) pour le même patient virtuel.

5.2 Méthodologie

Nous étendons dans cette section le pipeline d'échographie initialement développé dans [Alessandrini *et al.* (2015)] à la génération des séquences d'IRM synthétiques. Le but est de dériver un cadre générique qui simule des séquences cardiaques multimodales pour le même patient virtuel. Comme une grande partie des innovations présentées dans ce travail réside dans les aspects IRM, nous nous concentrerons principalement sur les différentes étapes que nous introduisons pour simuler des séquences réalistes d'IRM cine et d'IRM marquée. Le même pipeline a également été utilisé dans cette thèse pour générer des images US synthétiques, comme indiqué dans la section 5.2.5 (seul le bloc "modélisation d'IRM" doit être remplacé par celui proposé dans [Alessandrini *et al.* (2015)]).

¹<http://humanheart-project.creatis.insa-lyon.fr/multimodalityStraus.html>

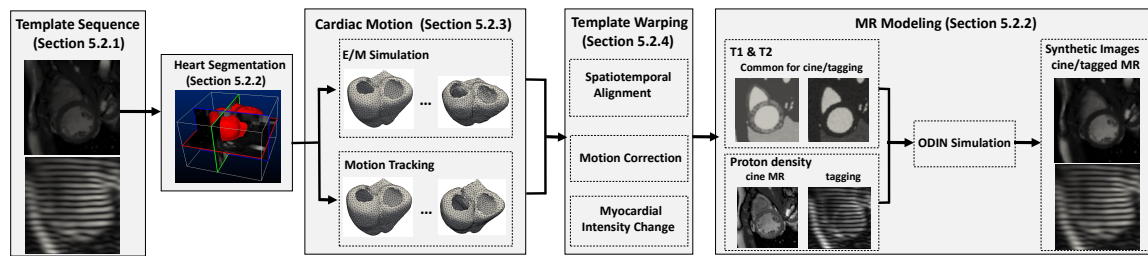


Figure VF.14: Le pipeline proposé pour la simulation des images d'IRM cine et d'IRM marquée.

Nous montrons un schéma du pipeline dans la Fig. VF.14. Chaque bloc spécifie le numéro de section où il est décrit en détail. Des acquisitions réelles (IRM cine/IRM marquée) sont utilisées comme des séquences type (Sect. 5.2.1) pour modéliser des textures d'image réalistes. La première étape consiste à segmenter le ventricule droit (VD) et le ventricule gauche (VG) dans la première image d'IRM cine. Le modèle E/M est alors appliqué à la géométrie 3D segmentée pour simuler des mouvements dans un cycle cardiaque. Des images d'IRM cine et d'IRM marquée sont générées par un simulateur physique qui prend des temps de relaxation T_1 et T_2 et des cartes de densité de protons comme entrées. Pour obtenir une texture d'image réaliste, des cartes de densité de protons sont dérivées des séquences type. Cela nécessite un alignement spatio-temporel entre des simulations E/M et des séquences type (Session 5.2.4).

5.2.1 Séquences type

Les séquences type utilisées dans cette étude proviennent de la base de données d'accès libre fournie dans [[Tobon-Gomez et al. \(2013\)](#)]. Pour chaque volontaire, on a acquis une séquence d'US, une séquence d'IRM cine et trois séquences d'IRM marquée. Étant donné que des images IRM ont été acquises dans le même système de coordonnées, des séquences IRM cine et IRM marquée sont naturellement alignées dans l'espace. Un ensemble de 24 points de repère identifiant les mêmes points clés dans toutes les modalités permet de dériver une simple transformation rigide pour passer du système d'IRM au système d'US [[Tobon-Gomez et al. \(2013\)](#)].

5.2.2 Modélisation d'IRM

Nous utilisons le simulateur ODIN [[Jochimsen et al. \(2006\)](#)] pour générer des images IRM cine et IRM marquée. Pour simuler une image 3D, nous devons fournir au simulateur ODIN deux cartes de temps de relaxation T_1 et T_2 ainsi qu'une carte de densité de proton. Dans cette étude, nous avons utilisé les mêmes cartes T_1 et T_2 pour générer des images d'IRM cine et d'IRM marquée, seules les cartes de densité de protons ont été calculées individuellement pour chaque modalité et pour chaque instant de la séquence simulée. La première étape est de calculer des cartes initiales de T_1 / T_2 pour la première image. Nous décrivons d'abord comment ces cartes initiales ont été générées. Nous donnons ensuite des détails sur la façon dont elles sont étendues à tous les instants.

Segmentation du cœur Parce que nous attribuons différentes valeurs de T_1 / T_2 par structure, nous devons d'abord segmenter la première image en différentes classes, c'est-à-dire le myocarde, le sang, les poumons et l'air. Puisque l'IRM cine fournit le meilleur

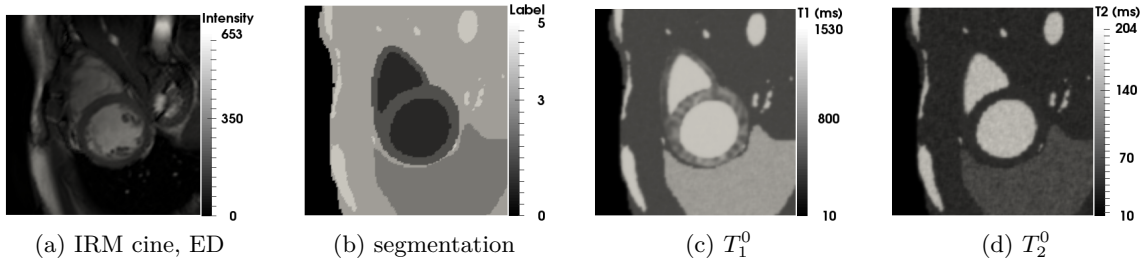


Figure VF.15: Illustration des différentes étapes impliquées pour simuler les cartes T_1 et T_2 initiales par rapport à la première image (ED).

contraste entre le myocarde et l'arrière-plan, elle représente un choix naturel pour extraire la géométrie cardiaque. Nous avons utilisé le pipeline de segmentation VP2HF proposé dans [Groth *et al.* (2012)] pour segmenter le myocarde et le sang. Nous avons ensuite segmenté le poumon et l'air à l'extérieur du corps manuellement. Enfin, les pixels restants ont été classés par seuillage: pixels à haute intensité appartenant au sang et le reste aux muscles. Fig. VF.15b montre un résultat de segmentation typique obtenu en utilisant cette procédure.

Cartes initiales de T_1 et T_2 Nous avons attribué des cartes de T_1 et T_2 en utilisant des valeurs moyennes et des valeurs d'écart type (désignées par u et σ) publiées dans [Tobon-Gomez *et al.* (2011)b]. À chaque pixel, des valeurs T_1 et T_2 sont échantillonnées à partir des distributions gaussiennes, donnant des cartes initiales désignées par T_1^0 et T_2^0 (voir Fig. VF.15c et VF.15d). Nous donnons les valeurs u et σ utilisées dans cette étude dans le tableau VF.1. De plus, comme les changements d'intensité d'IRM marquée contiennent beaucoup d'informations sur T_1 , il est possible d'en déduire les valeurs locales de T_1 à partir des intensités d'image. En particulier, les changements d'intensité au cours de la séquence d'IRM marquée peuvent être décrits comme suivant [Fischer *et al.* (1993)] [Wang *et al.* (2011)]:

$$I_{tag}^n = I_{tag}^0 \exp\left\{-\frac{n\Delta t}{T_1}\right\} \frac{\sin(\alpha_n)}{\sin(\alpha_0)} \prod_{j=0}^{n-1} \cos(\alpha_j), \quad \forall n \geq 1 \quad (\text{VF.19})$$

Où Δt est la résolution temporelle et I_{tag}^n sont les intensités d'image à l'instant n . α_n sont les angles de basculement de radiofréquence. Ils sont calculés par la méthode décrite dans [Ryf *et al.* (2005)].

l'équation VF.19 donne ainsi accès à des informations T_1 . Afin d'estimer la carte T_1 du myocarde, la procédure suivante a été répétée pour tous les pixels du myocarde. Pour un point donné en fin de diastole, nous l'avons suivi au travers de la séquence d'IRM marquée (cette étape est décrite plus loin dans la section 5.2.3). La valeur correspondante de T_1 a ensuite été estimée en résolvant un problème de minimisation:

$$\arg \min_{T_1} \sum_n \left(\log \left(\frac{I_{tag}^n \sin(\alpha_0)}{I_{tag}^0 \sin(\alpha_n) \prod_{j=0}^{n-1} \cos(\alpha_j)} \right) T_1 + n\Delta t \right)^2 \quad (\text{VF.20})$$

Étant donné qu'il existe trois séquences d'images IRM marquées par sujet, nous avons dérivé trois valeurs T_1 différentes pour le même point de myocarde. Un filtrage médian a

Table VF.1: Les valeurs de référence de T_1 et T_2 attachées à chaque type de tissu.

Label	Class	T1 (ms)		T2 (ms)	
		u	σ	u	σ
0	Air	0	0	0	0
1	Sang	1516	21	189	26
2	Myocarde	982	46	54	12
3	Poumon	1199	117	79	29
4	Autre (bas)	549	52	49	20
5	Autre (haut)	1516	21	189	26

ensuite été appliqué pour éliminer les valeurs aberrantes, donnant la carte finale T_1^0 (Fig. VF.15c).

Cartes dynamiques de T_1 et T_2 Étant donné que chaque image de la séquence simulée est générée de manière indépendante, les cartes initiales T_1^0 et T_2^0 doivent être déformées au cours du temps. Cela a été réalisé par une stratégie de recalage qui est décrite plus tard à la section 5.2.4. Les cartes dynamiques correspondantes sont désignées par T_1^k et T_2^k , avec k indexant l'instant de la séquence simulée.

Cartes de densité de proton Pour chaque instant de simulation, nous avons calculé la carte de densité de protons à partir des séquences type correspondantes. Cela garantit une texture d'image visuellement similaire à celle de la séquence du modèle. Pour ce faire, il faut aligner spatialement et temporellement la séquence du modèle avec les simulations. Ceci est réalisé par une stratégie de recalage détaillée dans la section 5.2.4. Les résultats de cette étape correspondent à une autre séquence d'images déformées désignée par \tilde{I}_{cine}^k ou \tilde{I}_{tag}^k .

Les images IRM cine cardiaques sont acquises par la séquence de précession de l'état d'équilibré (bSSFP) [Scheffler and Lehnhardt (2003)]. La carte de densité de protons ρ_{cine}^k peut ensuite être calculée par [Scheffler and Lehnhardt (2003)]:

$$\rho_{cine}^k = \tilde{I}_{cine}^k \sqrt{T_1^k / T_2^k} \quad (\text{VF.21})$$

En IRM marquée, les caractéristiques de la séquence CSPAMM fournissent des cartes ρ_{tag}^k [Wang *et al.* (2011)] comme:

$$\rho_{tag}^k = \tilde{I}_{tag}^k \exp^{\frac{TE}{T_2^*}} / \sin(\alpha_k^s) \quad (\text{VF.22})$$

Où α_k^s correspond à l'angle de basculement de radiofréquence. TE est le temps d'écho défini à 21 ms. T_2^* correspond au temps de relaxation spin-spin réel et est ici approximé par le temps de relaxation théorique T_2 [Haase (1990)]. Nous supposons donc $T_2^* = T_2^k$ dans la suite.

Simulation par ODIN Chaque image de la séquence simulée a été générée indépendamment à partir d'ODIN en utilisant les cartes T_1^k , T_2^k et ρ_{mod}^k dérivées ci-dessus (avec $mod = cine$ ou Tag) comme entrées. Nous avons utilisé respectivement les séquences IRM *odinfisp* et *odinepi* disponibles sous ODIN pour simuler des images d'IRM cine et d'IRM

marquée. En effet, ces séquences sont cohérentes avec le protocole d’acquisition, c’est-à-dire le bSSFP pour la séquence d’IRM cine [Tobon-Gomez *et al.* (2013)] et le EPI pour la séquence d’IRM marquée [Rutz *et al.* (2008)].

5.2.3 Mouvement cardiaque

La première image de l’IRM cine a été segmentée en différentes classes, y compris les régions du myocarde (VG et VD). À partir de ce masque, un maillage volumétrique (VG et VD) a été généré en utilisant la méthode décrite dans [Alessandrini *et al.* (2015)].

Simulation E/M Un maillage tétraédrique a été généré à partir du masque myocardique de la première image à l’aide du logiciel CGAL. Ce maillage est utilisé par le simulateur E/M pour générer une séquence de maillages volumétriques \mathcal{S}_k qui représente le mouvement myocardique d’un cycle cardiaque. Le simulateur E/M est basé sur le modèle Bestel-Clement-Sorine qui estime l’activation électrique et la contraction mécanique [Marchesseau *et al.* (2013)]. Il est implémenté dans le cadre de SOFA². Ce modèle a déjà démontré son efficacité pour la génération des séquences d’images US [Alessandrini *et al.* (2015)]. Les paramètres biophysiques tels que la contractilité, la rigidité et la conduction myocardiques locales régissent les équations du modèle E/M. En faisant varier ces paramètres, des champs de mouvement cardiaque (normal et pathologique) peuvent être simulés. Pour chaque patient, nous avons généré dans cette étude un cas sain, une dyssynchronie (LBBB) et quatre coeurs ischémiques. Pour la dyssynchronie, seul l’endocarde droit a été initialement activé. Pour l’ischémie, on a simulé l’occlusion artérielle dans différentes régions du VG: l’une pour l’artère descendante antérieure de gauche (LAD), une pour l’artère circonflexe gauche (LCX) et deux pour l’artère coronaire droite (RCA) [Duchateau *et al.* (2016)].

Suivi de mouvements cardiaques Étant donné que l’IRM cine et l’IRM marquée sont acquises dans le même système de coordonnées, nous avons utilisé la séquence d’IRM marquée pour effectuer le suivi de mouvement. Le VG et le VD du premier maillage du modèle E/M \mathcal{S}_0 ont été extraits. Ils sont ensuite suivis séparément par deux algorithmes de suivi afin d’optimiser la précision. La bordure du VG a été suivie par l’algorithme HarpAR, étant donné sa bonne fiabilité dans l’estimation de la déformation radiale [Zhou *et al.* (2015)]. L’algorithme dit SparseDemons a ensuite été utilisé pour effectuer le suivi du VD, compte tenu de sa bonne précision pour l’estimation de trajectoires et de son faible coût de calcul [Somphone *et al.* (2013)]. Pour éviter les éventuelles discontinuités à la frontière entre le VG et le VD parce qu’ils sont suivis indépendamment, nous avons raffiné les déplacements du VD en combinant les résultats de HarpAR et ceux de SparseDemons par une technique décrite dans l’appendice B.2.

5.2.4 Recalage des séquences type

Un alignement spatio-temporel entre les séquences du modèles et les simulation E/M est nécessaire pour dériver des cartes de densité de protons. Nous avons développé un nouveau cadre de recalage pour résoudre ce problème. Similairement à la méthode présentée dans [Alessandrini *et al.* (2015)], nous avons utilisé deux stratégies différentes pour le myocarde et l’arrière-plan, mais nous avons développé une stratégie dédiée pour assurer une transition lisse entre le myocarde et le reste de l’image.

²<https://www.sofa-framework.org/>

Modèle de transformation générique Comme [Alessandrini *et al.* (2015)], nous avons utilisé des points de repères myocardiques extraits des deux séquences de maillages \mathcal{S}_k et \mathcal{R}_t pour calculer des champs de déplacement. Cependant, nous avons également impliqué dans cette étude des repères statiques (dénommés \mathcal{B}) pour limiter la présence d'artefact de déformation irréaliste dans l'arrière-plan. Ces repères sont détectés à partir de la séquence d'images IRM cine. En particulier, pour chaque position de pixel, nous avons calculé la variation d'intensité d'IRM cine au cours de toute la séquence. Nous avons gardé les points qui ont la plus petite variation et forcé un espacement minimal de 5mm entre les points choisis.

Le but du modèle générique introduit est de calculer une transformation globale pour combiner efficacement un espace source (représenté par le maillage cardiaque \mathcal{M}_0) avec un espace cible (représenté par le maillage cardiaque \mathcal{M}_1) où \mathcal{M}_0 et \mathcal{M}_1 ont le même nombre de points. Dans les deux espaces, nous supposons la présence des mêmes points de repère de fond statique \mathcal{B} . La transformation envoie un pixel \mathbf{x} de l'espace source vers une position correspondante \mathbf{y} dans l'espace cible. Comme indiqué ci-dessus, différentes stratégies de transformation ont été appliquées au myocarde et à l'arrière-plan.

Pour des points myocardiques, puisqu'ils se trouvent tous à l'intérieur du maillage volumétrique \mathcal{M}_0 , la transformation correspondante a été calculée directement à partir des deux maillages volumétriques $\mathcal{M}_0 \rightarrow \mathcal{M}_1$. Il est facile de calculer la position correspondante \mathbf{y} . Cette procédure est désignée par $\mathbf{y} = MESH_{\{\mathcal{M}_0 \rightarrow \mathcal{M}_1\}}(\mathbf{x})$. En ce qui concerne des points d'arrière-plan, nous avons utilisé l'algorithme TPS pour modéliser la transformation sous-jacente. Nous avons sélectionné au hasard une fraction de points de maillage qui, avec les repères statiques, ont été utilisés pour calculer une transformation de type TPS. Cette procédure est désignée par $\mathbf{y} = TPS_{\{\mathcal{M}_0, \mathcal{B} \rightarrow \mathcal{M}_1, \mathcal{B}\}}(\mathbf{x})$. La transformation globale est ainsi écrite comme suit:

$$\begin{aligned} & \mathcal{T}_{\{\mathcal{M}_0, \mathcal{B} \rightarrow \mathcal{M}_1, \mathcal{B}\}}(\mathbf{x}) \\ &= \begin{cases} MESH_{\{\mathcal{M}_0 \rightarrow \mathcal{M}_1\}}(\mathbf{x}), & \text{si } \mathbf{x} \in \text{Myocarde} \\ TPS_{\{\mathcal{M}_0, \mathcal{B} \rightarrow \mathcal{M}_1, \mathcal{B}\}}(\mathbf{x}), & \text{autrement} \end{cases} \end{aligned} \quad (\text{VF.23})$$

Alignement temporel Les repères temporels correspondent à la fin diastole (ED) et à la fin systole (ES) on été choisis afin de calculer la transformation. Chaque instant k de la simulation correspond à un temps cardiaque (ms) de la séquence du modèle par l'opérateur ϕ qui est défini comme suit:

$$\phi(k) = \begin{cases} \frac{t^{es}}{k^{es}} k, & \text{if } k \leq k^{es} \\ t^{es} + \frac{k - k^{es}}{K - k^{es}} (t^{max} - t^{es}), & \text{autrement.} \end{cases} \quad (\text{VF.24})$$

K est le nombre d'images simulées et k^{es} correspond à l'instant ES. De même, t^{max} est le cycle cardiaque du modèle, alors que t^{es} est le temps cardiaque correspond au moment ES. La séquence d'IRM cine et la séquence d'IRM marquée sont rééchantillonnées aux temps cardiaques $\phi(k)$, avec $k \in [0, K - 1]$. Cela produit des séquences d'images alignées temporellement avec les simulations E/M (denommées \tilde{I}_{mod}^k).

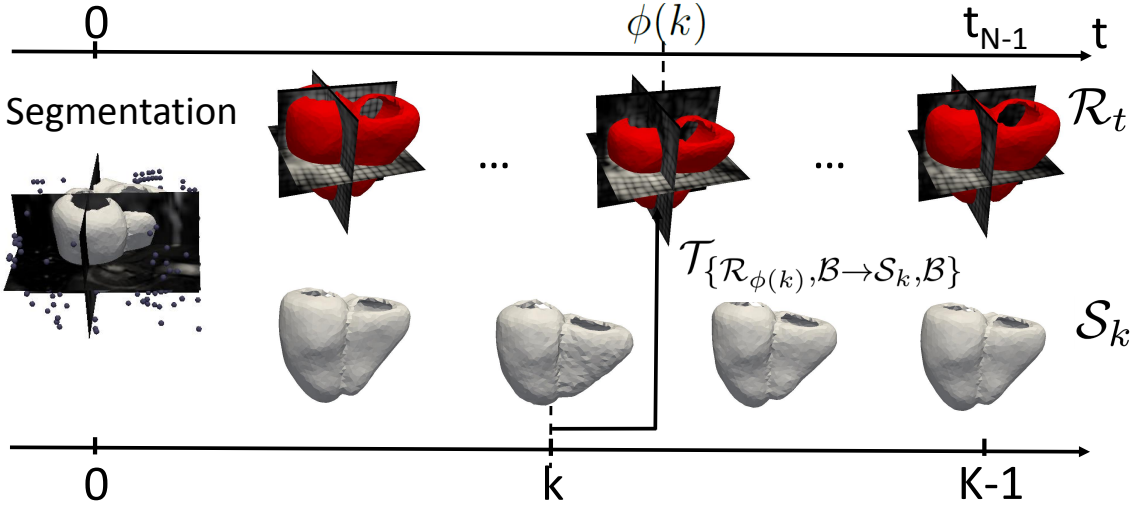


Figure VF.16: Illustration de l’alignement spatio-temporel utilisé pour le recalage de la séquence du modèle. Le maillage de segmentation est d’abord suivi dans la séquence d’images, ce qui conduit à une séquence de maillages (illustré en rouge). Ensuite, le modèle E/M est utilisé pour simuler des champs de mouvement myocardique, à partir du même maillage de segmentation. Cela génère une autre séquence de maillages (de couleur blanche). Pour l’alignement temporel, chaque instant de simulation k est mappé au temps cardiaque $\phi(k)$ de la séquence du modèle. L’alignement spatial consiste à déformer l’image de l’instant $\phi(k)$ vers le maillage de simulation \mathcal{S}_k .

L’alignement spatial Après la synchronisation temporelle, un alignement spatial est nécessaire pour aligner les images rééchantillonées \hat{I}_{mod}^k avec la géométrie E/M correspondante \mathcal{S}_k . Pour ce faire, nous utilisons la transformation générique:

$$\hat{I}_{mod}^k = \hat{I}_{mod}^k \circ \mathcal{T}_{\{\mathcal{R}_{\phi(k)}, \mathcal{B} \rightarrow \mathcal{S}_k, \mathcal{B}\}} \quad (\text{VF.25})$$

Où \hat{I}_{mod}^k est l’image déformée qui est alignée avec le maillage \mathcal{S}_k dans le temps et l’espace. La procédure d’alignement spatio-temporel est illustrée dans la Fig. VF.16.

Correction des mouvements myocardiques La séquence d’image alignée sur le résultat du modèle E/M est basée sur une approche de recalage. Cela peut introduire des artefacts dans les images synthétiques en ajoutant un résidu de mouvement au mouvement réel simulé par le modèle E/M. Contrairement à [Prakosa *et al.* (2013)], nous avons introduit dans cette étude une stratégie dédiée qui corrige le mouvement myocardique dans les images simulées. Pour assurer une cohérence avec le modèle E/M, les intensités myocardiques de chaque image de la séquence simulée ont été échantillonées à partir de la première image. Ceci est réalisé en déformant I_{mod}^0 à tous les instants de simulation, donnant une séquence complémentaire dénommée \bar{I}_{mod}^k :

$$\bar{I}_{mod}^k = I_{mod}^0 \circ \mathcal{T}_{\{\mathcal{S}_0, \mathcal{B} \rightarrow \mathcal{S}_k, \mathcal{B}\}} \quad (\text{VF.26})$$

Cette séquence déformée est utilisée pour fournir des intensités myocardiques tandis que la séquence \hat{I}_{mod}^k est utilisée pour obtenir des intensités du reste de l’image. Afin d’assurer une interface lisse entre ces deux régions, nous avons calculé une fonction de pondération gaussienne qui est centrée sur le myocarde pour chaque instant de simulation.

Nous avons extrait la surface myocardique de VG à partir de \mathcal{S}_k et l'avons convertie en une fonction implicite dénommée Γ_k . Cette fonction vaut 0 à l'endocarde et l'épicarde, est négative à l'intérieur du myocarde et positive à l'extérieur. Sa valeur minimale est désignée par τ_k^{min} . La fonction de pondération a ensuite été définie comme suit:

$$w_k(\mathbf{x}) = \exp\left\{-\frac{(\Gamma_k(\mathbf{x}) - \tau_k^{min})^2}{2\sigma^2}\right\} \quad (\text{VF.27})$$

Où σ contrôle le profile transmural de la fonction de pondération et est mis à 5 dans nos expériences. Des séquences déformées avec la correction de mouvement myocardique ont ensuite été calculées comme suit:

$$\tilde{I}_{mod}^k = w_k \bar{I}_{mod}^k + (1 - w_k) \hat{I}_{mod}^k \quad (\text{VF.28})$$

l'équation VF.28 révèle que la plupart des intensités de myocarde sont attribuées à partir de la première image, assurant un mouvement myocardique cohérent avec le modèle E/M. Les intensités de l'arrière-plan sont principalement récupérées à partir de la séquence alignée, préservant la nature réaliste des structures environnantes.

Variation d'intensité myocardique La séquence déformée (l'équation VF.28) implique des intensités constantes du myocarde au cours du cycle cardiaque. Ceci est irréaliste. Nous optons pour modéliser des variations d'intensité pour l'IRM cine et l'IRM marquée. En IRM marquée, la variation d'intensité temporelle est révélée par l'équation VF.19. Étant donné que les valeurs de T_1 sont déjà estimées, nous avons calculé le changement d'intensité et l'avons ajouté au \tilde{I}_{tag}^k . En IRM cine, nous avons utilisé un modèle linéaire pour modéliser le changement d'intensité. Nous supposons que l'intensité d'un point du myocarde varie linéairement entre ED et ES. Les paramètres du modèle sont estimés par la méthode des moindres carrés en utilisant la séquence réelle de l'IRM cine. Les changements d'intensité que nous avons calculés sont ajoutés aux images déformées \tilde{I}_{cine}^k .

5.2.5 Simulation US

Comme indiqué au début de cette section, le même pipeline général (Fig. VF.14) a été appliqué pour simuler des séquences US. Étant donné que les systèmes de coordonnées IRM et US peuvent facilement être alignés grâce aux points de repère manuels décrits dans la section 5.2.1, le même maillage initial segmenté à partir de la première image est utilisé. Seul le bloc "Modélisation d'IRM" a été remplacé par celui proposé dans [Alessandrini *et al.* (2015)] (bloc C dans l'article). Les intensités du speckle permettent de dériver des cartes de dispersion 3D avec des amplitudes de rétrodiffusion calculées à partir de la séquence US. À partir de ces cartes, un volume US a été simulé par convolution avec la fonction de PSF. COLE [Gao *et al.* (2009)] est choisi comme environnement de simulation en raison de son efficacité et sa précision du calcul.

5.3 Résultat

Nous avons utilisé dans cette étude trois volontaires de [Tobon-Gomez *et al.* (2013)]. Pour chaque volontaire, nous avons simulé un cas sain et cinq cas pathologiques, donnant une base de données d'accès libre composée de 18 patients virtuels. Pour chaque patient, cinq séquences synthétiques ont été générées (un IRM cine, trois IRM marquées et un US). Toutes les simulations ont été lancées à partir de la plate-forme d'imagerie virtuelle

VIP [Glatard *et al.* (2013)]³ qui permet l'exécution d'applications telles que ODIN en tant que service web et bénéficie de la puissance de calcul EGI⁴.

5.3.1 Propriétés d'image: évaluation qualitative

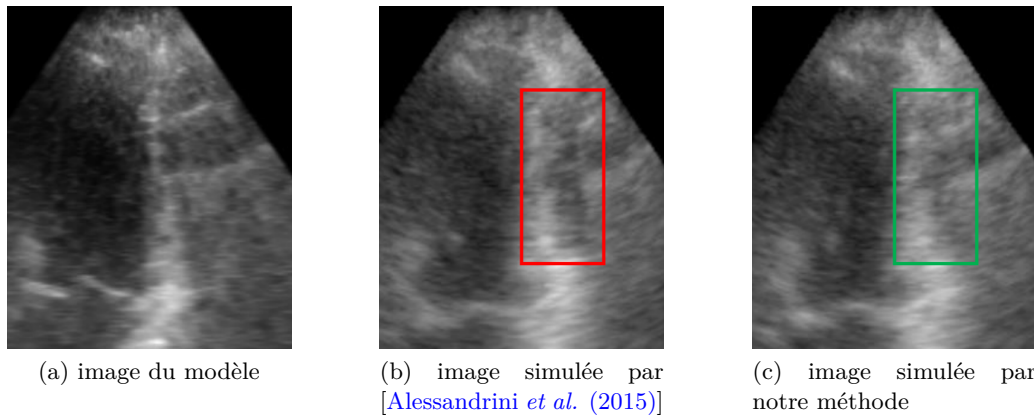


Figure VF.17: Illustration de l'intérêt de la méthode proposée pour mieux gérer l'interface entre le myocarde et les structures environnantes. a) image du modèle; b) image simulée par [Alessandrini *et al.* (2015)]; c) image simulée par notre méthode.

Le pipeline générique proposé permet la simulation des images multimodales réalistes, comme montrées dans les figures VF.18, VF.20 et VF.19. Fig. VF.17 révèle également l'efficacité de la fonction de pondération gaussienne (section 5.2.4) pour lisser l'interface entre le myocarde et les structures environnantes. En effet, le schéma proposé permet une transition lisse entre les différentes structures de cette région tout en préservant un mouvement myocardique cohérent avec le modèle E/M.

5.3.2 Propriétés d'image: évaluation quantitative

Nous nous concentrons dans cette section sur les caractéristiques des images IRM simulées. En particulier, le niveau de réalisme a été évalué quantitativement en mesurant la distribution d'intensité dans le myocarde puisqu'il s'agit de la caractéristique couramment exploitée pour l'analyse du mouvement. Les histogrammes correspondant à une séquence d'IRM cine simulée sont montrés dans la Fig. VF.22. À l'instant ED, les histogrammes calculés présentent des formes très similaires en IRM cine et IRM marquée. À l'instant ES, les histogrammes sont toujours en accord, même si une légère différence peut être observée. C'est parce que les intensités de T1 et T2 n'ont pas été mises à jour au cours du cycle cardiaque. Néanmoins, la similitude des distributions valide la stratégie proposée pour gérer les changements d'intensité du myocarde tout en préservant un mouvement cohérent avec le modèle E/M.

5.3.3 Propriétés mécaniques

Indices globaux Table VF.2 affiche les volumes du VG à ED et ES ainsi que la fraction d'éjection correspondante pour les cas sains et pathologiques. Ces valeurs sont calculées

³<https://vip.creatis.insa-lyon.fr>

⁴<https://www.egi.eu>

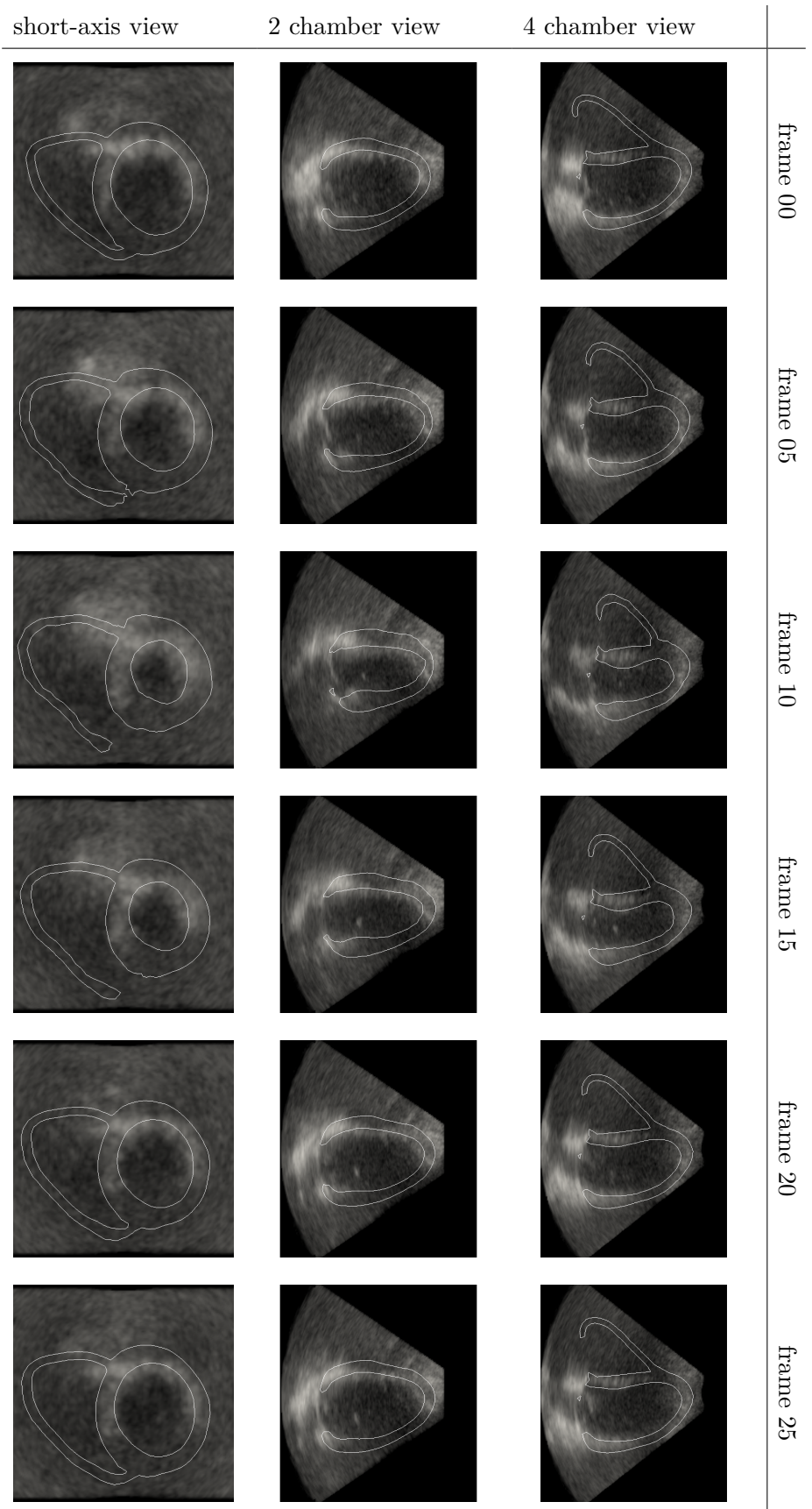


Figure VF.18: Des images US simulées par notre méthode.

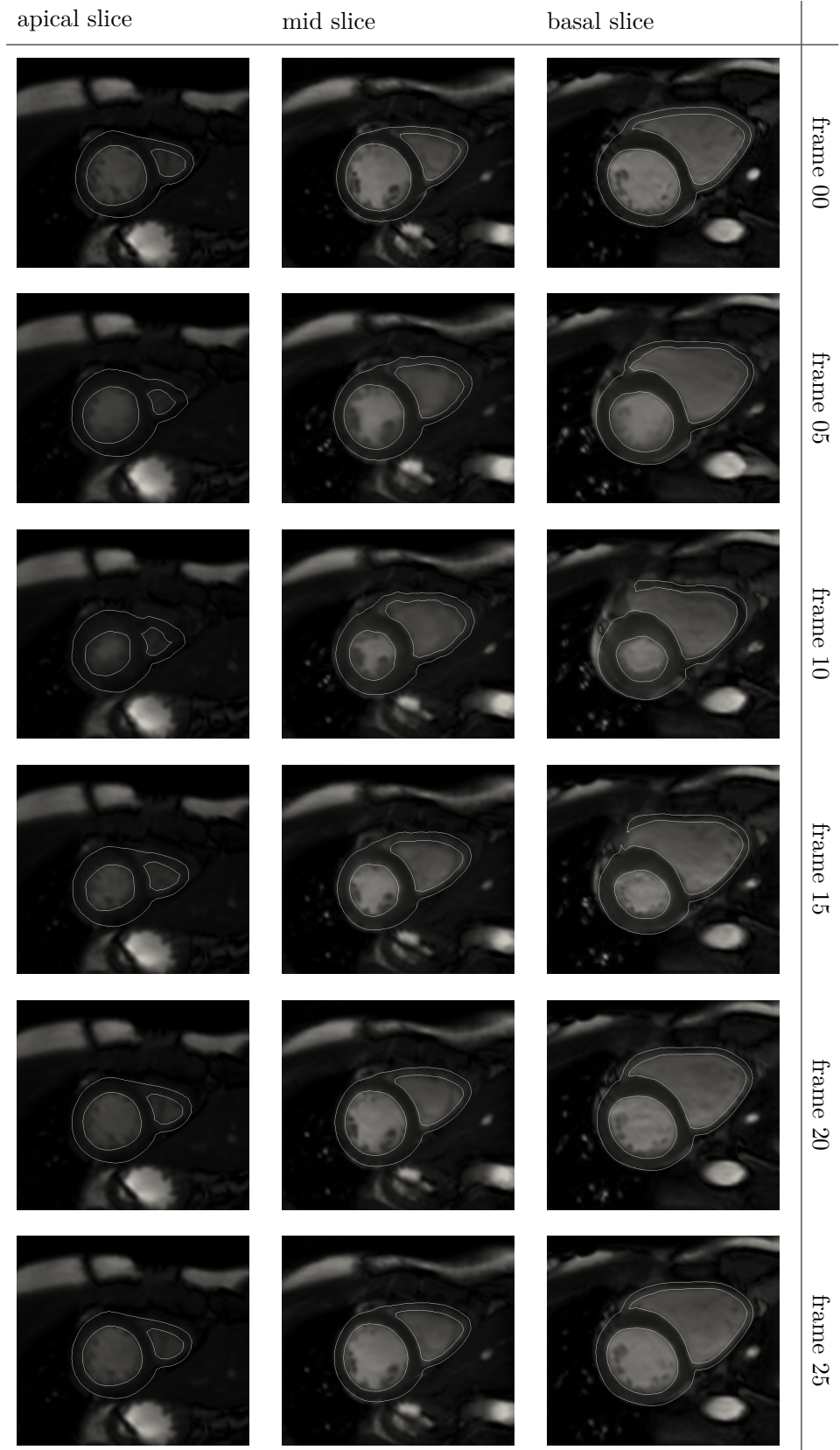


Figure VF.19: Des images IRM cine simulées par notre méthode.

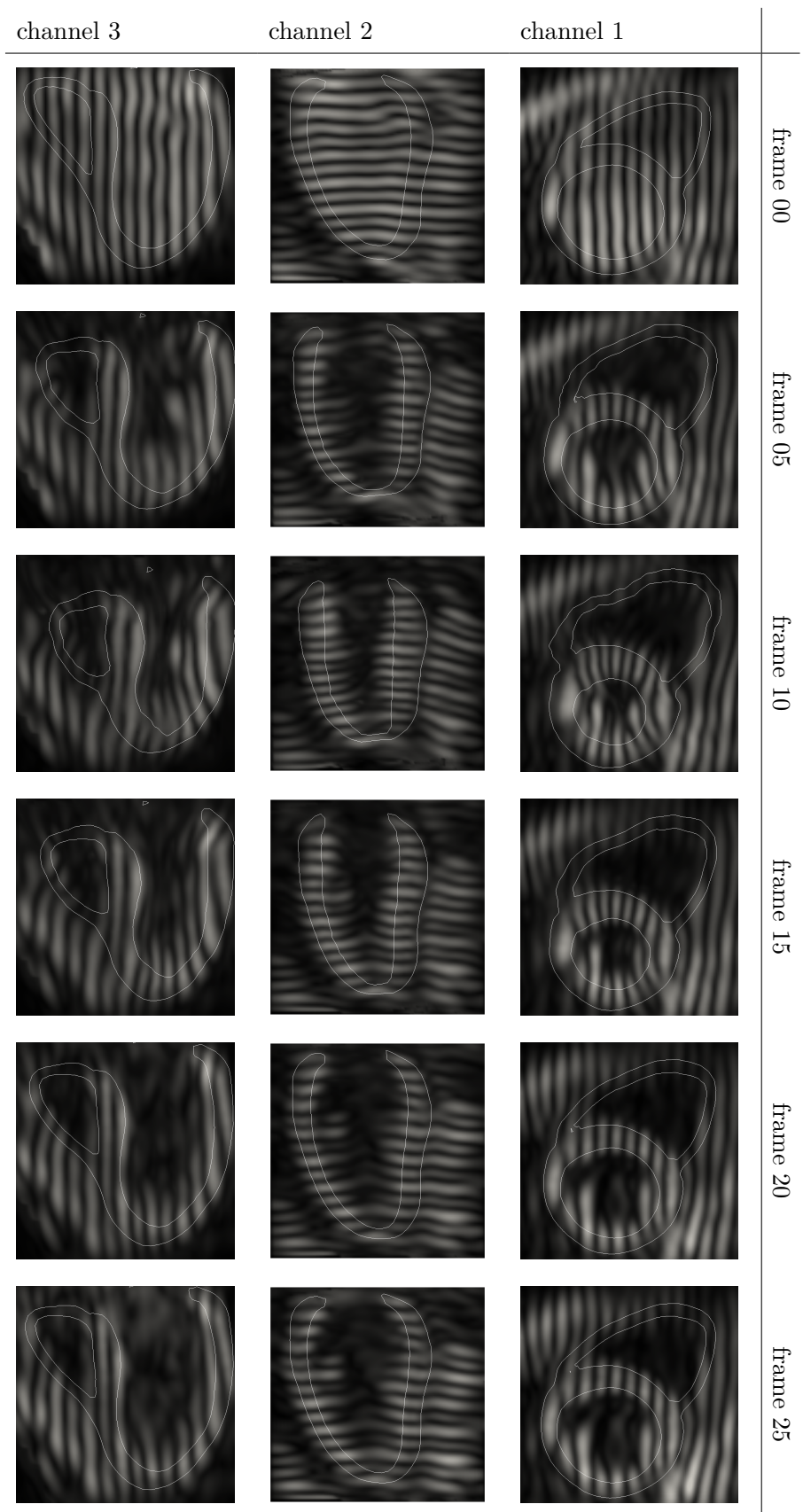


Figure VF.20: Des images IRM marquées simulées par notre méthode.

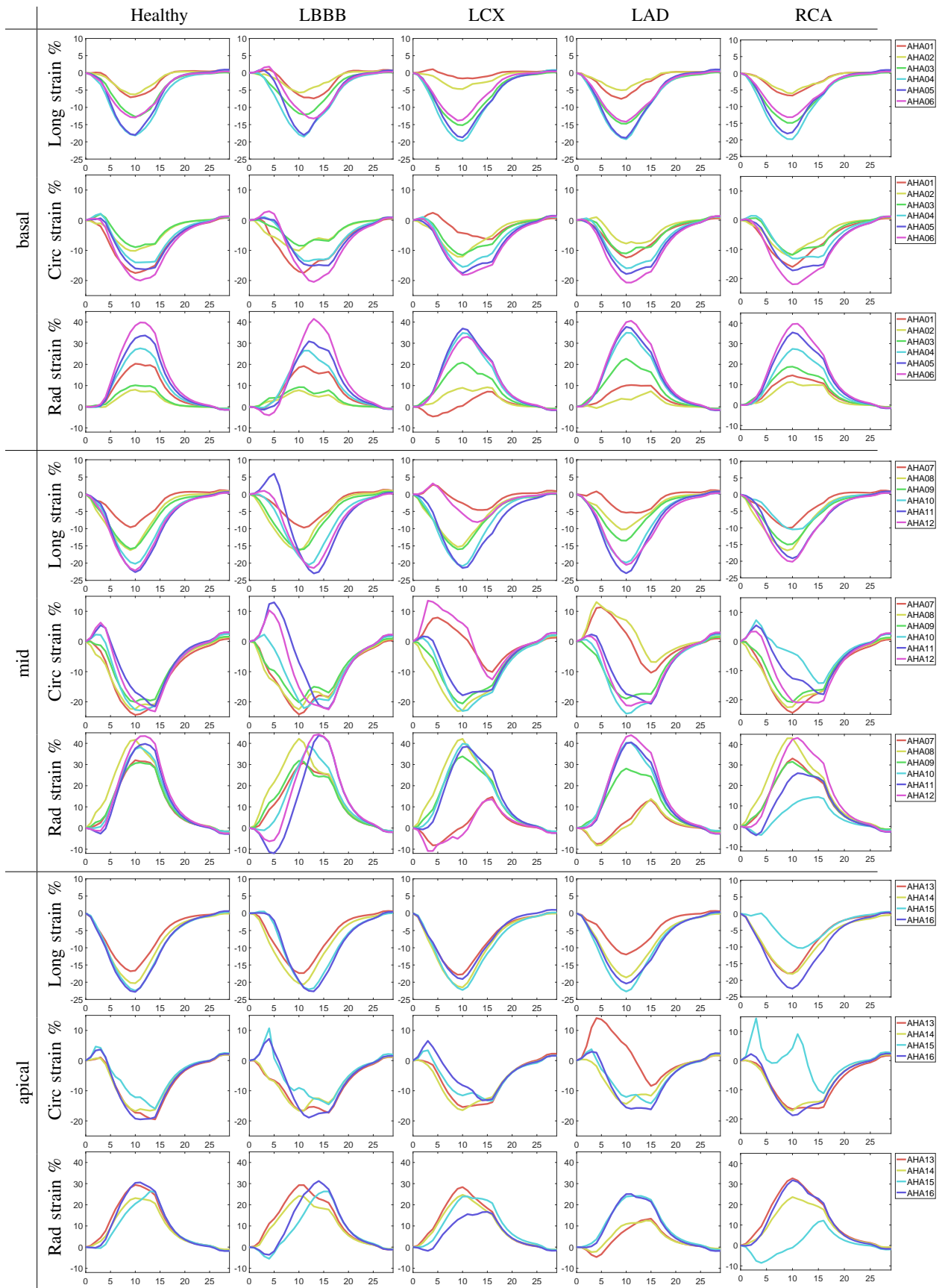


Figure VF.21: Un exemple des courbes de déformations régionales pour les 5 cas simulés.

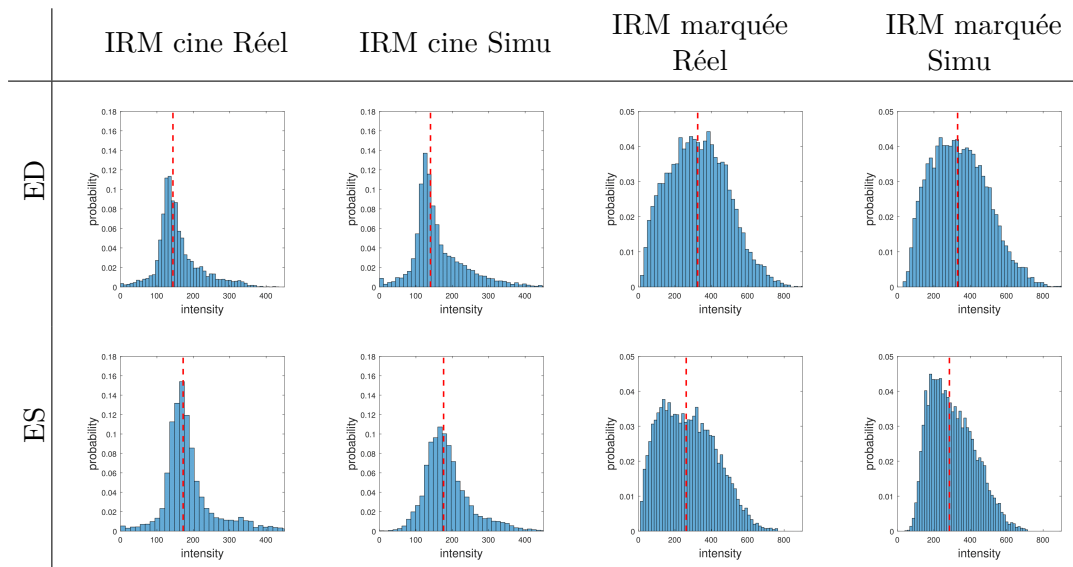


Figure VF.22: Les histogrammes sur les intensités du myocarde dans les données IRM réelles et simulées. Les lignes rouges montrent l'intensité médiane.

Table VF.2: Les volumes moyens du VG aux instants ED/ES et les valeurs d'EF réparties entre la population virtuelle.

	Healthy	LBBB	LCX	LAD	RCA	RCA2
ED (mL)	104.0	104.0	104.0	104.0	104.0	104.0
ES (mL)	49.6	52.8	65.7	60.9	60.3	63.4
EF (%)	52.3	49.2	36.8	41.4	42.0	39.0

à partir des maillages simulés \mathcal{S}_k . Pour le cas sain, les volumes du VG présentent des valeurs autour de 104 mL à ED et 50 mL à ES, ce qui correspond aux valeurs de référence publiées dans [Aune *et al.* (2010)]. Pour la dyssynchronie, les volumes à ES augmentent légèrement (environ 53 mL), montrant une réduction du débit cardiaque. Cette tendance est plus claire dans les cas ischémiques où les volumes sont supérieurs à 60 mL à ES. En ce qui concerne la fraction d'éjection, les valeurs sont autour de 52 % pour les cas sains et 40 % pour les cas ischémiques, ce qui correspond également aux valeurs données dans la littérature.

Courbes de déformation Nous fournissons dans la Fig. VF.21 l'ensemble des courbes de déformations régionales (radiales, longitudinales et circonférentielles) aux niveaux basal, centre et apical du VG pour un cas sain et quatre cas pathologiques. La carte de couleur utilisée pour afficher les courbes est fournie dans l'appendice B.3. Leurs propriétés sont conformes à celles décrites dans la littérature. Par exemple, dans le cas de LBBB, les temporisations à l'instant ES diffèrent entre le septum (AHA n 2,3,8,9,14) et la paroi latérale (AHA n 5,6,11,12,16). Le septum est activé légèrement avant la paroi latérale, ce qui signifie que le myocarde se contracte de manière asynchrone. De plus, les cas ischémiques présentent de grandes disparités entre les segments sains et les segments pathologiques. Des valeurs de déformation réduites sont observées pour les segments affectés.

5.4 Résumé

Dans ce chapitre, nous avons développé un pipeline générique pour simuler des images d'IRM cine, l'IRM marquée et l'US. Des champs de mouvement de référence ont été générés par un modèle électromécanique. Des séquences du modèle ont été alignées avec les simulations électromécanique par une nouvelle technique de recalage qui assure que i) le mouvement représenté dans des séquences synthétiques correspond au modèle E/M et ii) une transition lisse entre le myocardium et l'arrière-plan. Les images IRM et US ont été générées par des simulateurs physiques appropriés. Nous avons analysé les propriétés d'image tant sur le plan qualitatif que quantitatif. Au total, nous avons simulé 18 sujets virtuels, représentant 90 séquences synthétiques. Cette base de données a été rendue publique via un site web dédié.

Chapitre 6. Un algorithme générique HarpAR et une étude préliminaire de benchmarking

6.1 Introduction

Dans le chapitre 4, nous avons présenté une extension 3D de l'algorithme de suivi HARP développé pour l'IRM marquée 3D [Rutz *et al.* (2008)]. L'algorithme que nous avons proposé utilise la nature multicanale de l'acquisition d'IRM marquée et combine le suivi de flux optique avec un modèle de régularisation anatomique. L'algorithme du suivi de la phase HARP avec la régularisation anatomique (HarpAR) a été validé sur des séquences synthétique et réelles. Toutefois, la validation sur des données réelles se limite principalement aux mesures qualitatives. La validation quantitative en utilisant la déformation du myocarde est importante puisque nous visons à quantifier des déformations myocardiques de manière précise, grâce au modèle de régularisation anatomique.

Dans le chapitre 5, nous avons introduit un nouveau pipeline de simulation afin de générer des séquences d'images réalistes en US et IRM pour le même sujet virtuel. Au total, 18 sujets virtuels ont été simulés. Pour chaque patient virtuel, nous avons simulé une séquence d'IRM marquée 3D, une séquence d'IRM cine 3D et une séquence d'échographie 3D. Cette base de données peut être utilisée pour comparer la performance des différents algorithmes de suivi de mouvements.

Dans ce chapitre, nous présentons un algorithme de suivi de mouvement générique et évaluons sa performance sur le suivi de mouvements cardiaques par rapport à une autre méthode dite SparseDemons [Somphone *et al.* (2013)]. Ce chapitre est organisé comme suit: premièrement, nous présentons un algorithme de recalage basé sur la phase HARP (Section 6.2). Ensuite, dans la section 6.3 nous proposons une version généralisée de l'algorithme de HarpAR (dénommée comme gHarpAR) et montrons un exemple de benchmarking en comparant sa performance par rapport à SparseDemons sur des données synthétiques générée dans le chapitre 5.

6.2 Le recalage des images IRM marquées basé sur la phase

Le suivi de mouvements myocardiques peut être considéré comme un problème de recalage. Nous présentons ici le modèle du mouvement utilisé pour représenter le déplacement du cœur de l'instant t à $t - 1$.

6.2.1 Modèle de mouvement

Nous avons déjà introduit dans le chapitre 4 le modèle de mouvement anatomique. Le domaine du myocarde du VG est partitionné en fenêtres locales. Les fonctions de fenêtre $\varphi^{(i)}(\mathbf{x})$ ont une forme gaussienne. Elles sont définies en satisfaisant les propriétés de la *partition de l'unité* [Makram-Ebeid and Somphone (2007)] (i.e. $\forall \mathbf{x}, \forall i, \varphi^{(i)}(\mathbf{x}) \geq 0$; $\forall \mathbf{x}, \sum_i \varphi^{(i)}(\mathbf{x}) = 1$). À l'intérieur de chaque fenêtre i , le mouvement cardiaque de $t \rightarrow t - 1$ est modélisé par une transformation affine dans l'espace anatomique $\{r^{(i)}, l^{(i)}, c^{(i)}\}$ (Chapitre 4):

$$\mathbf{u}_t^{(i)}(\mathbf{x}) = L_r^{(i)}(\mathbf{x})\hat{\mathbf{e}}_r(\mathbf{x}) + L_l^{(i)}(\mathbf{x})\hat{\mathbf{e}}_l(\mathbf{x}) + L_c^{(i)}(\mathbf{x})\rho(\mathbf{x})\hat{\mathbf{e}}_c(\mathbf{x}) \quad (\text{VF.29})$$

$$L_d^{(i)}(\mathbf{x}) = a_{dr}^{(i)}r^{(i)}(\mathbf{x}) + a_{dl}^{(i)}l^{(i)}(\mathbf{x}) + a_{dc}^{(i)}c^{(i)}(\mathbf{x}) + b_d^{(i)} \quad (d = r, l, c) \quad (\text{VF.30})$$

Où $\hat{\mathbf{e}}_d(\mathbf{x})$ (avec $d = r, l, c$) sont les directions *radiales*, *longitudinales* et *circonférentielles*. $\rho(\mathbf{x})$ est la distance au long axe du VG. $a_{mn}^{(i)}(m, n = r, l, c)$ et $b_m^{(i)}(m = r, l, c)$ sont les paramètres du modèle (Chapitre 4).

Imposer l'incompressibilité du myocarde permet de remplacer $a_{rr}^{(i)}$ par une combinaison linéaire de tous les autres paramètres, donnant lieu à un modèle de 11 paramètres par fenêtre. Pour cela, le lecteur peut trouver plus de détails dans le chapitre 4. Le mouvement final est obtenu en mélangeant les mouvements locaux pondérés par les fonctions de fenêtre:

$$\mathbf{u}_t(\mathbf{x}) = \sum_i \varphi^{(i)}(\mathbf{x}) \mathbf{u}_t^{(i)}(\mathbf{x}) \quad (\text{VF.31})$$

$\mathbf{u}_t(\mathbf{x})$ est un modèle de mouvement qui a $11 \times \mathcal{N}$ paramètres (\mathcal{N} étant le nombre de fenêtre). Contrairement à la méthode introduite dans le chapitre 4 où le suivi de mouvement est effectué en deux phases consécutives: 1) le suivi en utilisant l'algorithme de HARP et 2) l'ajustement des résultats de HARP au modèle paramétrique, nous proposons ici d'ajuster les paramètres du modèle en une seule fois en minimisant une énergie globale. Cette stratégie évite l'accumulation des erreurs de suivi. Nous prévoyons donc une meilleure précision de suivi. Nous décrivons le cadre de recalage dans la section suivante.

6.2.2 Recalage basé sur la phase

Pour suivre le mouvement cardiaque de $t \rightarrow t-1$, étant donné une estimation initiale de déplacement dénommée $\mathbf{u}(\mathbf{x})$, l'idée est de trouver un champ de déplacement incrémental $\mathbf{v}(\mathbf{x}) = \sum_i \varphi^{(i)}(\mathbf{x}) \mathbf{v}^{(i)}(\mathbf{x})$ en minimisant une énergie E définie comme suit:

$$\begin{aligned} E(\mathbf{v}; \mathbf{u}) &= \int_{\Omega} \sum_{k=0}^2 \omega_k(\mathbf{x}) \left(\mathcal{A}_k^t(\mathbf{x}) - \mathcal{A}_k^{t-1}(\mathbf{x} + \mathbf{u}(\mathbf{x})) + \mathbf{v}(\mathbf{x}) \right)^2 d\mathbf{x} \\ \text{avec } \omega_k(\mathbf{x}) &= \sqrt{\mathcal{M}_k^t(\mathbf{x}) \mathcal{M}_k^{t-1}(\mathbf{x} + \mathbf{u}(\mathbf{x}))} \end{aligned} \quad (\text{VF.32})$$

Où \mathcal{A}_k^t et \mathcal{A}_k^{t-1} sont des images de phase. Nous appliquons les approximations du premier ordre sur \mathcal{A}_k^{t-1} , ce qui conduit à l'équation suivante:

$$\begin{aligned} E(\mathbf{v}; \mathbf{u}) &\approx \int_{\Omega} \sum_{k=0}^2 \omega_k(\mathbf{x}) \left(\xi_k(\mathbf{x}) - \boldsymbol{\eta}_k(\mathbf{x}) \cdot \mathbf{v}(\mathbf{x}) \right)^2 d\mathbf{x} \\ \text{with } \xi_k(\mathbf{x}) &= \mathcal{A}_k^t(\mathbf{x}) - \mathcal{A}_k^{t-1}(\mathbf{x} + \mathbf{u}(\mathbf{x})) \\ \boldsymbol{\eta}_k(\mathbf{x}) &= \nabla \mathcal{A}_k^{t-1}(\mathbf{x} + \mathbf{u}(\mathbf{x})) \end{aligned} \quad (\text{VF.33})$$

ξ_k et $\boldsymbol{\eta}_k$ sont calculés à partir de la phase repliée [Osman et al. (1999)]. En utilisant les propriétés de la *partition de l'unité* de $\varphi^{(i)}$, il est facile de prouver que l'énergie globale

E est bornée par la somme des énergies locales:

$$\begin{aligned}
 E(\mathbf{v}; \mathbf{u}) &\approx \\
 &\int_{\Omega} \sum_{k=0}^2 \omega_k(\mathbf{x}) \left(\sum_i \varphi^{(i)}(\mathbf{x}) \left(\xi_k(\mathbf{x}) - \boldsymbol{\eta}_k(\mathbf{x}) \cdot \mathbf{v}^{(i)}(\mathbf{x}) \right) \right)^2 d\mathbf{x} \\
 &\leq \sum_i \int_{\Omega} \varphi^{(i)}(\mathbf{x}) \sum_{k=0}^2 \omega_k(\mathbf{x}) \left(\xi_k(\mathbf{x}) - \boldsymbol{\eta}_k(\mathbf{x}) \cdot \mathbf{v}^{(i)}(\mathbf{x}) \right)^2 d\mathbf{x} \\
 &= \sum_i E^{(i)}(\mathbf{v}^{(i)}; \mathbf{u})
 \end{aligned} \tag{VF.34}$$

Cela signifie que l'énergie globale $E(\mathbf{v}; \mathbf{u})$ peut être minimisée en optimisant toutes les énergies locales $E^{(i)}(\mathbf{v}^{(i)}; \mathbf{u})$ [Makram-Ebeid and Somphone (2007)]. Le problème d'optimisation est donc décomposé en un ensemble des problèmes locaux. Comme $v^{(i)}$ est linéaire par rapport à ses paramètres, $E^{(i)}$ a une forme quadratique. Nous minimisons $E^{(i)}$ en résolvant un système linéaire.

La procédure décrite ci-dessus permet d'estimer le mouvement entre deux images successives. Les mouvements du myocarde au cours du cycle cardiaque sont obtenus en répétant les suivis.

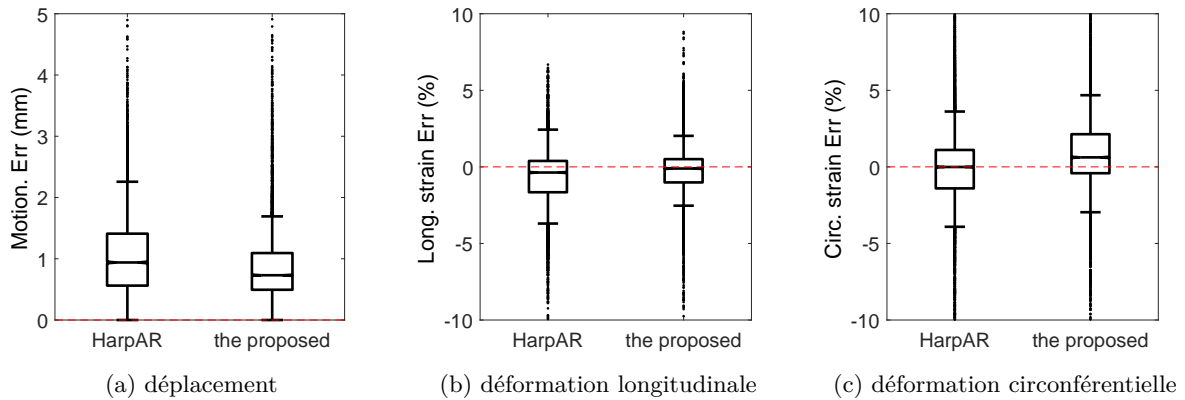


Figure VF.23: La comparaison entre l'algorithme HarpAR et la méthode proposée en utilisant la précision sur l'estimation du mouvement et de la déformation.

6.2.3 Résultats sur des images synthétiques

L'algorithme que nous avons proposé a été comparé à la méthode HarpAR (chapitre 4) en utilisant les 18 séquences d'IRM marquées simulées dans le chapitre 5. Le mouvement cardiaque est suivi par ces deux algorithmes. Nous avons calculé les erreurs du mouvement et de la déformation au niveau des segments AHA. Les erreurs de tous les instants et l'ensemble des 18 séquences sont combinées et s'affichent dans la figure VF.23. Nous observons que notre méthode obtient les erreurs de mouvement et de déformation longitudinale légèrement réduites par rapport à HarpAR. Ceci est confirmé par le calcul de RMSE: pour HarpAR, les RMSEs sur le mouvement et la déformation longitudinale sont respectivement 1,26 mm et de 2,13%. Ceux deux valeurs obtenues par la méthode proposée sont réduites aux 1,05 mm et 1,71% respectivement.

6.3 Une version généralisée de HarpAR: l'algorithme gHarpAR

Dans la section 6.2, le modèle de mouvement introduit dans le chapitre 4 est intégré dans un cadre de recalage d'image classique. Les paramètres du modèle sont estimés en minimisant la dissemblance de phase. La méthode de recalage proposée est ensuite évaluée sur des images d'IRM marquées synthétiques. Les résultats montrent une légère amélioration de la précision de quantification par rapport à l'algorithme HarpAR présenté dans le chapitre 4. En fait, le même concept peut être étendu aux images d'échographie et d'IRM cine. Dans cette section, nous proposons une version généralisée de l'algorithme HarpAR (dénommé gHarpAR) et montrons un premier exemple de benchmarking en utilisant des séquences d'images synthétiques simulées dans le chapitre 5.

6.3.1 L'algorithme générique gHarpAR

La formulation mathématique Le suivi de mouvements cardiaques peut être formulé comme un problème de recalage. Le suivi du mouvement de l'instant ref à l'instant t nécessite de résoudre les paramètres de \mathbf{u} en minimisant une énergie définie comme suit:

$$\underset{\mathbf{u}}{\operatorname{argmin}} \int_{\Omega} \sum_{k=0}^{K-1} w_k(\mathbf{x}) \left(I_k^{ref}(\mathbf{x}) - I_k^t(\mathbf{x} + \mathbf{u}(\mathbf{x})) \right)^2 d\mathbf{x} \quad (\text{VF.35})$$

Où \mathbf{u} représente le mouvement de l'instant ref à t . Il est défini sur le modèle anatomique du VG et le nombre de paramètres est $11 \times \mathcal{N}$ (\mathcal{N} étant le nombre de fenêtres). Ω représente le domaine du myocarde. k indexe le canal de la séquence et K est le nombre de canaux. Par exemple, en IRM marquée, $K = 3$. L'échocardiographie et l'IRM cine ont un seul canal, donc $K = 1$. I_k^t est la séquence d'images d'intensité ou de la phase. I_k^{ref} est l'information (intensité ou phase) de l'instant ref . Enfin, w_k est le poids de confiance.

Le suivi de mouvements Nous avons introduit la manière que nous calculons le champ de mouvement de l'instant ref à l'instant t . Nous optons pour une stratégie de suivi de l'instant courant au suivant. Le suivi du mouvement myocardique au cours du cycle cardiaque est donc considéré comme une succession des problèmes de recalage.

L'implémentation pour différentes modalités L'algorithme générique gHarpAR doit être implémenté selon la modalité d'imagerie. Par exemple, nous devons décider quel type d'information (intensité ou phase) doit être utilisé dans l'équation VF.35. En IRM marquée, l'intensité du myocarde diminue en fonction du temps à cause de *tag fading* [Osman *et al.* (1999)]. La phase HARP est alors préférée à l'intensité afin d'assurer une meilleure précision de suivi. De plus, dans Eq VF.35, $K = 3$ (il y a trois canaux d'IRM marquée). Par ailleurs, l'image non marquée est utilisée comme les poids de confiance w_k où k indexe le canal.

En US et IRM cine, un seul canal est disponible, donc $K = 1$. De plus, il est naturel de supposer que pour un point matériel donné, son intensité reste la même entre deux images consécutives. Nous choisissons donc de suivre le mouvement à partir des images d'intensité. w_k est définie comme une carte constante qui vaut 1 partout.

6.3.2 Résultats sur des images synthétiques

Grâce aux données synthétiques générées dans le chapitre 5, nous pouvons maintenant évaluer la performance des deux algorithmes de suivi (gHarpAR et SparseDemons) au travers des modalités d'imagerie (US, IRM cine et IRM marquée). Au total, 18 patients

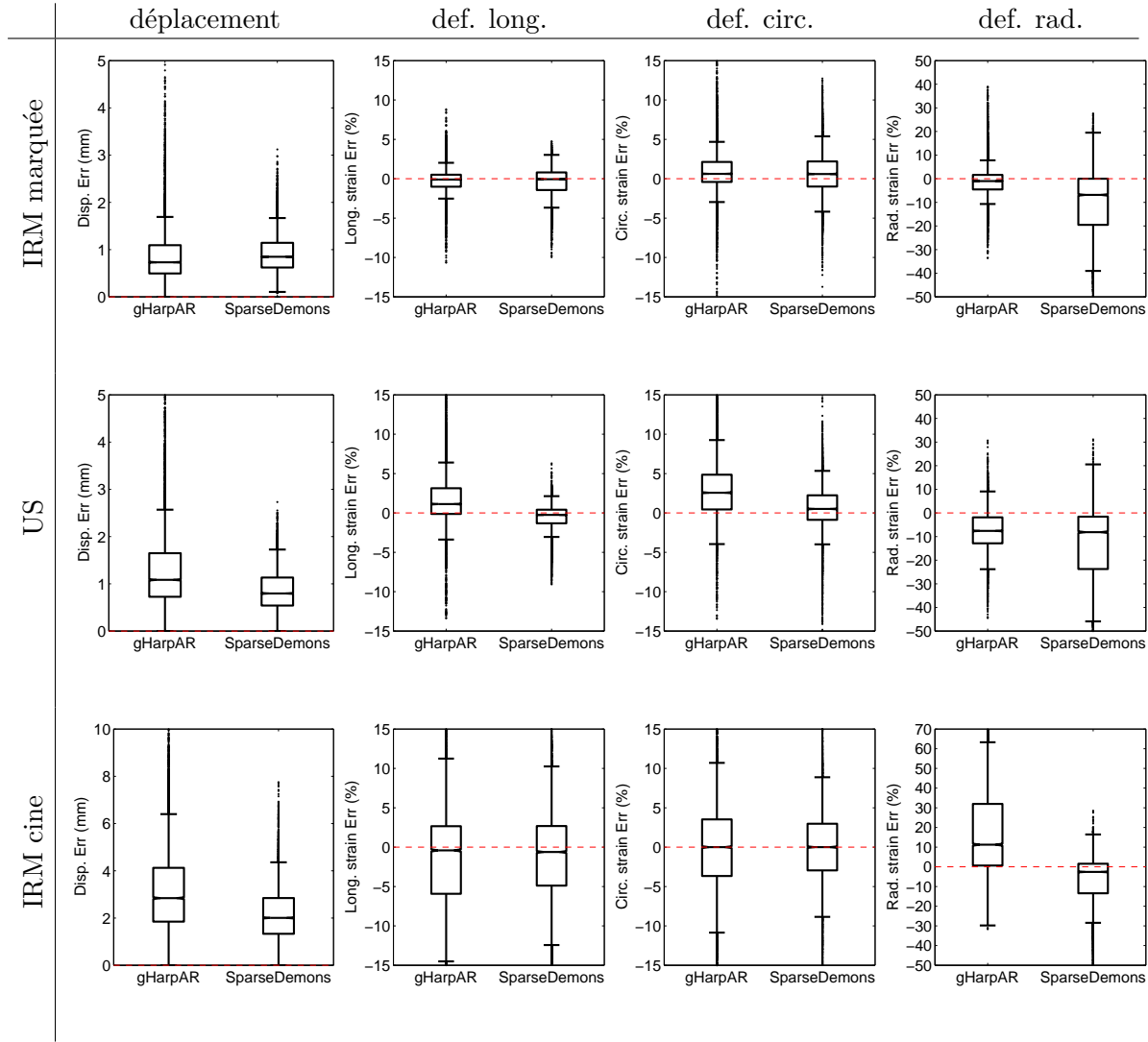


Figure VF.24: La comparaison entre gHarpAR et SparseDemons en utilisant les erreurs du mouvement et de la déformation. Les deux algorithmes ont été évalués sur les 18 patients virtuels simulés dans le chapitre 5. Les erreurs de quantifications sont calculées au niveau des segments AHA. Les erreurs de tous les instants et tous les sujets sont combinées.

virtuels sont inclus dans cette étude, donnant 54 séquences synthétiques. Les erreurs de tous les instants et tous les patients virtuels sont combinées et nous affichons les résultats sous forme de boxplot (Fig. VF.24). Nous observons que globalement, le mouvement et les déformations quantifiées à partir d'IRM marquée et d'US montrent des erreurs plus petites que celles d'IRM cine. C'est parce que contrairement à l'IRM marquée ou l'US, il n'existe aucun marqueur dans le myocarde en IRM cine. Le myocarde montre donc des intensités presque homogènes. Cela entrave l'estimation de mouvement. Par exemple, sur les résultats de l'algorithme SparseDemons, nous observons que l'erreur médiane sur le déplacement est inférieure à 1 mm en IRM marquée et US. Toutefois, en IRM cine, cette valeur augmente de 100% à environ 2 mm.

Entre gHarpAR et SparseDemons, nous observons que les deux algorithmes ont atteint des précisions de mouvement et déformation similaires en IRM marquée. Pourtant, sur la déformation radiale, gHarpAR obtient des valeurs beaucoup plus précises. En IRM cine,

il est clair que SparseDemons surclasse gHarpAR sur le mouvement et sur les trois composantes de déformations. En US, SparseDemons estime des déformations longitudinales et circonférentielles de manière plus précise, tandis que gHarpAR obtient de meilleures précisions sur la déformation radiale grâce à la régularisation d'incompréssibilité. De plus, à partir des résultats obtenus en IRM marquée, nous observons que SparseDemons surclasse légèrement gHarpAR sur l'estimation du mouvement, mais montre des erreurs plus importantes sur les déformations longitudinales et circonférentielles. Cependant, sur la déformation radiale, l'erreur obtenue par SparseDemons est presque deux fois supérieure à celle de gHarpAR. Cela confirme l'intérêt de la régularisation radiale [Zhou *et al.* (2015)].

Les analyses ci-dessus sont soutenues par le test de Levene réalisé sur les données montrées dans la figure VF.24. En IRM marquée, sur le mouvement et les trois composantes de déformation, le test de Levene obtient une valeur p inférieure à 0,05, rejetant l'hypothèse nulle selon laquelle les variances sont égales. Nous combinons ce résultat avec une inspection visuelle de la figure VF.24, nous considérons que SparseDemons obtient une variance plus petite sur l'erreur de mouvement alors que la dispersion est plus grande sur les erreurs de déformations longitudinales et circonférentielles.

6.4 Résumé

Dans cette section, nous avons proposé un algorithme générique dénommé gHarpAR. L'algorithme est évalué sur des séquences synthétiques d'US, d'IRM marquée et d'IRM cine générées dans le chapitre 5. Sur l'estimation du mouvement et de la déformation, nous avons observé que gHarpAR surclasse l'algorithme SparseDemons pour quantifier des images IRM marquées. En ce qui concerne l'IRM cine, SparseDemons est le meilleur choix car il permet d'imposer une régularisation spatiale plus forte, menant de meilleurs résultats de suivi. En US, grâce à la régularisation radiale, gHarpAR a estimé des déformations radiales beaucoup plus précises que celles obtenues par SparseDemons. Toutefois, SparseDemons obtient de meilleures précisions sur des déformations longitudinales et circonférentielles ainsi que le mouvement.

IV. Conclusions et perspectives

Chapitre 7. Conclusions et perspectives

7.1 Conclusion

Dans cette thèse, nous avons proposé une nouvelle extension 3D de la célèbre méthode de suivi de la phase harmonique. Le suivi de flux optique basé sur les phases a été combiné avec un modèle de régularisation anatomique afin d'estimer les mouvements cardiaques spatialement lisses et anatomiquement cohérents. En particulier, des efforts particuliers ont été faits pour assurer une estimation précise de la déformation radiale en imposant l'incompressibilité du myocarde. Le modèle a été optimisé par une technique de régression pondérée par fenêtre, ce qui a réduit la complexité du calcul en décomposant un système global en un nombre de systèmes locaux qui sont plus facile à résoudre. Nous avons réglé les paramètres du modèle sur un ensemble de données d'IRM marquées synthétiques. L'algorithme HarpAR proposé a été évalué à la fois sur des volontaires sains et sur des patients ayant différents niveaux d'ischémie.

De plus, nous avons proposé un nouveau pipeline de simulation multimodale pour générer des séquences d'images US et IRM réalistes pour le même sujet virtuel. Des acquisitions de modèle, le modèle électromécanique et les simulateurs physiques ont été combinés dans le cadre de simulation. La géométrie du cœur a été segmentée à partir d'images réelles d'IRM cine. Le modèle électromécanique a été utilisé pour simuler des champs de déformation, y compris des coeurs sains et pathologiques. Des séquences de modèles ont été recalées aux simulations par une nouvelle technique de recalage visant à assurer un modèle de mouvement cohérent avec le modèle électromécanique. De plus, une fonction de pondération gaussienne a été proposée pour lisser la transition entre le myocarde et l'arrière-plan. Enfin, les amplitudes de rétrodiffusion et les densités de protons ont été dérivées des images déformées afin d'exploiter les simulateurs physiques correspondants pour générer des images. Au total, nous avons simulé 18 patients virtuels (3 sains, 3 dyssynchronies et 12 ischémies), chacun avec une séquence d'IRM cine, une séquence d'échocardiographie 3D et trois canaux d'IRM marquée.

Enfin, nous avons montré une étude préliminaire de benchmarking à l'aide des images simulées. Nous avons comparé la performance de deux méthodes de suivi de mouvements en fonction de la précision sur le mouvement et la déformation. L'algorithme HarpAR développé initialement pour la gestion de données IRM marquées a été généralisé, ce qui a conduit à un algorithme générique nommé gHarpAR. Il a été comparé à un autre algorithme générique SparseDemons sur toutes les trois modalités (US, IRM cine, IRM marquée). Les résultats ont montré que SparseDemons surclasse gHarpAR dans la quantification d'IRM cine. En effet, une régularisation plus importante est nécessaire en IRM ciné, où le myocarde n'est pas marqué. Étant donné que l'algorithme SparseDemons impose une régularisation plus forte au-delà du domaine de myocarde, il permet d'obtenir de meilleures précisions. Concernant l'IRM marquée, les deux méthodes obtiennent des précisions similaires sur le mouvement ainsi que deux composants de déformations (circumférentielle et longitudinale). Cependant, gHarpAR estime des déformations radiales beaucoup plus précises, grâce à la contrainte d'incompressibilité.

7.2 Perspective

Le suivi de mouvements cardiaques et la simulation d'images sont des domaines de recherche très actifs et il existe encore beaucoup de questions ouvertes. Tout d'abord,

malgré l'adoption d'un cadre multi-résolution visant à traiter de gros mouvements cardiaques, l'erreur de *tag jumping* [Osman *et al.* (1999)] peut encore se produire. De part notre expérience, le *tag jumping* se passe généralement sur la paroi latérale où le déplacement longitudinal entre deux instants consécutifs pourrait être significatif. Bien que le *tag jumping* soit largement un problème reconnu, il y a eu peu d'études pertinentes adressant ce problème. Il serait intéressant de concevoir des techniques spécifiques pour les traiter. Pour nous, il s'agit d'un sujet qui nécessite une recherche approfondie dans le domaine du traitement d'images IRM marquées.

Deuxièmement, les patients virtuels multimodaux simulés pourraient être utilisés pour comparer le suivi des caractéristiques d'IRM cine par rapport à la quantification d'IRM marquée et au suivi des speckles en US. Dernièrement, on constate que de plus en plus de travaux cherchent à prouver que le suivi des caractéristiques d'IRM ciné peut égaler les estimations de déformations à partir de l'IRM marquée. Sur les patients, [Hor *et al.* (2010)] [Moody *et al.* (2013)] [Moody *et al.* (2015)] a rapporté respectivement que la déformation circonférentielle, longitudinale et la déformation globale calculées à partir du suivi des caractéristiques d'IRM cine est fortement corrélées aux résultats dérivés des images IRM marquées. De plus, Onishi *et al.* [Onishi *et al.* (2013)] montrent que les mesures de la dyssynchronie calculées à partir du suivi des caractéristiques d'IRM cine sont en accord avec ceux de l'échocardiographie sur les données de patients. Cependant, toutes les études ci-dessus montrent simplement que le suivi des caractéristiques d'IRM cine quantifient des valeurs de déformation similaires à l'IRM marquée ou l'échographie en montrant la corrélation entre les deux résultats. Quelle modalité surclasse les autres, dans quel aspect et dans quelle mesure sont encore des questions ouvertes. Nous pensons qu'il serait important d'effectuer une comparaison quantitative en utilisant des séquences synthétiques multimodales simulées. Cela permettrait d'évaluer le suivi des caractéristiques d'IRM cine à un niveau beaucoup plus détaillé.

Appendix

Appendix A

Appendix 1

A.1 Computation of the spatial derivatives and the temporal differences of the true phase

This section aims to provide more details about the HARP phase tracking introduced in Section 4.3.1 of Chapter 4. The dense motion estimation is formulated on the true phase ϕ_k^t , *i.e.* phases without wrarpping artifacts. However, in practice, only wrapped HARP phases a_k^t can be computed due to numerical issues. Fortunately, for the optical flow computation, only the spatial derivatives and the temporal differences of the true phase are required as is seen in Eq. 4.12 and Eq. 4.13. Both of them can actually be computed from the wrapped HARP phases a_k^t by the method described in [Osman *et al.* (1999)]. To do so, we need first define a wrapping operator \mathcal{W} :

$$\mathcal{W}(x) = \text{mod}(x + \pi, 2\pi) - \pi \quad (\text{A.1})$$

The spatial derivatives in Eq. 4.12 were then computed as follows:

$$\nabla \phi_k^{t-1} = \begin{cases} \nabla a_k^{t-1}, & \text{if } \|\nabla a_k^{t-1}\| \leq \|\nabla \mathcal{W}(a_k^{t-1} + \pi)\| \\ \nabla \mathcal{W}(a_k^{t-1} + \pi), & \text{otherwise} \end{cases} \quad (\text{A.2})$$

Under the small motion assumption, more precisely, provided that $|\phi_1^t(\mathbf{x}) - \phi_1^{t-1}(\mathbf{x} + \tilde{\mathbf{u}}_t)| < \pi$, the phase difference between two consecutive time frames (Eq. 4.13) can be computed in the following way:

$$\phi_1^t(\mathbf{x}) - \phi_1^{t-1}(\mathbf{x} + \tilde{\mathbf{u}}_t) = \mathcal{W}\left(a_1^t(\mathbf{x}) - a_1^{t-1}(\mathbf{x} + \tilde{\mathbf{u}}_t)\right) \quad (\text{A.3})$$

For those interested, please refer to [Osman *et al.* (1999)] for more detailed descriptions.

Appendix B

Appendix 2

B.1 Compute RF flip angles

In Sect. 5.2.2 of Chapter 5, we mentioned that RF flip angles could be easily computed. We explain the details in the following part. In CSPAMM acquisitions [Fischer *et al.* (1993)], RF flip angles are ensured to satisfy the following condition [Ryf *et al.* (2005)]:

$$\alpha_{n-1} = \arctan(\sin(\alpha_n)) \cdot \exp\left\{-\frac{\Delta t}{T_1^{myo}}\right\} \quad (\text{A.1})$$

where α_n is the flip angle for acquiring the frame n , Δt is the temporal resolution and T_1^{myo} is the average myocardial T_1 relaxation time. Since the last RF flip angle was available from the DICOM header, we then derived all the RF flip angles backward by Eq. A.1. Similarly, Eq. A.1 was used for computing all the flip angles of the simulations denoted as α_k^s .

B.2 Refine the tracking of RV

In Sect. 5.2.3 of Chapter 5, LV and RV were tracked separately. To avoid possible distortions at the LV/RV border, we propose to update RV displacements by a method detailed in the following. We first built a Thin plate spline transformation Ψ upon LV displacements tracked by HarpAR. The displacements of RV points \mathbf{x} are then corrected *a posteriori* by weighted sums of $\Psi(\mathbf{x})$ and SparseDemons tracking results denoted as $\mathbf{u}^s(\mathbf{x})$:

$$\begin{aligned} \mathbf{u}(\mathbf{x}) &= v(\mathbf{x})\Psi(\mathbf{x}) + (1 - v(\mathbf{x}))\mathbf{u}^s(\mathbf{x}) \\ \text{with } v(\mathbf{x}) &= e^{-\frac{d(\mathbf{x})}{r}} \end{aligned} \quad (\text{A.2})$$

where $d(\mathbf{x})$ is the distance of \mathbf{x} to the LV. r is a constant with default value equals 5mm in our experiments.

B.3 Colormap used for displaying strain curves

Fig. A.1 shows the colormap used for displaying the regional strain curves (Sect. 5.3.3 of Chapter 5).

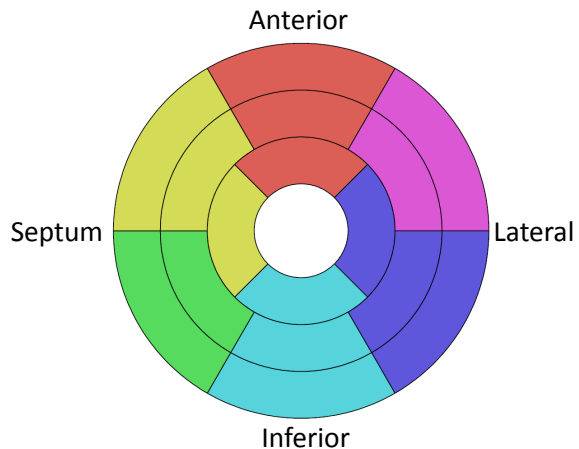


Figure A.1: The colormap used for displaying the regional strain curves at the segmental AHA level.

Publications

Journal article

1. **Y. Zhou**, S. Giffard-Roisin, M. De Craene, S. Camarasu-Pop, J. D'hooge, M. Alessandrini, D. Friboulet, M. Sermesant, O. Bernard, "A framework for the generation of realistic synthetic cardiac ultrasound and magnetic resonance imaging sequences from the same virtual patients", *Special Issue on Simulation and Synthesis in Medical Imaging, IEEE Transactions on Medical Imaging*, accepted (minor revision), 2017.
2. **Y. Zhou**, O. Bernard, E. Saloux, A. Manrique, P. Allain, S. Makram-Ebeid, M. De Craene, "3D harmonic phase tracking with anatomical regularization", *Medical Image Analysis*, 26(1): 70-81, 2015.

International conference paper

1. **Y. Zhou**, M. De Craene, O. Somphone, M. Sermesant, O. Bernard, "Generation of realistic 4D synthetic CSPAMM tagged MR sequences for benchmarking cardiac motion tracking algorithms", *In International Workshop on Simulation and Synthesis in Medical Imaging*, Athens, Greece, pp. 108-117, 2016.
2. **Y. Zhou**, M. De Craene, M. Sermesant, O. Bernard, "Phase-Based registration of cardiac tagged MR images by incorporating anatomical constraints", *In International Workshop on Statistical Atlases and Computational Models of the Heart*, Athens, Greece, pp. 39-47, 2016.
3. **Y. Zhou**, M. De Craene, O. Bernard, "Phase-based registration of cardiac tagged MR images using anatomical deformation model", *IEEE International Symposium on Biomedical Imaging (ISBI)*, Prague, Czech Republic, pp. 617-620, 2016.

Bibliography

- [Alessandrini *et al.* (2012)a] Alessandrini, M., Liebgott, H., Basarab, A., Clarysse, P., and Bernard, O. (2012a). Monogenic signal for cardiac motion analysis from tagged magnetic resonance image sequences. In *Computing in Cardiology (CinC), 2012*, pages 685–688. IEEE.
- [Alessandrini *et al.* (2012)b] Alessandrini, M., Liebgott, H., Friboulet, D., and Bernard, O. (2012b). Simulation of realistic echocardiographic sequences for ground-truth validation of motion estimation. In *2012 19th IEEE International Conference on Image Processing*, pages 2329–2332. IEEE.
- [Alessandrini *et al.* (2013)] Alessandrini, M., Basarab, A., Liebgott, H., and Bernard, O. (2013). Myocardial motion estimation from medical images using the monogenic signal. *Image Processing, IEEE Transactions on*, 22(3):1084–1095.
- [Alessandrini *et al.* (2015)] Alessandrini, M., De Craene, M., Bernard, O., Giffard-Roisin, S., Allain, P., Waechter-Stehle, I., Weese, J., Saloux, E., Delingette, H., Sermesant, M., *et al.* (2015). A pipeline for the generation of realistic 3d synthetic echocardiographic sequences: methodology and open-access database. *IEEE transactions on medical imaging*, 34(7):1436–1451.
- [Alessandrini *et al.* (2016)] Alessandrini, M., Heyde, B., Queirós, S., Cygan, S., Zontak, M., Somphone, O., Bernard, O., Sermesant, M., Delingette, H., Barbosa, D., *et al.* (2016). Detailed evaluation of five 3d speckle tracking algorithms using synthetic echocardiographic recordings. *IEEE transactions on medical imaging*, 35(8):1915–1926.
- [Aletras *et al.* (1999)] Aletras, A. H., Ding, S., Balaban, R. S., and Wen, H. (1999). Dense: displacement encoding with stimulated echoes in cardiac functional mri. *Journal of Magnetic Resonance*, 137(1):247–252.
- [Amini *et al.* (2001)] Amini, A., Chen, Y., Elayyadi, M., and Radeva, P. (2001). Tag surface reconstruction and tracking of myocardial beads from spamm-mri with parametric b-spline surfaces. *Medical Imaging, IEEE Transactions on*, 20(2):94–103.
- [Aquaro *et al.* (2017)] Aquaro, G. D., Camastra, G., Monti, L., Lombardi, M., Pepe, A., Castelletti, S., Maestrini, V., Todiere, G., Masci, P., Giovine, G., *et al.* (2017). Reference values of cardiac volumes, dimensions, and new functional parameters by mr: A multicenter, multivendor study. *Journal of Magnetic Resonance Imaging*, 45(4):1055–1067.
- [Arts *et al.* (2010)] Arts, T., Prinzen, F., Delhaas, T., Milles, J., Rossi, A., and Clarysse, P. (2010). Mapping displacement and deformation of the heart with local sine-wave modeling. *Medical Imaging, IEEE Transactions on*, 29(5):1114–1123.

- [Aune *et al.* (2010)] Aune, E., Bækkevar, M., Rødevand, O., and Otterstad, J. E. (2010). Reference values for left ventricular volumes with real-time 3-dimensional echocardiography. *Scandinavian Cardiovascular Journal*, 44(1):24–30.
- [Axel *et al.* (2005)] Axel, L., Montillo, A., and Kim, D. (2005). Tagged magnetic resonance imaging of the heart: a survey. *Medical image analysis*, 9(4):376–393.
- [Axel and Dougherty (1989)a] Axel, L. and Dougherty, L. (1989a). Mr imaging of motion with spatial modulation of magnetization. *Radiology*, 171(3):841–845.
- [Axel and Dougherty (1989)b] Axel, L. and Dougherty, L. (1989b). Mr imaging of motion with spatial modulation of magnetization. *Radiology*, 171(3):841–845.
- [Blessberger and Binder (2010)] Blessberger, H. and Binder, T. (2010). Two dimensional speckle tracking echocardiography: basic principles. *Heart*, 96(9):716–722.
- [Bogarapu *et al.* (2016)] Bogarapu, S., Puchalski, M. D., Everitt, M. D., Williams, R. V., Weng, H.-Y., and Menon, S. C. (2016). Novel cardiac magnetic resonance feature tracking (cmr-ft) analysis for detection of myocardial fibrosis in pediatric hypertrophic cardiomyopathy. *Pediatric cardiology*, 37(4):663–673.
- [Boltz *et al.* (2010)] Boltz, T. F., Pavlicek, W., Paden, R., Renno, M., Jensen, A., and Akay, M. (2010). An anthropomorphic beating heart phantom for cardiac x-ray ct imaging evaluation. *Journal of applied clinical medical physics*, 11(1).
- [Bookstein (1989)] Bookstein, F. L. (1989). Principal warps: Thin-plate splines and the decomposition of deformations. *IEEE Transactions on pattern analysis and machine intelligence*, 11(6):567–585.
- [Chandrashekara *et al.* (2004)] Chandrashekara, R., Mohiaddin, R., and Rueckert, D. (2004). Analysis of 3-d myocardial motion in tagged mr images using nonrigid image registration. *Medical Imaging, IEEE Transactions on*, 23(10):1245–1250.
- [Chen *et al.* (2005)] Chen, X., Xie, H., Erkamp, R., Kim, K., Jia, C., Rubin, J., and O’donnell, M. (2005). 3-d correlation-based speckle tracking. *Ultrasonic Imaging*, 27(1):21–36.
- [Chen *et al.* (2010)] Chen, T., Wang, X., Chung, S., Metaxas, D., and Axel, L. (2010). Automated 3d motion tracking using gabor filter bank, robust point matching, and deformable models. *Medical Imaging, IEEE Transactions on*, 29(1):1–11.
- [Cheng *et al.* (2013)] Cheng, S., Larson, M. G., McCabe, E. L., Osypiuk, E., Lehman, B. T., Stanchev, P., Aragam, J., Benjamin, E. J., Solomon, S. D., and Vasan, R. S. (2013). Reproducibility of speckle-tracking-based strain measures of left ventricular function in a community-based study. *Journal of the American Society of Echocardiography*, 26(11):1258–1266.
- [Clark *et al.* (1991)] Clark, N. R., Reichek, N., Bergey, P., Hoffman, E. A., Brownson, D., Palmon, L., and Axel, L. (1991). Circumferential myocardial shortening in the normal human left ventricle. assessment by magnetic resonance imaging using spatial modulation of magnetization. *Circulation*, 84(1):67–74.
- [Clarysse *et al.* (2011)] Clarysse, P., Tafazzoli, J., Delachartre, P., and Croisille, P. (2011). Simulation based evaluation of cardiac motion estimation methods in tagged-mr image sequences. *Journal of Cardiovascular Magnetic Resonance*, 13(1):1–1.

- [Cressie and Whitford (1986)] Cressie, N. and Whitford, H. (1986). How to use the two sample t-test. *Biometrical Journal*, 28(2):131–148.
- [Crosby *et al.* (2009)] Crosby, J., Amundsen, B. H., Hergum, T., Remme, E. W., Langeland, S., and Torp, H. (2009). 3-d speckle tracking for assessment of regional left ventricular function. *Ultrasound in medicine & biology*, 35(3):458–471.
- [Crum *et al.* (1997)] Crum, W. R., Berry, E., Ridgway, J. P., Sivananthan, U. M., Tan, L.-B., and Smith, M. A. (1997). Simulation of two-dimensional tagged mri. *Journal of Magnetic Resonance Imaging*, 7(2):416–424.
- [Crum *et al.* (1998)] Crum, W. R., Berry, E., Ridgway, J. P., Sivananthan, U. M., Tan, L. B., and Smith, M. A. (1998). Frequency-domain simulation of mr tagging. *Journal of Magnetic Resonance Imaging*, 8(5):1040–1050.
- [De Craene *et al.* (2011)] De Craene, M., Tobon-Gomez, C., Butakoff, C., Duchateau, N., Piella, G., Rhode, K. S., and Frangi, A. F. (2011). Temporal diffeomorphic free form deformation (tdffd) applied to motion and deformation quantification of tagged mri sequences. In *International Workshop on Statistical Atlases and Computational Models of the Heart*, pages 68–77. Springer.
- [De Craene *et al.* (2013)] De Craene, M., Marchesseau, S., Heyde, B., Gao, H., Alessandrini, M., Bernard, O., Piella, G., Porras, A. R., Tautz, L., Hennemuth, A., *et al.* (2013). 3d strain assessment in ultrasound (straus): A synthetic comparison of five tracking methodologies. *Medical Imaging, IEEE Transactions on*, 32(9):1632–1646.
- [Duan *et al.* (2006)] Duan, Q., Angelini, E., Gerard, O., Homma, S., and Laine, A. (2006). Comparing optical-flow based methods for quantification of myocardial deformations on rt3d ultrasound. In *Biomedical Imaging: Nano to Macro, 2006. 3rd IEEE International Symposium on*, pages 173–176. IEEE.
- [Duan *et al.* (2009)a] Duan, Q., Angelini, E. D., Herz, S. L., Ingrassia, C. M., Costa, K. D., Holmes, J. W., Homma, S., and Laine, A. F. (2009a). Region-based endocardium tracking on real-time three-dimensional ultrasound. *Ultrasound in medicine & biology*, 35(2):256–265.
- [Duan *et al.* (2009)b] Duan, Q., Parker, K. M., Lorsakul, A., Angelini, E. D., Hyodo, E., Homma, S., Holmes, J. W., and Laine, A. F. (2009b). Quantitative validation of optical flow based myocardial strain measures using sonomicrometry. In *Biomedical Imaging: From Nano to Macro, 2009. ISBI'09. IEEE International Symposium on*, pages 454–457. IEEE.
- [Duchateau *et al.* (2016)] Duchateau, N., De Craene, M., Allain, P., Saloux, E., and Sermesant, M. (2016). Infarct localization from myocardial deformation: Prediction and uncertainty quantification by regression from a low-dimensional space. *IEEE transactions on medical imaging*.
- [EchoNoRMAL *et al.* (2015)] EchoNoRMAL, T. *et al.* (2015). Ethnic-specific normative reference values for echocardiographic la and lv size, lv mass, and systolic function: The echonormal study. *JACC: Cardiovascular Imaging*, 8(6):656–665.
- [Fischer *et al.* (1993)] Fischer, S. E., McKinnon, G., Maier, S., and Boesiger, P. (1993). Improved myocardial tagging contrast. *Magnetic resonance in medicine*, 30(2):191–200.

- [Fischer *et al.* (1999)] Fischer, S. E., Wickline, S. A., and Lorenz, C. H. (1999). Novel real-time r-wave detection algorithm based on the vectorcardiogram for accurate gated magnetic resonance acquisitions. *Magnetic Resonance in Medicine*, 42(2):361–370.
- [Florack *et al.* (2007)] Florack, L., van Assen, H., and Suinesiaputra, A. (2007). Dense multiscale motion extraction from cardiac cine mr tagging using harp technology. In *Computer Vision, 2007. ICCV 2007. IEEE 11th International Conference on*, pages 1–8. IEEE.
- [Gao *et al.* (2009)] Gao, H., Choi, H. F., Claus, P., Boonen, S., Jaecques, S., Lenthe, G. H. V., Perre, G. V. D., Lauriks, W., and D’hooge, J. (2009). A fast convolution-based methodology to simulate 2-d/3-d cardiac ultrasound images. *IEEE Transactions on Ultrasonics, Ferroelectrics, and Frequency Control*, 56(2):404–409.
- [Garrison *et al.* (1982)] Garrison, J., Ebert, W., Jenkins, R., Yionoulis, S., Malcom, H., Heyler, G., Shoukas, A. A., Maughan, W. L., and Sagawa, K. (1982). Measurement of three-dimensional positions and motions of large numbers of spherical radiopaque markers from biplane cineradiograms. *Computers and biomedical research*, 15(1):76–96.
- [Gilbert *et al.* (2014)] Gilbert, K., Cowan, B. R., Suinesiaputra, A., Occleshaw, C., and Young, A. A. (2014). Rapid d-affine biventricular cardiac function with polar prediction. In *Medical Image Computing and Computer-Assisted Intervention—MICCAI 2014*, pages 546–553. Springer.
- [Glatard *et al.* (2013)] Glatard, T., Lartizien, C., Gibaud, B., Da Silva, R. F., Forestier, G., Cervenansky, F., Alessandrini, M., Benoit-Cattin, H., Bernard, O., Camarasu-Pop, S., *et al.* (2013). A virtual imaging platform for multi-modality medical image simulation. *IEEE Transactions on Medical Imaging*, 32(1):110–118.
- [Groth *et al.* (2012)] Groth, A., Weese, J., and Lehmann, H. (2012). Robust left ventricular myocardium segmentation for multi-protocol mr. In *SPIE Medical Imaging*. International Society for Optics and Photonics.
- [Haase (1990)] Haase, A. (1990). Snapshot flash mri. applications to t1, t2, and chemical-shift imaging. *Magnetic Resonance in Medicine*, 13(1):77–89.
- [Haddad *et al.* (2005)] Haddad, R., Clarysse, P., Orkisz, M., Croisille, P., Revel, D., and Magnin, I. E. (2005). A realistic anthropomorphic numerical model of the beating heart. In *International Workshop on Functional Imaging and Modeling of the Heart*, pages 384–393. Springer.
- [Haddad *et al.* (2007)] Haddad, R., Magnin, I. E., and Clarysse, P. (2007). A new fully-digital anthropomorphic and dynamic thorax/heart model. In *Engineering in Medicine and Biology Society, 2007. EMBS 2007. 29th Annual International Conference of the IEEE*, pages 5999–6002. IEEE.
- [Heyde *et al.* (2013)] Heyde, B., Barbosa, D., Claus, P., Maes, F., and D’hooge, J. (2013). Three-dimensional cardiac motion estimation based on non-rigid image registration using a novel transformation model adapted to the heart. In *STACOM*, volume 7746 of *LNCS*, pages 142–150. Springer.
- [Heyde *et al.* (2016)a] Heyde, B., Alessandrini, M., Hermans, J., Barbosa, D., Claus, P., and D’hooge, J. (2016a). Anatomical image registration using volume conservation to

- assess cardiac deformation from 3d ultrasound recordings. *IEEE transactions on medical imaging*, 35(2):501–511.
- [Heyde *et al.* (2016)b] Heyde, B., Bottemus, N., D’hooge, J., and Trahey, G. E. (2016b). Evaluation of the transverse oscillation technique for cardiac phased-array imaging: a theoretical study. *IEEE Transactions on Ultrasonics, Ferroelectrics, and Frequency Control*.
- [Ho and Solomon (2006)] Ho, C. Y. and Solomon, S. D. (2006). A clinician’s guide to tissue doppler imaging. *Circulation*, 113(10):e396–e398.
- [Hor *et al.* (2010)] Hor, K. N., Gottliebson, W. M., Carson, C., Wash, E., Cnota, J., Fleck, R., Wansapura, J., Klimeczek, P., Al-Khalidi, H. R., Chung, E. S., *et al.* (2010). Comparison of magnetic resonance feature tracking for strain calculation with harmonic phase imaging analysis. *JACC: Cardiovascular Imaging*, 3(2):144–151.
- [Hor *et al.* (2011)] Hor, K. N., Baumann, R., Pedrizzetti, G., Tonti, G., Gottliebson, W. M., Taylor, M., Benson, D. W., and Mazur, W. (2011). Magnetic resonance derived myocardial strain assessment using feature tracking. *JoVE (Journal of Visualized Experiments)*, (48):e2356–e2356.
- [Jenkins *et al.* (2009)] Jenkins, C., Moir, S., Chan, J., Rakhit, D., Haluska, B., and Marwick, T. H. (2009). Left ventricular volume measurement with echocardiography: a comparison of left ventricular opacification, three-dimensional echocardiography, or both with magnetic resonance imaging. *European heart journal*, 30(1):98–106.
- [Jochimsen *et al.* (2006)] Jochimsen, T. H., Schäfer, A., Bammer, R., and Moseley, M. E. (2006). Efficient simulation of magnetic resonance imaging with bloch–torrey equations using intra-voxel magnetization gradients. *Journal of Magnetic Resonance*, 180(1):29–38.
- [Kause *et al.* (2014)] Kause, H. B., Filatova, O. G., Duits, R., Bruurmijn, L. M., Fuster, A., Westenberg, J. J., Florack, L. M., and van Assen, H. C. (2014). Direct myocardial strain assessment from frequency estimation in tagging mri. In *Statistical Atlases and Computational Models of the Heart. Imaging and Modelling Challenges*, pages 212–219. Springer.
- [Kleijn *et al.* (2012)] Kleijn, S. A., Aly, M. F., Terwee, C. B., van Rossum, A. C., and Kamp, O. (2012). Reliability of left ventricular volumes and function measurements using three-dimensional speckle tracking echocardiography. *European Heart Journal-Cardiovascular Imaging*, 13(2):159–168.
- [Kuijer *et al.* (2001)] Kuijer, J., Jansen, E., Marcus, J. T., van Rossum, A. C., and Heethaar, R. M. (2001). Improved harmonic phase myocardial strain maps. *Magnetic Resonance in Medicine*, 46(5):993–999.
- [Kwan *et al.* (1999)] Kwan, R.-S., Evans, A. C., and Pike, G. B. (1999). Mri simulation-based evaluation of image-processing and classification methods. *IEEE transactions on medical imaging*, 18(11):1085–1097.
- [Leung *et al.* (2011)] Leung, K. E., Danilouchkine, M. G., van Stralen, M., de Jong, N., van der Steen, A. F., and Bosch, J. G. (2011). Left ventricular border tracking using cardiac motion models and optical flow. *Ultrasound in medicine & biology*, 37(4):605–616.

- [Liang *et al.* (2007)] Liang, J., Wang, Y., and Jia, Y. (2007). Cardiac motion estimation from tagged mri using 3d-harp and nurbs volumetric model. In *Computer Vision–ACCV 2007*, pages 512–521. Springer.
- [Lin and Duncan (2004)] Lin, N. and Duncan, J. S. (2004). Generalized robust point matching using an extended free-form deformation model: Application to cardiac images. In *Biomedical Imaging: Nano to Macro, 2004. IEEE International Symposium on*, pages 320–323. IEEE.
- [Liu *et al.* (2012)] Liu, X., Abd-Elmoniem, K. Z., Stone, M., Murano, E. Z., Zhuo, J., Gullapalli, R. P., and Prince, J. L. (2012). Incompressible deformation estimation algorithm (idea) from tagged mr images. *Medical Imaging, IEEE Transactions on*, 31(2):326–340.
- [Liu and Prince (2010)] Liu, X. and Prince, J. L. (2010). Shortest path refinement for motion estimation from tagged mr images. *Medical Imaging, IEEE Transactions on*, 29(8):1560–1572.
- [Lopata *et al.* (2011)] Lopata, R. G., Nillesen, M. M., Thijssen, J. M., Kapusta, L., and de Korte, C. L. (2011). Three-dimensional cardiac strain imaging in healthy children using rf-data. *Ultrasound in medicine & biology*, 37(9):1399–1408.
- [Makram-Ebeid and Somphone (2007)] Makram-Ebeid, S. and Somphone, O. (2007). Non-rigid image registration using a hierarchical partition of unity finite element method. In *Computer Vision, 2007. ICCV 2007. IEEE 11th International Conference on*, pages 1–8. IEEE.
- [Marchesseau *et al.* (2013)] Marchesseau, S., Delingette, H., Sermesant, M., and Ayache, N. (2013). Fast parameter calibration of a cardiac electromechanical model from medical images based on the unscented transform. *Biomechanics and modeling in mechanobiology*, 12(4):815–831.
- [Maret *et al.* (2009)] Maret, E., Todt, T., Brudin, L., Nylander, E., Swahn, E., Ohlsson, J. L., and Engvall, J. E. (2009). Functional measurements based on feature tracking of cine magnetic resonance images identify left ventricular segments with myocardial scar. *Cardiovascular ultrasound*, 7(1):53.
- [McLeod *et al.* (2013)] McLeod, K., Seiler, C., Toussaint, N., Sermesant, M., and Pennec, X. (2013). Regional analysis of left ventricle function using a cardiac-specific polyaffine motion model. In *Functional Imaging and Modeling of the Heart*, pages 483–490. Springer.
- [Mendis (2014)] Mendis, S. (2014). *Global status report on noncommunicable diseases 2014*. World Health Organization reports.
- [Miller Jr (1997)] Miller Jr, R. G. (1997). *Beyond ANOVA: basics of applied statistics*. CRC Press.
- [Mondillo *et al.* (2011)] Mondillo, S., Galderisi, M., Mele, D., Cameli, M., Lomoriello, V. S., Zacà, V., Ballo, P., D’Andrea, A., Muraru, D., Losi, M., *et al.* (2011). Speckle-tracking echocardiography. *Journal of Ultrasound in Medicine*, 30(1):71–83.
- [Moody *et al.* (2013)] Moody, W. E., Taylor, R. J., Edwards, N. C., Umar, F., Chue, C. D., Taylor, T. J., Ferro, C. J., Townend, J. N., Leyva, F., and Steeds, R. (2013). Comparison of magnetic resonance feature tracking for longitudinal strain calculation

- with spatial modulation of magnetization imaging analysis. *Journal of Cardiovascular Magnetic Resonance*, 15(S1):P123.
- [Moody *et al.* (2015)] Moody, W. E., Taylor, R. J., Edwards, N. C., Chue, C. D., Umar, F., Taylor, T. J., Ferro, C. J., Young, A. A., Townend, J. N., Leyva, F., *et al.* (2015). Comparison of magnetic resonance feature tracking for systolic and diastolic strain and strain rate calculation with spatial modulation of magnetization imaging analysis. *Journal of Magnetic Resonance Imaging*, 41(4):1000–1012.
- [Mor-Avi *et al.* (2011)] Mor-Avi, V., Lang, R. M., Badano, L. P., Belohlavek, M., Cardim, N. M., Derumeaux, G., Galderisi, M., Marwick, T., Nagueh, S. F., Sengupta, P. P., *et al.* (2011). Current and evolving echocardiographic techniques for the quantitative evaluation of cardiac mechanics: Ase/eae consensus statement on methodology and indications: endorsed by the japanese society of echocardiography. *Journal of the American Society of Echocardiography*, 24(3):277–313.
- [Mory *et al.* (2012)] Mory, B., Somphone, O., Prevost, R., and Ardon, R. (2012). Real-time 3d image segmentation by user-constrained template deformation. In *Medical Image Computing and Computer-Assisted Intervention–MICCAI 2012*, pages 561–568. Springer.
- [O'Donnell *et al.* (1994)] O'Donnell, M., Skovoroda, A. R., Shapo, B. M., and Emelianov, S. Y. (1994). Internal displacement and strain imaging using ultrasonic speckle tracking. *IEEE transactions on ultrasonics, ferroelectrics, and frequency control*, 41(3):314–325.
- [Onishi *et al.* (2013)] Onishi, T., Saha, S. K., Ludwig, D. R., Onishi, T., Marek, J. J., Cavalcante, J. L., Schelbert, E. B., Schwartzman, D., and Gorcsan, J. (2013). Feature tracking measurement of dyssynchrony from cardiovascular magnetic resonance cine acquisitions: comparison with echocardiographic speckle tracking. *Journal of Cardiovascular Magnetic Resonance*, 15(1):95.
- [Osman *et al.* (1999)] Osman, N. F., Kerwin, W. S., McVeigh, E. R., and Prince, J. L. (1999). Cardiac motion tracking using cine harmonic phase (harp) magnetic resonance imaging. *Magnetic resonance in medicine: official journal of the Society of Magnetic Resonance in Medicine/Society of Magnetic Resonance in Medicine*, 42(6):1048.
- [Osman *et al.* (2000)] Osman, N. F., McVeigh, E. R., and Prince, J. L. (2000). Imaging heart motion using harmonic phase mri. *IEEE transactions on medical imaging*, 19(3):186–202.
- [Pan *et al.* (2005)] Pan, L., Prince, J. L., Lima, J. A., and Osman, N. F. (2005). Fast tracking of cardiac motion using 3d-harp. *Biomedical Engineering, IEEE Transactions on*, 52(8):1425–1435.
- [Papademetris *et al.* (2002)] Papademetris, X., Sinusas, A. J., Dione, D. P., Constable, R. T., and Duncan, J. S. (2002). Estimation of 3-d left ventricular deformation from medical images using biomechanical models. *IEEE transactions on medical imaging*, 21(7):786–800.
- [Pedrizzetti *et al.* (2016)] Pedrizzetti, G., Claus, P., Kilner, P. J., and Nagel, E. (2016). Principles of cardiovascular magnetic resonance feature tracking and echocardiographic speckle tracking for informed clinical use. *Journal of Cardiovascular Magnetic Resonance*, 18(1):51.

- [Perperidis *et al.* (2005)] Perperidis, D., Mohiaddin, R. H., and Rueckert, D. (2005). Spatio-temporal free-form registration of cardiac mr image sequences. *Medical image analysis*, 9(5):441–456.
- [Prakosa *et al.* (2013)] Prakosa, A., Sermesant, M., Delingette, H., Marchesseau, S., Sa-loux, E., Allain, P., Villain, N., and Ayache, N. (2013). Generation of synthetic but visually realistic time series of cardiac images combining a biophysical model and clinical images. *Medical Imaging, IEEE Transactions on*, 32(1):99–109.
- [Prince and McVeigh (1992)] Prince, J. and McVeigh, E. (1992). Motion estimation from tagged mr image sequences. *Medical Imaging, IEEE Transactions on*, 11(2):238–249.
- [Qian *et al.* (2011)] Qian, Z., Liu, Q., Metaxas, D. N., and Axel, L. (2011). Identifying regional cardiac abnormalities from myocardial strains using nontracking-based strain estimation and spatio-temporal tensor analysis. *Medical Imaging, IEEE Transactions on*, 30(12):2017–2029.
- [Queirós *et al.* (2014)] Queirós, S., Barbosa, D., Heyde, B., Morais, P., Vilaça, J. L., Fri-boulet, D., Bernard, O., and DâŽhooge, J. (2014). Fast automatic myocardial segmentation in 4d cine cmr datasets. *Medical image analysis*, 18(7):1115–1131.
- [Rademakers *et al.* (1994)] Rademakers, F. E., Rogers, W. J., Guier, W. H., Hutchins, G. M., Siu, C. O., Weisfeldt, M. L., Weiss, J. L., and Shapiro, E. P. (1994). Relation of regional cross-fiber shortening to wall thickening in the intact heart. three-dimensional strain analysis by nmr tagging. *Circulation*, 89(3):1174–1182.
- [Reisner *et al.* (2004)] Reisner, S. A., Lysyansky, P., Agmon, Y., Mutlak, D., Lessick, J., and Friedman, Z. (2004). Global longitudinal strain: a novel index of left ventricular systolic function. *Journal of the American Society of Echocardiography*, 17(6):630–633.
- [Reiter *et al.* (2013)] Reiter, U., Reiter, G., Dorr, K., Greiser, A., Maderthaner, R., and Fuchsjäger, M. (2013). Normal diastolic and systolic myocardial t1 values at 1.5-t mr imaging: correlations and blood normalization. *Radiology*, 271(2):365–372.
- [Ropers *et al.* (2003)] Ropers, D., Baum, U., Pohle, K., Anders, K., Ulzheimer, S., Ohne-sorge, B., Schlundt, C., Bautz, W., Daniel, W. G., and Achenbach, S. (2003). Detection of coronary artery stenoses with thin-slice multi-detector row spiral computed tomog-raphy and multiplanar reconstruction. *Circulation*, 107(5):664–666.
- [Roth *et al.* (2015)] Roth, G. A., Forouzanfar, M. H., Moran, A. E., Barber, R., Nguyen, G., Feigin, V. L., Naghavi, M., Mensah, G. A., and Murray, C. J. (2015). Demographic and epidemiologic drivers of global cardiovascular mortality. *New England Journal of Medicine*, 372(14):1333–1341.
- [Rutz (2008)] Rutz, A. K. (2008). *Advances in whole-heart MRI tagging for the assessment of myocardial motion*. PhD thesis, Diss., Eidgenössische Technische Hochschule ETH Zürich, Nr. 17902.
- [Rutz *et al.* (2008)] Rutz, A. K., Ryf, S., Plein, S., Boesiger, P., and Kozerke, S. (2008). Accelerated whole-heart 3d cspamm for myocardial motion quantification. *Magnetic Resonance in Medicine*, 59(4):755–763.

- [Ryf *et al.* (2005)] Ryf, S., Schwitter, J., Spiegel, M. A., Rutz, A. K., Luechinger, R., Crelier, G. R., and Boesiger, P. (2005). Accelerated tagging for the assessment of left ventricular myocardial contraction under physical stress. *Journal of Cardiovascular Magnetic Resonance*, 7(4):693–703.
- [Sakuma *et al.* (1993)] Sakuma, H., Fujita, N., Foo, T., Caputo, G. R., Nelson, S. J., Hartiala, J., Shimakawa, A., and Higgins, C. B. (1993). Evaluation of left ventricular volume and mass with breath-hold cine mr imaging. *Radiology*, 188(2):377–380.
- [Scheffler and Lehnhardt (2003)] Scheffler, K. and Lehnhardt, S. (2003). Principles and applications of balanced ssfp techniques. *European radiology*, 13(11):2409–2418.
- [Segars *et al.* (2010)] Segars, W., Sturgeon, G., Mendonca, S., Grimes, J., and Tsui, B. M. (2010). 4d xcat phantom for multimodality imaging research. *Medical physics*, 37(9):4902–4915.
- [Sermesant *et al.* (2006)] Sermesant, M., Moireau, P., Camara, O., Sainte-Marie, J., Andriantsimavona, R., Cimrman, R., Hill, D. L., Chapelle, D., and Razavi, R. (2006). Cardiac function estimation from mri using a heart model and data assimilation: advances and difficulties. *Medical Image Analysis*, 10(4):642–656.
- [Sheikh *et al.* (1991)] Sheikh, K. H., SMITH, S. W., RAMM, O. V., and KISSLO, J. (1991). Real-time, three-dimensional echocardiography: Feasibility and initial us. *Echocardiography*, 8(1):119–125.
- [Shi *et al.* (1999)] Shi, P., Sinusas, A. J., Constable, R. T., and Duncan, J. S. (1999). Volumetric deformation analysis using mechanics-based data fusion: Applications in cardiac motion recovery. *International Journal of Computer Vision*, 35(1):87–107.
- [Shi *et al.* (2012)] Shi, W., Zhuang, X., Wang, H., Duckett, S., Luong, D. V., Tobon-Gomez, C., Tung, K., Edwards, P. J., Rhode, K. S., Razavi, R. S., *et al.* (2012). A comprehensive cardiac motion estimation framework using both untagged and 3-d tagged mr images based on nonrigid registration. *Medical Imaging, IEEE Transactions on*, 31(6):1263–1275.
- [Shiino *et al.* (2016)] Shiino, K., Yamada, A., Ischenko, M., Khandheria, B. K., Hudaverdi, M., Speranza, V., Harten, M., Benjamin, A., Hamilton-Craig, C. R., Platts, D. G., *et al.* (2016). Intervendor consistency and reproducibility of left ventricular 2d global and regional strain with two different high-end ultrasound systems. *Eur Heart J Cardiovasc Imaging*, page jew120.
- [Singh *et al.* (2010)] Singh, G. K., Cupps, B., Pasque, M., Woodard, P. K., Holland, M. R., and Ludomirsky, A. (2010). Accuracy and reproducibility of strain by speckle tracking in pediatric subjects with normal heart and single ventricular physiology: a two-dimensional speckle-tracking echocardiography and magnetic resonance imaging correlative study. *Journal of the American Society of Echocardiography*, 23(11):1143–1152.
- [Smiseth *et al.* (2015)] Smiseth, O. A., Torp, H., Opdahl, A., Haugaa, K. H., and Urheim, S. (2015). Myocardial strain imaging: how useful is it in clinical decision making? *European heart journal*, page ehv529.
- [Somphone *et al.* (2013)] Somphone, O., De Craene, M., Ardon, R., Mory, B., Allain, P., Gao, H., D’hooge, J., Marchesseau, S., Sermesant, M., Delingette, H., *et al.* (2013). Fast

- myocardial motion and strain estimation in 3d cardiac ultrasound with sparse demons. In *Biomedical Imaging (ISBI), 2013 IEEE 10th International Symposium on*, pages 1182–1185. IEEE.
- [Suhling *et al.* (2005)] Suhling, M., Arigovindan, M., Jansen, C., Hunziker, P., and Unser, M. (2005). Myocardial motion analysis from b-mode echocardiograms. *IEEE Transactions on image processing*, 14(4):525–536.
- [Sundar *et al.* (2009)] Sundar, H., Litt, H., and Shen, D. (2009). Estimating myocardial motion by 4d image warping. *Pattern recognition*, 42(11):2514–2526.
- [Tavakoli and Sahba (2014)] Tavakoli, V. and Sahba, N. (2014). Cardiac motion and strain detection using 4d ct images: comparison with tagged mri, and echocardiography. *The international journal of cardiovascular imaging*, 30(1):175–184.
- [Taylor *et al.* (2015)] Taylor, R. J., Moody, W. E., Umar, F., Edwards, N. C., Taylor, T. J., Stegemann, B., Townend, J. N., Hor, K. N., Steeds, R. P., Mazur, W., *et al.* (2015). Myocardial strain measurement with feature-tracking cardiovascular magnetic resonance: normal values. *Eur Heart J Cardiovasc Imaging*, page jev006.
- [Tessa *et al.* (2015)] Tessa, C., Diciotti, S., Landini, N., Lilli, A., Del Meglio, J., Salvatori, L., Giannelli, M., Greiser, A., Vignali, C., and Casolo, G. (2015). Myocardial t1 and t2 mapping in diastolic and systolic phase. *The international journal of cardiovascular imaging*, 31(5):1001–1010.
- [Thirion (1998)] Thirion, J.-P. (1998). Image matching as a diffusion process: an analogy with maxwell’s demons. *Medical image analysis*, 2(3):243–260.
- [Tobon-Gomez *et al.* (2011)a] Tobon-Gomez, C., De Craene, M., Dahl, A., Kapetanakis, S., Carr-White, G., Lutz, A., Rasche, V., Etyngier, P., Kozerke, S., Schaeffter, T., *et al.* (2011a). A multimodal database for the 1 st cardiac motion analysis challenge. In *International Workshop on Statistical Atlases and Computational Models of the Heart*, pages 33–44. Springer.
- [Tobon-Gomez *et al.* (2011)b] Tobon-Gomez, C., Sukno, F., Bijnens, B., Huguet, M., and Frangi, A. (2011b). Realistic simulation of cardiac magnetic resonance studies modeling anatomical variability, trabeculae, and papillary muscles. *Magnetic Resonance in Medicine*, 65(1):280–288.
- [Tobon-Gomez *et al.* (2013)] Tobon-Gomez, C., Craene, M. D., McLeod, K., Tautz, L., Shi, W., Hennemuth, A., Prakosa, A., Wang, H., Carr-White, G., Kapetanakis, S., Lutz, A., Rasche, V., Schaeffter, T., Butakoff, C., Friman, O., Mansi, T., Sermesant, M., Zhuang, X., Ourselin, S., Peitgen, H.-O., Pennec, X., Razavi, R., Rueckert, D., Frangi, A., and Rhode, K. (2013). Benchmarking framework for myocardial tracking and deformation algorithms: An open access database. *Medical Image Analysis*, 17(6):632 – 648.
- [Tsadok *et al.* (2016)] Tsadok, Y., Friedman, Z., Haluska, B. A., Hoffmann, R., and Adam, D. (2016). Myocardial strain assessment by cine cardiac magnetic resonance imaging using non-rigid registration. *Magnetic resonance imaging*, 34(4):381–390.
- [Voigt *et al.* (2014)] Voigt, J.-U., Pedrizzetti, G., Lysyansky, P., Marwick, T. H., Houle, H., Baumann, R., Pedri, S., Ito, Y., Abe, Y., Metz, S., *et al.* (2014). Definitions for

- a common standard for 2d speckle tracking echocardiography: consensus document of the eacvi/ase/industry task force to standardize deformation imaging. *European Heart Journal-Cardiovascular Imaging*, page jeu184.
- [Voigt and Flachskampf (2004)] Voigt, J.-U. and Flachskampf, F. (2004). Strain and strain rate. *Zeitschrift für Kardiologie*, 93(4):249–258.
- [Waks *et al.* (1996)] Waks, E., Prince, J. L., and Douglas, A. S. (1996). Cardiac motion simulator for tagged mri. In *Mathematical Methods in Biomedical Image Analysis, 1996.*, *Proceedings of the Workshop on*, pages 182–191. IEEE.
- [Wang *et al.* (2011)] Wang, H., Kadbi, M., Kotys, M., Ersoy, M., Chatzimavroudis, G. P., Setser, R. M., Alshaher, M., Fischer, S. E., and Amini, A. A. (2011). Orthogonal cspamm (ocspamm) mr tagging for imaging ventricular wall motion. In *2011 Annual International Conference of the IEEE Engineering in Medicine and Biology Society*, pages 535–538. IEEE.
- [Wang *et al.* (2013)] Wang, H., Stoeck, C. T., Kozerke, S., and Amini, A. A. (2013). 3d left-ventricular deformation analysis from 3d cspamm with 3d sinmod. *Proc. Intl. Soc. Mag. Reson. Med.*
- [Wang and Amini (2012)] Wang, H. and Amini, A. A. (2012). Cardiac motion and deformation recovery from mri: a review. *Medical Imaging, IEEE Transactions on*, 31(2):487–503.
- [Wissmann *et al.* (2014)] Wissmann, L., Santelli, C., Segars, W. P., and Kozerke, S. (2014). Mrxcat: Realistic numerical phantoms for cardiovascular magnetic resonance. *Journal of Cardiovascular Magnetic Resonance*, 16(1):1.
- [Woolson (2007)] Woolson, R. (2007). Wilcoxon signed-rank test. *Wiley Encyclopedia of Clinical Trials*.
- [Yeon *et al.* (2001)] Yeon, S. B., Reichek, N., Tallant, B. A., Lima, J. A., Calhoun, L. P., Clark, N. R., Hoffman, E. A., Ho, K. K., and Axel, L. (2001). Validation of in vivo myocardial strain measurement by magnetic resonance tagging with sonomicrometry. *Journal of the American College of Cardiology*, 38(2):555–561.
- [Young (1999)] Young, A. A. (1999). Model tags: direct three-dimensional tracking of heart wall motion from tagged magnetic resonance images. *Medical image analysis*, 3(4):361–372.
- [Young *et al.* (1995)] Young, A., Kraitchman, D. L., Dougherty, L., Axel, L., *et al.* (1995). Tracking and finite element analysis of stripe deformation in magnetic resonance tagging. *Medical Imaging, IEEE Transactions on*, 14(3):413–421.
- [Young and Axel (1992)] Young, A. A. and Axel, L. (1992). Three-dimensional motion and deformation of the heart wall: estimation with spatial modulation of magnetization—a model-based approach. *Radiology*, 185(1):241–247.
- [Zerhouni *et al.* (1988)] Zerhouni, E. A., Parish, D. M., Rogers, W. J., Yang, A., and Shapiro, E. P. (1988). Human heart: tagging with mr imaging—a method for noninvasive assessment of myocardial motion. *Radiology*, 169(1):59–63.

- [Zhou *et al.* (2015)] Zhou, Y., Bernard, O., Saloux, E., Manrique, A., Allain, P., Makram-Ebeid, S., and De Craene, M. (2015). 3d harmonic phase tracking with anatomical regularization. *Medical Image Analysis*, 26(1):70–81.



INSA

FOLIO ADMINISTRATIF

THESE DE L'UNIVERSITE DE LYON OPEREE AU SEIN DE L'INSA LYON

NOM : ZHOU

DATE de SOUTENANCE : 03/07/2017

Prénoms : Yitian

TITRE : Quantification du mouvement et de la déformation cardiaques à partir d'IRM marquée tridimensionnelle sur des données acquises par des imageurs Philips

NATURE : Doctorat

Numéro d'ordre :

Ecole doctorale : ELECTRONIQUE, ELECTROTECHNIQUE, AUTOMATIQUE

Spécialité : Traitement du Signal et de l'Image

RESUME : Cardiovascular disease is one of the major causes of death worldwide. A number of heart diseases, such as hypertrophy, dilated cardiomyopathy and myocardial infarction, can be diagnosed through the analysis of cardiac images after quantifying shape and function. Recently, there is a surge in the development of fast 3D cardiac imaging techniques in both ultrasound (US) and magnetic resonance (MR) imaging, making it possible to quantify myocardial motion and strain fully in 3D. However, the application of these deformation quantification algorithms in clinical routine is somewhat held back by the lack of a solid validation. These quantification algorithms need to be thoroughly validated before being used in clinics. In this thesis, we mainly introduce a fast 3D tagged MR quantification algorithm, as well as a novel pipeline for generating synthetic cardiac US and MR image sequences for validation purposes. The main contributions are described below.

First, we proposed a novel 3D extension of the well-known harmonic phase tracking method. The point-wise phase-based optical flow tracking was combined with an anatomical regularization model in order to estimate anatomically coherent myocardial motions. In particular, special efforts were made to ensure a reasonable radial strain estimation by enforcing myocardial incompressibility through the divergence theorem. We tuned the parameters on a synthetic tagged MR dataset. The proposed HarpAR algorithm was further evaluated on both healthy volunteers and patients having different levels of ischemia. On volunteer data, the tracking accuracy was found to be as accurate as the best candidates of a recent benchmark. On patient data, strain dispersion was shown to correlate with the extent of transmural fibrosis. Besides, the ischemic segments were distinguished from healthy ones from the strain curves.

Second, we proposed a simulation pipeline for generating realistic synthetic cardiac US, cine and tagged MR sequences from the same virtual subject. Template sequences, a state-of-the-art electro-mechanical (E/M) model and physical simulators were combined in a unified framework. The E/M model was exploited for simulating groundtruth cardiac motion fields. The template sequences were registered to the simulations by a novel warping technique aimed at ensuring a synthetic motion consistent with the E/M model and a smooth transition between the myocardium and the background. Finally, backscattering amplitudes and effective proton densities were derived from the warped templates respectively for US and MR simulations to exploit the corresponding physical simulators for generating image data. In total, we simulated 18 virtual patients (3 healthy, 3 dyssynchrony and 12 ischemia), each with synthetic sequences of 3D cine MR, US and tagged MR. The synthetic images were assessed both qualitatively and quantitatively. They showed realistic image textures similar to real acquisitions. Besides, both the ejection fraction and regional strain values are in agreement with reference values published in the literature.

Finally, we showed a preliminary benchmarking study using the synthetic database. The HarpAR algorithm initially developed for processing tagged MR was extended to a generic motion tracking algorithm named as gHarpAR. We performed a comparison between gHarpAR and another tracking algorithm SparseDemons using the virtual patients simulated in this thesis. The results showed that SparseDemons outperformed gHarpAR in processing cine MR and US images. Regarding tagged MR, both methods obtained similar accuracies on motion and two strain components (circumferential and longitudinal). However, gHarpAR quantified radial strains more accurately, thanks to the myocardial incompressibility constraint. We conclude that motion quantification solutions can be improved by designing them according to the image characteristics of the modality and that a solid evaluation framework can be a key asset in comparing different algorithmic options.

MOTS-CLÉS : Cardiac motion tracking, myocardial deformation, synthetic image, quantitative validation

Laboratoire (s) de recherche : Centre de Recherche en Acquisition et Traitement de l'Image pour la Santé (CREATIS), UMR 5220, U1206, INSA-Lyon.

Directeur de thèse: FRIBOULET Denis, Professeur des Universités

Président de jury : BLOCH Isabelle

Composition du jury : BLOCH Isabelle (Rapporteur), BIJNENS Bart (Rapporteur), THIRAN Jean-Philippe (Examinateur), DE CRAENE Mathieu (Examinateur), BERNARD Olivier (Co-directeur de thèse), FRIBOULET Denis (Directeur de thèse).